PNNL-39696

Pacific Northwest
NATIONAL LABORATORY

Proudly Operated by Battelle Since 1965

Integrated Capture and Conversion of CO_2 into Materials (IC3M): Expanding IC_3M for C1 and C2 Production

Final Report, October 2026

Robert A. Dagle (co-PI, PM)
Jothi Kothandaraman (co-PI)
David J. Heldebrant (co-PI)
Johnny Saavedra Lopez
Mike Hubbard
Yuan Jiang
Cadianne Chambers
Jim Floyd
Hao Xu (WSU)
Gokce Gulfidan (WSU)
Yong Wang (WSU)

U.S. DEPARTMENT OF ENERGY

Prepared for the U.S. Department of Energy
under Contract DE-AC05-76RL01830

PNNL-39696



Pacific Northwest
NATIONAL LABORATORY

Proudly Operated by **Battelle** *Since 1965*

U.S. DEPARTMENT OF
ENERGY

Prepared for the U.S. Department of Energy
under Contract DE-AC05-76RL01830

DISCLAIMER

This report was prepared as an account of work sponsored by an agency of the United States Government. Neither the United States Government nor any agency thereof, nor Battelle Memorial Institute, nor any of their employees, makes **any warranty, express or implied, or assumes any legal liability or responsibility for the accuracy, completeness, or usefulness of any information, apparatus, product, or process disclosed, or represents that its use would not infringe privately owned rights**. Reference herein to any specific commercial product, process, or service by trade name, trademark, manufacturer, or otherwise does not necessarily constitute or imply its endorsement, recommendation, or favoring by the United States Government or any agency thereof, or Battelle Memorial Institute. The views and opinions of authors expressed herein do not necessarily state or reflect those of the United States Government or any agency thereof.

PACIFIC NORTHWEST NATIONAL LABORATORY
operated by
BATTELLE
for the
UNITED STATES DEPARTMENT OF ENERGY
under Contract DE-AC05-76RL01830

Printed in the United States of America

Available to DOE and DOE contractors from
the Office of Scientific and Technical Information,
P.O. Box 62, Oak Ridge, TN 37831-0062
www.osti.gov
ph: (865) 576-8401
fax: (865) 576-5728
email: reports@osti.gov

Available to the public from the National Technical Information Service
5301 Shawnee Rd., Alexandria, VA 22312
ph: (800) 553-NTIS (6847)
or (703) 605-6000
email: info@ntis.gov
Online ordering: http://www.ntis.gov

PNNL-39696

Integrated Capture and Conversion of CO_2 into Materials (IC3M): Expanding IC3M for C1 and C2 Production

Final Report, October 2026

Robert A. Dagle (co-PI, PM)
Jothi Kothandaraman (co-PI)
David J. Heldebrant (co-PI)
Johnny Saavedra Lopez
Mike Hubbard
Yuan Jiang
Cadianne Chambers
Jim Floyd
Hao Xu (WSU)
Gokce Gulfidan (WSU)
Yong Wang (WSU)

Prepared for the U.S. Department of Energy

Under Contract DE-AC05-76RL01830

Pacific Northwest National Laboratory

Richland, Washington 99352

Submitted to:	U.S. Department of Energy (DOE) Hydrocarbons and Geothermal Energy Office (HGEO)/ National Energy Technology Laboratory (NETL)
FWP Award:	FWP-80562
Project Title:	Integrated Capture and Conversion of CO_2 into Materials (IC3M): Expanding IC3M for C1 and C2 Production
Project Manager:	Robert Dagle Phone: 509-371-6264 Robert.dagle@pnnl.gov
Submitting Official:	Project Manager
Date Submitted:	January 30, 2026
Recipient Organization:	Pacific Northwest National Laboratory P.O. Box 999, MS K2-44 Richland, WA 99352
Project Period:	January 1, 2023, through December 31, 2025
Reporting Period	January 1, 2023, through December 31, 2025
Reporting Term:	Final Report

Contents

I Accomplishments and Milestone Update 5

I.1 Synopsis of Accomplishments 6

I.2 Milestones 8

I.3 Project Accomplishments by Task 9

I.4 Cost Status 132

II Issues, Risks, and Mitigation 133

III Changes in Approach 134

IV Key Personnel 134

V Project Output 134

VI Project Schedule 135

VII References 139

I.1 Synopsis of Accomplishments

Leveraging the successes of our earlier DOE-TCF project, this FWP funded by DOE-HGEO with a 20% cost share from Southern California Gas Company was launched on January 1, 2023. In this effort, we further developed PNNL's Integrated Capture of CO_2 into Materials (IC^3M) process technology for producing C_1 and C_2 products. The following key accomplishments were achieved during Budget Periods 1–3:

IC^3M Process Demonstration: We successfully demonstrated the integrated IC_3M process for CO_2 capture and conversion to methanol using the EEMPA solvent and Pt/TiO_2 catalyst. PNNL's two independently tested systems, the Laboratory Continuous Flow System (LCFS) and the Thermochemical Catalytic Conversion System (TCCS), were integrated to achieve a semi-closed-loop process, where CO_2 capture was performed in closed-loop mode and conversion occurred in single-pass mode. This demonstration validated the feasibility of coupling capture and conversion in a single process loop and achieved improved performance for eight continuous hours on stream. These results confirm that the IC^3M approach can operate under realistic conditions and maintain stability during extended runs, marking a significant step toward commercial viability.

Methanol Catalyst Discovery and Performance: Two advanced catalyst systems, Pt/MoO_3 and Pt/ZrO_2, were identified as high-performing candidates for methanol synthesis from captured CO_2. Both catalysts exhibited exceptional durability, maintaining stable activity for over 100 hours on stream. Notably, Pt/ZrO_2 achieved nearly 100% selectivity for methanol, representing a major improvement over earlier-generation catalysts. Through detailed characterization, we established a clear correlation between catalyst acid-base properties, metal site characteristics, and methanol productivity/selectivity. These insights provide a strong foundation for rational catalyst design and optimization in future development phases.

Techno-Economic Assessment (TEA): A comprehensive TEA was conducted to evaluate the economic competitiveness of the IC^3M process. Results indicate that the 2024 State of Technology (SOT) methanol minimum selling price (MSP) is approximately 30% lower than the best 2022 cases, primarily due to reductions in catalyst costs and capital depreciation. Furthermore, the analysis shows that IC^3M (goal case) can achieve more than a 25% reduction in methanol MSP compared to the conventional separate capture and conversion approach (SC^3M). These findings underscore the potential for IC_3M to deliver significant cost advantages in commercial applications.

Formate Production: Beyond methanol, the IC^3M platform demonstrated the feasibility of producing formate, a valuable commodity chemical, from captured CO_2. This achievement expands the product portfolio and highlights the versatility of the IC_3M process for generating multiple CO_2-derived products.

Methane Production: The project achieved over 90% single-pass conversion of captured CO_2 to methane, surpassing performance observed in traditional gas-phase reactions. Among the catalysts evaluated, Ru/Al_2O_3 proved most effective, delivering >99% CO_2 conversion and 97.9% methane selectivity under optimal conditions—outperforming typical Ru catalysts reported in the literature for gas-phase conversion. Importantly, we also identified Ni/TiO_2 as a cost-effective alternative, capable of achieving complete CO_2

conversion with high methane selectivity. These findings demonstrate the adaptability of the IC^{3}M process for producing alternative fuels and chemicals, offering flexibility to meet diverse market demands.

Methanol and Glycol Co-Production: We developed a copper-based heterogeneous catalyst with an amine co-catalyst enabling one-step co-production of methanol and glycol from epoxide, CO_2, and H_2. This first-of-its-kind process achieved >75% selectivity and improved methanol productivity by more than five-fold compared to conventional CO_2 hydrogenation. The integrated approach can potentially reach 100% carbon and hydrogen efficiency. TEA indicates methanol costs could be reduced by 30–60% versus traditional gas-phase CO_2 conversion. The highly exothermic reaction allows waste heat recovery for electricity generation, improving thermal efficiency by 23% compared to the conventional route. LCA suggests coproduction could be a negative-emission technology: cradle-to-grave GHG emissions for methanol combustion were –45 g CO_2 eq/MJ versus +25 g CO_2 eq/MJ for conventional hydrogenation. This benefit stems from high atom/thermal efficiency and displacement credits from glycol co-production.

Solvent Durability Under Hydrogenation Conditions: To assess solvent durability under IC3M hydrogenation conditions, we analyzed spent amines by GC-MS and ran standardized CO_2-rich screening to directly compare how molecular structure affects stability. Degradation varied widely: EAE showed the highest breakdown (~20%), HEP/HEEP/TMED/PEH showed moderate degradation, and substituted amines such as CRABMO, DMP variants, and DSBA showed excellent stability (<5%). Across the full dataset, solution pH and temperature emerged as the primary drivers of solvent degradation and methanol selectivity, with steric hindrance most likely acting through its influence on these factors. DSBA was a standout performer, meeting productivity targets while maintaining strong thermal and catalytic durability. **These results support the IC3M 3.0 strategy of α- and β-carbon substitution; however, they also indicate that simply controlling pH, water content, and high-temperature exposure time may significantly extend solvent lifetimes without requiring changes to the current EEMPA structure.** Future work should prioritize further understanding how pH and temperature govern solvent behavior under IC3M conditions.

IC$_3$M 3.0: The objectives, goals, tasks, and milestone schedule for IC^{3}M 3.0 were first developed and presented to DOE on November 15, 2024, with the Statement of Work submitted on January 31, 2025. This next phase focuses on advancing the TRL of IC^{3}M for methanol production from TRL 4 to TRL 5. Our approach targets two critical development needs: (a) Enhancing solvent durability under catalytic reduction conditions. (b) Increasing catalyst productivity using a newly designed, more durable solvent to meet TEA target criteria. The team will demonstrate continuous-flow IC^{3}M methanol production from simulated flue gas for over 40 hours of steady-state operation, supported by TEA and LCA based on experimental data. Additionally, the project will explore expanding the product portfolio and design a new IC^{3}M approach for formate/formic acid production, further broadening the commercial potential of the platform.

Gas-Phase CO_2 hydrogenation to Ethanol: Efforts to convert CO_2 to ethanol in the gas phase using Rh–Fe/SiO_2 catalysts achieved ~8% CO_2 conversion with ~50% selectivity to mixed alcohols (methanol and ethanol). However, overall conversion remains low, and methane selectivity is still significant, limiting alcohol yield. The original hypothesis that the IC^{3}M system could drive higher conversion was not realized due to catalyst–solvent incompatibility. While recent improvements have reduced methane byproduct formation, further optimization is required to achieve commercially viable performance. A deeper

understanding of the reaction mechanism will be critical to guide future catalyst design and improve selectivity toward ethanol.

Publications and Intellectual Property

Published:

- Selective and Stable Pt Catalysts for the Catalytic Conversion of Captured CO_2 to Methanol in an Advanced Water-Lean Post Combustion Solvent, **ACS Catalysis**, 2026, DOI: 10.1021/acscatal.5c07059
- Combined Capture and Conversion of CO_2 to Methanol in a Post Combustion Capture Solvent, **US Patent Application**, 2025, App. No. 18/354,571
- Single-Pass Demonstration of Integrated Capture and Catalytic Conversion of CO_2 from Simulated Flue Gas to Methanol in a Water-Lean Carbon Capture Solvent, **ACS Omega**, 2024, DOI: 10.1021/acsomega.4c06919
- Mechanistic Insights to Drive Catalytic Hydrogenation of Formamide Intermediates to Methanol via Deaminative Hydrogenation, **Frontiers in Energy Research**, 2023, DOI: 10.3389/fenrg.2023.1158499

Manuscripts In Progress / Submitted:

- Techno-economic and Life-cycle Analyses of Energy-Efficient Carbon Capture and Utilization Platform: Integrated Capture and Conversion of CO_2 into Materials (IC^3M) – In peer review
- Single-Step Simultaneous Production of Methanol and Glycol from Epoxide, CO_2 and H_2 Using Heterogeneous Cu-based Catalysts – In peer review; patent filing in progress
- Indispensable roles of Rh and Fe in multi-functional bimetallic CO_2 hydrogenation catalysts for ethanol production (WSU lead) – Drafted
- Integrated CO_2 Capture and Hydrogenation to Formic Acid Using Amine Solvents: Process Optimization, Techno-economic and Life-cycle Assessment – Drafted
- Integrated CO_2 to Methanol: Two manuscripts in progress focusing on catalyst and solvent development

More details for the technical progress made are described below.

I.2 Milestones Completed

The following milestones shown in **Table 1** were completed with more details reported below.

Table 2. Milestones completed this budget period.

Year 1	QTR	Due Date
[T1] Synthesize catalysts and test for conversion of captured CO_2 to EEMPA N-formamide (step A). Achieve high conversion (>90%) and selectivity (>95%) for N-formamide between 90-140 °C.	1	March 31, 2023
[T1] Evaluate the catalyst/solvent system at temperature below 100 °C to produce formate. Demonstrate at least 50% conversion with >95% selectivity for formate.	2	June 30, 2023

[T1] Identify catalyst formulations that leads to at least 95% selectivity for C-N cleavage to produce methanol (Step B).	3	Sept. 30, 2023
[T6] Preliminary LCA for IC^{3}M process for GHG reduction [T4] Establish baseline performance of single atom catalyst for gas phase CO_2 conversion to ethanol.	4	Dec 31, 2023
[T1] Combine steps A and B, and achieve >20% single pass conversion of captured CO_2 to methanol. Also, assess separability of methanol and at least one other target product when mixed with EEMPA (w/ 5% water) with bench scale distillation/ flash separation experiments to inform TEA	5	Mar 31, 2024
[T1] Characterize at least 5 new catalyst formulations using NH3 TPD, and H2 chemisorption (or XRD) and correlate properties of acid and metal sites on methanol productivity	6	Jun 30, 2024
Go/No-Go: Demonstrate feasibility for IC^{3}M concept by meeting intermediate target for methanol of 20% conversion, > 80% selectivity (Target A) and establishing technical feasibility for producing and separating at least two other C1 or C2 oxygenates (> 10% conversion, Target B) using post-combustion capture solvent.	7	Sept. 30, 2024
[T2] Coproduce methanol and glycol in the presence of a post combustion capture solvent. Sequential reactions will be performed to produce >90% yield for cycle carbonate from epoxide and CO_2, which then will be hydrogenated in the presence of a catalyst to produce methanol and glycol with conversion >90% and selectivity >95%	8	Dec 31, 2024
(A).[T3] Improve the rate of hydrogenation of condensed phase CO_2 to methane comparable to or better than gas phase reaction and achieve >90% single pass conversion **(B)**.[T4] Demonstrate if catalyst can achieve at least 10% CO_2 conversion with >70% selectivity to ethanol in the gas phase.* [T4] Determine if catalyst can achieve at least 10% CO_2 conversion with >20% selectivity to ethanol in the liquid phase.* Decision point [T4]: if unable to achieve both criteria we will down select ethanol and redirect this scope to assist with methanol [T1]	9	March 31, 2024
[T1] Using the knowledge obtained from previous milestones/tasks, select capture solvent/catalyst/conditions to achieve single pass conversion of at least >50% and selectivity >90% to methanol in a continuous flow system	10	June 30, 2025
[T4] Assess at least 10 commercially available/inexpensive amine-based solvents, targeting methanol performance of at least 50% relative to the EEMPA baseline case	11	September 30, 2025
[T5] Report state of technology performance and costing for each of the three major catalytic pathways being investigated. [T6] Report full environmental LCA for process and compare to two baseline cases	12	December 31, 2025

I.3 Project Accomplishments

1. Background:

At the completion of our earlier project performed with DOE-TCF funding in FY20-FY22, we developed the proof of concept for a new process technology that utilizes EEMPA for synergistic capture and conversion in the condensed phase. In the processing, first CO_2 from flue gas is captured when using EEMPA. Then, in a second unit of operation, CO_2-captured EEMPA is co-fed with H_2 to produce either methanol [1] (and/or higher alcohols) or methane [2]. The product slate can be tuned by changing the catalyst and processing conditions. Major accomplishments and findings made on this earlier project included the following:

- Catalytically reacting CO_2 in capture medium bypasses CO_2 release and compression energy
- Captured CO_2 reacts differently in the condensed phase than gaseous CO_2, opening new doors for reactivity.
- Catalytic with respect to capture solvent
- Parallel production of methanol [1] (and higher alcohols) and methane [2] demonstrated by changing reagent feed, conditions, and catalyst
- Market adaptability, helps avoid oversaturation of a single market/product.
- Heterogenous catalysts developed that are selective for C-N cleavage, therefore leading to selective methanol [1] or methane [2] formation and without the need for additional co-feeds (e.g., ethanol)
- Combined capture and conversion of CO_2 demonstrated with simulated flue gas.
- Three patent applications were granted (2) or pending (1)
- Two manuscripts were published.

For the current effort, we are building upon prior successes to further develop the PNNL Integrated Capture and Conversion of CO_2 into Materials (IC3M) process technology, with the goal of increasing methanol yields. Efficient methanol production is the primary C_1 target of choice due to its promising applications as a fuel, chemical precursor, and energy carrier. We also evaluate the feasibility of synthesizing other products by adapting other catalysts and reagent co-feeds using the same capture solvent system. This approach will enable us to tune the catalyst and processing conditions to target a number of different large market C_1 and C_2 products, including products that require less hydrogen (formic acid and methyl formate) using the same post-combustion solvent. Methanol, formic acid, and methyl formate can in principle all be produced leveraging the same catalytic mechanism. Glycols, such as ethylene glycol, could be produced simultaneously with methanol by introducing additional epoxide co-feed [3]. Further, methane can also be produced from captured CO_2 with high selectivity, and at the same conditions, by simply flowing the solvent over a different catalyst [2]. A final target of IC^3M is to expand to C2 products, such as ethanol, leveraging new selective single-step conversion catalysts [4]. Ethanol is an attractive transportable liquid product, with an established distribution network, and can be used for producing a number of chemicals and fuels [5].

Taken together, there are **six objectives** for this project:

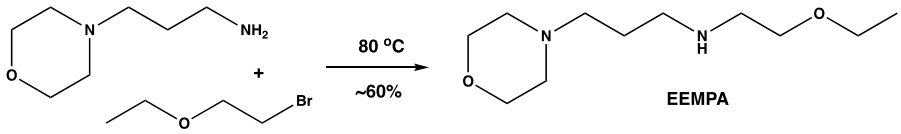
1. Through improvements to catalyst design, achieve high single-pass yields (>50%) for **methanol** and >90% selectivities, required to increase commercial viability. Targeted processing ranges are 100-180˚C and 1-60 bar.

2. Adapt the IC^{3}M methanol platform to **produce formic acid** or **methyl formate** and **ethylene/propylene glycol**. Modifications will include the control of catalyst and processing conditions, and epoxide co-feeding in the case of glycol. Single-pass yields of >50% are targeted for formic acid or methyl formate, with selectivities >90%.
3. Further develop and optimize the processing conditions to producing **methane**, with the goal of achieving > 90% single-pass yields and > 90% selectivity.
4. Adapt recent reported catalysts, developed for producing ethanol in one step from CO_2, into the IC3M platform. Target > 20% single-pass yields and > 70% selectivity under continuous flow conditions.
5. Adapt existing **techno-economic analyses (TEA)** for methanol and methane production, for the new targeted products (formic acid, glycol, and ethanol).
6. Assess the **life-cycle analyses (LCA**) across the value chain for production of methanol and up to two additional products made from the IC^{3}M platform.

2. Task Accomplishments:

I. Third demonstration of PNNL's two independently tested systems, the Laboratory Continuous Flow System (LCFS) and the Thermochemical Catalytic Conversion System (TCCS) for integrated capture (LCFS) and conversion (TCCS):

In the first project quarter, we prepared 1.1 L of EEMPA for 2-step integrated testing of CO_2 capture (simulated flue gas) and conversion. 900 mL of the solvent was freshly synthesized in one step by a known procedure using N-(3-aminopropyl)morpholine and 2-bromoethyl ethyl ether with a yield of approximately 63% (see **Scheme 1**). 200 mL was recovered from previous experiments and purified by distillation. This solvent was used for a third demonstration of capture and conversion of simulated flue gas CO_2 to methanol this quarter.



Scheme 1. EEMPA synthetic route

The third demonstration (herein Demo 3) of the integrated CO_2 capture and conversion to methanol (IC^{3}M) apparatus was performed to evaluate the effect of water content in the solvent on the conversion of CO_2 to methanol. The CO_2 capture unit contains an absorber column which was packed with two 8" pieces of Sulzer Mellapak 500.Y structured packing sections and a stripper column that is packed with 0.24" Pro-Pak 316 stainless steel Cannon Instruments random packing material. The conversion unit (TCCS) consists of a temperature-controlled, pressurized, cylindrical packed bed that houses 1 g of catalyst. The LCFS and TCCS systems were integrated through the use of HPLC pumps which allowed CO_2-rich 2-EEMPA to be drawn from the LCFS system to the TCCS system. Subsequently, fresh 2-EEMPA was pumped to the inlet of the absorber column to replace the drawn solvent to keep the LCFS system at steady-state.

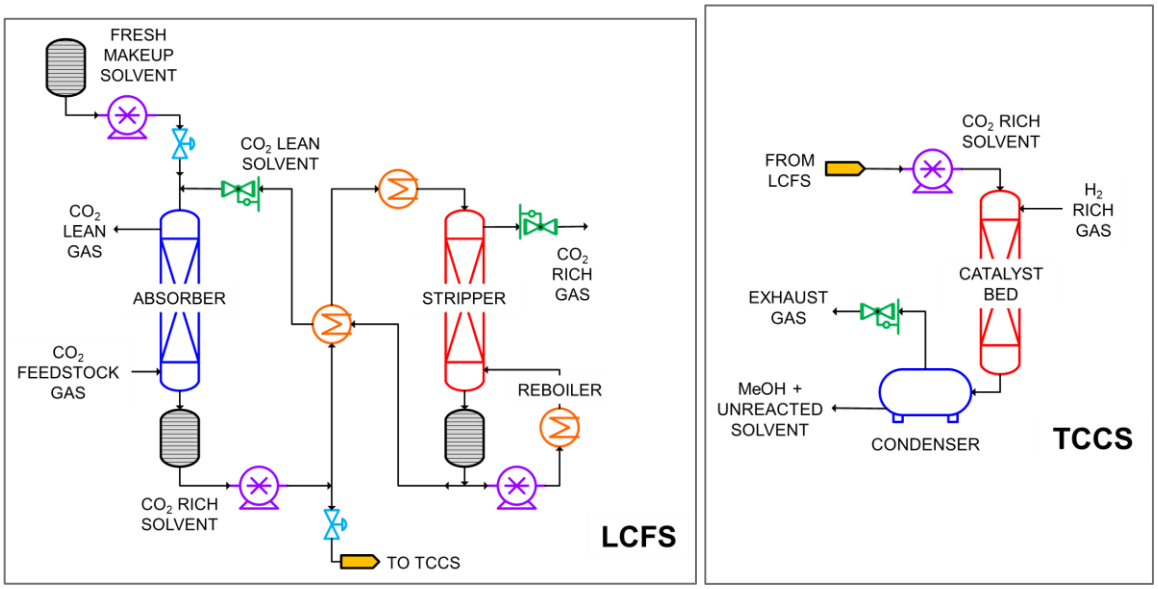


Figure 1. Process flow diagrams of the LCFS and TCCS systems that together make up the IC^{3}M apparatus.

The process conditions of the LCFS system for Demo 3 were comparable to previous integrations, Demo 1 and Demo 2, with the exception of the dew point. The LCFS dew point in Demo 1 and Demo 2 was 15.6 °C which corresponded to a water loading of about 2 wt.% in 2-EEMPA. It was hypothesized that the difference in catalyst performance between the previously performed integrated demonstrations and the isolated laboratory experiments was attributed to the water loading in 2-EEMPA. Thus, 2-EEMPA was dehydrated prior to Demo 3 and water was not continuously added to the capture system via the inlet gas stream. All other process conditions remained the same. Process conditions for all of the demonstrations are shown in **Table 2**. The process conditions of the TCCS system for Demo 3 remained the same as in Demo 1 and Demo 2 with the exception of the catalyst regeneration process. After the first day of integration, the catalyst was regenerated under 1.8 % O_2 at 550 °C for 5 h.

Table 2. Relevant process conditions at steady state for the LCFS and TCCS for all three demonstrations.

LCFS Process Parameter		Demo 1	Demo 2		Demo 3		Units
			Before Regen	After Regen	Before Regen	After Regen	
Feed	CO_2/N_2 [dry basis]	15 / 85	15 / 85	15 / 85	15 / 85	15 / 85	[mol %]
	Dew Point	15.6	15.6	15.6	-	-	[°C]
Absorber	Avg. Temperature	32.3	31.8	31.7	32.4	32.7	[°C]
	Avg. Pressure	0.08	0.23	0.22	0.26	0.27	[psig]
Stripper	Avg. Temperature	95.1	103.4	102.8	103.4	103.5	[°C]
	Avg. Pressure	14.39	14.8	14.9	15.1	15.3	[psig]
Reboiler	Temperature	114.9	116.6	115.6	116.1	116.2	[°C]
Flow	Liquid	15.3	12.6	12.8	11.94	11.56	[kg/h]
	Gas	0.61	0.60	0.60	0.60	0.60	[kg/h]
	L/G	25.2	20.9	21.1	19.7	19.1	[-]
SS CO_2 Capture Efficiency		88.3	92.6	92.7	92.3	91.5	[%]

TCCS Process Parameter		Demo 1	Demo 2		Demo 3		Units
			Before Regen	After Regen	Before Regen	After Regen	
Gas Feed	H_2 / N_2	93 / 7	93 / 7	93 / 7	93 / 7	93 / 7	[mol %]
	Flowrate	5.9 E -4	5.9 E -4	5.9 E -4	5.9 E-4	5.9 E -4	[kg/h]
Liquid Feed	2-EEMPA/CO_2/H_2O	78 / 5 / 17	79 / 4 / 17	76 / 3 / 21	96 / 3 / 1	95 / 4 / 1	[mol %]
	Flowrate	6.7 E -3	6.7 E -3	6.7 E-3	6.7 E-3	6.7 E -3	[kg/h]
Reactor	Temperature	170	190	190	190	190	[°C]
	Pressure	865	865	865	865	865	[psig]
	Catalyst: 5wt% Pt on TiO_2	1	1	1	1	1	[g]
CO_2 Conversion		35 → 0.8	50 → 10	19 → 7	67 → 50	100 → 43	[%]
Methanol Produced		70 → 0	41 → 0	62 → 0	69 → 74	57 → 85	[%]

Capture Performance

Removal of water from the inlet gas stream did not affect the capture efficiency of the 2-EEMPA as indicated in **Figure 2**. After the LCFS system reached steady-state and was integrated with the TCCS system, the overall capture efficiencies for Demo 3 were 92.3 % on Day 1 and 91.5 % on Day 3 of the study. The result is comparable to Demo 2 where the capture efficiencies were 92.6 % and 92.7 % on Day 1 and Day 3, respectively. As observed in the previous demonstrations, the LCFS system is producing a reproducible capture efficiency.

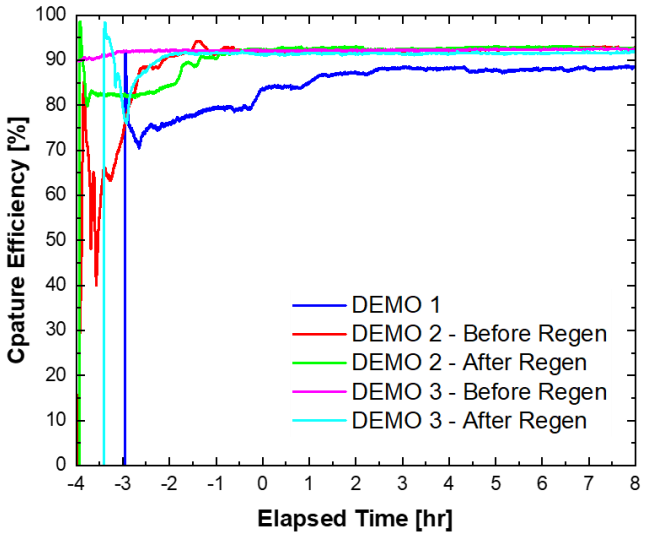


Figure 2. CO_2 capture efficiency data from the LCFS for Demo 1, 2 and 3. An elapsed time of 0h is defined as the point at which integration between the LCFS and TCCS systems began.

CO_2-rich and -lean solvents were sampled from the LCFS system every other hour for analysis. Water content analysis was performed using Karl Fischer titration and Raman spectroscopy. CO_2 content was performed using Raman spectroscopy. As expected, the water content of the rich solvent in Demo 3 was significantly lower compared to that of Demo 2. The average water composition of the rich solvent stream in Demo 3 (before catalyst regeneration) was 0.22 mol % while the average water composition of the rich solvent stream in Demo 2 (before catalyst regeneration) was 16.8 mol % as indicated in **Figure 3**. Additionally, the average CO_2 content in the rich solvent stream for Demo 3 (before catalyst regeneration) was 3.78 mol % while that of Demo 2 (before catalyst regeneration) was 3.61 mol %.

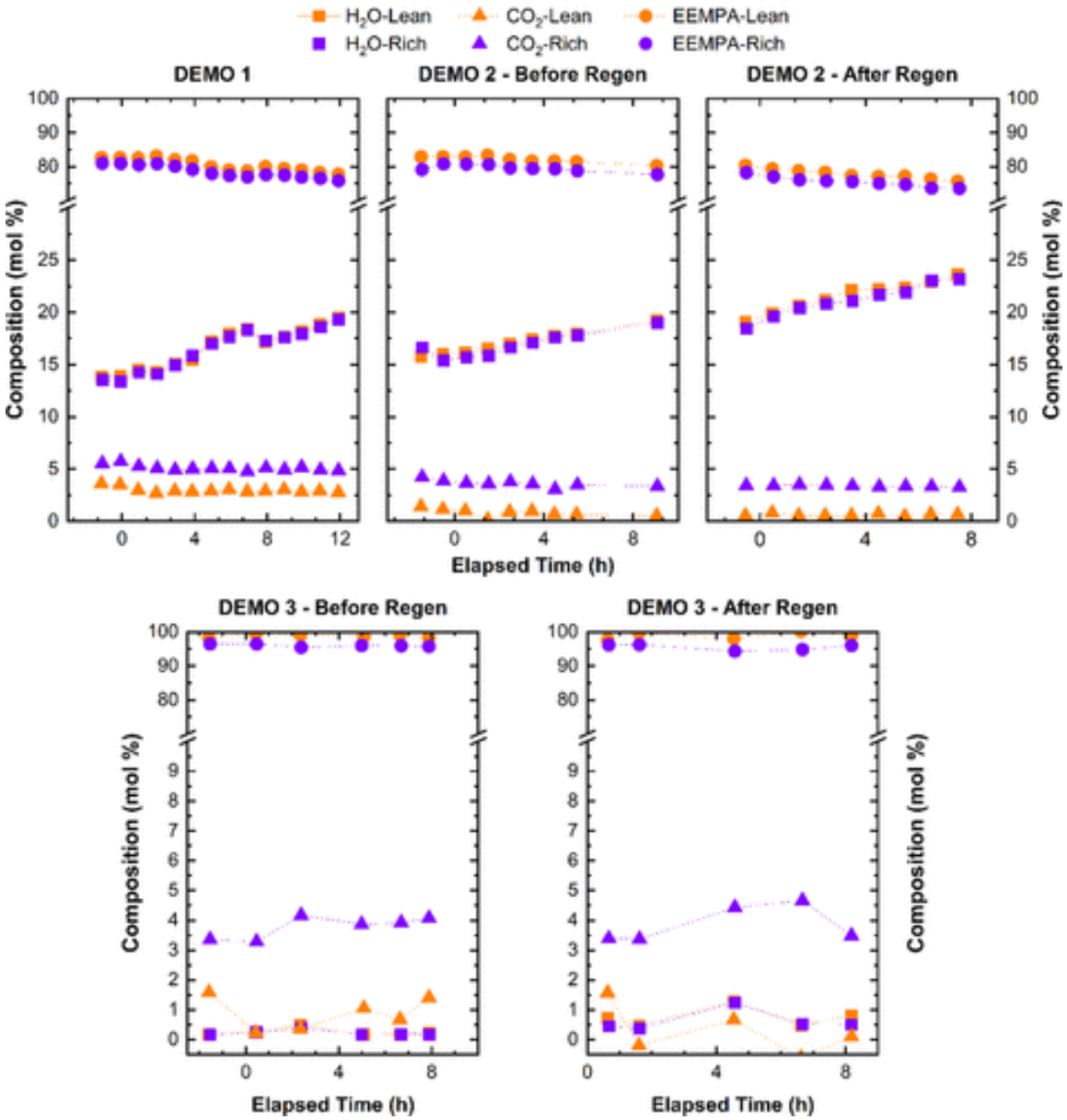


Figure 3. Liquid phase analysis from the LCFS system for Demo 1, 2 and 3.

Conversion Performance

Gaseous products produced in the TCCS system were analyzed via GC every 0.5 h. A summary of the analysis is shown in **Figure 4**. Demo 3 showed the most methane produced by mol % compared to Demo 1 and Demo 2. The methane profile is sustained over time compared to Demo 2 and Demo 1. Very little CO was produced in Demo 3 compared to Demo 2. No CO_2 was observed to be released into gaseous phase at these catalytic conditions, which implies that CO_2 was either converted and/or remained solubilized in solution.

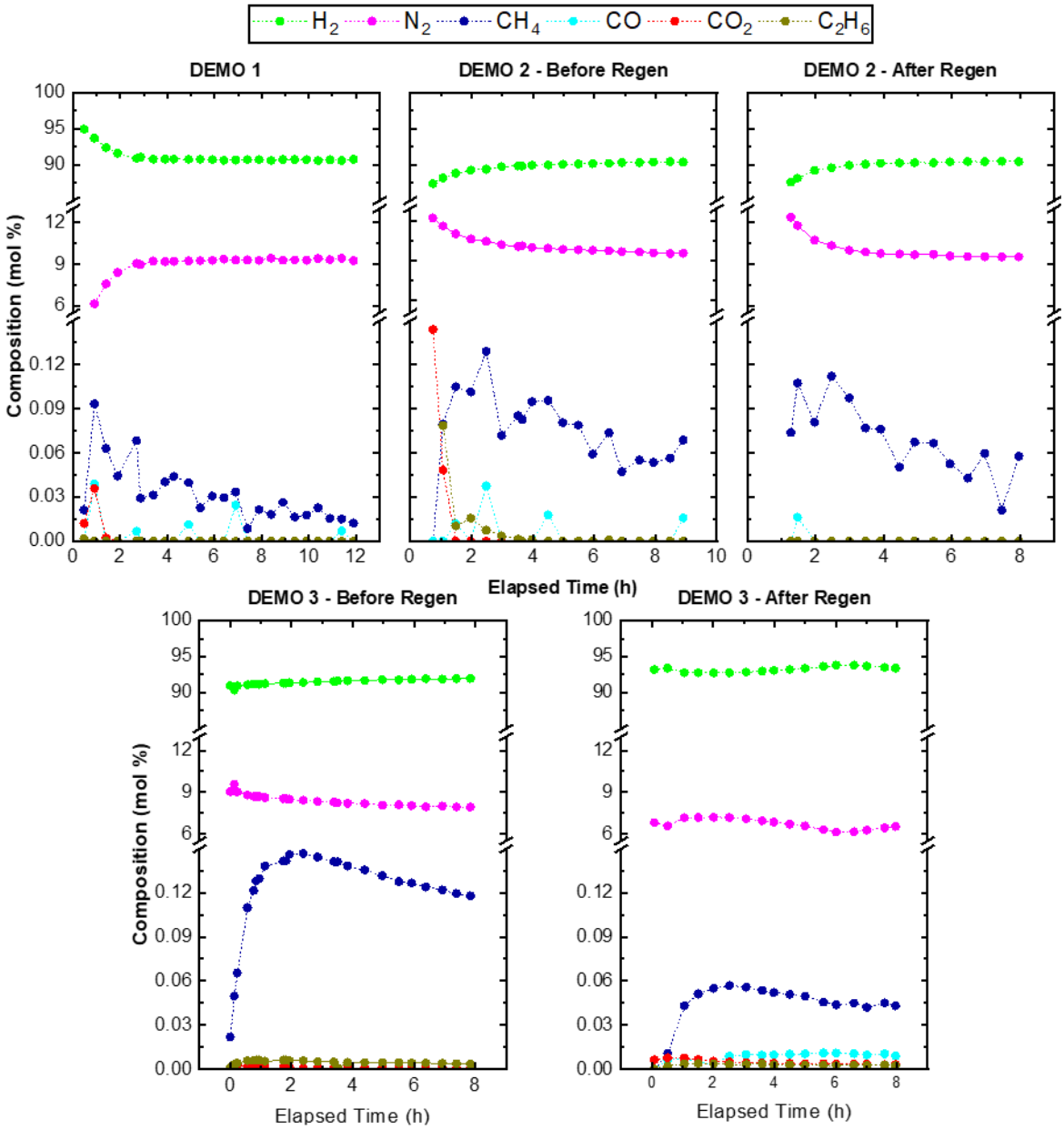


Figure 4. Gas phase analysis from the effluent stream exiting the TCCS for Demo 1, 2 and 3.

The collected liquid product condensed from the exit stream of the catalyst bed in the TCCS system was sampled every hour. The liquid was analyzed via Karl Fischer, Raman spectroscopy and GC to determine the composition of EEMPA, water, CO_2, methanol, and ethanol. Summary of the liquid analysis is shown in **Figure 5**. The average methanol content for Demo 3 (before catalyst regeneration) was 1.53 mol % while the average methanol content for Demo 2 before catalyst regeneration was 0.20 mol %. Demo 3 showed more methanol was produced compared to Demo 2 and Demo 1. Moreover, the methanol production was maintained throughout the Demo 3 duration compared to a decay in production observed in Demo 1 and Demo 2.

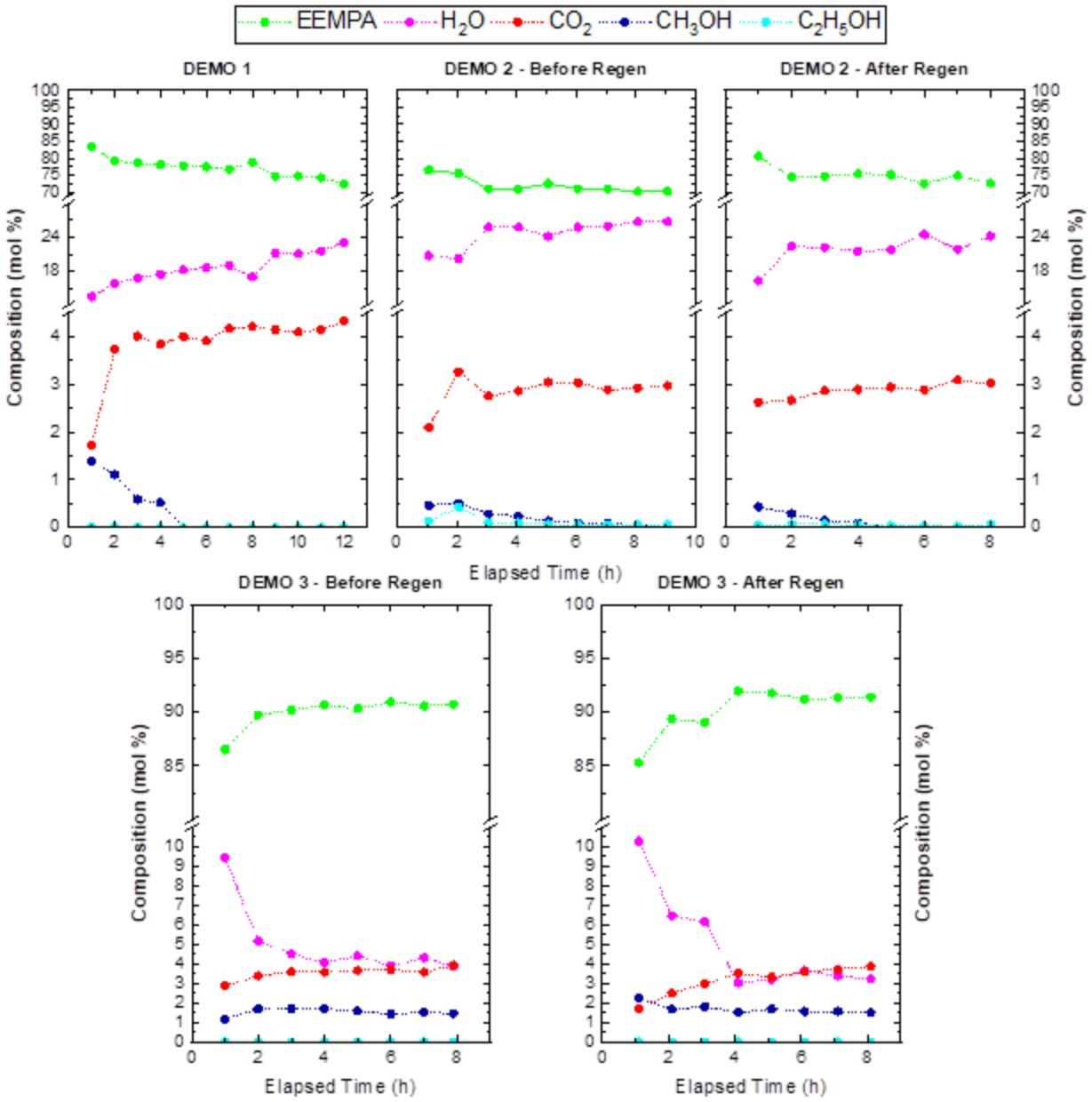


Figure 5. Liquid phase analysis of the condensed liquid product from the effluent stream exiting the catalyst bed in the TCCS system for Demo 1, 2, and 3.

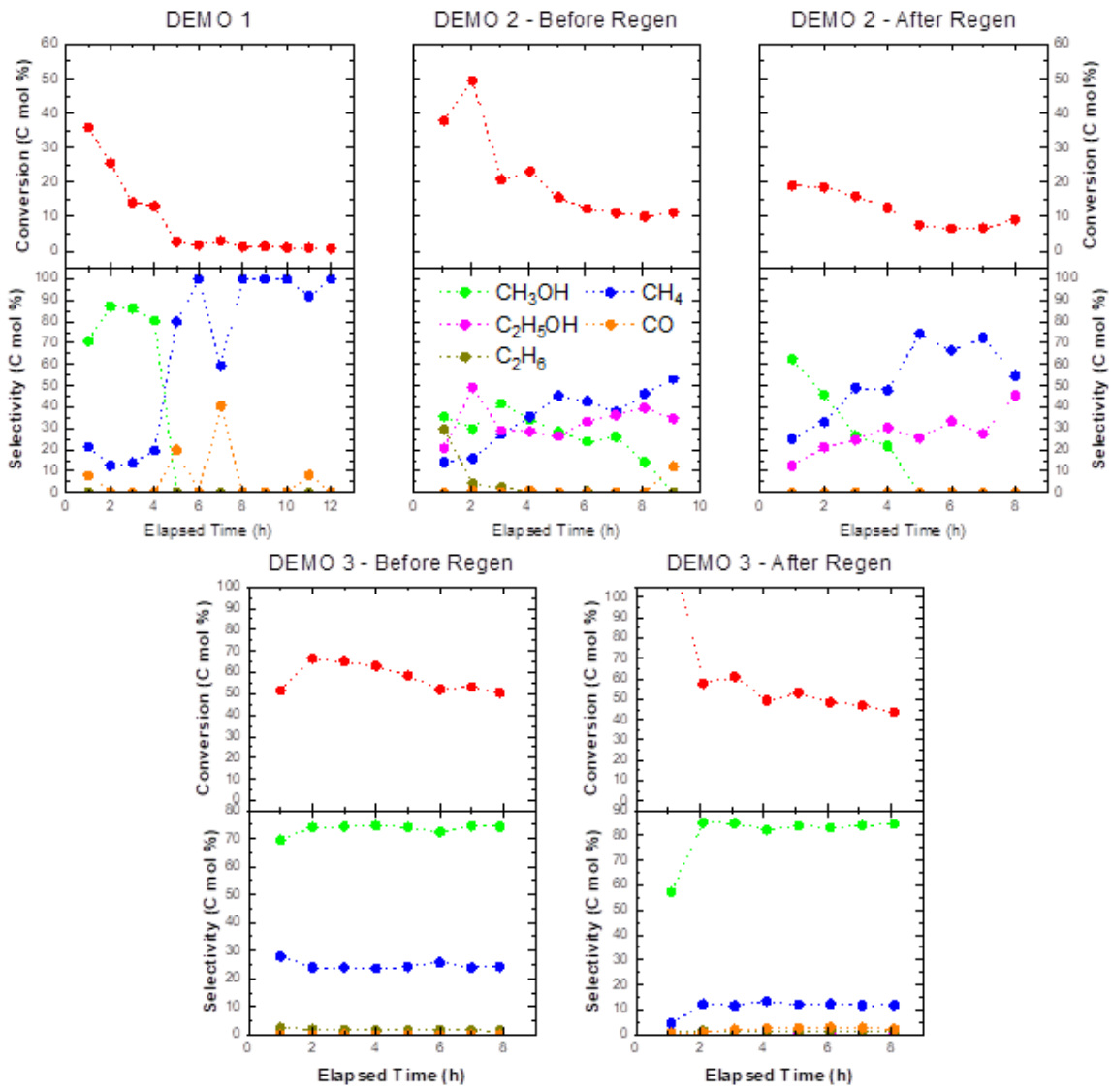


Figure 6. CO_2 conversion and product species selectively as a function of reaction time on stream during Demo 1, 2 and 3.

The selectivity and CO_2 conversion of each demo before and after regeneration (except for Demo 1) is depicted in **Figure 6**. Demo 3 had an average CO_2 conversion of 60 mol % compared to Demo 2 which had an average CO_2 conversion of 20 mol %. Methanol selectivity remained high throughout Demo 3 with an average value of 75 mol % compared to Demo 2. Overall, it appears that the absence of water in the 2-EEMPA "CO_2-carrier" solvent system has significant implications in improving the sustainable productivity and conversion of CO_2. Selective conversion of methanol (>60%) has been observed at these low water-content reactions.

The catalyst productivity for Demo 1, 2 and 3 as defined by total mass flowrate of CO_2 converted to the mass of catalyst utilized (Equation 11) is summarized in **Figure 7**. This metric, also known as the weight hourly space velocity (WHSV), with a similar observed trend as with CO_2 conversion

allows for comparison of both runs on the basis of catalyst amount. The absolute value of WHSV can also be used to compare with larger scale reactions to evaluate industrial viability. At peak activity, the productivity of this catalyst is observed to be as high as ~0.06 g CO_2 converted/g catalyst·h occurring at initial operation. Throughout the course of operation, for Demo 1 and 2, the productivity remains <0.02 g CO_2 converted/g catalyst·h. Between the two, higher reaction temperature seemingly shows lower productivity (event though conversion is higher). Unsurprisingly, there is likely a tradeoff for productivity vs conversion as a function of reaction temperature. Alternatively, when minimal water is present in the TCCS (Demo 3), the productivity steadies at ~0.03 g CO_2 converted/g catalyst·h. Clearly, the lack of water minimizes the catalyst poisoning and benefits productivity.

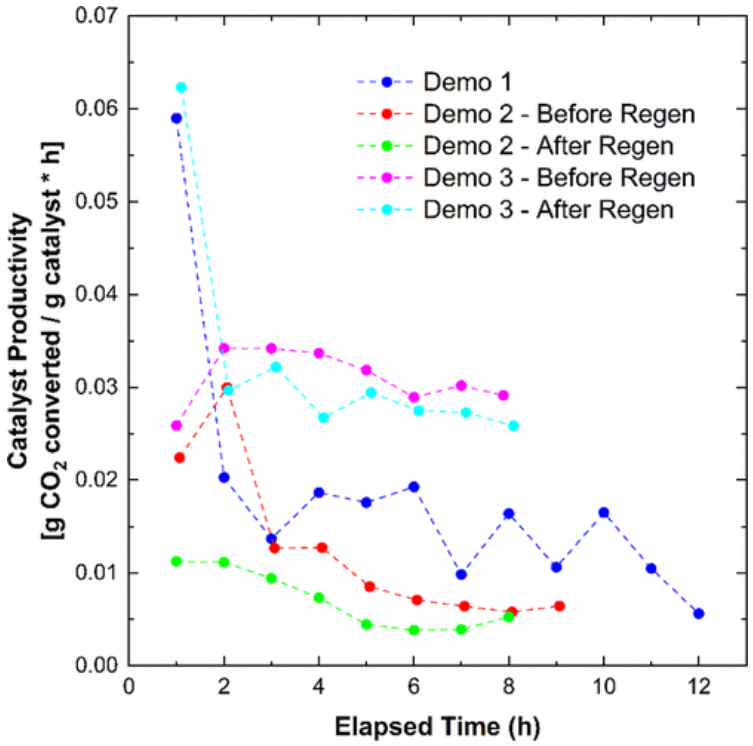


Figure 7. Catalyst productivity for Demo 1, 2 and 3 as a function of elapsed reaction time. Experimental data is shown in points, while dashed lines are added just as a guide.

II. Comparison of the spent catalysts from Demo 1, 2 and 3 experiments

To understand the mechanism of deactivation of the catalyst, we characterized the spent catalyst and the fresh catalyst by diffuse reflectance infrared Fourier transform spectroscopy (DRIFTS), X-ray powder diffraction (XRD), and temperature-programmed oxidation with mass spectrometry (TPO-MS). DRIFTS characterization shows that there were more adsorbed species in Demo 1 spent catalyst compared to Demo 3 spent catalyst (**Figure 8**). Spent catalysts showed C-H bands (~3000-2800 cm^{-1}) corresponding to the capture solvent EEMPA. Demo 1 catalyst showed a strong band corresponding to terminal Pt-CO at 2100 cm^{-1}. In Demo 1 and 3 spent catalysts, we observed bands between 1700 and 1200 cm^{-1}, which are likely bicarbonate and carbonate. The bicarbonate and carbonate sources could be the water in the feedstock in

the case of Demo 1. Water could react with the captured CO_2 and form bicarbonates and carbonates (carbamate/CO_2 + H_2O → HCO_3^-/CO_3^-), which can bind strongly with the catalyst at low reaction temperatures. In Demo 3 case, bicarbonate and carbonate are likely formed by the reaction of the water byproduct with the captured CO_2.

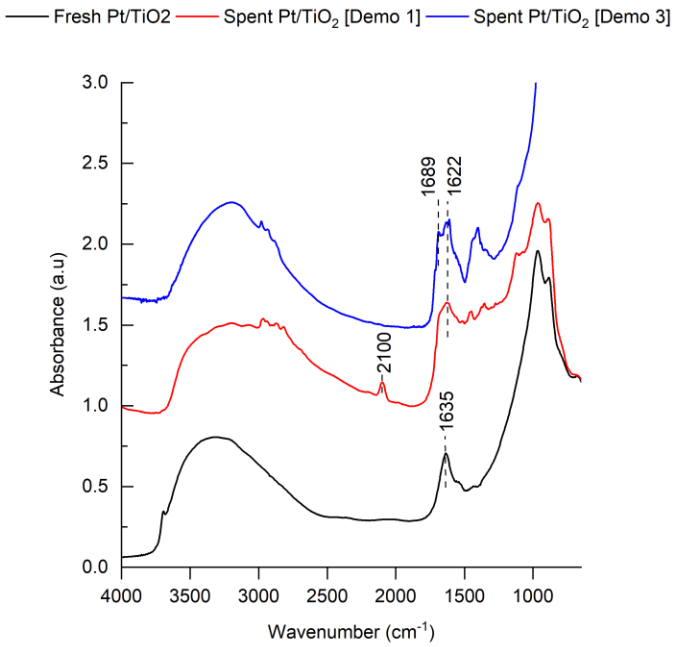


Figure 8. DRIFTS spectra of the fresh and spent Pt/TiO_2 catalysts.

The fresh and spent (Demo 1 and 3) catalysts showed similar XRD patterns (**Figure 9**). Peaks corresponding to Pt particles were not seen in the XRD. Strong diffraction patterns corresponding to the anatase phase of the TiO_2 support were observed in both the fresh and spent catalysts, in addition to minor peaks for the rutile phase. The TiO_2 support phases remained the same in all the cases. TPO-MS analysis of the fresh catalyst showed small concentrations of H_2O and CO_2 (**Figure 10**). On the other hand, the spent catalyst showed significant liberation of H_2O, CO_2 and CO all starting at 100°C. This indicates the presence of these species sorbed on the catalyst which likely causes diminished activity observed during reaction in the TCCS. It is interesting to note that significant CO_2 liberation was observed on spent catalyst after Demo 1 compared to Demo 3 corroborating our conversion performance which indicated that much more of the captured CO_2 in the solvent was converted in Demo 3. The source of CO_2 can be the decomposition of sorbed bicarbonate, carbonate, and carbamate species on the catalyst surface. The peak for CO_2 liberation for Demo 3 catalyst occurred at a much higher temperature (~235°C) than for Demo 1 catalyst (~130-190°C) likely corresponding to minimal residual sorbed bicarbonate, carbonate, and carbamate species on Demo 3 catalyst that remain tightly bound. Together, DRIFTS, TPO-MS and DEMO conversion results suggest that the presence of water in the feedstock is enriching the formation of carbonates and blocking the active sites of the catalysts. In addition, from the DRIFTS and TPO-MS results it is likely that the excess carbonate concentration on the catalyst surface is getting converted to CO, which can bind with the Pt strongly and deactivate the catalyst.

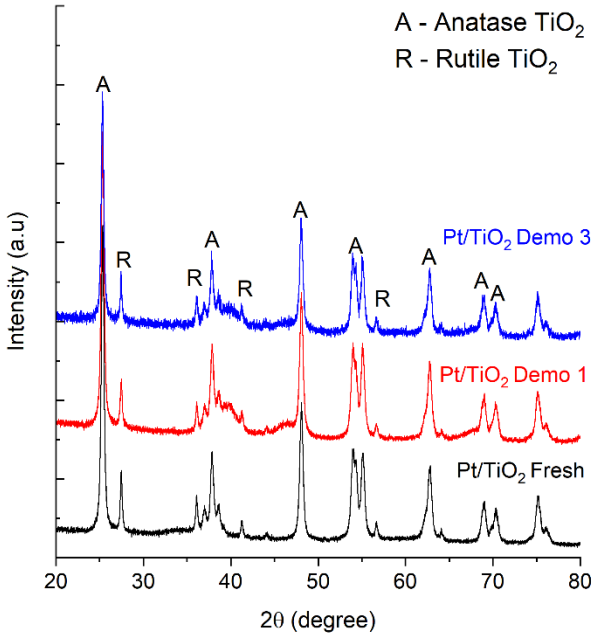


Figure 9. Powder XRD patterns of fresh and spent Pt/TiO_2 catalyst.

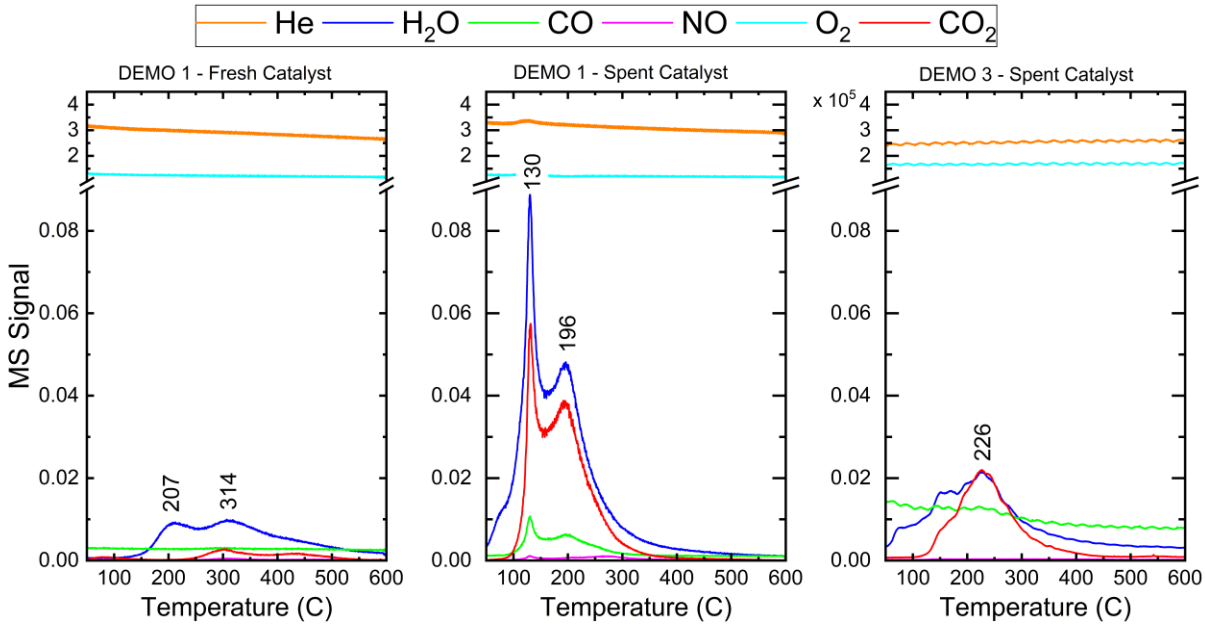


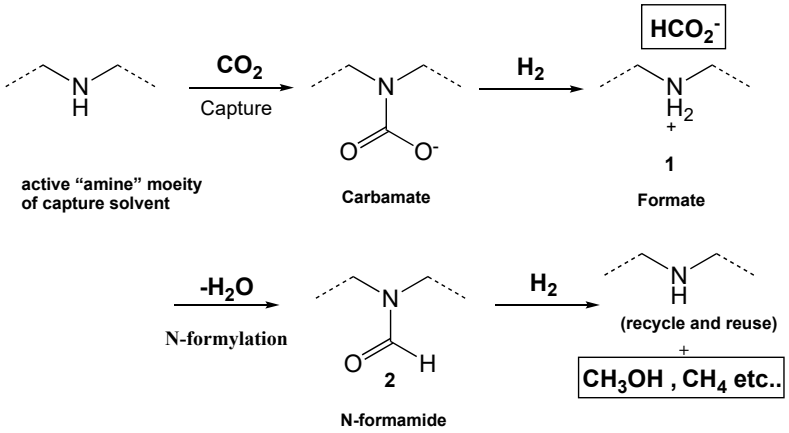
Figure 10. Temperature programmed oxidation (TPO) analysis for the fresh (left), spent after Demo 1 (middle) and spent after Demo 3 (right) Pt/TiO_2 catalyst. TPO conditions for both experiments utilized 10% O_2/He stream at 50 cc/min ramping in temperature at 10°C/min.

The stability of the 2-EEMPA solvent was tested after the reaction by ^{1}H NMR. Only product observed by NMR was methanol at 3.3 ppm. There was no detectable amount of decomposition products from EEMPA solvent, which suggests the solvent is durable under the conversion

conditions. Given the observed deactivation of catalytic activity during operation in the presence of water, two approaches can be pursued: 1) identify a new catalyst that is optimized for higher selectivity even in the presence of water or 2) reduce the water concentration in the feedstock for the IC^{3}M process.

III. First quarter's (FY23-Q2) milestone: *(Task 1: methanol) Synthesize catalysts and test for conversion of captured CO_2 to EEMPA N-formamide (step A). Achieve high conversion (>90%) and selectivity (>95%) for N-formamide between 90-140 °C.*

To achieve sequential hydrogenation of carbamate to formamide (step A) and formamide to methanol (step B), as shown in **Scheme 2** below, and to meet this quarter's milestone, PNNL's water lean solvent EEMPA was used to show the conversion of captured CO_2 (i.e., carbamate) to EEMPA formamide intermediate (step A). First, we tested the known commercial methanol synthesis catalyst, $Cu/ZnO/Al_2O_3$ (Cu: 65 wt.%) at different reaction conditions. The moles of CO_2 loaded in the EEMPA (5 g) was ~8 mmol and the hydrogenation was carried out between 50-100 °C using 0.4 g of catalyst in a batch reactor under 60 bar H_2 pressure. The yields of formamides were calculated from the ^{1}H NMR using 1,3, 5-trimethoxy benzene (TMB) an internal standard and d-acetonitrile as a solvent. The effect of temperature was studied using $Cu/ZnO/Al_2O_3$ as shown in entries 1-3. The yield of formamide decreased with the increase in reaction temperature (entries 1-3, **Table 3**) because of the overreduction of formamide to methanol and N-methyl EEMPA (solvent deactivation product). Based on this observation, 100 °C is the suitable temperature (entry 1, **Table 3**) to optimize the conditions further to achieve higher yield and selectivity for the formation of formamide intermediate. The addition of CO_2 pressure improved the formamide yield from 18.3% to 34.2% (entry 1 vs 5, **Table 3**). Longer reaction time improved the formamide yield significantly to more than 100% (NMR shown in **Figure 11**), relative to the amount of CO_2 captured. This is because the solvent (EEMPA) is typically in excess concentration compared to captured CO_2 and the use of excess CO_2 pressure in the headspace facilitated the formation of formamide. Overall, this finding indicates that a higher CO_2 loading will increase the formamide yield.



Scheme 2. Intermediates formed upon CO_2 hydrogenation in post-combustion capture solvents.

Next, similar conditions were used with 5 wt.% Pd/C and 5 wt.% Pd/TiO_2 (entry 7-9, **Table 3**). Compared to Cu/ZnO/Al_2O_3, these Pd catalysts gave lower yield for N-formamide at 100 °C (Entry 1 vs 7 and 9). At lower reaction temperatures (50 °C, entry 8, **Table 3**), both N-formamide and formic acid were produced at 50 °C, showing that lower temperatures will reduce selectivity to N-formamide. According to these findings, Cu/ZnO/Al_2O_3 is currently the best catalyst for the formation of N-formamide.

Table 3: Hydrogenation of captured CO_2 in the presence of heterogeneous catalysts using a batch reactor system.

Entry	Catalyst	Conditions	Yield of Formamide (%)	Yield of Formic acid (%)
1	65 wt.% Cu/ZnO/ Al_2O_3	60 bar H_2 100 °C	18.3	-
2		60 bar H_2 120 °C	3.11	-
3		60 bar H_2 140 °C	0.23	-
4		60 bar H_2 100 °C[a]	22.3	-
5		60 bar H_2, 5 bar CO_2 100 °C	34.2	-
6		**60 bar H_2, 5 bar CO_2 100 °C[a]**	**>100[b]**	**-**
7	5 wt.% Pd/C	60 bar H_2 100 °C	4.67	-
8		60 bar H_2 50 °C	3.11	5.34
9	5 wt.% Pd/TiO_2	60 bar H_2 100 °C	3.30	-

Reaction conditions: Catalyst = 0.40 g, 2-EEMPA-5g (CO_2 loaded 2-EEMPA was used), CO_2 captured=8 mmol, initial pressure of H_2 at room temperature= 60 bar, time=16h, [a]75h. b. Greater than 100% yield to formamide is achieved relative to the amount of CO2 captured. This is because the solvent (EEMPA) is typically in excess concentration compared to captured CO2 and the use of excess CO2 pressure in the headspace facilitated the formation of formamide.

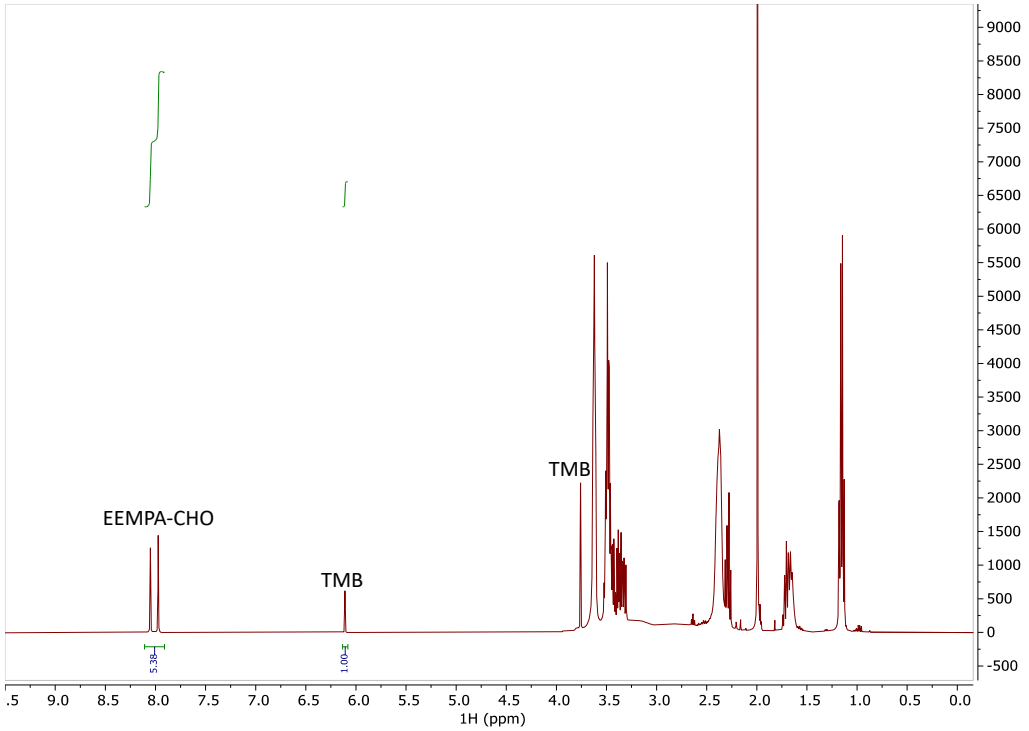


Figure 11. ^{1}H NMR of the reaction mixture from entry 6, **Table 2**.

IV. Second quarter's (FY23-Q3) milestone: *(Task 1: formic acid) Evaluate the catalyst/solvent system at temperature below 100 °C to produce formate. Demonstrate at least 50% conversion with >95% selectivity for formate.*

Here, we first screened the conversion of CO_2 captured in our leading post combustion solvent, EEMPA in the presence of $Cu/ZnO/Al_2O_3$ and Pd/C at lower temperatures (<100 °C). As shown in **Table 4**, $Cu/ZnO/Al_2O_3$ did not form any detectable amount of formic acid, instead formamide was formed, indicating that *insitu* formic acid or formate species is reactive and gets converted to formamide even at 50 °C. On the other hand, Pd/C catalyst formed a mixture of formic acid and formamide at 50 °C. Lower temperatures and addition of CO_2 pressure further improved the selectivity to methanol. However, the yield to formic acid was very slow. The low conversion could be because of the strong binding of the active secondary amine moiety in EEMPA with the Pd/C catalyst at lower temperatures, preventing higher conversion to formic acid. To test this hypothesis, we screened a different capture solvent, DBU/hexanol containing a non-nucleophilic base. We evaluated both $Cu/ZnO/Al_2O_3$ and Pd/C for the conversion of CO_2 captured in DBU/hexanol mixture. Conversion as high as 78% was obtained using Pd/C catalyst with high selectivity to formate. Thus, the milestone 2 was reached by using Pd/C catalyst and a non-nucleophilic base-based capture solvent.

Table 4: Hydrogenation of captured CO_2 to formate in the presence of heterogeneous catalysts using a batch reactor system.

Entry	Catalyst	Conditions	Yield of formamide (%)	Yield of formic Acid (%)
1	65 wt.% Cu/ZnO/ Al_2O_3	60 bar H_2 50 °C	0.43	0
2	5 wt.% Pd/C	60 bar H_2 50 °C	3.11	5.34
3		60 bar H_2 40 °C	1	4.09
4		60 bar H_2, 5 bar CO_2 25 °C	0	10.4
5[a]		60 bar H_2 50 °C	0	78.3

Reaction conditions: Catalyst = 0.40 g, 2-EEMPA-5g (CO_2 loaded 2-EEMPA was used), CO_2 captured=8 mmol, initial pressure of H_2 at room temperature= 60 bar, time=16h, [a]DBU-hexanol was used as a model capture solvent.

V. Third quarter's (FY23-Q4) milestone: *(Task 1: methanol) Identify catalyst formulations that leads to at least 95% selectivity for C-N cleavage to produce methanol (Step B).*

The N-formyl piperidine was chosen as a model substrate to understand the C–O vs C–N bond cleavage selectivity during the amide hydrogenation to methanol step (**Scheme 2**). We studied the effect of reaction temperature, time and different additives on the C-O and C-N cleavage selectivity during catalytic hydrogenation of formamide. In the absence of any additives, hydrogenation of N-formyl piperidine formed N-methyl piperidine by C–O bond cleavage with high selectivity (**Table 5**). We also learned that the (in situ formed) product methanol can also act as a N-methylating agent upon longer residence time. On the other hand, in the presence of a base additive, the selectivity switched to methanol formation by C–N bond cleavage. Such reactivity trend has been identified for the first time across a range of heterogeneous catalysts and the homogeneous catalyst, Ru-MACHO. The strong base additive can deprotonate the hemiaminal intermediate, preventing the subsequent dehydration step to form N-methyl piperidine. The results from this study show the crucial role of base additives in determining the product selectivity. The ease of which the selectivity can be shifted from C–O cleavage to C–N cleavage provides a simple and effective means to suppress amine deactivation by N-methylation. This provides new fundamental understandings on how to better design integrated capture and conversion systems to upcycle CO_2 into methanol.

Table 5: Hydrogenation of N-formyl piperidine in the presence of different catalysts

Entry	Catalyst	Conditions	Additives	Conversion (%)	CH_3OH Selectivity (%)	N-Methyl Piperidine Selectivity (%)
1	$Cu/ZnO/Al_2O_3$	170 °C, 12 h, THF	-	94.2	4.9	95.1
2	$Cu/ZnO/Al_2O_3$	170 °C, 12 h, THF	KO^{t}Bu	48.8	49.9	50.1
3	$Cu/ZnO/Al_2O_3$	150 °C, 12 h, THF	KO^{t}Bu	4.3	83	17
4	Copper chromite	170 °C, 12 h, THF	-	29.8	4.5	95.5
5	Copper chromite	170 °C, 12 h, THF	KO^{t}Bu	1.3	83	17
6	35wt.% Cu/Al_2O_3	170 °C, 12 h, THF	KO^{t}Bu	10.7	63.8	36.2
7	5wt.%Ag/Al_2O_3	170 °C, 12 h, THF	-	5	9.5	90.5
8	**5wt.%Ag/Al_2O_3**	**170 °C, 12 h, THF**	**KO^{t}Bu**	**9.4**	**86**	**14**
9	5wt.%Pd/Al_2O_3	170 °C, 12 h	-	5.4	21	79
10	5wt.%Pd/Al_2O_3	170 °C, 12 h, THF	KO^{t}Bu	7	75	25
11	5wt.%$Pd/ZnO/Al_2O_3$	170 °C, 12 h, THF	-	72	2	98
12	5wt.%$Pd/ZnO/Al_2O_3$	170 °C, 12 h, THF	KO^{t}Bu	5.4	76.8	23.3
13	Ru-MACHO	160 °C, 3 h	-	17.6	33	67
14	**Ru-MACHO**	**160 °C, 3 h, THF**	**KO^{t}Bu**	**72**	**94**	**6**

VI. Evaluation of new catalyst formulations for methanol synthesis in a post-combustion capture solvent in a batch reactor:

The following catalysts were synthesized and tested for the hydrogenation of captured CO_2: (1wt%, 5wt% and 10wt%) Pt-K/TiO_2, Pt-Sn/TiO_2, Co-Mo/TiO_2, Co-Mo/Al_2O_3, Re/TiO_2 and Pt/ZrO_2. Among the different catalysts evaluated, higher Pt loading resulted in higher conversion of captured CO_2 while maintaining C-N cleavage selectivity (entry 3, **Table 6**). The 5wt% Pt/ZrO_2 catalyst produced methanol at high selectivity albeit with a lower conversion (entry 10, **Table 6**). In the next budget period, 10wt% Pt/ TiO_2 and Pt/ZrO_2 will be evaluated in a continuous flow reactor.

Table 6: Hydrogenation of captured CO_2 to methanol in the presence of new heterogeneous catalyst formulations using a batch reactor system.

Entry	Catalysts	CO_2 Conv. (%)	Methanol Sel (%)	N-Methylation Sel (%)	CH_4 Sel (%)	C_2H_6 Sel (%)	C-N Cleavage Sel (%)
1	1wt.% Pt/TiO_2	7.4	41.7	0.0	53.9	4.3	100.0
2	5wt.% Pt/TiO_2	21.9	34.9	15.7	47.6	1.8	68.9
3	**10wt.% Pt/TiO_2**	**56.1**	**40.9**	**14.0**	**43.8**	**1.4**	**74.5**
4	5wt.%Pt-1% K/TiO_2	0.0	0.0	0.0	0.0	0.0	0.0
5	5wt.% Pt/TiO_2-0.05wt% K	13.5	49.9	20.6	27.2	2.4	70.8
6	5wt.% Pt-1 wt.%Sn/TiO_2	50.8	5.3	44.0	50.5	0.2	10.8
7	5wt.% Co 5 wt.% Mo/TiO_2	28.7	0.0	0.0	89.6	10.4	0.0
8	5wt.% Co-5 wt.% Mo/Al_2O_3	13.7	0.0	0.0	98.5	1.5	0.0
9	1wt.%Re/TiO_2	0.0	0.0	0.0	0.0	0.0	0.0
10	5wt.% Pt/ZrO_2	9.7	55.2	28.9	16.0	0.0	65.7

Reaction conditions: Catalyst=200 mg, 12h, 170 °C, H_2=60 bar.

VII. WSU Update: Identify catalysts and conditions for the conversion of CO_2 to ethanol.

- **Reported data in the literature for the hydrogenation of CO_2 to ethanol.** Some of the catalysts with outstanding performance are listed in **Table 7**. Excellent ethanol selectivity of more than 90% or even 99% has been reported in the literature by both batch and continuous flow reactors with different catalyst formulations.

Table 7. Reported data in the literature for the hydrogenation of CO_2 to ethanol.

Entry	**Heterogeneous Catalyst Type**	**Reactor Type**	**Process Conditions**	**Ethanol Selectivity (%)**	**Ref.**
1	Ir_1-In_2O_3	Batch	*T*=200 °C, *P*=6 MPa, H_2:CO_2=5:1, t=5 h	99.7	[4]
2	$CoAl_x$-600	Batch	*T*=140 °C, *P*=4 MPa, H_2:CO_2=3:1, t=15 h	92.1	[6]
3	Pd_2Cu-NPs/P25	Batch	*T*= 200 °C, *P*=3.2 MPa, H_2:CO_2=3:1, t=5 h	92	[7]
4	Pd_2/CeO_2	Continuous Flow	*T*= 240 °C, *P*=3 MPa, H_2:CO_2=5:1, GHSV=3000 mL $gcat^{-1}h^{-1}$	99.2	[8]
5	$CeTiO_x$	Batch	*T*=250 °C, *P*=3 MPa, H_2:CO_2=5:1, t=5 h	99.1	[9]

- **Attempts for reproducing the reported values.** The results are listed in **Table 8**. However, no phenomenal ethanol selectivity is observed, the highest value is 12.8%, which is far below the best

value of 99.7% reported in the literature. CO is constantly observed as a main byproduct with no less than 70% selectivity, which is reported to be negligible in some publications above. CH_4 is also commonly seen as a product, which is also reported to be undetectable in some publications above.

Table 8. Performance of catalysts synthesized according to literature report. Reaction conditions: Batch reactor, 120 mg catalyst, 18 mL DI water as solvent, temperature=200 °C, 1 MPa CO_2 , 5 MPa H_2, reaction time 5 h, stirring 400 rpm, activation under 5 MPa H_2 at 200 °C for 5 h.

Catalyst	Yield(C%)					Selectivity(%)			
	Total	CO	CH_4	Methanol	Ethanol	CO	CH_4	Methanol	Ethanol
In_2O_3	0.0215	0.0197	0.0009	0.0006	0.0002	92.0	4.2	2.9	0.9
0.04 wt.%Ir/In_2O_3	0.0191	0.0165	0.0016	0.0009	0.0002	86.2	8.1	4.6	1.1
1 wt.%Ir/In_2O_3	0.0194	0.0173	0.0005	0.0014	0.0003	89.0	2.6	7.0	1.4
0.04 wt.% Ir/In_2O_3 (Commercial)	0.0433	0.0345	0.0060	0.0019	0.0010	79.5	13.8	4.5	2.2
0.04 wt.% Ir/In_2O_3 (Synthesis)	0.0505	0.0464	0.0029	0.0009	0.0004	91.8	5.6	1.8	0.7
Pd_2CeMOF@Si_{16}	0.0278	0.0212	0.0018	0.0012	0.0036	76.4	6.5	4.4	12.8

- **Catalyst systems with platinum group metals loaded onto different types of supports are explored.** The results are listed in **Table 9**. Rh/SiO_2 shows the best performance in terms of CO_2 conversion and ethanol selectivity, which deserves further exploration. Besides, methane is a common major byproduct over Rh-based catalysts compared to CO over catalysts with other metals.

Table 9. Performance of catalysts with platinum group metals loaded on different supports. Reaction conditions: Batch reactor, 120 mg catalyst, 18 mL DI water as solvent, temperature=200 °C, 1 MPa CO_2 , 5 MPa H_2, reaction time 5 h, stirring 400 rpm, activation under 5 MPa H_2 at 200 °C for 5 h.

Catalyst	Yield(C%)					Selectivity (%)			
	Total	CO	CH_4	Methanol	Ethanol	CO	CH_4	Methanol	Ethanol
0.9 % Pt/Ce NP/Al_2O_3	0.0276	0.0266	0	0.0008	0.0002	96.5	0	2.8	0.7
0.9 % Pt/Ce SA/Al_2O_3	0.1649	0.1608	0	0.0033	0.0008	97.5	0	2.0	0.5
0.9 % Pt/Ce SA/Al_2O_3-R	0.3243	0.3098	0	0.0113	0.0032	95.5	0	3.5	1.0
5 wt.% Pt/TiO_2	0.4564	0.4164	0.0041	0.0358	0	91.2	0.9	7.9	0.0
5 wt.% Pt/TiO_2 (PNNL)	0.5389	0.4776	0.0087	0.0526	0	88.6	1.6	9.8	0.0
5.56 wt.% Pt/CeO_2	0.1087	0.1034	0.0014	0.0032	0.0006	95.1	1.3	2.9	0.6
5.56 wt.% Rh/SiO_2	2.4179	0.5835	1.7675	0.0358	0.0310	24.1	73.1	1.5	1.3
5.56 wt.% Rh/CeO_2	1.0720	0.1826	0.8708	0.0112	0.0075	17.0	81.2	1.0	0.7
5.56 wt.% Rh/TiO_2	2.4031	0.2453	2.1140	0.0252	0.0186	10.2	88.0	1.1	0.8
5.56 wt.% Rh/Ce NP/Al_2O_3	1.3448	0.3658	0.9296	0.0321	0.0173	27.2	69.1	2.4	1.3
1 wt.%Pt deAlb[a]	0.4323	0.4264	0.0044	0.0012	0.0002	98.6	1.0	0.3	0.1

1 wt.%Rh deAlb[a]	1.1772	0.8789	0.2828	0.0127	0.0028	74.7	24.0	1.1	0.2
1 wt.%Cu deAlb[a]	0.1769	0.1617	0.0121	0.0025	0.0006	91.4	6.9	1.4	0.3

- **The effect of Rh loading on SiO_2 support is investigated.** The results are listed in **Table 10**. With increasing Rh loading, the CO_2 conversion increases along with a higher methane selectivity. Ethanol selectivity is also slightly enhanced but to a limited extent.

Table 10 Performance of Rh/SiO_2 catalysts with different Rh loadings. Reaction conditions: Batch reactor, 120 mg catalyst, 18 mL DI water as solvent, temperature=200 °C, 1 MPa CO_2 , 5 MPa H_2, reaction time 5 h, stirring 400 rpm, activation under 5 MPa H_2 at 200 °C for 5 h.

Catalyst	Yield(C%)					Selectivity(%)			
	Total	CO	CH_4	Methanol	Ethanol	CO	CH_4	Methanol	Ethanol
5.56 wt..%Rh/SiO_2	2.4179	0.5835	1.7675	0.0358	0.0310	24.1	73.1	1.5	1.3
1 wt..%Rh/SiO_2	0.3473	0.1759	0.1621	0.0070	0.0024	50.6	46.7	2.0	0.7
0.6 wt..%Rh/SiO_2	0.2430	0.1424	0.0941	0.0052	0.0014	58.6	38.7	2.1	0.6
0.1 wt..%Rh/SiO_2	0.1180	0.0911	0.0239	0.0024	0.0006	77.2	20.3	2.1	0.5

- **Metal loading on CeO_2-Al_2O_3 with different Ce nuclearity is used as an additional catalyst synthesis strategy.** The catalytic performance of the synthesized catalyst is listed in **Table 11**. While keeping the same reaction conditions, loading 0.09 wt.% metal such as Pt, Pd, Rh, and Cu onto ceria-alumina support does not lead to dramatically changed catalytic behavior, regardless of the Ce nuclearity. Rh catalysts provide the highest CO_2 conversion while Cu does not entail additional catalytic behavior besides the bare support.

Table 11 Performance of catalysts with metal loaded on CeO_2-Al_2O_3 supports with different Ce nuclearity. Reaction conditions: Batch reactor, 120 mg catalyst, 18 mL DI water as solvent, temperature=270 °C, 1 MPa CO_2, 5 MPa H_2, reaction time 5 h, stirring 400 rpm, activation under 5 MPa H_2 at 270 °C for 5 h.

Catalyst	Yield(C%)					Selectivity(%)			
	Total	CO	CH_4	Methanol	Ethanol	CO	CH_4	Methanol	Ethanol
Ce NP/Al_2O_3	0.1248	0.1157	0.0074	0.0013	0.0004	92.7	6.0	1.0	0.3
Ce SA/ Al_2O_3	0.1068	0.1012	0.0042	0.0011	0.0004	94.8	3.9	1.0	0.3
0.09 wt.%Pt/Ce NP/Al_2O_3	0.2050	0.1998	0.0028	0.0018	0.0007	97.4	1.4	0.9	0.3
0.09 wt.%Pt/Ce SA/Al_2O_3	0.1918	0.1841	0.0055	0.0016	0.0006	96.0	2.9	0.8	0.3
0.09 wt.%Pd/Ce NP/Al_2O_3	0.1915	0.1841	0.0038	0.0029	0.0008	96.1	2.0	1.5	0.4
0.09 wt.%Pd/Ce SA/Al_2O_3	0.2095	0.2026	0.0042	0.0021	0.0006	96.7	2.0	1.0	0.3
0.09 wt.%Rh/Ce NP/Al_2O_3	0.2528	0.2292	0.0202	0.0027	0.0006	90.7	8.0	1.1	0.3
0.09 wt.%Rh/Ce SA/Al_2O_3	0.2681	0.2604	0.0043	0.0028	0.0006	97.1	1.6	1.0	0.2
0.09 wt.%Cu/Ce NP/Al_2O_3	0.1230	0.1187	0.0031	0.0010	0.0002	96.5	2.5	0.8	0.2
0.09 wt.%Cu/Ce SA/Al_2O_3	0.1178	0.1129	0.0033	0.0012	0.0003	95.9	2.8	1.0	0.2

- **Operations in a continuous flow reactor are also performed.** Fe, Li and Sr are used as promoters to improve the catalytic performance of Rh/SiO_2 catalysts. The reactions were performed for 20 hours. In the beginning, the reactor system was stabilized at 210 °C under reaction gas for 2 h, then the temperature was kept at 210, 240, 270 and 300 °C for 4 h. 5 wt%Rh-2.7 wt%Fe/SiO_2 catalyst (Rh:Fe=1:1 molar) leads to promising results with a high ethanol selectivity of 8% observed at 210 °C (**Figure 12**). A higher CO_2 conversion of 35% can be achieved at 300 °C. However, at high temperature CO becomes the dominant product and C_{2+} starts to be formed, while ethanol selectivity decreases dramatically. It seems that a temperature of 210 °C-240 °C is more suitable for ethanol production over Rh-based catalysts. Li and Sr as promoters lead to inferior catalytic performance compared to Fe, in terms of maximal CO_2 conversion and ethanol selectivity.

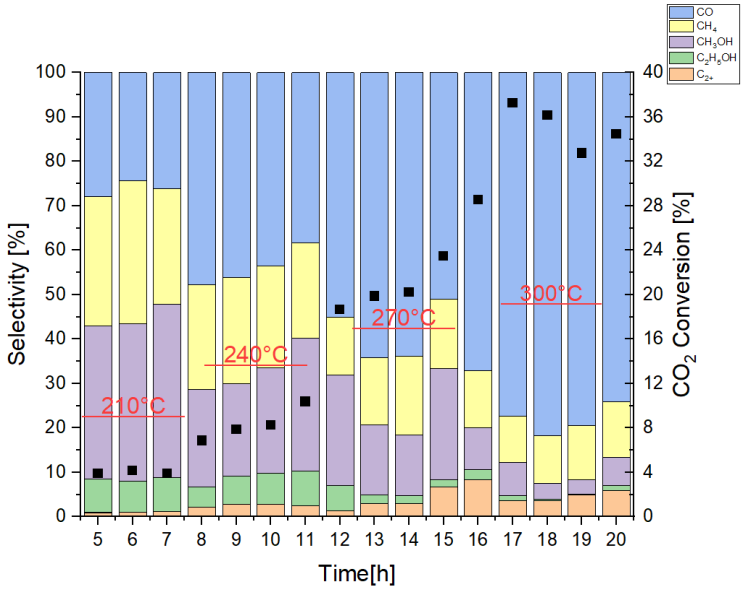


Figure 12. CO_2 hydrogenation over 5 wt%Rh-2.7 wt%Fe/SiO_2 catalyst. Flow reactor, temperature 210-300 °C, pressure 30 bar, CO_2 5 sccm, H_2 15 sccm, catalyst loading: 100 mg catalyst with 1000 mg SiC, activation under temperature 350 °C, H_2 20 sccm for 30 min.

VIII. Progress towards Q1-FY24 milestone: *(Task 6: LCA) Preliminary LCA for IC^{3}M process for GHG reduction*

In this reporting period, a preliminary life cycle analysis was conducted for the IC^{3}M technology. The cradle-to-grave greenhouse gas (GHG) emissions throughout the product life cycle was evaluated, including the extraction and processing of raw materials, manufacturing, distribution, use, and final disposal. The goal is to inform design targets for the remainder of the project from the GHG emission perspective.

A) LCA Goal and Scope

The purpose of the study is to evaluate the life cycle GHG emissions of methanol produced from PNNL's IC^{3}M technology and determine the corresponding GHG emission reduction compared to the industrial baseline and other GHG emission reduction technologies. As the performance of PNNL's IC^{3}M technology is improving during the on-going project, two IC^{3}M cases previously

published in Kothandaraman et al. (2022) were evaluated. One represents the state-of-technology (SOT) achieved in 2022, while the other represents the research goal.

Key specifications describing the scope of the performed LCA are as follows:

- **Functional Unit**. As all products from the technology will be used as energy carriers (methanol, ethanol, and electricity), g $CO_{2\ eq}$/MJ is selected as the function unit. The Lower Heating Value (LHV) is used to determine the energy density of methanol and ethanol.
- **System Boundary**. For the life cycle GHG emission analysis, the system boundary is set to cradle-to-grave as shown in **Figures** 1 to 2 for the two IC^{3}M cases.
- **Carbon Dioxide Source**. In this study, CO_2 is captured from a NGCC power plant.
- **Technology Representativeness**. As the IC^{3}M process produces electricity as a co-product, the results were compared with three Comparison Product Systems: one using a more conventional separated carbon capture and conversion to methanol (SC^{3}M) approach (as shown in **Figure 15**), one representing the current industrial benchmark (natural gas derived methanol, NG-methanol), and one representing electricity produced from a natural gas combined cycle (NGCC) power plant without carbon capture and sequestration (CCS).
- **Geographical Representativeness**. United States.
- **Temporal Representativeness**. Methanol and ethanol produced from this carbon capture and utilization process will be used as transportation fuel at the end of their life cycle. Global Warming Potential (GWP) will be reported using the 100-year characterization factors with climate carbon feedback based on the default values from the Intergovernmental Panel on Climate Change (IPCC) Fifth Assessment Report (AR5).
- **Completeness Requirements**. The key mass, energy, and carbon flow are documented in **Figures 13** to **15** for both IC^{3}M and SC^{3}M processes, following the NETL CO2U toolkit guidance. The NGCC and NG-methanol cases were well documented in NETL CO2U OpenLCA LCI Database, of which the cradle-to-gate LCI data were directly used in the LCA model for comparison.

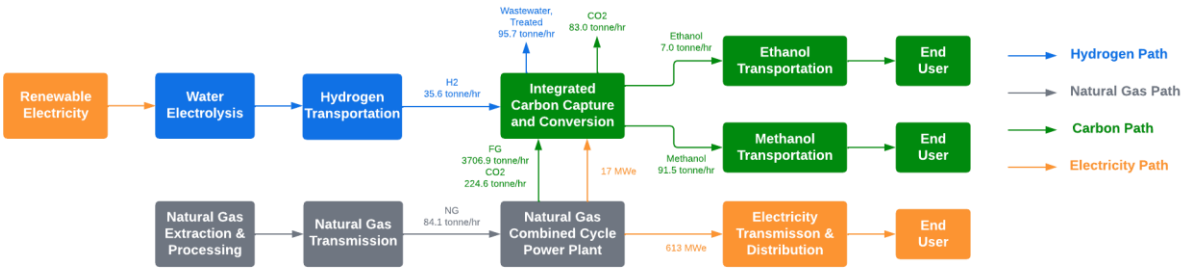


Figure 13. System boundary of the proposed product system: IC^{3}M – 2022 SOT.

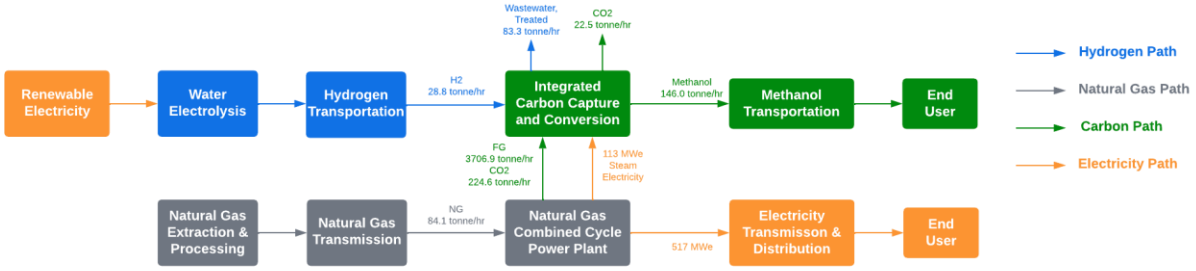


Figure 14. System boundary of the proposed product system: IC^{3}M – goal case.

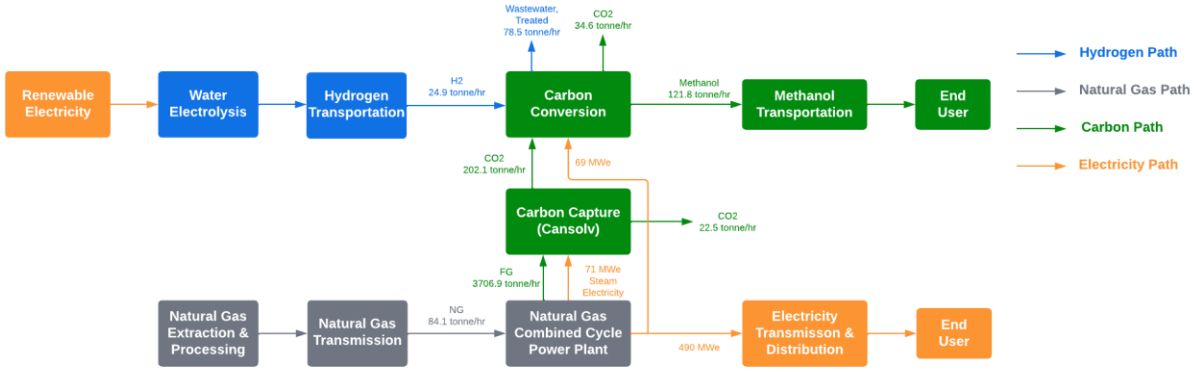


Figure 15. System boundary of the comparison product system: SC^{3}M.

B) Life Cycle Inventory Analysis

Modeling Platform. The LCA models were developed in OpenLCA with NETL CO2U OpenLCA LCI Database, USLCI Database from Federal LCA Commons, and Ecoinvent V3.8. Additional LCI data from GREET model developed by the Argonne National Laboratory were also used.

Unit Process Descriptions. The key unit processes of NGCC with and without CCS and NG-methanol product system were well document in previous reports [10, 11]. The key unit processes of the Proposed Product System (IC^{3}M) and the third Comparison Product System (SC^{3}M) were described below.

- **Integrated carbon capture and conversion**: In the proposed IC^{3}M process, 90% of CO_2 in the flue gas is captured in the absorber by countercurrent contact with EEMPA. The condensed-phase CO_2-rich solvent is pumped to the desired pressure to the reactor co-fed with H_2, where CO_2 is converted to methanol. In the 2022 SOT case, a small amount of methane and ethanol is produced in the reactor, where methane is burned to supply process heat, and ethanol is purified and sold as by-product. In the Goal case, methanol selectivity is set to 100%. Detailed process flow diagram could be found in [12].
- **Carbon capture (Cansolv)**: Cansolv is the NETL baseline technology for post-combustion carbon capture. In this process, 90% of CO_2 in the flue gas is captured in the absorber and regenerated at the stripper at near atmospheric pressure with significant steam consumption for heating.

- **Carbon conversion**: Pure CO_2 from the capture unit at near atmospheric pressure is compressed to the desired reactor operating pressure, preheated, and fed to the methanol synthesis reactor with excess H_2 co-feed. In the reactor, CO_2 is converted to methanol, while water is produced as by-product. Unreacted H_2 is recovered and recycled back to the reactor. Methanol and water are separated via distillation. Detailed process flow diagram can be found in [13].
- **Water electrolysis**: In this process, H_2 is produced from water electrolysis using the proton exchanger membrane (PEM) technology. The energy efficiency is set to 55.5 kWh/kg H_2, defined as the LHV of the produced H_2 divided by the total electricity used [14].
- **Hydrogen transportation**: This process includes gaseous H_2 compression (50 MPa) for loading onto a tube-trailer, followed by 100 miles of tube-trailer transportation to distillation, onboard storage, and precooling.
- **Product transportation**: Deliver methanol and ethanol to end users.
- **Product end user**: Methanol and ethanol are used as transportation fuel and combusted in the vehicle engine at the end of their life.

Data Sources, Quality Assessment, and Inventory Completeness Check. The life cycle inventory (LCI) data of the Proposed Product System, PNNL's IC^{3}M technology, were collected based on process models developed in Aspen Plus, as shown in **Table 13**. Key performance measures for the SOT and assumptions for the goal case were listed in **Table 12**, of which details were published in [12]. The LCI data of the Comparison Product Systems, NGCC, and NG-methanol, were collected from the NETL CO2U OpenLCA LCI Database. The LCI data of the SC3M process were collected from [13]. GHG emissions at the product transportation and end of life stages were collected from GREET 2022 database. The overall carbon and energy balance are also reported in **Table 14** for inventory completeness check. **Table 15** summarizes the unit processes used in the LCA model.

Table 12. Key performance measures and assumptions for PNNL's IC^{3}M technology.

	SOT	Goal Case
WHSV (gCO_2/gCat/hr)	0.075	0.15
Single-pass CO_2 conversion (%)	26.9	85.7
Methanol selectivity (C %)	63.6	100
Methane selectivity (C %)	26.4	0
Source	Experiment	R&D Target

Table 13. LCI of the proposed IC^{3}M and the conventional SC^{3}M processes.

		IC^{3}M-2022 SOT	IC^{3}M-Goal Case	SC^{3}M
Outputs				
Methanol	MJ, LHV	1.00	1.00	1.00
Ethanol	MJ, LHV	0.10	0.00	0.00
Electricity	MJ	1.21	0.64	0.73
Inputs				

Natural gas	g	46.13	28.90	34.63
Hydrogen	g	19.55	9.90	10.25
Emissions to air				
Carbon dioxide, fossil	g	45.52	7.72	23.56

Table 14. Carbon and energy balance of the IC^{3}M and SC^{3}M processes

		IC^{3}M-2022 SOT	IC^{3}M-Goal Case	SC^{3}M
Carbon In				
Natural gas	kg/hr	60,763	60,763	60,763
Carbon Out				
Methanol	kg/hr	34,282	54,725	45,668
Ethanol	kg/hr	3,650		
Carbon dioxide	kg/hr	22,656	6,130	15,624
Carbon Balance	%	99.7	100.2	100.9
Energy In				
Natural gas	MJ, LHV	1,105	1,105	1,105
Hydrogen	MJ, LHV	1,187	960	830
Energy Out				
Methanol	MJ, LHV	507	809	675
Ethanol	MJ, LHV	52		
Electricity	MJ	613	517	490
Energy efficiency	%, LHV	51.1	64.2	60.2

Table 15. List of unit processes used in the LCA models for the proposed and comparison product systems.

Unit Process	Product System	Database
IC^{3}M-2022 SOT Unit Process	IC^{3}M-2022 SOT	PI model
IC^{3}M-Goal Unit Process	IC^{3}M-Goal	PI model
SC^{3}M Unit Process	SC^{3}M	PI model [13]
Green Hydrogen Production (PME)	IC^{3}M-2022 SOT, IC^{3}M-Goal, SC^{3}M	GREET 2022
Hydrogen Transportation	IC^{3}M-2022 SOT, IC^{3}M-Goal, SC^{3}M	GREET 2022
Natural Gas Through Transmission – U.S. Mix	IC^{3}M-2022 SOT, IC^{3}M-Goal, SC^{3}M	NETL CO2U LCI
NGCC Power Plant, no capture, cradle-to-gate – US-IL	IC^{3}M-2022 SOT, IC^{3}M-Goal	NETL CO2U LCI
NGCC Power Plant, capture, cradle-to-gate – US-IL	SC^{3}M	NETL CO2U LCI
Renewables - US	IC^{3}M-2022 SOT, IC^{3}M-Goal, SC^{3}M	NETL CO2U LCI
Methanol from Natural Gas - GLO	NG-methanol	NETL CO2U LCI

Allocation Procedures. As shown in **Figures 13 to 15**, the proposed technology produces methanol, ethanol, and electricity. Therefore, two impact allocation methods were used, system expansion and energy allocation. When system expansion method is used, electricity is set as by-product by checking the box of "Avoided product" in OpenLCA, of which the associated GHG emission is credited with the load that would appear if it is produced from a NGCC power plant without carbon capture. The impact is allocated between methanol and ethanol based on their energy content. When energy allocation method is used, all products are treated the same, of which the impacts are allocated based on their energy content.

C) Life Cycle GHG Emissions Impact Assessment

The preliminary cradle-to-grave LCA results on GHG emissions of the proposed product system (IC3M) and the comparison product system (SC3M, NG-methanol, and NGCC power plant) are shown in **Figures 16** and **17** using system expansion or energy allocation method for electricity co-production. The results suggest the impact of impact allocation method on the LCA results is not negligible. It is mainly attributed to the fact that flue gas from a NGCC power plant is used as the carbon source in the proposed product system, resulting in a significant amount of electricity as a by-product.

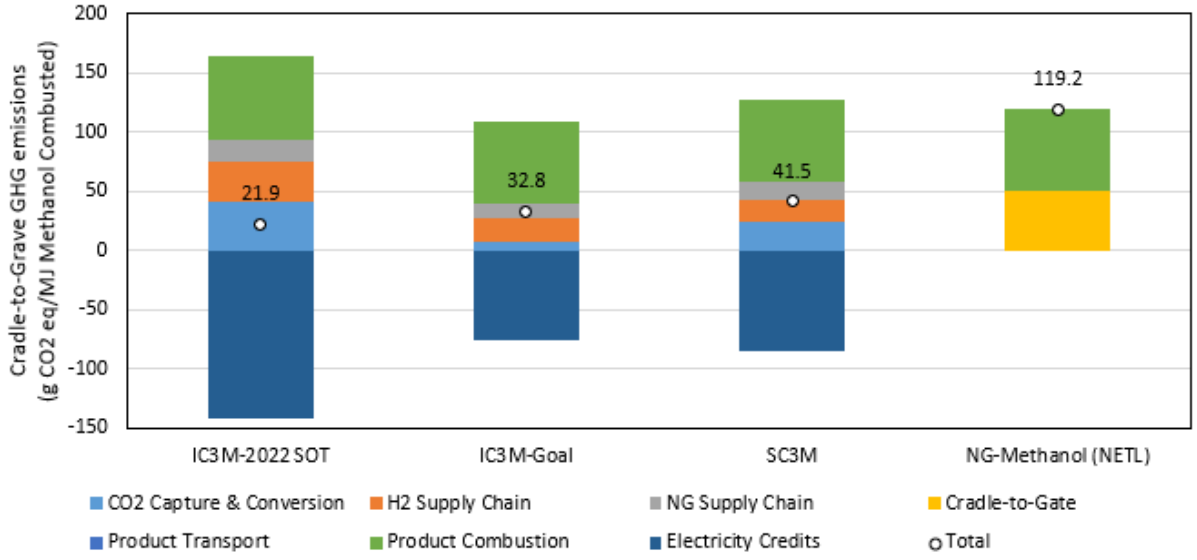


Figure 16. Cradle-to-grave GHG emission results for the proposed and comparison product systems using system expansion method for electricity by-product.

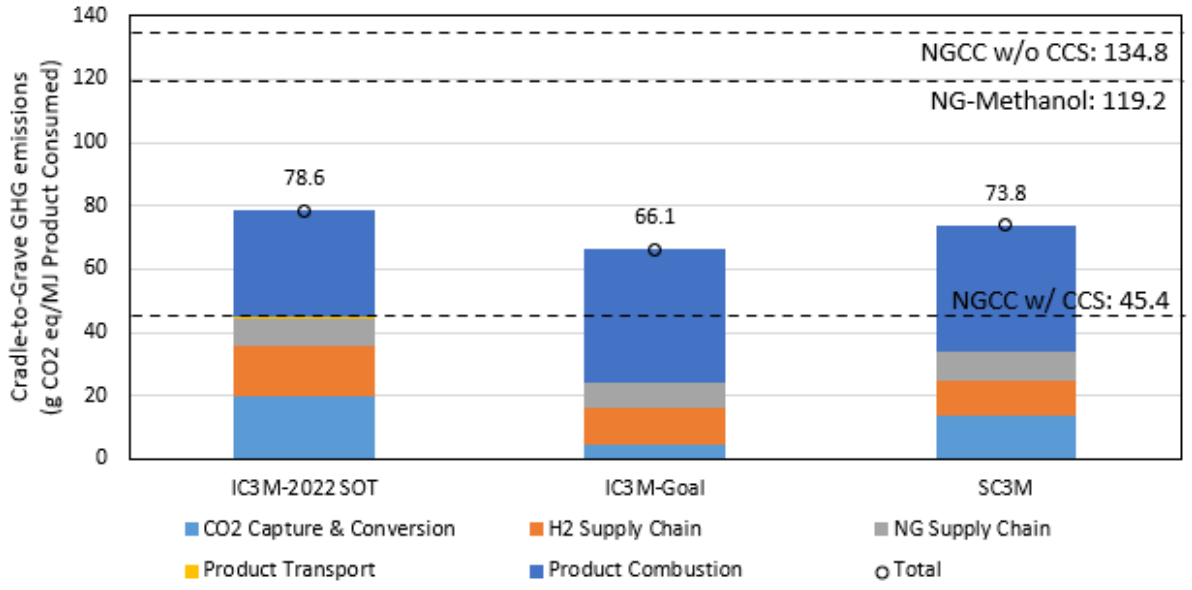


Figure 17. Cradle-to-grave GHG emission results for the proposed and comparison product systems using energy allocation method for electricity by-product.

D) Life Cycle Interpretation

When the system expansion method is used to deal with electricity by-product, the cradle-to-grave GHG emissions of both IC^{3}M cases is lower than those of the SC^{3}M cases. Compared with the industrial benchmark, natural gas derived methanol, a GHG emission reduction up to 81.6% can be achieved by using PNNL's IC3M technology to produce methanol from NGCC flue gas and green hydrogen. Even though the 2022 SOT case has less process-level efficiency than the goal case, it exhibits lower GHG emissions because more electricity is produced, resulting in a high electricity credit, as shown in **Table 14.** As presented in **Table 12**, a significant amount of methane is produced in the IC^{3}M-2022 SOT unit process, which is burned to supply heat and energy. Therefore, compared with the IC^{3}M-goal case, the IC^{3}M-2022 SOT case has more direct GHG emissions (marked by the light blue bar in **Figure 14**) and also higher electricity credits.
When the energy allocation method is used to treat methanol and electricity equally, the cradle-to-grave GHG emissions from the IC^{3}M-2022 SOT case is slightly higher than that of the SC^{3}M case. This is due to the lower methanol selectivity (**Table 12**), resulting in lower process-level energy efficiency (**Table 14**) and higher hydrogen consumption (**Table 13**). Once the selectivity is improved, the process-level energy efficiency as well as the cradle-to-grave GHG emission reduction can be significantly improved, making the IC^{3}M technology more attractive than the SC^{3}M technology.

Overall, the cradle-to-grave GHG emissions of both IC^{3}M cases is much lower than those of the NGCC power plant without CCS (134.8 g $CO_{2\ eq}$/MJ, or 485.1 kg $CO_{2\ eq}$/MWh) and natural gas derived methanol (119.2 g $CO_{2\ eq}$/MJ) [11, 15]. However, it is higher than that of the NGCC power plant with CCS because methanol and/or ethanol produced from NGCC flue gas is combusted at the end of their life, releasing fossil CO_2 back into the environment. This preliminary LCA suggests the proposed IC^{3}M technology can achieve a significant GHG emission reduction compared with

the industrial benchmark, even with the unoptimized 2022 SOT catalyst performance. The life cycle GHG emission reduction of the proposed technology can be further improved through continuous improvement in catalyst performance, particularly higher methanol selectivity.

IX. Progress towards Q1-FY24 milestone: *(Task 4: Ethanol) Establish baseline performance of single atom catalyst for gas phase CO_2 conversion to ethanol. (WSU)*

WSU attempted to reproduce the literature data for the hydrogenation of CO_2 to ethanol. In the last FY, WSU identified that the literature reports on the hydrogenation of CO_2 to ethanol are not reproducible. Some of the literature reported catalysts with outstanding performance are listed in **Table 16** . Excellent ethanol selectivity of more than 90% or even 99% has been reported in the literature using both batch and continuous flow reactors with different catalyst formulations. Our attempts to reproduce the reported values are listed in **Table 16.** However, no phenomenal ethanol selectivity is observed, the highest value is 6%, which is far below the best value of 99.7% reported in the literature. CO is constantly observed as a main product with no less than 70% selectivity, which is reported to be negligible in some publications. CH_4 is also commonly seen as a product, which is also reported to be undetectable in some publications.

Table 16. Reported performance of catalysts in the literature for the hydrogenation of CO_2 to ethanol. Synthesis procedure and experimental reaction conditions were same as the literature reports.

Heterogenous Catalyst	Literature Reports			WSU Results		
	Ethanol Sel. (%)	CO_2 Conv. (%)	TOF (h^{-1})	Ethanol Sel. (%)	CO_2 Conv. (%)	TOF (h^{-1})
Ir_1-In_2O_3	99.7	-	481	1.1	0.02	18.41
$CoAlO_x$-600	92.1	-	-	5.9	0.19	0.01
Pd_2Cu-NPs/P25	92	-	359	2.5	0.24	20.03
Pd_2/CeO_2	99.2	9.2	211.7	2.9	1.05	27.88
$Rh/CeTiO_x$	99.1	6.3	493.1	3.9	0.57	15.74

In addition to these catalysts listed in **Table 16**, WSU team has also investigated different modified catalysts such as, different wt% Ir on In_2O_3, Pt on different supports such as Al_2O_3, TiO_2 and CeO_2, Rh on different supports such as CeO_2, TiO_2 and SiO_2. Among the different catalysts investigated, Rh/SiO_2 gave the highest CO_2 conversion and ethanol selectivity of 2.5% and 1.3% respectively. Methane and CO are the major products in all cases. Metal loading (0.09 wt.% of metal such as Pt, Pd, Rh, and Cu) on CeO_2-Al_2O_3 with different Ce nuclearity is used as an additional catalyst synthesis strategy. Metal loading onto ceria-alumina support does not lead to dramatically changed catalytic behavior, regardless of the Ce nuclearity.

Fe, Li and Sr are used as promoters to improve the catalytic performance of Rh/SiO_2 catalysts in a continous flow reactor. In the beginning, the reactor system was stabilized at 210 °C under reaction gas for 2 h, then the temperature was kept at 210, 240, 270 and 300 °C for 4 h. 5 wt%Rh-2.7 wt%Fe/SiO_2 catalyst (Rh:Fe=1:1 molar) leads to promising results with a high ethanol selectivity of 8% observed at 210 °C (**Figure 18**). A higher CO_2 conversion of 35% can be achieved at 300 °C. However, at high temperature CO becomes the dominant product and C_{2+} starts to be formed, while ethanol selectivity decreases dramatically. It seems that a temperature of 210 °C-240 °C is more suitable for ethanol production over Rh-based catalysts. Li and Sr as promoters lead to inferior catalytic performance compared to Fe, in terms of maximal CO_2 conversion and ethanol selectivity.

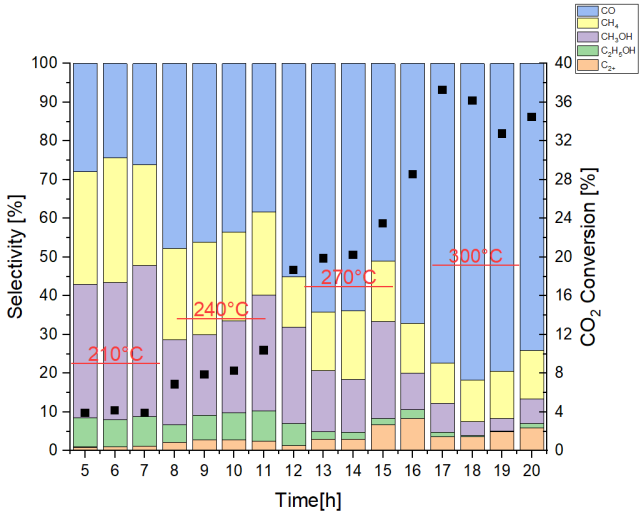


Figure 18. CO_2 hydrogenation over 5 wt%Rh-2.7 wt% Fe/SiO_2 catalyst. Flow reactor, temperature 210-300 °C, pressure 30 bar, CO_2 5 sccm, H_2 15 sccm, catalyst loading: 100 mg catalyst with 1000 mg SiC, activation under temperature 350 °C, H_2 20 sccm for 30 min.

As Pd_2/CeO_2 was identified to be one of the best catalysts for C-C coupling, we will explore this catalyst further this quarter. It is highly possible that the ethanol selectivity is closely related to the particle size of Pd, since the formation of ethanol requires a C-C coupling step which is more favored by the vicinal arrangement of metal active sites. To test the hypothesis, Pd/CeO_2 nanoglue/SiO_2 catalysts with different Pd loadings were synthesized. With the uniquely designed support material, the nuclearity of Pd can be well controlled and its impact on the CO_2 hydrogenation performance can be investigated. The larger Pd particles resulting from higher Pd loading may potentially facilitate a more vicinal arrangement of active sites for C-C coupling, enhancing ethanol selectivity. In contrast, single atom configuration may favor the formation of CO or CH_4 since there is not enough vicinal arrangement. We studied the effect of Pd loading on CeO_x-SiO_2 support and our initial findings are given in **Figure 19**, which indicate that a 2 wt.% Pd CeO_x nano-glue SiO_2 catalyst exhibits modest performance in the conversion of CO_2 to ethanol. Specifically, it achieves approximately 18% ethanol selectivity at 210°C and a maximum CO_2 conversion of 10% at 300 °C. As we decrease the Pd content to 1 wt.%, we observe a significant increase in ethanol selectivity, reaching 41% at 210 °C, and a corresponding rise in the maximum CO_2 conversion to 12%. Further reducing the Pd content to 0.5 wt.% results in a substantial drop in catalytic activity and selectivity, yielding only 3% ethanol selectivity and a maximum CO_2 conversion of 7% at 270°C.

When the Pd loading is reduced to 0.2 wt.%, the catalyst exhibits almost no activity in ethanol production. Reducing the metal loading appears to impede the efficient bonding of CO_2 molecules, resulting in fewer vicinal arrangements and insufficient active sites, particularly for ethanol production. Conversely, excessively high Pd loading leads to active centers that do not favor

ethanol formation, potentially due to the inappropriate active sites that do not induce C-C coupling. In the case of a 1 wt.% Pd loading, vicinal arrangements promote the formation of more active sites for C-C coupling, leading to increased ethanol selectivity. Additionally, altering the metal loading induces structural changes, thereby influencing activation energy and potentially contributing to differences in selectivity. However, it should be noted that the catalytic performance of Pd/CeO_x-SiO_2 catalysts is in general not stable in terms of both CO_2 conversion and ethanol selectivity.

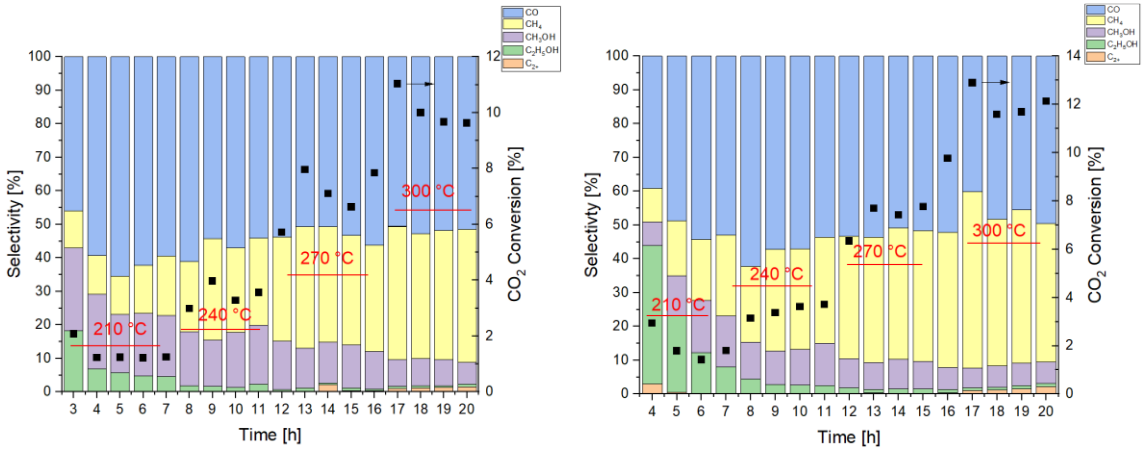


Figure 19. Performance of 2 wt.% Pd-CeO_x-SiO_2 (left) and 1 wt.% Pd-CeO_x-SiO_2 (right). Reaction conditions: Flow reactor, temperature 210-300 °C, pressure 30 bar, CO_2 5 sccm, H_2 15 sccm. Catalyst loading: 50 mg catalyst with 1000 mg SiC, activation under temperature 350 °C, H_2 20 sccm for 30 min.

Although Pd/CeO_2 nanoglue/SiO_2 catalysts show promising performance in terms of a strikingly high ethanol selectivity of 41%, we also noticed that the stability of the catalyst is unfavorable. The high ethanol selectivity drops to lower than 15% in 2 hours and the activity is also reduced by a factor of 2 in this period. Such unstable performance could be due to the structural change of Pd during the reaction, which leads to the varied particle size or vicinal arrangement. This problem needs to be addressed to improve the repeatability and practicability of the catalyst system, which may require modification of the synthesis methods and/or adding auxiliary components. Besides this, it is demonstrated in our last quarter that RhFe/SiO_2 exhibits a compromised initial ethanol selectivity compared to Pd/CeO_2 nanoglue/SiO_2 but much better stability. The activity and ethanol selectivity are well maintained for 10 hours based on current operation conditions. Since the operation conditions are not optimized for catalyst screening, the performance can be significantly improved by simple modifications of operational parameters and such efforts are highly controllable. Besides, the promotion effect of Fe to Rh is phenomenal based on the comparison of RhFe/SiO_2 and Rh/SiO_2 catalysts. Although this promotion effect is also found in some literature reports, the mechanism behind is still poorly understood. The follow-up study of the RhFe system, particularly the interaction between Rh and Fe, can not only help us to get better catalysts for meeting project targets but also provide valuable insights for the development of better CO_2 hydrogenation catalysts.

X. *Evaluation of new catalyst formulations for methanol synthesis in a post-combustion capture solvent in a continuous flow reactor*

After evaluating different catalysts (CoMo, Pt, and Cu on different supports) in the batch reactor during this quarter and the last quarter, Pt/ZrO_2 and Pt/MoO_3 catalysts were selected for further evaluation in a continuous flow reactor based on their superior performance in terms of CO_2 conversion and/or selectivity. The continuous flow experimental results are summarized in **Table 17**. The performance of 5wt% Pt/ZrO_2 and 5wt% Pt/MoO_3 catalysts was compared with our first-generation catalyst (5wt% Pt/TiO_2 catalyst).

At 190 °C and a high space velocity (0.15 $gCO_2/gCat/h$) (entries 1, 4, and 7, **Table 17**), CO_2 conversion and methanol selectivity were high with Pt/MoO_3 compared to 5wt% Pt/ZrO_2. In addition, CO was observed in all cases, with Pt/ZrO_2 showing very high CO selectivity (74%). However, at a lower space velocity (entries 2, 5, and 8, **Table 17**), CO selectivity significantly decreased, suggesting that CO is converting to methanol/methane with a longer contact time between the catalyst and CO_2 feed. Importantly, the selectivity to methanol was ~100% in the case of Pt/ZrO_2, although CO_2 conversion was low (33%) compared to Pt/TiO_2 and Pt/MoO_3. CO_2 conversion of about 77% was obtained with Pt/TiO_2 and Pt/MoO_3, with almost the same selectivity for methanol and methane. The conversion was high (86%) even at 170 °C in the case of Pt/MoO_3 (entry 10 vs. entry 3, **Table** 17). As shown in entry 11, at 150 °C, CO_2 conversion was ~48%, with high methanol selectivity of 77%. Overall, Pt/MoO_3 catalyst shows superior catalytic performance in terms of CO_2 conversion compared to Pt/TiO_2 and Pt/ZrO_2.

Table 17: Hydrogenation of captured CO_2 over various catalysts, employing a continuous-flow reactor system across a range of operating temperatures and space velocities.

Entry	Run	T (°C)	SV $gCO_2/gCat/h$	Conv. (%)	MeOH Sel. (%)	CH_4 Sel.(%)	CO Sel. (%)
	5wt% Pt/TiO_2 (1g), 5wt% CO2 EEMPA						
1	IC3M22	190	0.15	29.4	51.2	31.4	17.4
2	IC3M22	190	0.015	77.2	55.1	44.9	0.0
3	IC3M12	170	0.015	33.4	88.8	11.2	0.0
	5wt% Pt/ZrO_2 (1g), 5wt%CO_2 EEMPA feed						
4	IC3M14	190	0.15	10.8	25.8	0.0	74.2
5	IC3M14	190	0.015	33.3	100.0	0.0	0.0
	5wt% Pt/MoO_3 (1g), 5wt% CO_2 EEMPA						
6	IC3M17	190	0.15	32.1	59.4	24.3	16.3
7	IC3M19	190	0.06	57.1	64.6	33.0	2.4
8	IC3M17	190	0.015	77.6	59.1	40.9	0.0

9	IC3M16	170	0.15	16.5	58.2	23.1	18.7
10	IC3M16	170	0.015	86.6	52.6	47.4	0.0
11	IC3M18-1	150	0.015	47.6	76.8	23.2	0.0

Next, we investigated the durability of the solvent after the conversion through GC-MS analysis (**Table 18**). The order of the solvent's durability in the presence of different catalysts is as follows: Pt/MoO_3 > Pt/ZrO_2 >Pt/TiO_2. Both Pt/ZrO_2 and Pt/MoO_3 suppressed the degradation of the EEMPA solvent compared to our first-generation Pt/TiO_2 catalysts. The EEMPA solvent was ~10 fold more durable when using the Pt/MoO_3 catalyst compared to Pt/TiO_2.

Table 18: Durability of the spent EEMPA solvent after conversion in the presence of different catalysts

Run	Catalyst	Conv. (%)	EEMPA degradation (g/h)
IC3M22	5wt% Pt/TiO_2	29.4	0.84
IC3M14	5wt% Pt/ZrO_2	10.8	0.25
IC3M17	5wt% Pt/MoO_3	32.1	0.08

Reaction Conditions: SV1 (0.15 $gCO_2/gCat/h$), 190 °C, 5wt% CO_2 EEMPA

In this quarter (**Q1-FY24)**, we also studied the effect of CO_2 loading on the conversion and selectivity in the presence of the Pt/MoO_3 catalyst under different conditions (see **Table 19**). The CO_2 conversion rate increased as the CO_2 loading decreased. For instance, at 190 °C, the conversion using 1wt% and 10wt% CO_2-loaded EEMPA solvent was 81% and 36%, respectively. The CO content was higher at a high space velocity and when a high CO_2-loaded (i.e., 10wt%) solvent was used as the feed. This suggests that the reaction is potentially proceeding via a CO intermediate, which remains unreacted when a higher concentration of CO_2 is employed. Overall, CO_2 loading between 1-5wt% was ideal based on the conversion and selectivity to methanol.

Table 19: Effect of wt% CO_2 loading in the solvent on the conversion and selectivity

Run	SV $gCO_2/gCat/h$	Conv. (%)	MeOH Sel. (%)	CH_4 Sel. (%)	CO Sel. (%)
5wt% Pt/MoO_3 (1g), 10wt%CO_2 EEMPA feed					
IC3M23:190C	0.15	21.3	33.4	23.0	43.5
IC3M23: 190C	0.06	36.2	48.1	28.9	23.0
5wt% Pt/MoO_3 (1g), 5wt% CO_2 EEMPA					
IC3M17: 190C	0.15	32.1	59.4	24.3	16.3
IC3M19: 190C	0.06	57.1	64.6	33.0	2.4

IC3M17: 190C	**0.015**	**77.6**	**59.1**	**40.9**	**0.0**
5wt% Pt/MoO_3 (1g), 1wt%CO_2 EEMPA feed					
IC3M24: 190C	**0.15**	**57.1**	**42.1**	**37.8**	**20.1**
IC3M24: 190C	**0.06**	**81.1**	**49.9**	**43.9**	**6.2**

XI. Progress towards Q2-FY24 milestone: *[T1] (M1) Combine steps A and B, and achieve >20% single pass conversion of captured CO_2 to methanol. (M2) Also, assess separability of methanol and at least one other target product when mixed with EEMPA (w/5% water) with bench scale distillation/ flash separation experiments to inform TEA*

After evaluating different catalysts (CoMo, Pt, and Cu on different supports) in the batch reactor, Pt/ZrO_2 and Pt/MoO_3 catalysts were selected for further evaluation in a continuous flow reactor based on their superior performance in terms of CO_2 conversion and/or selectivity. In the continuous flow, the CO_2 conversion and methanol selectivity were high with Pt/MoO_3 compared to 5wt% Pt/ZrO_2 and our first-generation catalyst (5wt% Pt/TiO_2 catalyst). Importantly, the selectivity to methanol was ~100% in the case of Pt/ZrO_2, although CO_2 conversion was low (33%) compared to Pt/TiO_2 and Pt/MoO_3. In summary, we achieved the milestone of attaining >20% *single pass conversion of captured CO_2 to methanol (M1).*

During this quarter, to achieve our milestone (*M2*), we assessed the separability of methanol (with a boiling point of 64.7°C) from EEMPA using bench-scale distillation with a fractional column setup. By maintaining the distillation flask at around 120°C and cooling the receiving flask to 0°C, we recovered 88% of methanol (as shown in **Figure 20**) with a purity >90% at a vapor temperature ~64.7°C from an EEMPA (70 mol%)-methanol (15 mol%)-water (15 mol%) mixture. The methanol purity was slightly low due to contamination with water, likely originating from atmospheric moisture during NMR sample preparation, compounded by the hygroscopic nature of the NMR solvent, DMSO-d_6. Importantly, ^{1}H NMR analysis confirmed the absence of EEMPA, indicating successful separation. Subsequently, we increased the distillation flask's temperature to 165°C to separate water from EEMPA, resulting in the quantitative recovery of water from the distillation flask, along with traces of methanol.

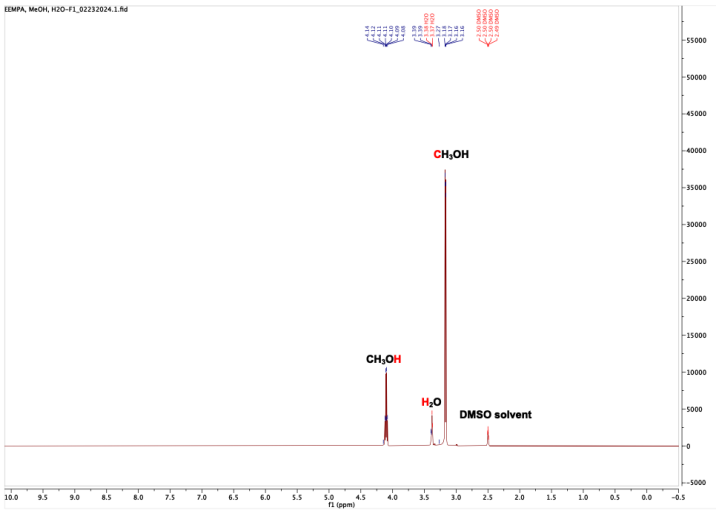


Figure 20. ^{1}H NMR (in DMSO-d_6 NMR solvent) of the fraction containing methanol distilled from an EEMPA (70 mol%)-methanol (15 mol%)-water (15 mol%) mixture, showing no trace of EEMPA.

As methanol and ethanol are our main target products, we evaluated their separability from two different mixtures: (a) an EEMPA (55 mol%)-methanol (15 mol%), ethanol (15 mol%)-water (15 mol%) mixture, and (b) an EEMPA (65 mol%)-methanol (15 mol%), ethanol (3 mol%)-water (15 mol%) mixture, using the same distillation setup as above. In the case of mixture (a), the initial distillation fraction predominantly contained methanol, but its purity decreased to 70% due to ethanol contamination, as shown in **Figure 21**. Following the separation of methanol fractions, we raised the temperature of the flask to further isolate ethanol. As anticipated due to azeotrope formation, ethanol distilled out alongside water at ~78°C (**Figure 22**). Despite the quantitative removal of ethanol from EEMPA, the purity of ethanol was diminished to less than 50% due to the presence of water and some residual methanol.

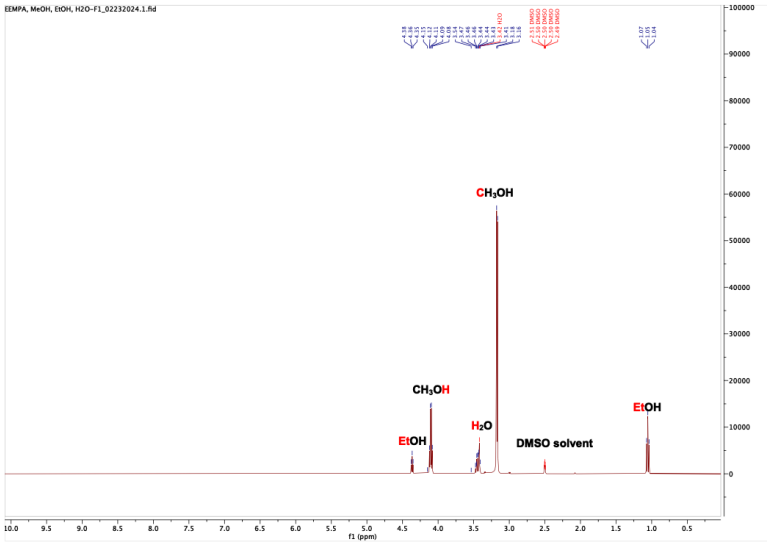


Figure 21. ^{1}H NMR of the fraction containing methanol distilled from an EEMPA (55 mol%)-methanol (15 mol%), ethanol (15 mol%)-water (15 mol%) mixture.

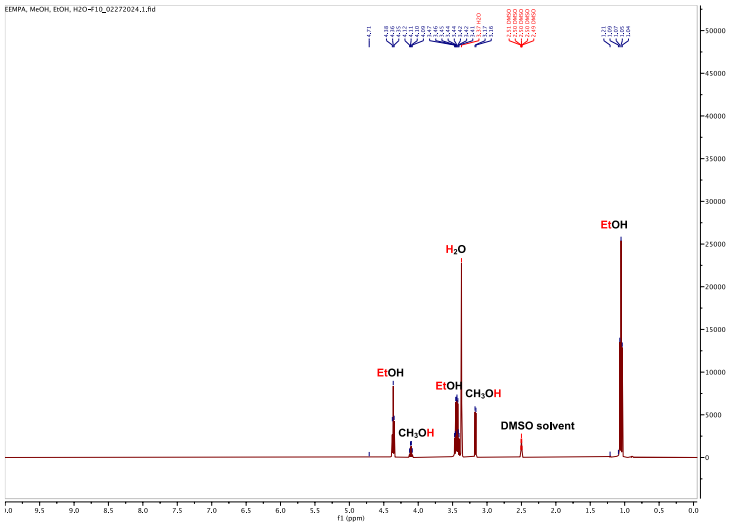


Figure 22. ^{1}H NMR of the fraction containing ethanol distilled from an EEMPA (55 mol%)-methanol (15 mol%), ethanol (15 mol%)-water (15 mol%) mixture.

In the case of mixture (b), over 90% of methanol was successfully recovered with a purity exceeding 90% at a vapor pressure of ~64.7°C (shown in **Figure 23**). The purity of methanol was slightly lower due to contamination with ethanol and water, but it was higher than in case (a), where the ethanol content was higher. Following the distillation of methanol, the temperature of the flask was raised to facilitate the separation of ethanol from the distillation mixture. Subsequently, over 99% of ethanol was recovered, but its purity was below 50% due to the presence of methanol and water contaminants. Post-distillation, EEMPA was successfully recovered without any loss in all the above distillations (**Figure 24**).

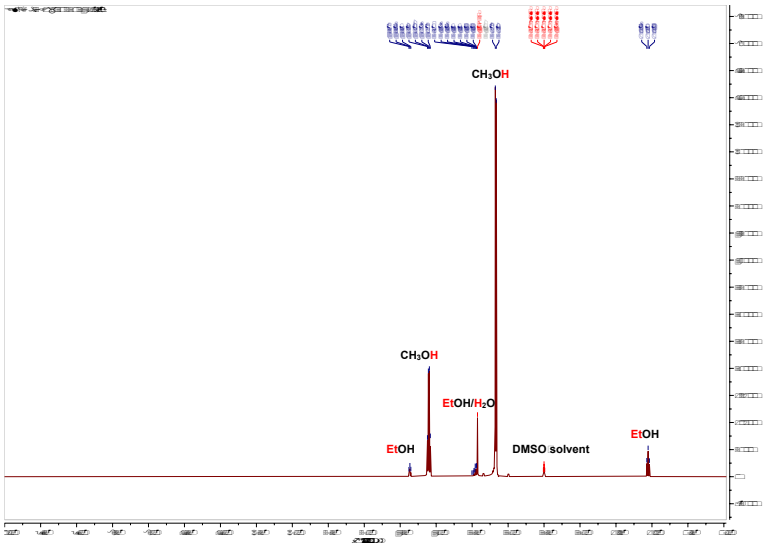


Figure 23. ^{1}H NMR of the fraction containing methanol distilled from an EEMPA (65 mol%)-methanol (15 mol%), ethanol (3 mol%)-water (15 mol%) mixture.

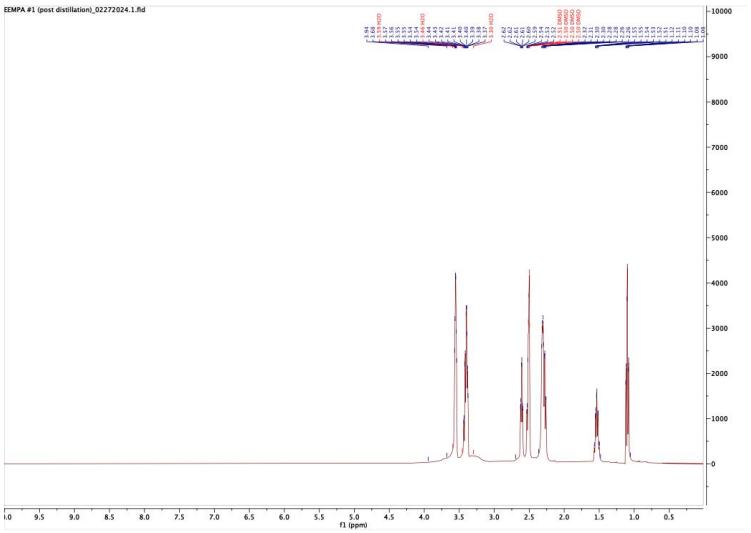


Figure 24. ^{1}H NMR of EEMPA (65 mol%)-methanol (15 mol%), ethanol (3 mol%)-water (15 mol%) mixture post-distillation shows complete removal of methanol, ethanol, and water. EEMPA was quantitatively recovered after distillation.

In summary, we have showed that methanol, ethanol and water can be separated from EEMPA via distillation. As expected, ethanol forms an azeotrope with water, making it impossible to separate them by simple or fractional distillation. However, extractive distillation, which employs a known method [16] using a third component, ethylene glycol, as an extractive agent, can facilitate the separation of ethanol from water.

XII. *Evaluation of new catalyst formulations for methanol synthesis in a post-combustion capture solvent in a continuous flow reactor*

In this quarter (**Q2-FY24)**, we investigated the impact of water content (in EEMPA solvent) and catalyst metal loading on the CO_2 conversion product yield and selectivity using our new catalyst formulation, Pt/MoO_3 (**Table 20)**. Experiments in entries 4 and 5 specifically focused on assessing how the presence of water in the solvent (EEMPA) affects these parameters. ***The addition of water to the feed resulted in a significant reduction in conversion, roughly by a factor of two, indicating an inhibitory effect on the conversion process.*** Moreover, the selectivity to methanol decreased due to the presence of unreacted CO intermediate. Additionally, the CO_2 conversion was found to be influenced by the Pt loading of the catalyst. Lower Pt loading led to decreased conversion (entries 6 and 7), as expected, accompanied by reduced selectivity for methanol, attributed to the presence of unreacted CO intermediate. Conversely, higher Pt loading (entries 8 and 9) resulted in increased conversion rates, albeit with a slight decline in methanol selectivity. This suggests that higher metal loading promotes the conversion process, potentially through additional active sites, though it may also induce some undesired side reactions.

Table 20: Effect of water in the solvent (EEMPA) and the wt% Pt loading of the catalyst on the conversion and selectivity

Entry	Run	SV gCO2/gCat/h	Conv. (%)	MeOH Sel. (%)	CH_4 Sel. (%)	CO Sel. (%)
	5wt% Pt/MoO_3 (1g), 5wt% CO_2 EEMPA					
1	IC3M17: 190C	0.15	32.1	59.4	24.3	16.3
2	IC3M19: 190C	0.06	57.1	64.6	33.0	2.4
3	IC3M17: 190C	0.015	77.6	59.1	40.9	0.0
	5wt% Pt/MoO_3 (1g), 1%H_2O 5%CO_2 EEMPA feed					
4	IC3M25: 190C	0.15	20.6	35.9	19.6	44.5
5	IC3M25: 190C	0.06	33.5	45.9	24.1	30.0
	1wt% Pt/MoO_3 (1g), 5wt% CO_2 EEMPA					
6	IC3M20: 190C	0.15	21.0	33.2	15.0	51.8
7	IC3M20: 190C	0.06	28.3	54.4	23.5	22.1
	10wt% Pt/MoO_3 (1g), 5wt% CO_2 EEMPA					
8	IC3M21: 190C	0.15	44.1	46.7	31.6	21.7
9	IC3M21: 190C	0.06	66.8	55.4	35.7	8.9

Next, the stability of two catalysts, the new Pt/MoO_3 and the first-generation Pt/TiO_2, was assessed over a 100-hour TOS period at a temperature of 190°C and a rate of 0.015g CO2 per gram of catalyst per hour (**Figure 25**). The results showcase a significant difference in the performance and stability between the two catalysts. Firstly, the Pt/TiO_2 catalyst, containing 5wt% Pt, exhibited a decline in catalytic activity over time. Initially, it showed a conversion rate of 77%, indicating its effectiveness in catalyzing the hydrogenation reaction. However, over the course of approximately 80 hours, this conversion rate dropped to 49%. In contrast, the Pt/MoO_3 catalyst, also containing 5wt% Pt, demonstrated notably higher stability and performance throughout the 100-hour TOS period. ***Operating under the same conditions as the Pt/TiO_2 catalyst, the Pt/MoO_3 catalyst maintained a consistently high conversion rate of around 85%. Moreover, it exhibited a methanol selectivity of approximately 60%. Overall, the Pt/MoO_3 catalyst showcased superior catalytic stability compared to the first-generation Pt/TiO_2 catalyst***

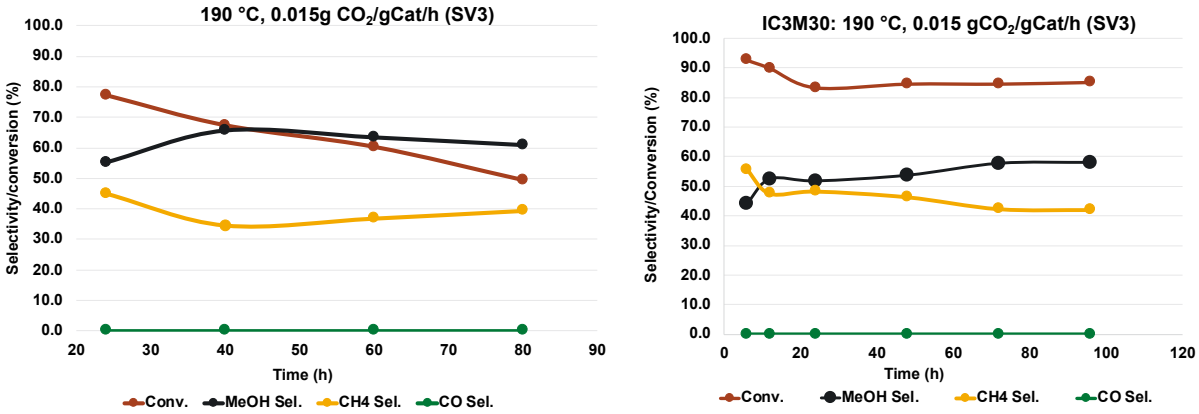


Figure 25. 100 h time-on-stream performance of (a) 5wt% Pt/TiO_2 (left) and (b) 5wt% Pt/MoO_3 (right), at 190°C and 0.015g CO_2/gcatalyst/h.

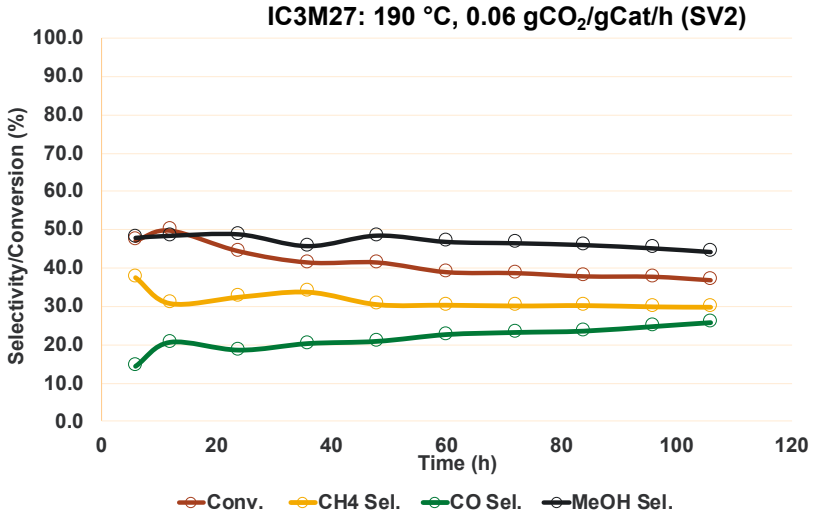


Figure 26. 100 h time-on-stream performance of 5wt% Pt/MoO_3 at 190°C and 0.06g CO_2/gcatalyst/h.

Following this, we increased the rate of CO_2 per gram of catalyst per hour to 0.06 in order to conduct a comprehensive assessment of the stability and productivity of the Pt/MoO_3 catalyst (**Figure 26**). The CO_2 conversion rate decreased as the CO_2 loading increased. The CO content was higher, which suggests that the reaction is potentially also proceeding via a CO intermediate, which remains unreacted when a higher concentration of CO_2 is employed. This underscores the need for further evaluation of new catalysts to improve both conversion productivity and methanol selecitivity.

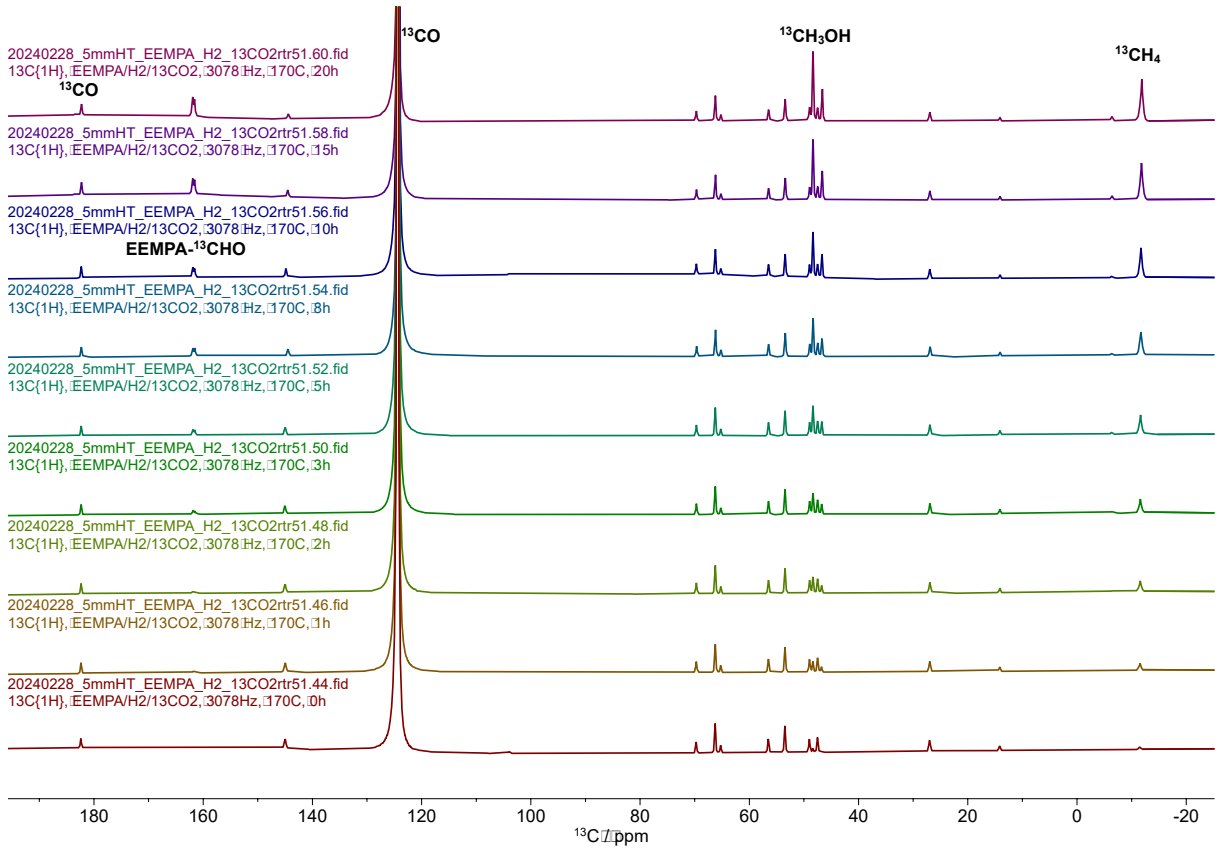


Figure 27: Operando ^{13}C MAS-NMR during the hydrogenation of captured $^{13}CO_2$ using 5 wt % Pt/MoO_3 at 170 °C.

An operando NMR experiment was conducted using ^{13}C-enriched CO_2 to investigate the reaction pathway in the condensed phase and verify the absence of N-methylation with a Pt/MoO_3 catalyst. At 25°C, under a $^{13}CO_2$ and H_2 atmosphere, the 2-EEMPA-$^{13}CO_2$ (carbamate) species was predominantly observed at ~159 ppm, alongside $^{13}CO_2$ at ~125 ppm. Upon heating, new species emerged, including ^{13}CO, 2-EEMPA-^{13}CHO (formamide), $^{13}CH_3OH$, and $^{13}CH_4$, at both the reaction temperatures of 170 °C (**Figure 27**) and 190 °C. The simultaneous detection of these species suggests that methanol could potentially be generated through both CO and -CHO intermediates. Notably, there was no detectable amount of the undesired 2-EEMPA-CH_3 observed during the analysis, indicating a favorable reaction pathway to methanol.

XIII. Progress towards Q3-FY24 milestone: ***[T1]*** Characterize at least 5 new catalyst formulations using NH_3 TPD, and H_2 chemisorption (or XRD) and correlate properties of acid and metal sites on methanol productivity

Both the reaction mechanism and the composition of methanol synthesis catalysts are very active research field; however, there is no clear path for designing more active catalysts (e.g. Pt dispersion, hydrogen spillover, acidity of the support), particularly using captured CO_2 as a feed. The goal for this section is to elucidate differences between the catalysts chosen (5%Pt over TiO_2, MoO_3, ZrO_2)

and understand structure-activity relationships. Catalysts were characterized for surface area using BET surface area analysis (Brunauer-Emmett-Teller), crystalline structure using X-ray diffraction (XRD), acid/base properties using CO_2 and NH_3 chemisorption, Pt dispersion and H_2 adsorption using H_2 chemisorption. Additionally, the spent catalysts were characterized using TPO and FTIR. Characterization results are presented below.

a) Surface area/ textural characterization (BET, TEM)

Table 21 summarizes the surface area and pore volume of the calcined samples. The Pt/ZrO_2 exhibited a higher surface area of 92 m^2/g compared to Pt/TiO_2, which has a surface area of 57 m^2/g; however, both have similar pore volumes, with Pt/ZrO_2 at 0.25 cm^3/g and Pt/TiO_2 at 0.23 cm^3/g. The N_2 sorption isotherms for the $5\%Pt/ZrO_2$ and $5\%Pt/TiO_2$ samples correspond to type IV with hysteresis type H3, suggesting that the stacking of plate-like crystallites results in the formation of mesopores. The Pt/MoO_3 samples, on the other hand, show a very low surface area (~3 m^2/g).

Table 21. Surface Area and Pore Volume

Catalysts	BET surface area ($m^2.g^{-1}$)	Pore volume at at P/P0= 0.995 ($cm^3.g^{-1}$)
5 wt% Pt/TiO_2	57.14	0.231
5 wt% Pt/ZrO_2	92.01	0.25
1 wt% Pt/MoO_3	2.78	0.018
5 wt% Pt/MoO_3	3.03	0.011
10 wt% Pt/MoO_3	2.95	0.022

The morphology of Pt particles on various supports (previously reduced under H_2) was assessed by ex situ HAADF-TEM (**Figure 28**), where Pt appears with a lighter contrast compared to the support. The $5\% Pt/TiO_2$ (**Figure 28A**) and $5\% Pt/ZrO_2$ (**Figure 28B**) catalysts display well-defined Pt nanoparticles. **Table 22** and histograms shown in **Figure 29** indicate that the mean Pt particle size and distribution are ~ 2 nm (±0.7-1 nm) for these catalysts. The main variation is observed with Pt/MoO_3, where most of the Pt exists as a thin-film like coating, with Pt nanoparticles aggregating along the ridges of the MoO_3 support.

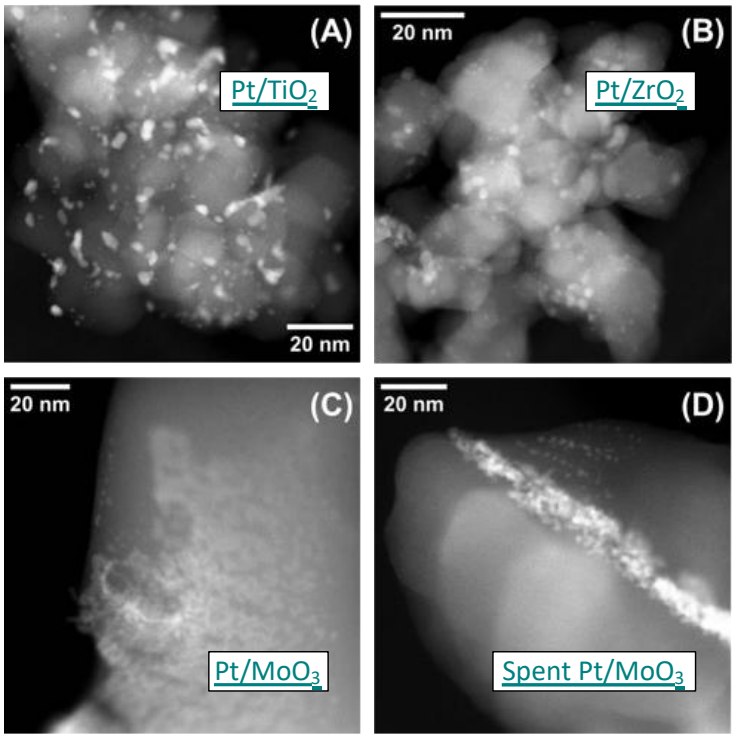


Figure 28. HAADF-TEM micrographs of (A) 5% Pt/TiO_2 and (B) 5% Pt/ZrO_2 (C) 5% Pt/MoO_3 (D) spent 5% Pt/MoO_3.

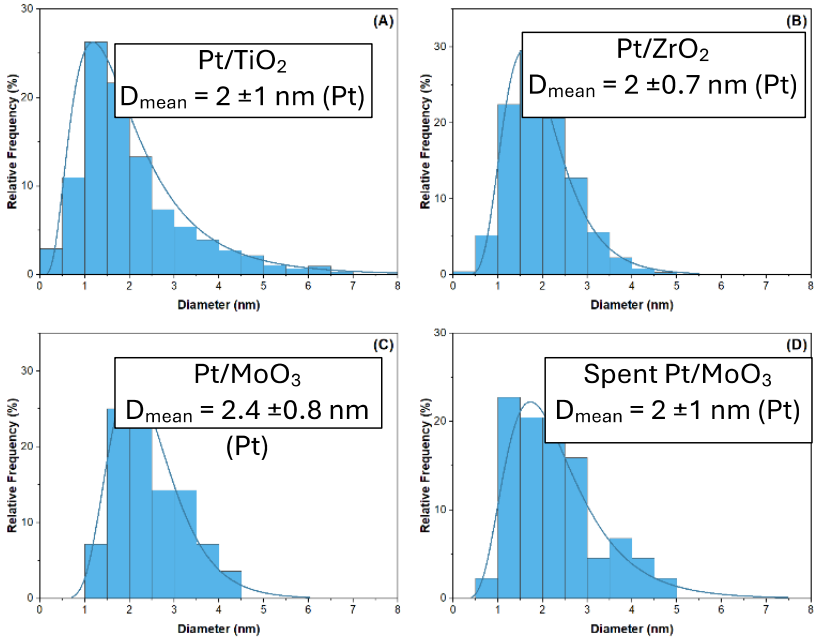


Figure 29. Histogram from TEM particle size analysis for (A) 5% Pt/TiO_2, (B) 5% Pt/ZrO_2, (C) 5% Pt/MoO_3, and (D) spent 5% Pt/MoO_3. Data were fit with lognormal distributions.

Table 22. Statistical parameters from TEM particle size analysis, where n is the number of particles measured, D_{mean} is the mean particle diameter, exp(μ) and exp(σ) are e raised to the μ and σ power, respectively, where μ and σ are the mean and standard deviation of logarithmic values for the lognormal distribution.

Catalyst	**n**	**D_{mean} (nm)**	**exp(μ) (nm)**	**exp(σ) (nm)**
5% Pt/MoO_3	28	2.4 ± 0.8	2.3 ± 0.1	1.39 ± 0.06
Spent 5% Pt/MoO_3	45	2 ± 1	2.1 ± 0.2	1.57 ± 0.06
5% Pt/TiO_2	1020	2 ± 1	1.72 ± 0.03	1.84 ± 0.02
5% Pt/ZrO_2	1017	2.0 ± 0.7	1.82 ± 0.02	1.47 ± 0.01

b) X-ray diffraction crystalline structure

Here, we analyzed the Pt on MoO_3, TiO_2, and ZrO_2 (H_2-reduced catalysts) for their crystalline structure prior to being used in CO_2 hydrogenation. Pt nanoparticles on oxide supports are known to exhibit characteristic XRD patterns. The results for the XRD patterns of our catalysts are shown in **Figure 30**. The XRD patterns for 5 wt%Pt/TiO_2 and 5 wt%Pt/ZrO_2 show the characteristic peaks for anatase and tetragonal phases of TiO_2 and ZrO_2, respectively. The high dispersion of Pt prevents the observation of features related to Pt crystallites in 5 wt%Pt/TiO_2 and 5 wt%Pt/ZrO_2.

In contrast to Pt/TiO_2 and Pt/ZrO_2, Pt/MoO_3 catalysts exhibit significant changes in the crystalline structure of the support after the incorporation of Pt. The 5%Pt/MoO_3 primarily shows a non-crystalline pattern, in contrast to the orthorhombic structure characteristic of the MoO_3 support. The only notable features presumably correspond to a PtMo alloy, with some residual crystalline MoO_3. Pt particles are evident as small broad peaks at 2θ= 39.8°, 46.2°, 67.5°, and 81.3°. The changes in crystalline structure might be due to two reasons: 1) MoO_3 transforming into an amorphous structure after reduction (without the assistance of Pt particles), 3) Pt either creating oxygen vacancies in the MoO_3 lattice or modifying the crystallite size (resulting in strained crystallites).

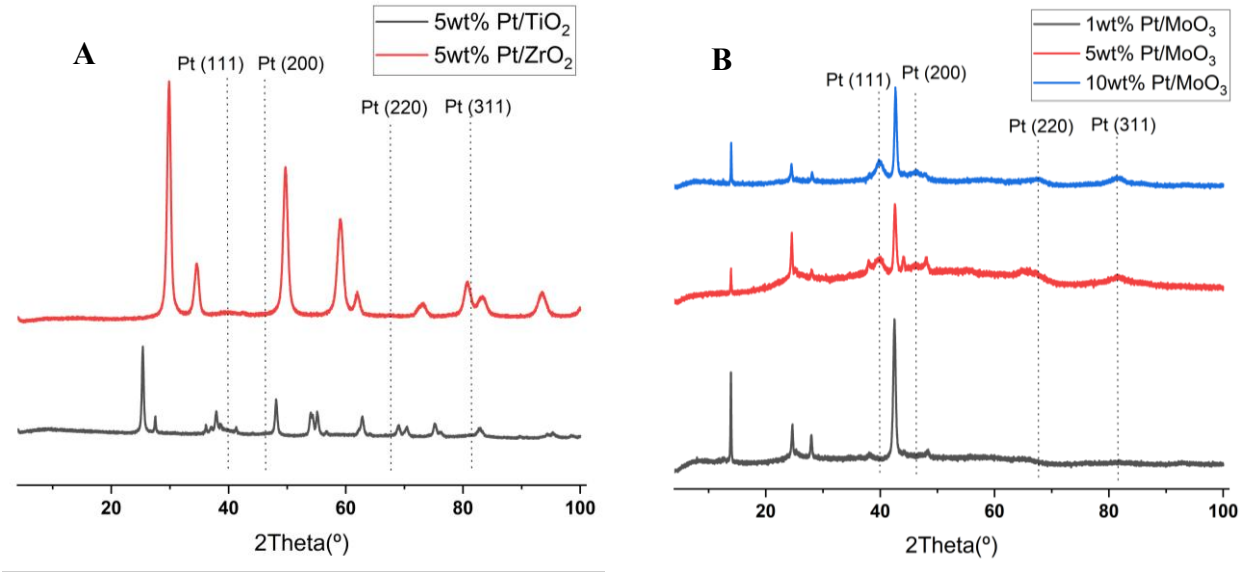
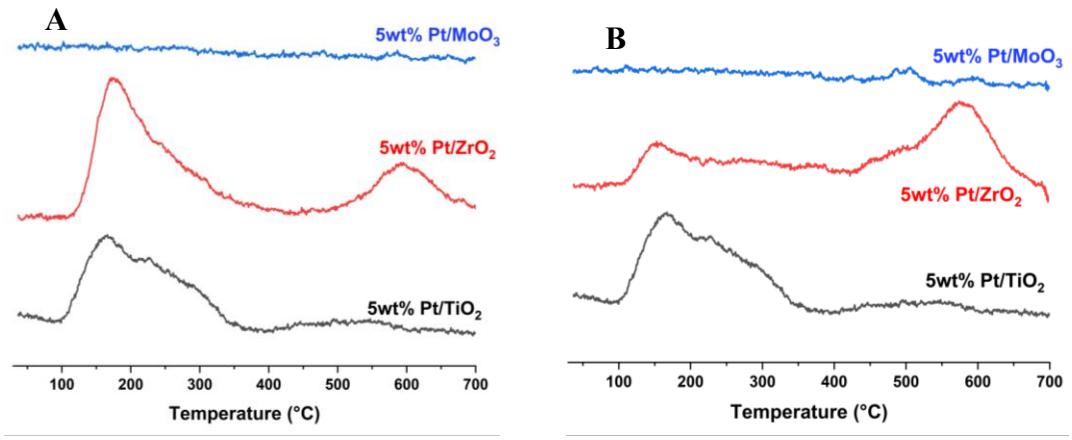


Figure 30: XRD patterns.

c) CO_2 and NH_3 adsorption. Acid/base properties

To elucidate the role of the support in the reaction mechanism, we conducted NH_3-TPD (Temperature Programmed Desorption) and CO_2-TPD analyses to assess the acidic and basic characteristics of Pt/TiO_2, Pt/ZrO_2, and Pt/MoO_3 catalysts (**Figure 31**). The results revealed that Pt/TiO_2 possesses both acidic and basic sites. Similarly, the Pt/ZrO_2 catalyst also exhibits both types of sites; however, it includes some stronger acidic and basic sites compared to Pt/TiO_2. Notably, the Pt/MoO_3 catalyst lacks any detectable acidic or basic sites. These findings imply that the acidic and basic properties provided by the TiO_2 and ZrO_2 supports are likely responsible for the degradation of the EEMPA capture solvent.



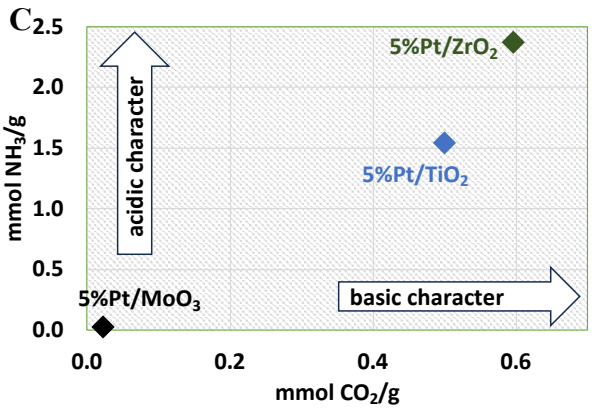


Figure 31. (A) NH_3-TPD, (B) CO_2-TPD of the calcinated post synthesis catalysts, and (C) the number of acidic and basic sites quantifies using NH_3-TPD and CO_2-TPD data. NH_3 (10 mol% NH_3 in He) and CO_2 (10 mol% CO_2 in He) were adsorbed onto 100 mg of the sample.

d) H_2 chemisorption. Pt dispersion and hydrogen spillover

The 5% Pt/TiO_2 catalyst exhibited a dispersion (**Table 23**) that was consistent with what was expected from the particle size analysis by TEM. The Pt dispersion was somewhat larger than earlier determined by CO chemisorption for the same batch of catalyst. This larger dispersion may be consistent with earlier reports of hydrogen spillover for Pt/TiO_2. The barrier for hydrogen spillover from Pt onto anatase TiO_2 was determined to be 43 kJ/mol, while electron and proton transfer among TiO_2 sites was found to be ~60 – 70 kJ/mol. Additionally, the quantity of H* adsorbed at 190 °C was lower than that at 40 °C, indicating that hydrogen spillover was not kinetically hindered at 40 °C for the TiO_2 support.

The 5% Pt/ZrO_2 catalyst exhibited dispersion that was consistent with what was expected from the particle size analysis by TEM. Furthermore, the slightly larger dispersion of 5% Pt/ZrO_2 compared to 5% Pt/TiO_2 was consistent with a lower percentage of Pt particles that were >3 nm in size for 5% Pt/ZrO_2 compared to 5% Pt/TiO_2 as observed by TEM analysis. The quantity of H* adsorbed at 190 °C was larger than at 40 °C. The fact that $\theta_{H*/Pt,190°C} > 1$ for 5% Pt/ZrO_2 is attributed to an activated hydrogen spillover process. In general, hydrogen adsorption on Pt sites is rapid, while surface diffusion can kinetically hinder spillover of H* onto the support.

The Pt/MoO_3 catalysts were poorly dispersed **(Table 23**), with the dispersion linearly decreasing with increasing Pt loading. This poor dispersion was consistent with TEM analysis that showed large regions of aggregated Pt domains. The quantity of chemisorbed H* at 190 °C was dramatically larger than that obtained at 40 °C, with the calculated H* coverage greatly exceeding one monolayer of exposed Pt sites. These findings are consistent with results for Pt/MoO_3 by Triwahyono *et al.*, who found that H* undergoes activated surface diffusion from Pt sites to the MoO_3 support (i.e. activated spillover) with a barrier of 83.1 kJ/mol. At 100 °C, Triwahyono *et al.* found that H_2 adsorption was initially rapid, attributed to adsorption on Pt sites, but did not equilibrate after 10 h, attributed to kinetically-limited spillover. At and above 200 °C, H_2 adsorption was equilibrated in 2 h. For the Pt/MoO_3 adsorption isotherms reported herein, adsorption was within the specified tolerance for equilibration for the first data point within 0.5 – 0.75 h for 40 °C

adsorption and within 3 – 9 h for 190 °C adsorption. Therefore, 40 °C results likely reflect chemisorption exclusively on Pt sites while 190 °C results likely include spillover onto the MoO_3 support.

The H_2 chemisorption results indicate that at 190 °C, the extent of hydrogen spillover follows the order Pt/MoO_3 >> Pt/ZrO_2 > Pt/TiO_2. These varying degrees of hydrogen spillover can alter the adsorption and activation of intermediates, potentially explaining the higher selectivity to methanol observed with the Pt/ZrO_2 catalyst. In addition, the high H_2 spillover of Pt/MoO_3 catalysts can promote H_2 activation and subsequent conversion of HCOO* intermediate to $*OCH_3$.

Table 23. Volumetric H_2 chemisorption results for supported Pt catalysts. The last digit in parentheses reports the standard error for the last significant digit(s), i.e. 100.1 ± 0.5 = 100.1 (5) and 300 +/- 50 = 300 (50).

Catalyst	$N_{H*,40°C}$ *(μmol/g)*	$N_{H*,190°C}$ *(μmol/g)*	*D (%)*	$\theta_{H*/Pt,190°C}$ *(-)*
5% Pt/TiO_2	106.3	58.9 (9)	42	0.554 (9)
5% Pt/ZrO_2	129 (2)	226 (3)	50	1.75 (3)
1% Pt/MoO_3	1.51 (9)	1140 (6)	3.0	753 (43)
5% Pt/MoO_3	4.4 (2)	750 (10)	1.7	170 (31)
10% Pt/MoO_3	4 (1)	1014 (9)	0.8	263 (67)

XIV. WSU Update (Task 4. Ethanol): Identify catalysts and conditions for the conversion of CO_2 to ethanol (Q3-FY24).

a) Gas phase CO_2 hydrogenation to ethanol (Rh-Fe-SiO_2)

In this quarter (Q3-FY24), we focused on how activation and reaction temperatures affect ethanol selectivity. It is found that lower both lower activation temperature (210 ^oC) and reaction temperature (210 ^oC) favor ethanol production. The reaction temperature has a greater effect than the activation temperature. See **Figure 32**, the catalyst is 5% Rh-2.7% Fe/SiO_2 catalyst (Rh:Fe=1:1 molar, synthesized by co-loading method).

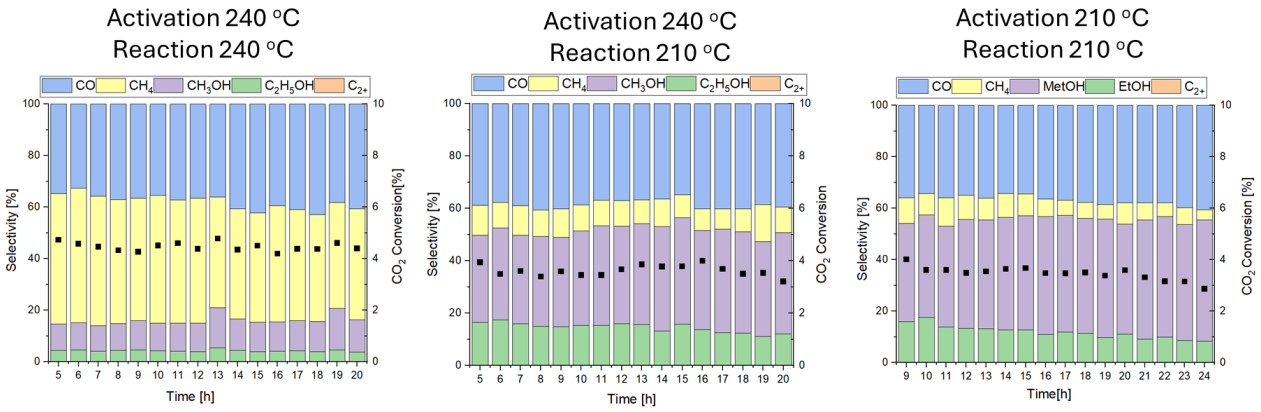


Figure 32. Common reaction conditions: flow reactor, pressure 30 bar, CO_2 5 sccm, H_2 15 sccm. Catalyst loading: 100 mg with 1000 mg SiC, activation in 20 sccm H_2 for 30 min.

b) Triple tandem catalysis approach

We evaluated some promising catalysts for the triple tandem system, including (1) CuZnAl for CO_2 to methanol, (2) Ir/MOR for methanol carbonylation and (3) Re/SiO_2 for methanol carbonylation.

(1) Cu/ZnO/Al_2O_3 for CO_2 hydrogenation into methanol

The CuZnAl catalyst achieves a notable 78% methanol selectivity and 16% CO_2 conversion at 210 °C (**Figure 33**). This demonstrates its strong performance in methanol synthesis, setting a strong foundation for the first step of the triple tandem catalyst approach.

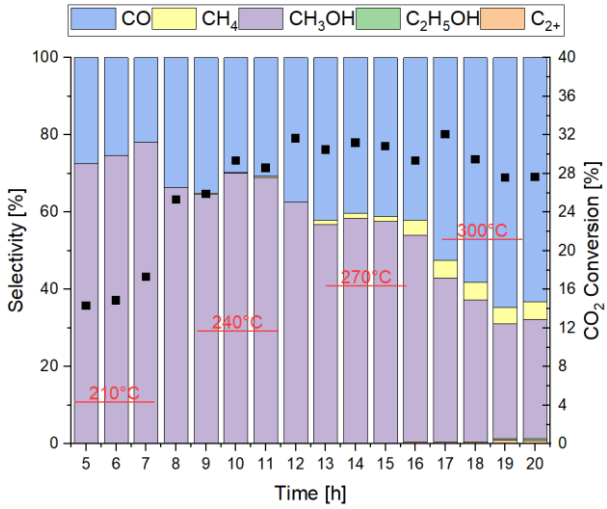


Figure 33. Reaction conditions: flow reactor, temperature 210-300 °C, pressure 30 bar, CO_2 5 sccm, H_2 15 sccm. Catalyst loading: 500 mg catalyst with 1000 mg SiC, activation under temperature 210 °C, H_2 20 sccm for 30 min.

(2) Methanol Carbonylation by MOR-based catalysts

The performance of the mordenite(MOR)-based catalyst is significantly improved by multiple strategies, including ion exchange (IE), 0.1 wt% Ir loading and pyridine adsorption. (**Figure 34** and **Table 24**).

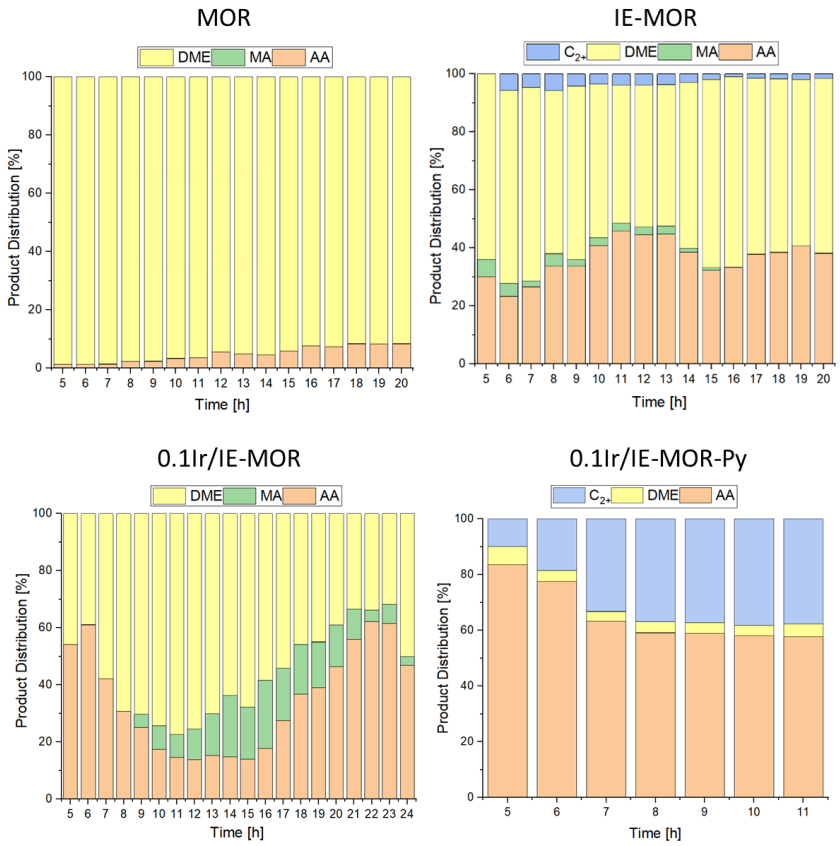


Figure 34. Reaction conditions: flow reactor, temperature 310 °C, pressure 30 bar, CO:Methanol=10:1, 20 sccm. Catalyst loading: 500 mg catalyst with 1000 mg SiC.

Table 24 Performances of MOR-based catalysts for CO carbonylation

Catalyst	*Methanol Conversion (%)*	*Acetic acid selectivity (%, CO_2 excluded)*
MOR	40	8
IE-MOR	70	46
0.1Ir/IE-MOR	80	62
0.1Ir/IE-MOR-Py	97	85

3) Methanol carbonylation by Re/SBA-15

Re/SBA-15 is identified as another promising catalyst for methanol carbonylation (**Figure 35**).

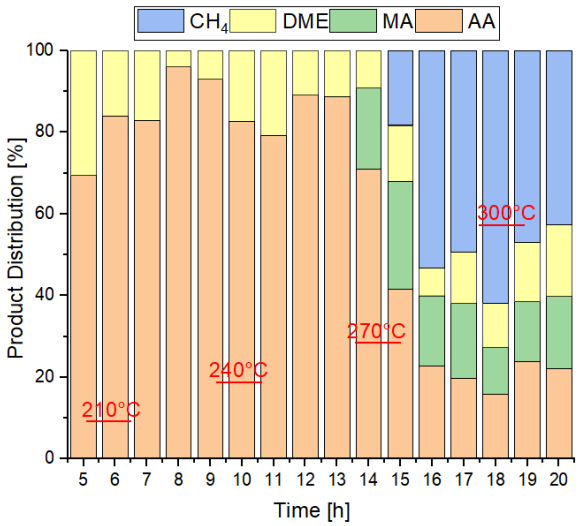


Figure 35. Reaction conditions: flow reactor, temperature 210-300 °C, pressure 30 bar, CO:Methanol=2:1, 20 sccm, 500 mg catalyst.

XV. Go/No-Go (Q4 FY24):

(a) Demonstrate feasibility for IC^{3}M concept by meeting intermediate target for methanol of 20% conversion, > 80% selectivity.

We successfully met the Go/No-Go target for methanol (20% CO_2 conversion and 80% selectivity in previous quarters using Pt/ZrO_2 catalysts. The key results pertinent to this target are illustrated in **Figure 36**. The catalyst reactivity and stability for methanol synthesis were evaluated in a post-combustion capture solvent (EEMPA) in a continuous flow reactor

As shown in **Figure 36**, our best first-generation catalyst (Pt/TiO_2) demonstrated noticeable deactivation throughout the experiment. Although methanol selectivity remained stable at around 60%, the conversion rate decreased significantly from 77% to 49% over approximately 80 hours. In contrast, Figures 24B and 24C reveal that the Pt/MoO_3 and Pt/ZrO_2 catalysts exhibit exceptional stability. **Pt/MoO_3 maintained a conversion rate of about 80%, while Pt/ZrO_2 maintained a conversion rate of ~40%**. A key distinction among these catalysts is their selectivity. **The Pt/ZrO_2 catalyst achieved near-total selectivity (100%) towards methanol**, whereas Pt/MoO_3 demonstrated 60% selectivity for methanol and 40% for methane. Notably, in all these experiments, the low space velocity enables good CO_2 conversion

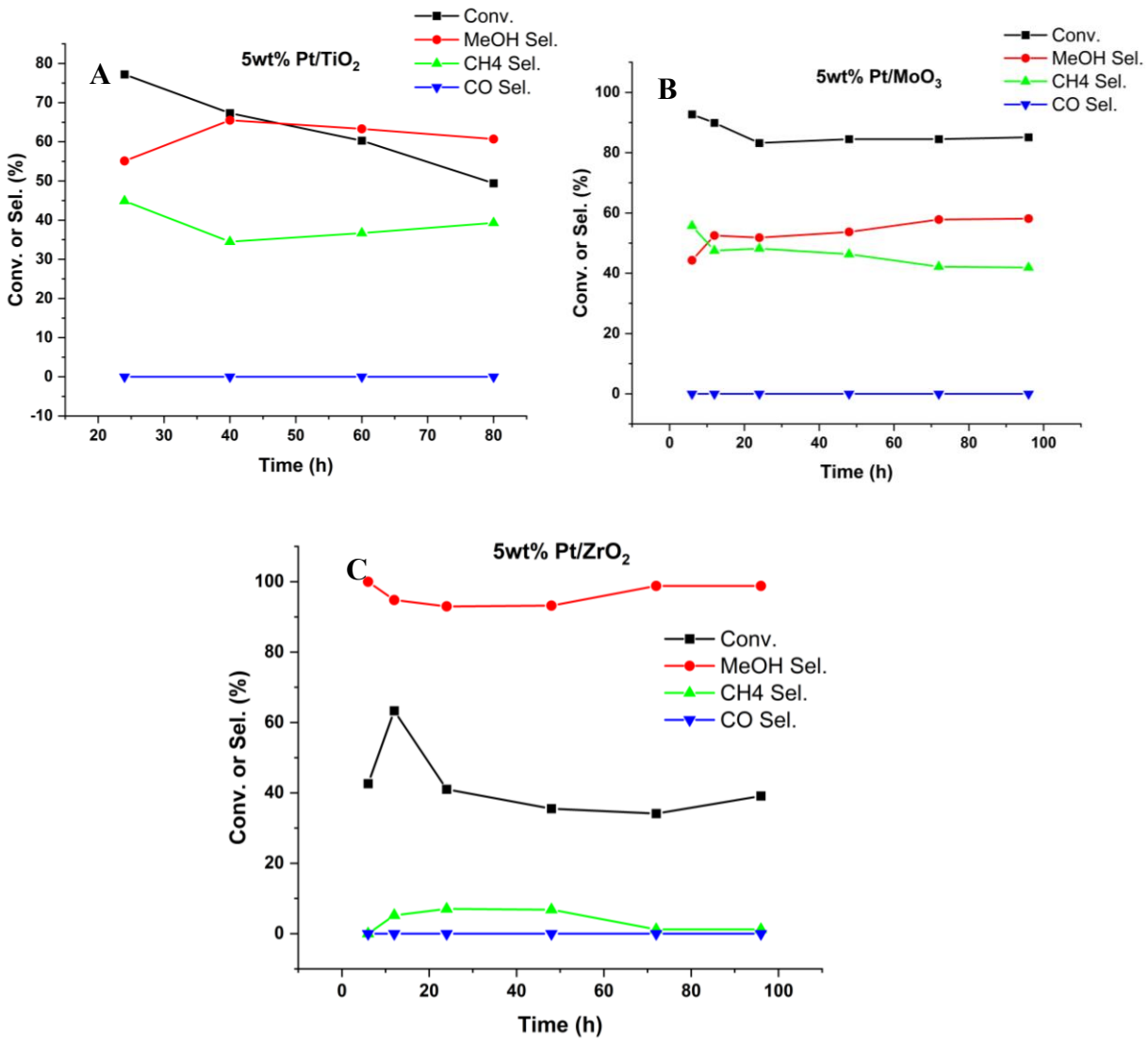


Figure 36. 100 h time-on-stream catalytic experiments for the conversion of CO_2 adsorbed in 2-EEMPA (5%CO_2) performance over (A) 5wt% Pt/TiO_2 (top left), (B) 5wt% Pt/MoO_3 (top right), and (C) 5%Pt/ZrO_2 (bottom). Reaction conditions: pressure: 860 psi, temperature: 190°C, space velocity 0.015g CO_2/g catalyst/h (1g of catalyst).

Solvent durability is as important as catalyst durability for industrial adoption, as the spent capture solvent must be reused for multiple combined CO_2 capture and conversion processes to be industrially viable. Therefore, we investigated the durability of the EEMPA solvent post-conversion through GC-MS analysis in the presence of different catalysts (**Table 1**). At 190°C and high space velocity (SV1), the order of the solvent's durability in the presence of different catalysts is as follows: Pt/MoO_3 > Pt/ZrO_2 > Pt/TiO_2 (**Figure 37**). Both Pt/ZrO_2 and Pt/MoO_3 suppressed the degradation of the EEMPA solvent compared to our first-generation Pt/TiO_2 catalysts. The degradation of EEMPA was observed to depend on both space velocity and reaction temperature. At 190°C, the EEMPA degradation products were reduced at SV1 compared to SV3, where the contact time between the catalyst and solvent is greater. At 170°C, the EEMPA degradation

products were significantly lower. Notably, for the Pt/MoO_3 catalyst at 170°C and SV3, both CO_2 conversion (~87%) and solvent durability were higher, indicating that these conditions are optimal for achieving high conversion efficiency and stability in the performance of the solvent and catalyst.

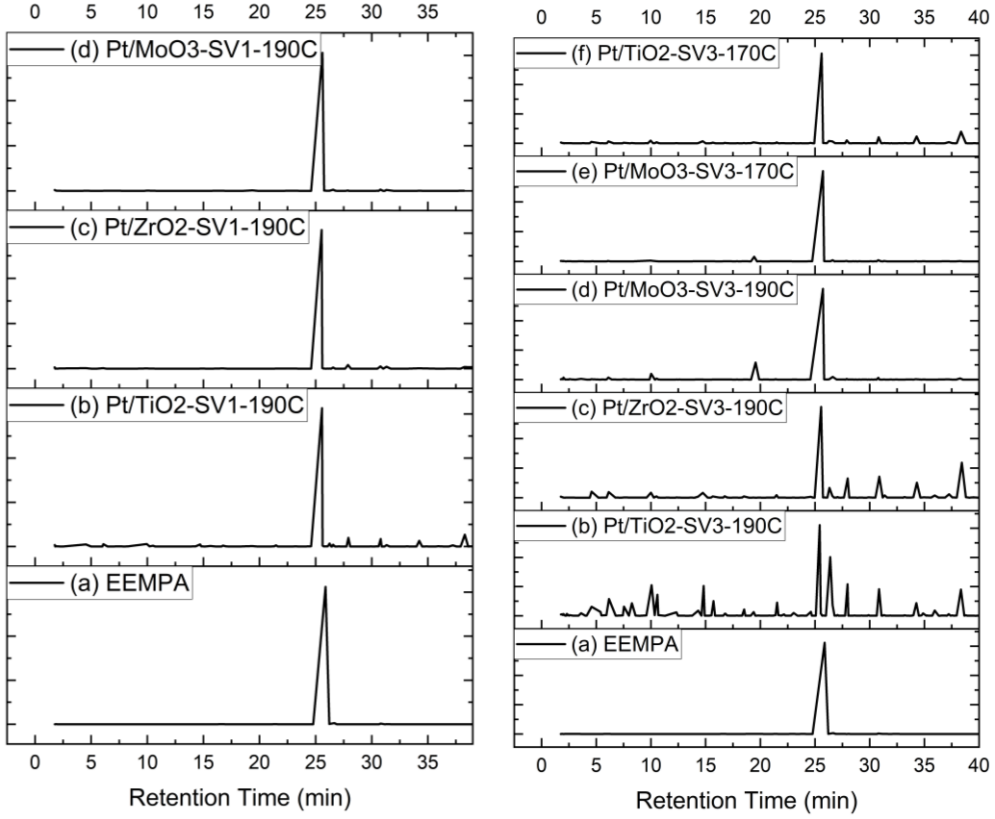


Figure 37. GC-MS profiles of the spent solvent under different reactions in the presence of 5%Pt/TiO_2, 5%Pt/ZrO_2 and 5wt% Pt/MoO_3.

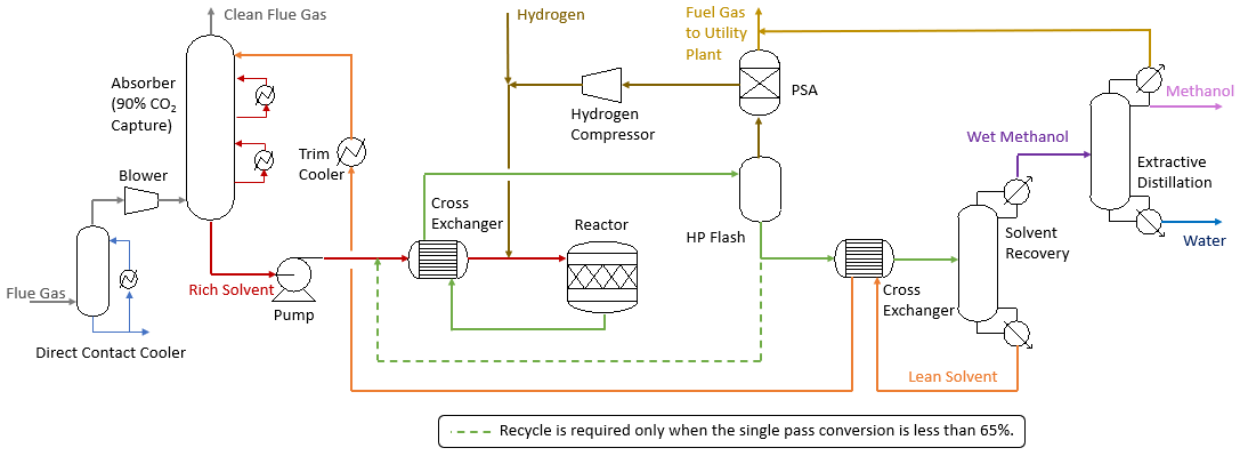


Figure 38. Process flow diagram of the IC^{3}M CO_2 capture and conversion to methanol process.

In this reporting period (Q4 FY24), a technoeconomic analysis (TEA) was performed on the integrated process of CO_2 capture and methanol conversion based on the newly collected experimental data, as depicted in the accompanying **Figure 38**. This process captures 90% of the CO_2 from the flue gas of an NGCC power plant using countercurrent contact with 2-EEMPA in the absorber. Rather than directing the CO_2-rich solvent to a solvent regenerator to produce low-pressure pure CO_2 for high-pressure methanol conversion, the entire condensed-phase rich solvent is pumped directly to the required pressure. This method eliminates the need for a costly and energy-intensive CO_2 compressor. The pressurized solvent is then heated and introduced into the main reactor, which contains either Pt/TiO_2 or Pt/MoO_3 catalyst, operating at 190°C and 60 bar, along with H_2.

Table 25. SOT and goal cases with different reactor performances

	2022 SOT Low WHSV (Pt/TiO_2)	***2022 SOT High WHSV (Pt/TiO_2)***	***2024 SOT High WHSV (Pt/MoO_3)***	***Goal 1***	***Goal 2***
WHSV ($gCO_2/gCat/hr$)	**0.015**	**0.075**	**0.06**	**0.15**	**0.15**
Single-pass CO_2 conversion (%)	**85.7**	**26.9**	**57.1**	**85.7**	**85.7**
CH_3OH selectivity (C%)	**51.5**	**63.6**	**64.6**	**51.5**	**100**
CH_4 and light gases selectivity (C%)	**36.3**	**26.4**	**35.4**	**36.3**	
C_{2+} alcohols selectivity (C%)	**12.2**	**4.8**	**0**	**12.2**	
Source	**Exp.**	**Exp.**	**Exp.**	**Target**	**Target**

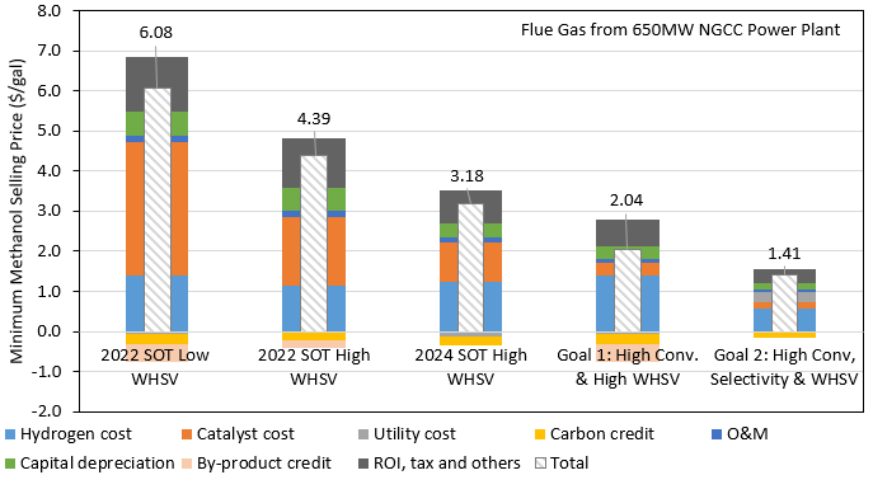


Figure 39: Breakdown in MSP of methanol.

Key performance and economic indicators, including the breakdown of the methanol's minimum selling price (MSP), are shown in the **Table 25** and **Figure 39** for five different scenarios. Our previous findings revealed that the MSP of methanol in the 2022 SOT case (utilizing Pt/TiO_2) was around $4.40 per gallon ($1,470 per metric ton), which is slightly lower than renewable methanol priced at $1,600 per metric ton, assuming CO_2 is sourced from a carbon capture facility at $50 per metric ton. Notably, in this combined CO_2 capture and conversion process, the reactor performs dual roles: it produces methanol as the final product and regenerates the CO_2 capture solvent for reuse in the CO_2 absorber. A conversion rate exceeding 65% is necessary to produce a CO_2-lean solvent for 90% CO_2 capture from NGCC flue gas with a CO_2 concentration of 4 mol%. The two goal cases suggest that the MSP of methanol can be significantly reduced and may reach price parity with conventional methanol synthesis (which was $1.20 per gallon in 2018) if faster kinetics and higher selectivity can be achieved through advancements in catalyst and reactor technology.

As shown in **Table 25**, significant performance improvements were achieved in 2024 SOT case (using Pt/MoO_3) through catalyst R&D, bringing results much closer to what the research team had anticipated in Goal 1. Compared to the 2022 performance data, the IC^3M process can now achieve mid-level conversion (>50%) and methanol selectivity (>50%) at high weight hourly space velocity (WHSV). This has resulted in a much smaller reactor size and reduced catalyst consumption. Additionally, no ethanol or other higher alcohols were generated as by-products, which further simplifies the product purification and separation unit by eliminating the need for extractive distillation.

With the performance improvements mentioned above, the TEA results for the 2024 SOT are presented in **Figure 39** and compared with the 2022 SOT and two goal cases. The 2024 SOT minimum selling price (MSP) of methanol is approximately 29% lower than that of the best 2022 SOT cases, due to significant savings in catalyst and capital depreciation. The 2024 SOT estimates the methanol MSP at $3.18 per gallon ($1,070 per metric ton), which is 33% lower than the E-methanol MSP of $1,600 per metric ton, produced from captured CO_2 available at $50 per metric ton (IHS Markit, 2021). The results also suggest a clear path from the 2022 SOT toward achieving our ultimate performance and cost goals through continued catalyst and reactor development. Key cost driver assumptions are: H_2 = $1/kg, solvent loss = <0.01%, and catalyst lifetime = 3 years.

(b) Establishing technical feasibility for producing and separating at least two other C_1 or C_2 oxygenates (> 10% conversion) using post-combustion capture solvent

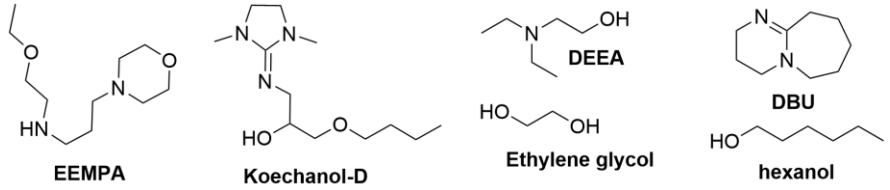
The two other oxygenated products targeted to meet our go/go-no criteria are **formate** and **cyclic carbonate**. **Formate** (formic acid) is a promising option due to its relatively low hydrogen requirement (CO_2: H_2 = 1:1) and favorable cost projections for production via the IC_3M route. Similarly, cyclic carbonate formation from CO_2 does not require H_2; instead, epoxide is used as a co-feed. **Cyclic carbonates** are used as solvents, in polymer production, as battery electrolytes, in pharmaceuticals, in chemical synthesis, and in coatings and adhesives. They also serve as key intermediates for the simultaneous co-production of two value-added products: glycol and methanol (Task 2).

In addition, as discussed in **Table 17**, using the Pt/ZrO_2 catalyst at high space velocity, **CO (another C1 oxygenate)** was produced with a selectivity of 74% and a CO_2 conversion of ~11% from CO_2 captured in EEMPA.

(i) <u>Formic acid</u>: Here, we first screened the conversion of CO_2 captured in our leading post-combustion solvent, EEMPA, in the presence of $Cu/ZnO/Al_2O_3$ and Pd/C at lower temperatures (<100 °C). As shown in **Table 26**, the $Cu/ZnO/Al_2O_3$ catalyst did not produce any detectable amount of formic acid; instead, formamide was formed, indicating that in situ formic acid or formate species are reactive and convert to formamide even at 50 °C. In contrast, the Pd/C catalyst produced a mixture of formic acid and formamide at 50 °C. Lower temperatures, along with the addition of CO_2 pressure, further improved the selectivity for formic acid. However, the overall yield of formic acid remained low. This low conversion may be attributed to the strong binding of the active secondary amine moiety in EEMPA to the Pd/C catalyst at lower temperatures, which hinders the conversion to formic acid. To test this hypothesis, we screened a different capture solvent, DBU/hexanol, which contains a non-nucleophilic base, in previous quarters. Using the Pd/C catalyst with CO_2 captured in the DBU/hexanol mixture, we achieved a conversion as high as 78%, with a high selectivity for formate.

In this quarter (Q4 FY24), we investigated a new capture solvent developed by PNNL that does not contain a primary or secondary amine group, known as Koechanol-D (**Table 26**). This solvent achieved approximately 18% conversion of captured CO_2 to formate, with nearly 100% selectivity. Following this, we screened a tertiary amine-containing solvent (DEEA-EG), which demonstrated exceptional performance, resulting in about 80% conversion of captured CO_2 to formate, with over 99% selectivity. As a result, **we successfully met the Go/No-Go target, which involved producing formate (C_1 oxygenates with over 10% CO_2 conversion) using a Pd/C catalyst in combination with non-nucleophilic or tertiary amine-based post-combustion capture solvents**. Formic acid, which has a boiling point of 100.8 °C, can be thermally cleaved from high-boiling capture solvents via distillation.

Table 26. Hydrogenation of captured CO_2 to formate in the presence of heterogeneous catalysts using a batch reactor system.



Entry	Catalyst	Solvents	Conditions	CO_2 conversion	Yield of formamide (%)	Yield of formic	Selectivity to formic acid

						Acid (%)	
1	65 wt% Cu/ZnO/ Al_2O_3	EEMPA-CO_2	60 bar H_2 50 °C	0.43	0.43	0	0
2	5 wt% Pd/C	EEMPA-CO_2	60 bar H_2 50 °C	8.4	3.11	5.34	63.2
		EEMPA-CO_2	60 bar H_2 100 °C	4.5	4.5	0	0
3		EEMPA-CO_2	60 bar H_2 40 °C	5.09	1	4.09	80.4
4		**EEMPA-CO_2**	**60 bar H_2, 5 bar CO_2 25 °C**	**10.4**	**0**	**10.4[a]**	**>99**
5		**DBU-hexanol-CO_2**	**60 bar H_2 50 °C**	**78.3**	**0**	**78.3**	**>99**
6		**Koechanol-D-CO_2**	**60 bar H_2 50 °C**	**18.5**	**0**	**18.5**	**>99**
7		**DEEA-EG-CO_2**	**60 bar H_2 50 °C**	**80.3**	**0**	**80.3**	**>99**

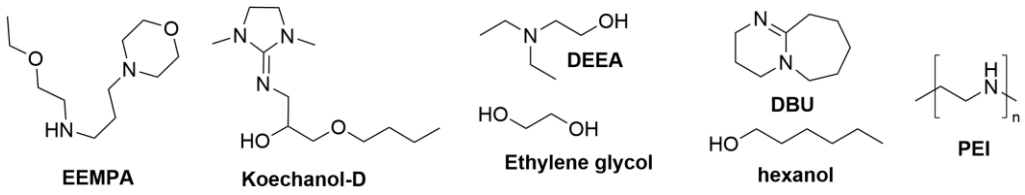
Catalyst=400 mg. [a]Yield not including gas phase CO_2

(ii) ***Cyclic carbonate:*** Various catalysts, capture solvents, and conditions were systematically evaluated to facilitate the synthesis of cyclic carbonate (pr from CO_2 and propylene oxide. Utilizing our leading post-combustion solvent, EEMPA, both with and without different catalysts, yielded only trace amounts of cyclic carbonate. This limited production is attributed to the reaction between EEMPA and propylene oxide, resulting in an aminoalcohol side product, likely formed through the ring-opening of propylene oxide by EEMPA. This reaction effectively inactivates EEMPA as a CO_2 capture solvent.

In contrast, the use of catalytic amounts of EEMPA or polyethyleneimine (PEI) resulted in significantly higher yields of propylene carbonate (cyclic carbonate), as demonstrated in entries 2 and 3 of Table 17. Furthermore, the Koechanol-D solvent achieved a yield of 20% for cyclic carbonate production. DBU-hexanol-based solvents also generated cyclic carbonate at reasonable yields, particularly when utilized in catalytic amounts. In summary, **we achieved the Go/No-Go target by producing cyclic carbonate (C_1 oxygenates) with more than 10% CO_2 conversion using various capture solvents**, as demonstrated in **Table 27**. Propylene or ethylene carbonate (boiling point: ~242 °C) can be separated from EEMPA (boiling point: >300 °C at atmospheric pressure) through distillation. If distillation proves challenging, cyclic carbonate can alternatively be separated from EEMPA using acid-base extraction.

Our current efforts are focused on optimizing the selection of catalysts, refining reaction conditions (including CO_2 pressure, temperature, and reaction time), and exploring additional solvents. Importantly, the next milestone, targeted for Q1 FY25, aims to achieve a 90% yield of cyclic carbonate.

Table 27. Cycloaddition of CO_2 to epoxide.



Entry	Capture solvents	Conditions	CO_2 conversion	Yield of Cyclic carbonate (%)
1	EEMPA-CO_2	PO w/ and w/o catalysts 50-120°C	<1	<1
2	**Catalytic EEMPA-CO_2**	**PO 110°C**	**19.4**	**70.1**
3	**Catalytic PEI-CO_2**	**PO 140 °C**	**26.9**	**97**
4	Koechanol-D-CO_2	PO 110 °C	5.6	19.8
5	DBU-hexanol-CO_2	PO 60 °C	5.8	20.7
6	**Catalytic DBU-hexanol-CO_2**	**PO 60 °C**	**13.9**	**50**
7	DEEA-EG-CO_2	PO 110°C	<1	traces
8	DEEA-EG-CO_2	PO + TBAI (cat.) 110°C	<1	traces

PO = propylene oxide, PC = propylene carbonate (cyclic carbonate), CO_2 pressure = 10 bar, cyclic carbonate yield was calculated with respect to the amount of PO used.

IX) WSU (Task 4. Ethanol): Q4 FY24 Update: Initial attempts in integrating the catalytic systems

1.3.1 Triple Tandem Approach-1

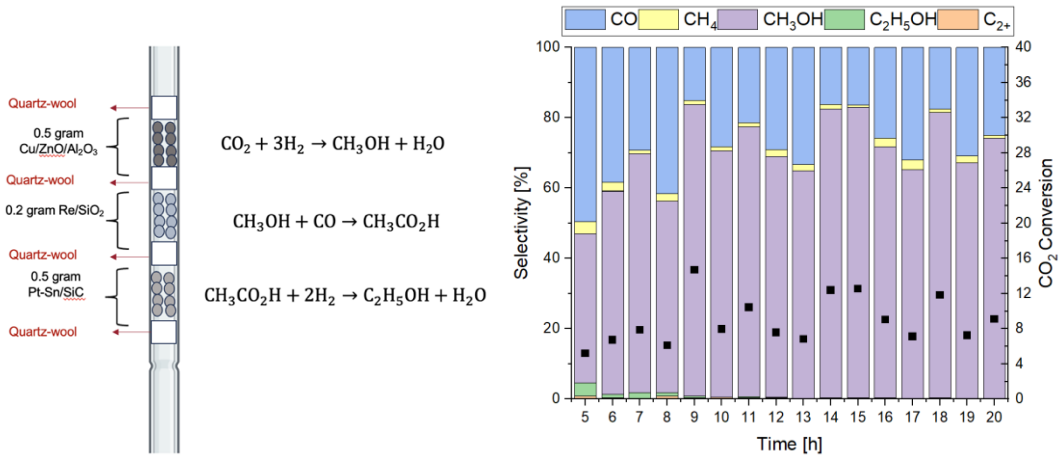


Figure 40. Reaction conditions: flow reactor, temperature 210°C, pressure 30 bar, CO_2 5 sccm, H_2 15 sccm Activation conditions: 210 °C, H_2, 20 sccm for 30 min

1.3.2 Triple Tandem Approach-2

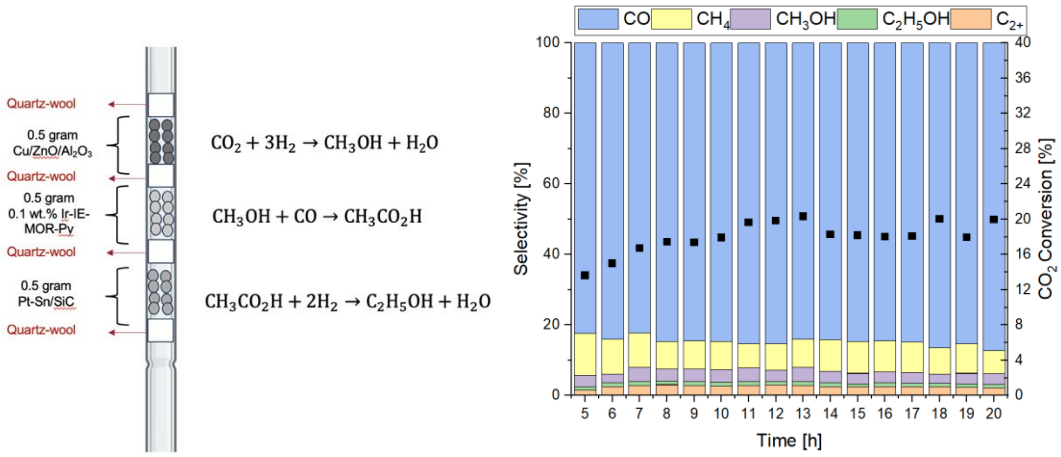


Figure 41. Reaction conditions: flow reactor, temperature 310°C, pressure 30 bar, CO_2 5 sccm, H_2 15 sccm. Activation conditions: 210 °C, H_2, 20 sccm for 30 min

When integrating the catalytic system, undesirable ethanol selectivity is observed (**Figures 40 and 41**). For the triple tandem approach-1, the CuZnAl catalyst successfully converts CO_2 to CO and methanol, but further methanol carbonylation to ethanol has been limited on Re/SiO_2. For the triple tandem approach-2, similarly, the 0.1% Ir/IE-MOR-Py catalyst does not effectively convert CO and methanol into acetic acid. Consequently, CO and methanol remain in the product, leading to low ethanol selectivity. This issue may arise from a mismatch in optimal working temperatures between the first two catalysts:210 ºC for CuZnAl and 310 ºC for 0.1% Ir/IE-MOR-Py).

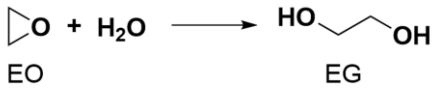
XVI. Q1 FY25 Milestone: Coproduce methanol and glycol in the presence of a post combustion capture solvent. Sequential reactions will be performed to produce >90% yield for cyclic carbonate from epoxide and CO_2, which then will be hydrogenated in the presence of a catalyst to produce methanol and glycol.

Background and Approach. Most of today's methanol is derived from natural gas, but transitioning to renewable sources can significantly reduce its carbon footprint. Methanol synthesis from renewable sources via CO_2 hydrogenation (eq. 1, below) under high-pressure and high-temperature conditions faces challenges, including competing reactions like the endothermic reverse water gas shift reaction ($\Delta H° = +41.2$ kJ/mol). There is growing interest in developing lower-temperature methods to improve conversion rates and selectivity, involving reactive carbon capture promoted by amines and alcohols to generate intermediates like formamides and formate esters. Additionally, water produced as a by-product in CO_2 hydrogenation deactivates catalysts and limits atom efficiency to 64%. Coupling this reaction with another process that utilizes the water could enhance atom efficiency towards 100% and improve catalyst stability.



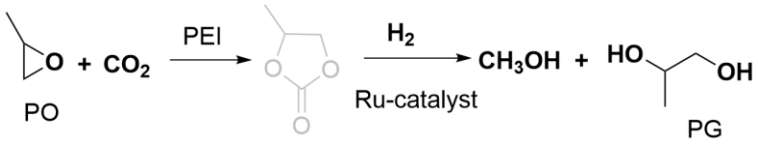
$\Delta H°= -49.5$ kJ/mol (eq. 1)

Ethylene glycol (EG) is produced from ethylene oxide using either a one-step or two-step method. In the one-step method (eq. 2, below), hydrolysis of epoxide in excess water under acidic conditions and temperatures above 150°C generates glycols but often results in contamination with glycol oligomers. To minimize higher homologues, a large surplus of water is required, leading to high energy costs for distillation. The Shell OMEGA process, a two-step method, converts ethylene oxide to EG via cyclic carbonate, followed by hydrolysis. This achieves high selectivity but involves an energy-intensive step to remove excess water.



$\Delta H°= -165.5$ kJ/mol (eq. 2)

Glycols are ideal for co-production with methanol as they consume water (eq. 2, above). Combining these processes allows for simultaneous production of methanol and glycol in a single vessel (eq 3, below), eliminating the need for separating surplus reagents or byproducts, since one reaction's byproduct serves as the feedstock for the other. PNNL confirmed this concept using epoxide, CO_2, and H_2 in a single-pot batch configuration with a homogeneous Ru catalyst tharough a cyclic carbonate intermediate, demonstrating the potential for 100% carbon and hydrogen efficiency.



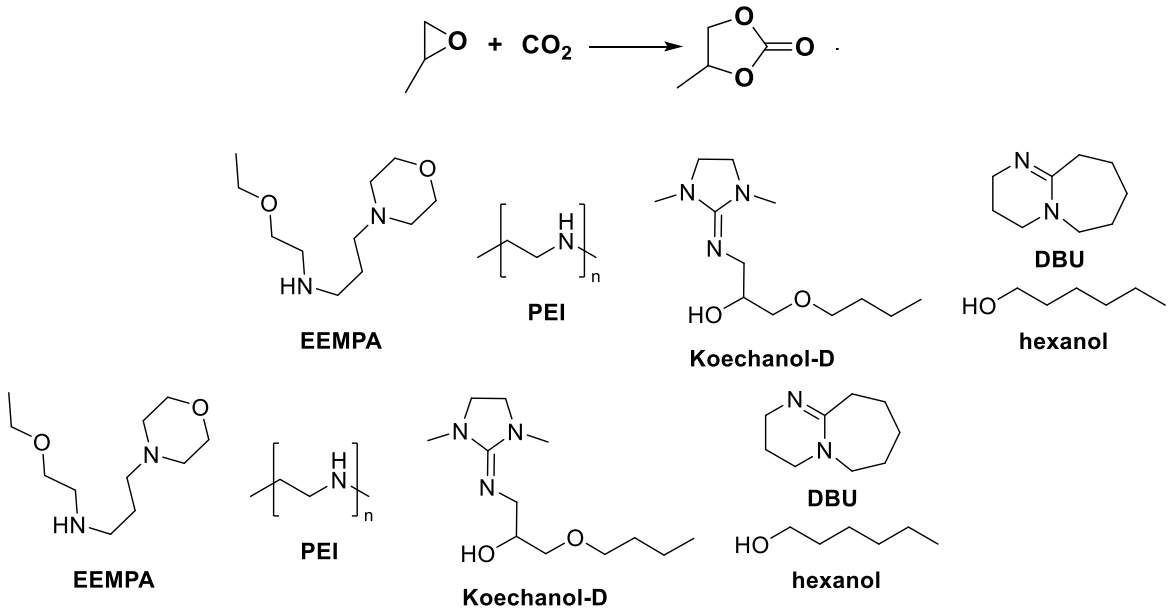
(eq. 3)

Cyclic carbonate from epoxide and CO_2:

During the previous quarter, we conducted a systematic evaluation of various catalysts, and conditions to facilitate the synthesis of cyclic carbonate from CO_2 and propylene oxide in the presence of post combustion solvents. When using our leading post-combustion solvent, EEMPA, either with or without different catalysts, we only observed trace amounts of cyclic carbonate. This limited cyclic carbonate formation was due to a reaction between EEMPA and propylene oxide (PO), leading to the formation of an aminoalcohol side product through the ring-opening of propylene oxide by EEMPA. Consequently, this reaction effectively deactivates EEMPA as a CO_2 capture solvent.

In contrast, employing catalytic amounts of EEMPA or polyethyleneimine (PEI) significantly increased the yields of propylene carbonate, as shown in entries 2 and 3 of **Table 28**. Additionally, the Koechanol-D solvent achieved a 20% yield of cyclic carbonate. DBU-hexanol-based solvents also produced cyclic carbonate with reasonable yields, especially when used in catalytic amounts. In summary, **when amine-based solvents were used in catalytic amounts, cyclic carbonate was produced from epoxide and CO_2 with yields exceeding 90%.**

Table 28. Cycloaddition of CO_2 to epoxide.



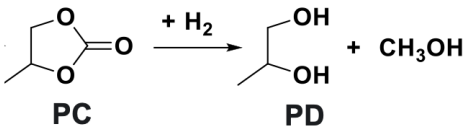
Entry	Capture solvents	Conditions	CO_2 conversion	Yield of Cyclic carbonate (%)
1	EEMPA-CO_2	PO w/ and w/o catalysts 50-120°C	<1	<1
2	**Catalytic EEMPA-CO_2**	**PO 110°C**	**19.4**	**70.1**

3	**Catalytic PEI-CO_2**	**PO 140 °C**	**26.9**	**97**
4	Koechanol-D-CO_2	PO 110 °C	5.6	19.8
5	DBU-hexanol-CO_2	PO 60 °C	5.8	15
6	**Catalytic DBU-hexanol-CO_2**	**PO 60 °C**	**13.9**	**50**

PO = propylene oxide, PC = propylene carbonate (cyclic carbonate), CO_2 pressure = 10 bar, cyclic carbonate yield was calculated with respect to the amount of PO used.

Hydrogenation of Cyclic Carbonate to Produce Methanol and Glycol:

Table 29. Cyclic carbonate hydrogenation to coproduce methanol and glycol.



Entry	Catalysts	PC Conv. (%)	Methanol Sel. (%)	CO Sel. (%)	CO_2 Sel. (%)	PD Sel. (%)
1	**Ru catalyst + PEI (homogeneous)**	**>99**	**>90**	**<5**	**<5**	**>99**
2	**Cu-catalyst X**	**88**	**15.4**	**29.9**	**54.7**	**74.3[a]**
3	**Cu-catalyst Y**	**>99**	**74.6**	**10.6**	**14.8**	**93.4[a]**
4	**Cu-catalyst Z**	**>99**	**65.2**	**16.1**	**18.7**	**98.5**
5	**Cu-catalyst Z [b]**	**>99**	**53.4**	**21.7**	**24.9**	**99.3**

Propylene carbonate (PC) = 20 mmol, H_2=45 bar, 170 °C, t=15h, [a]Low PD (propanediol) selectivity is due to over hydrogenation of PD, [b]t=7h

Previously, we demonstrated that a homogeneous Ru-based catalyst can co-produce methanol and diol from cyclic carbonate. This quarter, we screened different **heterogeneous catalysts** (entries 2-5, **Table 29**) to facilitate the separability of the catalyst from the products, focusing especially on copper-based catalysts for the co-production of glycol and methanol from cyclic carbonate. Using Cu-catalyst X, we achieved a high propylene carbonate (PC) conversion of ~88%. PD (propanediol) was formed with a conversion rate of ~93%. In addition to PD, some over-hydrogenation products of PD were also observed. The co-product methanol selectivity was low, at about 15%, due to the formation of side products CO and CO_2.

To prevent these side products, we tested Cu-catalyst Y and Z. The catalysts were synthesized using two different methods: ammonia evaporation hydrolysis (AEH) and precipitation-gel (PG). The conversion was very high with the Cu-catalyst Y. Methanol selectivity was significantly higher (~75%) compared to the Cu-catalyst X. The PD selectivity exceeded 90%, with only a small amount of PD over-hydrogenation products. With the Cu-catalyst Z, PD selectivity was even higher, reaching over 98%. However, methanol selectivity was lower with the Cu-catalyst Z catalyst compared to the Cu-catalyst Y. Overall, **both a homogeneous Ru-based catalyst and a heterogeneous Cu/SiO_2-based catalyst were identified to be selective for the co-production of methanol and glycol.**

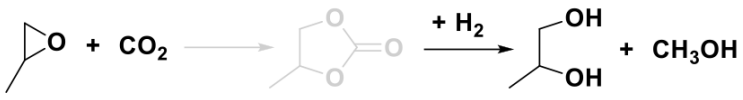
Single Step Coproduction of Methanol and Glycol

The selected catalysts identified for the hydrogenation of cyclic carbonate from **Table 29** were screened for the direct conversion of PO, CO_2, and H_2 to methanol and glycol (shown in **Table 30**). In all reactions, PO conversion was greater than 99%. With the Cu-catalyst Y (entry 1, **Table 30**), methanol selectivity was approximately 34%. The low methanol selectivity was attributed to the formation of CO. Additionally, PD selectivity was also low due to the formation of PD over-hydrogenation products.

In the case of Cu-catalyst X, methanol selectivity was high at 78%, with about 22% selectivity to CO (entry 2, **Table 31**). Although methanol selectivity was high, PD selectivity was moderate at around 42%. To further improve PD selectivity, polyethyleneimine (PEI) was added as a co-catalyst to promote cyclic carbonate formation (entry 3, **Table 31)**. As anticipated, the addition of PEI significantly improved PD selectivity to 87%. However, the methanol selectivity dropped to 21%.

Very recently, we identified that **methanol and PD can be co-produced at approximately 75% and 72% selectivities**, respectively, using Catalyst X (a heterogeneous catalyst) and a catalytic amount of PEI. Given the promising results from the initial runs, we then optimized conditions to further improve selectivity to both methanol and glycol. Detailed results are reported in the next quarter update. Overall, a proof of concept for the **one-step co-production of methanol and glycol was demonstrated for the first time from PO, CO_2, and H_2 using a heterogeneous catalyst.** In the coming months, we will draft a manuscript that compiles all these results and file a patent on these recent, exciting findings.

Table 31. Coproduction of Methanol and Glycol from PO, CO_2 and H_2



PO (20 mmol), 15 bar CO_2, 45 bar H_2, 170°C, 15h, [a]PD (propanediol) hydrogenation products

Techno-Economic Analysis and Life Cycle Assessment:

A preliminary techno-economic and life-cycle analysis was performed for the single-step co-production of methanol and ethylene glycol (EG) from ethylene oxide (EO), CO_2, and H_2. A preliminary process model, as shown in **Figure 42**, was developed in Aspen Plus to evaluate the mass and energy balance. In this process, H_2, CO_2, and EO are first mixed and heated to 120 °C before being sent to the main reactor. The main reactor is simulated as an equilibrium reactor operated at 160 °C. Reactions (**4**) to (**6**) were specified in the reactor, with conversions determined by chemical equilibrium. Ethylene carbonate (EC) is an intermediate product in this process.

As the combined reaction is extremely exothermic, a significant amount of heat is generated at the main reactor at 160 °C, which can be utilized for power generation via an organic Rankine cycle. The hot product from the reactor first pre-heats the reactor inlet stream and is then sent to a distillation column to be separated into off-gases, methanol, and EG. The capital cost was estimated using the Aspen Process Economic Analyzer. In both the techno-economic analysis (TEA) and life-cycle analysis (LCA), methanol was considered the main product. The minimum selling price of methanol was estimated using the simplified annualized cost approach, and cradle-to-grave GHG emissions were estimated using commercial LCA databases. EG was considered a by-product, and by-product credits were included based on its market wholesale value in TEA and its baseline cradle-to-gate GHG emissions in LCA via the displacement approach.

$$CO_2 + 3\ H_2 \leftrightarrow CH_3OH + H_2O \quad (4)$$

$$EO + CO_2 \leftrightarrow EC \quad (5)$$

$$EC + H_2O \leftrightarrow EG + CO_2 \quad (6)$$

Entry	Catalysts	PO Conversion (%)	Methanol Sel. (%)	CO Sel. (%)	PD Sel. (%)
1	Cu-catalyst Y	>99	33.6	66.4	17.5[a]
2	Catalyst X	>99	78.4	21.6	42.0[a]
3	Catalyst X + PEI (1:0.25)	>99	20.9	79.1	87
4	**Catalyst X + PEI (1:0.12)**	**>99**	**75**	**25**	**72**

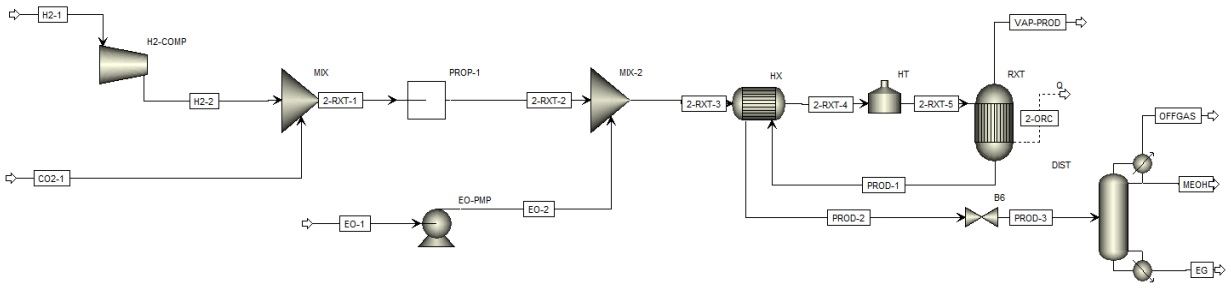


Figure 42. Process configuration of the single-step co-production technology.

The overall mass and energy balance for the proposed one-step co-generation process is summarized in **Table 32**, with preliminary TEA and LCA results presented in **Figures 43** and **44**, respectively. The results indicate that the proposed co-generation process has the potential to achieve near 100% atom efficiency and about 80% thermal efficiency. Additionally, the co-generation approach can reduce the minimum methanol selling price by up to 17% compared with the conventional CO_2 to methanol process. This process could potentially be a negative emission approach to methanol production mainly due to its high atom and thermal efficiency, as well as the co-production of EG.

Table 32. Mass and Energy Balance

	Unit	Value	Energy (GJ/h)
Raw Materials			
CO_2	kg/h	82,386	
H_2	kg/h	11,321	1,358
EO	kg/h	82,468	2,244
Catalyst	kg/h	7	
Utilities			
Natural gas	MMBtu/h	158	166
Cooling water	Mgal/h	1,392	
Products			
Methanol	kg/h	59,983	1,193
EG	kg/h	116,165	2,244
Electricity	kW		82
Mass Balance	%	99.98	
Thermal Efficiency (%)			83.67

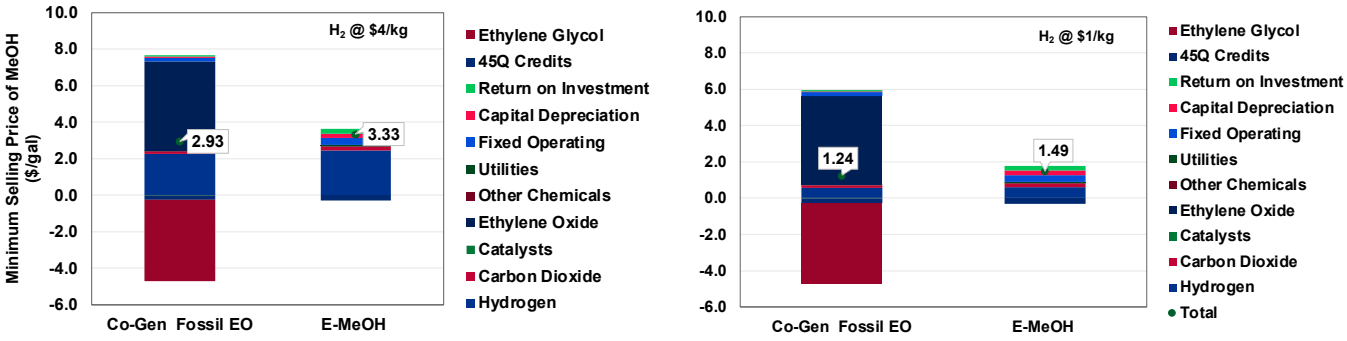


Figure 43. Estimated minimum methanol selling price.

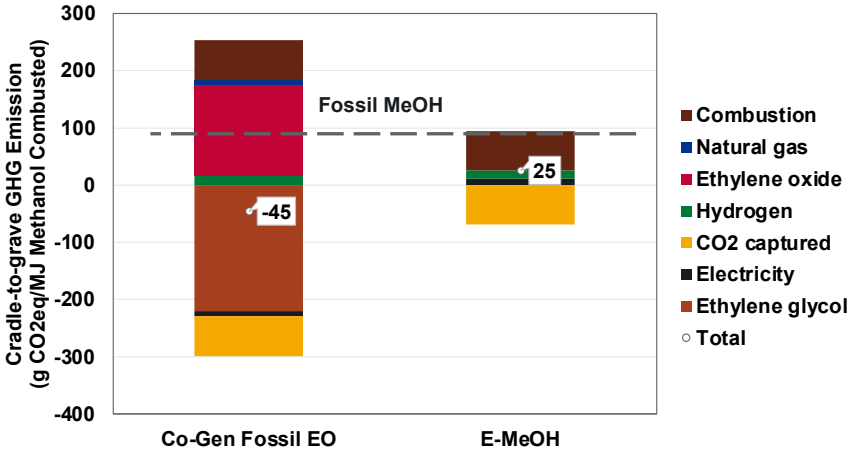


Figure 44. Estimated cradle-to-grave GHG emission.

XVII. *Evaluation of new catalyst formulations for methanol synthesis in a post-combustion capture solvent in a continuous flow reactor (Q1 FY25):*

During the last quarter, we performed the hydrogenation of captured CO_2 using a variety of catalysts in a continuous-flow reactor system. Our study encompassed a broad spectrum of operating temperatures and space velocities. The results revealed that the Pt/MoO_3 catalyst exhibited a markedly higher catalytic performance in terms of CO_2 conversion when compared to Pt/TiO_2 and Pt/ZrO_2 catalysts. Interestingly, Pt/ZrO_2 showed exceptional selectivity (~100%) towards methanol production. Moreover, we assessed the durability of the spent EEMPA solvent post-conversion. The results indicated a notably enhanced stability of the capture solvent when used with the Pt/MoO_3 catalyst, as opposed to the earlier version, Pt/TiO_2.

Our detailed characterization indicated that the increased methanol production using Pt/MoO_3 is due to the substantially high H_2 spillover observed under reaction conditions. On the other hand, the high methanol selectivity of Pt/ZrO_2 can be attributed to its basic sites, which lower methanol adsorption and inhibit methane formation. These findings highlight the critical role of adjusting the

acidic and basic sites on the catalyst surface to boost methanol selectivity while maintaining the structural integrity of the capture solvent.

In an effort to further enhance methanol selectivity, we incorporated basic sites into the Pt/MoO_3 catalyst, noting its efficient CO_2 conversion and minimal solvent degradation (**Table 33**). However, the methanol productivity was found to be lower in N-doped and K-doped Pt/MoO_3 catalysts as compared to the baseline Pt/MoO_3 catalyst (entries 1-6, **Table 33)**. Acknowledging the low surface area of the MoO_3 support (~3 m^2/g), we synthesized a high surface area (HSA) MoO_3 (~25 m^2/g) to study the impact of surface area on catalytic efficiency. The catalytic performance of the HSA MoO_3 was comparable to that of the baseline low surface area MoO_3 (entry 1 and 2 vs 7 and 8, **Table 33**).

Table 33. Hydrogenation of captured CO_2 over various catalysts, employing a continuous-flow reactor system across a range of operating temperatures and space velocities.

Entry	Run	T (°C)	SV ($gCO_2/gCat/h$)	Conv. (%)	MeOH Sel. (%)	CH_4 Sel.(%)	CO Sel. (%)
	5wt% Pt/MoO_3, 5wt%CO_2 EEMPA feed						
1	**IC3M17**	**190**	**0.15**	**32.1**	**59.4**	**24.3**	**16.3**
2	**IC3M17**	**190**	**0.015**	**77.6**	**59.1**	**40.9**	**0.0**
	5wt% Pt/N-doped MoO_3, 5wt%CO_2 EEMPA feed						
3	**IC3M47**	**190**	**0.15**	**16.9**	**17.2**	**15.3**	**67.5**
4	**IC3M47**	**190**	**0.015**	**58.3**	**45.7**	**33.7**	**20.6**
	5wt% Pt/K-doped MoO_3, 5wt%CO_2 EEMPA feed						
5	**IC3M46**	**190**	**0.15**	**5.6**	**21.7**	**78.3**	**0.0**
6	**IC3M46**	**190**	**0.015**	**14.3**	**31.6**	**68.4**	**0.0**
	5wt% Pt/HSA MoO_3, 5wt%CO_2 EEMPA feed						
7	**IC3M51**	**190**	**0.15**	**33.6**	**50.7**	**15.3**	**34.0**
8	**IC3M51**	**190**	**0.015**	**80.6**	**63.5**	**36.5**	**0.0**

Next, we explored the effects of adding mixed metal oxides to the Pt/MoO_3 catalyst by introducing 5 wt% of MgO, ZrO_2, and CeO_2 (**Table 34**). The addition of MgO completely suppressed the CO_2 hydrogenation performance, yielding only traces of methane and CO. This suppression is likely

due to the formation of a MgO layer on the MoO_3, which hindered the cooperativity between Pt and MoO_3. On the other hand, the introduction of 5 wt% ZrO_2 to the Pt/MoO_3 catalyst demonstrated reactivity comparable to the baseline Pt/MoO_3 catalyst.

Interestingly, adding **5 wt% CeO_2 to the Pt/MoO_3 catalyst significantly improved methanol selectivity to 80% (**entry 7 and 8**, Table 34).** This enhancement is likely due to the presence of optimal basic sites, which suppressed methane formation. Furthermore, we tested the effect of adding 5 wt% CeO_2 to the high surface area (HSA) MoO_3. The selectivity for methanol remained high, although there was a drop in CO_2 conversion.

Table 34: Hydrogenation of captured CO_2 over various catalysts, employing a continuous-flow reactor system across a range of operating temperatures and space velocities.

Entry	Run	T (°C)	SV ($gCO_2/gCat/h$)	Conv. (%)	MeOH Sel. (%)	CH_4 Sel.(%)	CO Sel. (%)
	5wt% Pt/(5wt% MgO)MoO_3, 5wt%CO_2 EEMPA feed						
1	**IC3M54**	**190**	**0.15**	**0.9**	**0.0**	**91.9**	**8.1**
2	**IC3M54**	**190**	**0.015**	**1.8**	**0.0**	**72.9**	**27.1**
	5wt% Pt/(5wt% ZrO_2)MoO_3, 5wt%CO_2 EEMPA feed						
3	**IC3M55**	**190**	**0.15**	**20.8**	**21.1**	**27.5**	**51.4**
4	**IC3M55**	**190**	**0.015**	**73.9**	**46.1**	**47.4**	**6.4**
	5wt% Pt/(5wt% ZnO)MoO_3, 5wt%CO_2 EEMPA feed						
5	**IC3M63**	**190**	**0.15**	**3.4**	**0.0**	**0.0**	**100.0**
6	**IC3M63**	**190**	**0.015**	**0.7**	**100.0**	**0.0**	**0.0**
	5wt% Pt/(5wt% CeO_2)MoO_3, 5wt%CO_2 EEMPA feed						
7	**IC3M69**	**190**	**0.15**	**19.4**	**22.3**	**6.9**	**70.8**
8	**IC3M69**	**190**	**0.015**	**78.8**	**78.0**	**16.5**	**5.4**
	5wt% Pt/(5wt% CeO_2)HSA MoO_3, 5wt%CO_2 EEMPA feed						

9	IC3M66	190	0.15	22.6	27.1	5.5	67.4
10	IC3M66	190	0.015	57.7	83.2	16.8	0.0

XVIII. WSU (Task 4. Ethanol): Q1 FY25 Update:

The following primary activities were performed this quarter:

1.1 The direct CO_2 hydrogenation

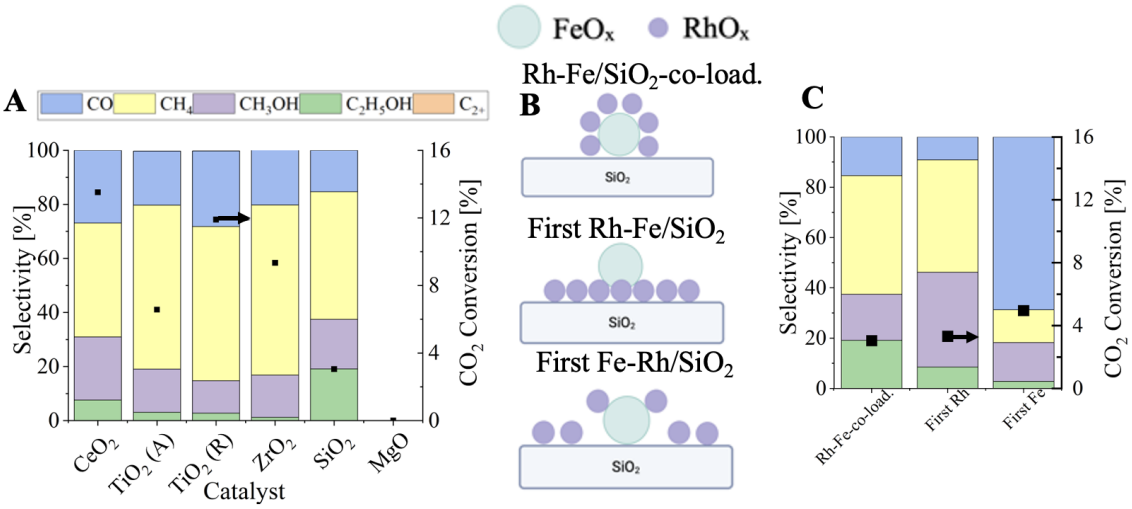


Figure 45. Reaction conditions: flow reactor, temperature 210°C, pressure 30 bar, CO_2 5 sccm, H_2 15 sccm. Activation under temperature 350°C, H_2 20 sccm for 30 min.

Various supports were tested to study the Rh-Fe interaction on ethanol selectivity from CO_2 hydrogenation (**Figure 45A**). Enhanced metal-metal interactions were observed on the inert SiO_2 support, leading to the highest selectivity. In contrast, CeO_2, TiO_2, ZrO_2, and MgO showed significantly lower ethanol selectivity due to stronger metal-support interactions. Therefore, SiO_2 was identified as the most promising support, and different loading sequences were then explored to modulate Rh-Fe interactions (**Figure 45B**). Better ethanol selectivity was achieved by controlling Rh-Fe loading sequences (**Figure 45C**). The Rh-Fe/SiO_2 co-loading resulted in the highest ethanol selectivity, while stepwise loadings, especially with Fe loaded first, showed significantly lower ethanol selectivity. It is hypothesized that co-loading Rh and Fe enhances metal-metal interactions, increasing the Rh-Fe coordination number and the electron density of Rh. The strong Rh-Fe bonds and enhanced electron transfer from Fe to Rh fine-tune the electronic structure of Rh, promoting selective C-C coupling for ethanol production. When Fe is loaded first, the acidic Rh nitrate solution protonates FeOx, making it positively charged. This causes repulsion with Rh^{3+} because the pH is below the point of zero charge (PZC) of FeOx. In contrast, RhOx has a much lower PZC. Therefore, when Rh is loaded first, the repulsion between RhOx and Fe^{3+} is limited. Thus, the Rh-Fe interaction is maintained but not as strong as in the co-loading case.

Furthermore, the Rh to Fe molar ratio in the co-loaded catalyst on the SiO_2 support was adjusted based on promising preliminary results. The objective is to determine the optimal Rh/Fe ratio for CO_2 hydrogenation to alcohols, specifically ethanol and methanol. At the optimal Rh/Fe ratio, Rh-Fe adjacent active sites are formed, leading to a higher electron density of Rh. This high electron density of Rh facilitates C-C coupling. However, when the catalyst contains an excess of Rh, the electron density of Rh sites decreases. Conversely, when the Rh/Fe ratio is low, Rh sites become overly electron-rich, which reduces their catalytic activity for ethanol production [Kusama, H., et al., (Vol. 22, Issue 3), 1997].

At a lower reaction temperature of 210°C, a Rh:Fe ratio of 1:1 demonstrates the highest selectivity, yielding 20% ethanol and 20% methanol (**Figure 46A**). Differently, at a higher reaction temperature of 300°C, a Rh:Fe ratio of 1:3 results in the highest alcohol selectivity, with 12% ethanol and 28% methanol (**Figure 46B**). These findings indicate that both the Rh:Fe ratio and reaction temperature significantly influence product distribution, emphasizing the importance of optimizing catalyst composition and reaction conditions for enhanced alcohol production.

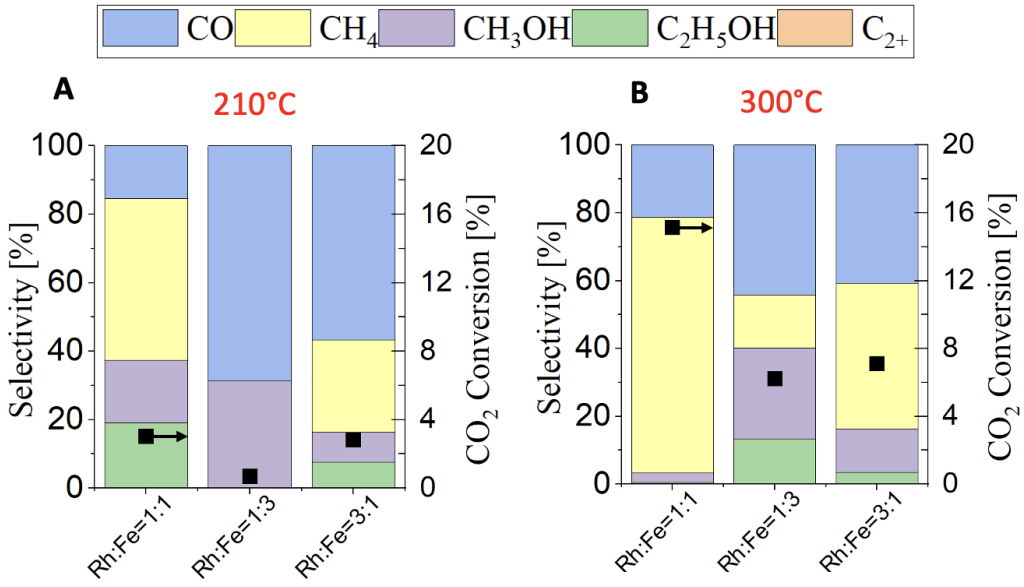


Figure 46. Reaction conditions: flow reactor, pressure 30 bar, CO_2 5 sccm, H_2 15 sccm. Activation under temperature 350 °C, H_2 20 sccm for 30 min.

1.2 The double tandem approach

Building on the promising ethanol selectivity of Rh-Fe/SiO_2 for CO_2 hydrogenation, and recognizing its capability for CO hydrogenation, a new tandem system approach is being investigated to bridge these processes and improve the overall efficiency of CO_2-to-ethanol conversion. This two-step approach involves first converting CO_2 to CO using a reverse water-gas shift (RWGS) catalyst, followed by the hydrogenation of CO to ethanol over Rh-Fe/SiO_2 (**Figure 47**). The RWGS reaction is described as:

$$CO_2 + H_2 \rightarrow CO + H_2O$$

And the subsequent CO hydrogenation to ethanol:

$$2CO + 4H_2 \rightarrow C_2H_5OH + H_2O$$

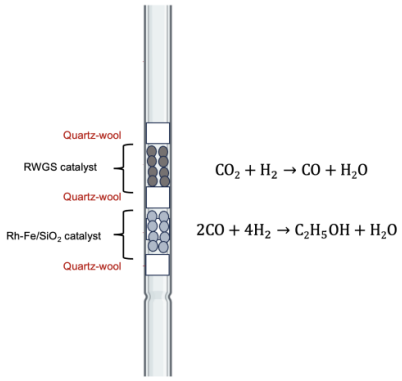


Figure 47. Schematic of double tandem approach system in the reactor tube.

1.2.1 Step-by-Step Exploration of a Double Tandem Catalyst Approach

After testing Rh-Fe/SiO_2 for CO_2 hydrogenation, this catalyst was also evaluated for CO hydrogenation (**Figure 48**). This catalyst demonstrates approximately 60% ethanol selectivity with 15% CO conversion at 230°C and maintains stability throughout the test, showing significantly improved performance over typical literature-reported results for CO hydrogenation. The experimental results are found to be consistent and reproducible, with ethanol selectivity reaching 60% at 230°C. However, at elevated reaction temperatures of 260°C and 290°C, methane production becomes dominant, indicating a shift in product distribution with increasing temperature.

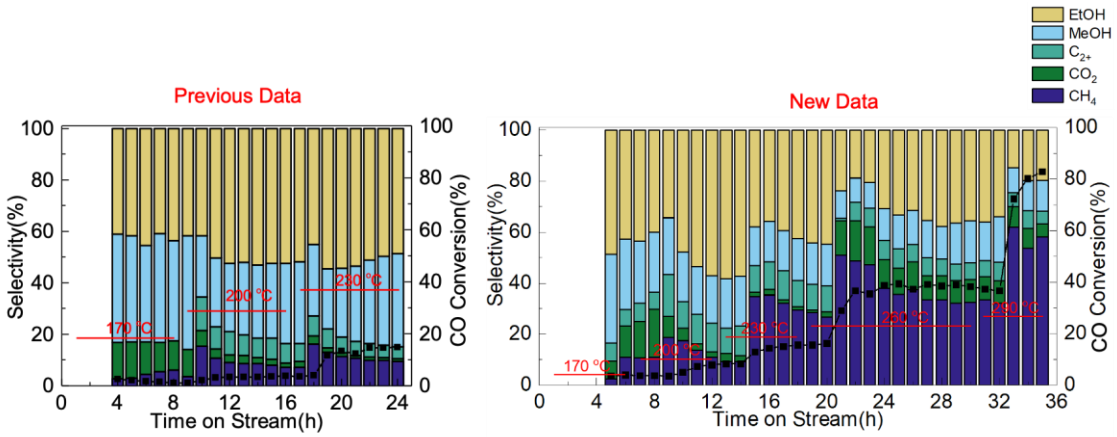


Figure 48. Reaction conditions: flow reactor. Pressure 30 bar, CO 5 sccm, H_2 10 sccm, (H_2:CO=2:1). Activation under temperature 320 °C, H_2 10 sccm for 30 min. The catalyst amount is reduced from 0.3 g to 0.2 g for the new run.

Therefore, the challenge lies in achieving both high CO_2 conversion and ethanol selectivity due to competing reactions that favor methanol and other byproducts. Due to the temperature-dependent

ethanol selectivity, we need to identify an RWGS catalyst that works effectively at 230°C to integrate into the system.

1.2.1 Challenge for the Double Tandem Approach

As discussed, the challenge with the tandem system lies in the high-temperature requirements of the RWGS reaction, which often needs temperatures above 400°C to achieve sufficient CO production. To address this, we are investigating RWGS catalysts that can function at a lower temperature, ideally around 300°C, to align more closely with the operating conditions of the CO hydrogenation step. Promising candidates showing desirable activity and CO selectivity near this lower temperature include 2%Pt-CeO_2, 3.2%PtCo-CeO_2, Cu-CeO_2, and 5%Ir-CeO_2, as shown in **Table 35**. These catalysts show potential in lowering the temperature requirements of the RWGS reaction, which could enable the seamless integration of the tandem process by aligning the reaction conditions of both the CO_2 hydrogenation and CO hydrogenation steps.

Table 35. Promising reported catalysts for low-temperature RWGS reactions.

Catalyst	**Temperature[°C]**	**CO_2 conversion[%]**	**CO selectivity[%]**	**Ref.**
2%Pt-CeO_2	290	21.7	100	a
3.2%PtCo-CeO_2	300	9.1	92.3	b
Cu-CeO_2	300	18	100	c
5%Ir-CeO_2	300	6.8	99	d

a. Goguet, A et al., *J. Catal.* 2004, *226*, 382–392.
b. Kattel, S.et al., *Angew. Chem. Int. Ed.* 2016, *55*, 7968–7973.
c. Yang, S. et al., *ACS Catal.* 2018, *8*, 12056–12066.
d. Li, S. et al., *Angew. Chem.* 2017, *129*, 1234.

XIX. Milestone (Q2 FY25): (A) Improve the rate of hydrogenation of condensed phase CO_2 to methane comparable to or better than gas phase reaction and achieve >90% single pass conversion

To meet this quarter's milestone (Q2 FY25) of achieving over 90% single-pass conversion of captured CO_2, our efforts focused on improving the hydrogenation rate of condensed phase CO_2 to methane. Here we demonstrate a significant improvement in the hydrogenation rate of condensed phase CO_2 to methane compared to the gas phase reaction, achieving over 90% single-pass conversion. The effectiveness of various catalysts was evaluated based on CO_2 conversion and methane selectivity at different space velocities.

CO_2 captured in EEMPA under expected carbon capture conditions (5 wt% CO_2 loading) was used as the CO_2 source and subjected to hydrogenation in the presence of different catalysts. The experimental results are shown in **Table 36**. The most notable performance was observed for the 5wt% Ru/Al_2O_3 catalyst (Entry 1), which achieved a CO_2 conversion rate exceeding 99% and a CH_4 selectivity of 97.9% at a space velocity of 0.15 $gCO_2/gCat/h$. This catalyst exhibited a remarkable turnover frequency (TOF) of 62.5 μmol CH4 g Ru^{-1} s^{-1} at 190°C,[17, 18] making it significantly more efficient than the Ru catalysts reported in the literature, which have a TOF range of 2-40 μmol CH_4 g Ru^{-1} s^{-1} at temperatures below 200°C.

Comparatively, the 35wt% Ni/MoO_3 catalyst demonstrated varied performance based on space velocity. At a space velocity of 0.15 $gCO_2/gCat/h$ (Entry 2), it achieved only 5% CO_2 conversion with excellent methane selectivity (100%). However, when the space velocity was reduced to 0.015 $gCO_2/gCat/h$ (Entry 3), the CO_2 conversion increased to 20.1%, maintaining high CH_4 selectivity.

The 35wt% Ni/TiO_2 catalyst demonstrated encouraging performance. With a space velocity of 0.15 $gCO_2/gCat/h$ (Entry 4), it achieved a CO_2 conversion rate of 37.1% while maintaining a methane selectivity of 97%. Remarkably, reducing the space velocity to 0.06 $gCO_2/gCat/h$ (Entry 5) resulted in a 100% CO_2 conversion rate with 98.7% CH_4 selectivity. This underscores the high efficiency and potential of the Ni/TiO_2 catalyst under optimal conditions. Additionally, the observed activity (TOF) of Ni/TiO_2 in the condensed phase is 3.75 $gCO_2/gCat/h$,[17] which is comparable to the gas phase performance of Ni-based catalysts at temperatures below 200°C

Finally, the 5wt% Pt/Fe_2O_3 catalyst presented in Entry 6 achieved a CO_2 conversion of 17.4% and a CH_4 selectivity of 92.5% at a space velocity of 0.015 $gCO_2/gCat/h$. Although less impressive than Ru/Al_2O_3 and Ni/TiO_2, this catalyst still demonstrated the ability to effectively convert CO_2 to methane under condensed phase conditions.

In summary, **the Ru/Al_2O_3 catalyst not only surpasses other tested catalysts and those described in the literature for gas phase conversion in terms of TOF and CO_2 conversion rate, but it, along with Ni/TiO_2, achieves over 90% single-pass conversion of captured CO_2 to methane**. Additionally, the performance of Ni/TiO_2 is comparable to gas phase performance. This highlights the potential of these catalysts for efficient CO_2 hydrogenation in condensed phases. The study confirms that by strategically selecting catalysts and optimizing reaction conditions, the hydrogenation rate of condensed phase CO_2 can be significantly enhanced, leading to superior conversion efficiency and methane selectivity.

Table 36. Hydrogenation of captured CO_2 in a continuous-flow reactor system across a range of operating temperatures and space velocities

Entry	Catalysts	Space Velocity ($gCO_2/gCat/h$)	CO_2 Conversion (%)	CH_4 Selectivity (%)
1	5wt% Ru/Al_2O_3	**0.15**	>99	97.9
2	35wt% Ni/MoO_3	**0.15**	5	100
3	35wt% Ni/MoO_3	**0.015**	20.1	100
4	35wt% Ni/TiO_2	**0.15**	37.1	97
5	35wt% Ni/TiO_2	**0.06**	100	98.7
6	5wt% Pt/Fe_2O_3	**0.015**	17.4	92.5

Reaction conditions: 1g of catalyst, pressure: 860psi, 33.8 sccm H_2, 5 sccm N_2, 5%w CO_2 loaded 2-EEMPA solvent, space velocity change is achieved by adjusting the flow of CO_2-loaded 2-EEMPA solvent to 0.05, 0.02, or 0.005 mL/min.

1.1 Techno-Economic Analysis and Life Cycle Assessment for Methane Production

In this quarter (Q2 FY25), TEA and LCA were conducted for SNG production via both IC^3M and conventional two-step CCUS technologies

1.1.1. Materials and Methods

Process Modeling: In this quarter, rigorous process models were developed in Aspen Plus V14 for SNG production via IC^3M, while published data were used for SC^3M routes. For both IC^3M process, PNNL's leading proprietary water-lean solvent, EEMPA, was used as the capture solvents. EEMPA has an estimated capture cost reduction up to 19% and energy saving up to 40% compared with industrial benchmarks, because its water-lean feature can minimize undesired water vaporization and condensation in the solvent regenerator [19]. In addition, EEMPA has the most complete experimental data set for process modeling TEA and LCA [12, 20], although other solvent candidates are being investigated for IC^3M platform.

Property Models. ENRTL-RK was selected as the base property method for unit operation involving carbon capture solvent, as it is widely used for solvent systems involving electrolyte chemistry. For other unit operation, Peng-Robinson equation-of-state was used. For most of chemicals involved in the process, pure component property parameters and binary interaction parameters can be retrieved from Aspen Property Database. For EEMPA, and its interaction with H_2O and CO_2, property parameters were regressed from experimentally measured property data including density, viscosity, vapor liquid equilibrium from PTx cell, and kinetics from wetted wall column. The chemical reaction between EEMPA and CO_2 is presented by Equations (1) and (2), below. Original data, selected ENRTL-RK parameters, regression approach, and model validation were detailed in our previous publication [19].

$$2\,EEMPA + CO_2 \leftrightarrow EEMPAH^+ + EEMPACO_2^- \quad (1)$$

$$EEMPA + CO_2 + H_2O \leftrightarrow EEMPAH'^{+} + HCO_3^- \quad (2)$$

Methane Production via IC^{3}M. The best experimental results (99% conversion and 90% selectivity at 170°C and 15 bar with a 5 wt% Ru/Al_2O_3 catalyst, batch experimental results) were simulated for TEA and LCA. The process flow diagram of SNG production via IC^{3}M technology are presented in **Figure 49**. Flue gas from the NGCC plant is first sent to the two-stage direct contact cooler with cooling water in the first stage and chilling water in the second stage to reduce flue gas temperature from 110 °C to 16 °C and reduce water content in the flue gas to 1.7 mol%. The lower temperature and water loading can improve the performance of the water-lean solvent. Then, the flue gas is fed to the bottom of the CO_2 absorber, while CO_2-lean solvent is fed to the top of the column. The clean flue gas with 90% CO_2 captured leaves from the column top, while the CO_2-rich solvent leaves from the column bottom. The rich solvent is pumped to 16 bar, preheated by exchanging heat with the hot reactor outlet stream, mixed with H_2, and then sent to the main reactor. The main reactor is filled with 5 wt% Ru/Al_2O_3 catalyst to promote methane formation from CO_2-rich solvent in the condensed phase at 170 °C, via Reactions (3)-(4), above. As the CO_2 hydrogenation reaction is highly exothermic, extra reaction heat is used to generate steam and preheat the reactor feed. The product stream is cooled to 35 °C and then sent to a flash drum operated at 15 bar to recover methane product in the gas phase. The liquid product from the flash drum are mainly CO_2-lean solvent and water by-products. Note that water is produced as by-product during hydrogenation, as shown in Equations (3)-(4), above. To avoid water accumulation in the system, the liquid product from the flash drum is first sent to a pressure driven membrane filtration unit, also called pervaporation, a technology widely used for remove water from industrial solvent [21, 22] to remove a portion of water before recycled back to the CO_2 absorber.

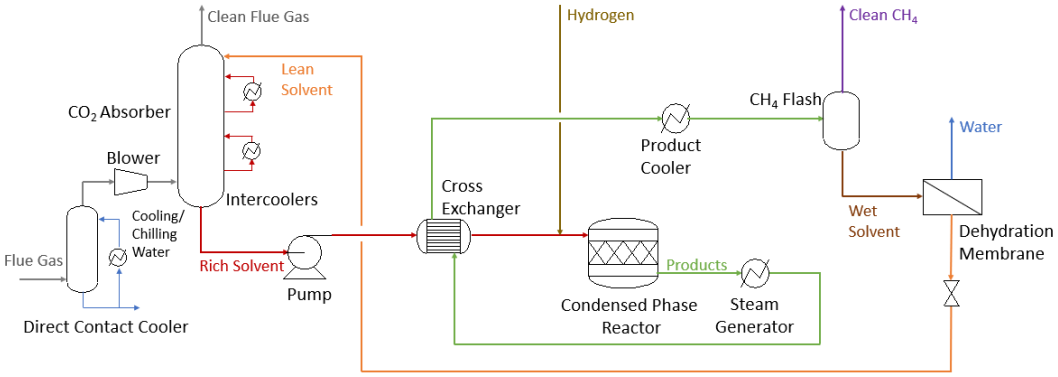


Figure 49. Process flow diagram of SNG production via IC^{3}M technology.

$$EEMPAH^+ + EEMPACO_2^- + 4\,H_2 \rightarrow 2\,EEMPA + CH_4 + 2\,H_2O \quad (3)$$

$$EEMPAH'^{+} + HCO_3^- + 4\,H_2 \rightarrow EEMPA + CH_4 + 3H_2O \quad (4)$$

In the process model, the flue gas composition was set to 74.28 mol% N_2, 12 mol% O_2, 8.75 mol% H_2O and 4.08 mol% CO_2. It was defined based on Case B31B representing a 650 MW NGCC plant with carbon capture in the baseline performance report published by U.S. National Energy Technology Laboratory (NETL) [23]. The direct contact cooler was modeled as RadFrac columns with equilibrium stages as this was not kinetic limited. The absorber was modeled as a rate based RadFrac column with CO_2 absorption reaction kinetics. The absorber was filled with Sulzer Mellapak 250Y packing and included two intercoolers to remove heat generated from the exothermic CO_2 absorption process and maintain column temperature. More details about CO_2 absorber modeling can be found in [19]. The main reactor was modeled as an adiabatic RStoic reactor in Aspen Plus based on experimental data detailed in previous publication [20]. The reactor pressure and conversion were set to 15 bar and 99% accordingly. A design specification was used to set the reactor outlet temperature set to 170 °C by varying the cold stream outlet temperature of the cross heat exchanger right before the reactor. The weighted hourly space velocity (WHSV) was set to 6.9 g CO_2/g catalyst/h, the same as what used in the experiment [20], for reactor sizing. Due to the lack of experimental data, the dehydration membrane unit was model as a component separator. Based on the existing membrane separation studies for liquid mixture [21, 22, 24], it was reasonable to assume that 15 bar pressure difference would be sufficient to remove 33% water in the inlet stream, and no additional pumping were required. The 33% water removal was a desired splitting ratio to maintain an optimal water loading of 4 wt% in the CO_2-lean solvent [19] before recycling back to the CO_2 absorber.

Conventional SC^{3}M Technologies. The process flow diagram of SNG production via the conventional SC^{3}M route are shown in **Figure 50**. A typical absorber-stripper configuration is used to capture CO_2 from flue gas using aqueous amine solvent, of which detailed description can be found in NETL's baseline performance report [23]. CO_2 from the carbon capture unit is compressed from 2 bar to 20 bar and then sent to the carbon conversion unit. In the conversion unit, SNG is produced from CO_2 at 20 bar and 175 °C via the well-known Sabatier reaction as shown in Equation (5). A H_2:CO_2 ratio higher than 4:1 is used for higher conversion, while membrane is used to separate unreacted H_2 from SNG product. Detailed process description can be found in the study of [25].

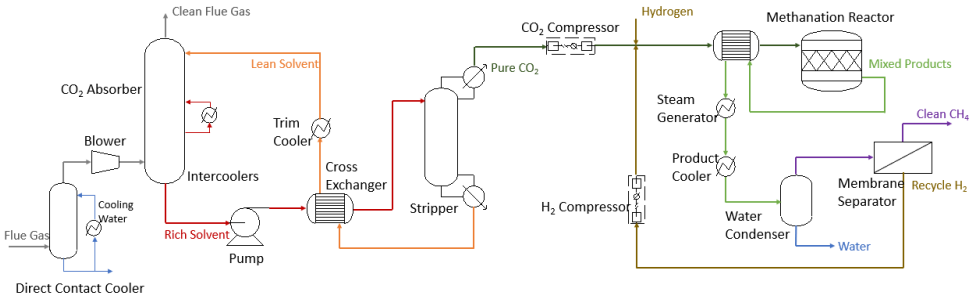


Figure 50. Process configuration of SNG production via conventional SC^{3}M route.

Table 37. Mass and energy balance of the conventional SC^{3}M cases based on literature data.

	SNG Production (per kg Methane)
H_2 (kg)	0.49
CO_2 (kg)	2.68
Electricity (kWh)	0.18
Methanation catalyst (kg)	1.2E-5
RWGS catalyst (kg)	0
Methanol synthesis catalyst (kg)	0

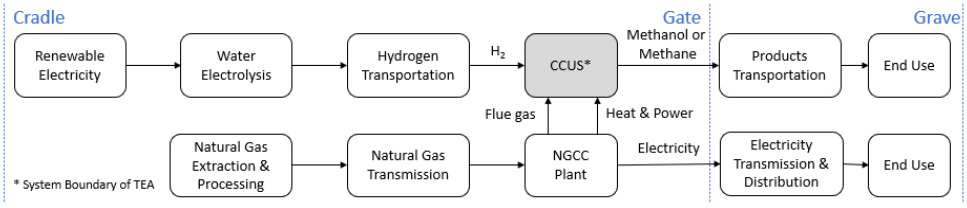


Figure 51. System boundary of TEA and LCA studies.

$$CO_2 + 4\,H_2 \;\leftrightarrow\; CH_4 + 2\,H_2O \quad (5)$$

Techno-economic Analysis. Annualized cost models were developed in Excel to evaluate the minimum product selling price (MPSP) using general economic assumptions listed in **Table 38**. For IC^{3}M cases, mass and energy balance data from the process models were used to calculate the variable cost, while stream information was used as inputs for equipment sizing. All standard equipment was sized and costed using Aspen Process Economic Analyzer V14, while the capital cost of special equipment, such as the PSA unit, was calculated from vendor cost or literature correlations. Eq. (6) was used to convert the equipment cost available via quote or literature for a given scale (S_0) and pricing base year (C_0) to the desired scale (S) and pricing base year, where sf, and chemical engineering plant cost index (CEPCI) are the scaling factor, and chemical engineering plant cost index, respectively. **Table 39** summarized the pricing data used for variable cost calculation, which are all in 2020 U.S. dollars. For commodity chemicals and utilities, pricing data came from PEP Yearbook [26], U.S. EIA database and literature [13]. For catalysts not fully commercialized, pricing data came from the open-source CatCost Tool [27].

$$C = C_0 \times (S/S_0)^{sf} \times (CEPCI/CEPCI_0) \quad (6)$$

Table 38. General economic assumptions.

Assumption	Value	Assumption	Value
Pricing base year	2020	CO_2 in flue gas (tonne/h)	224
Maintenance materials & labor (% of total fixed capital)	4	Taxes & insurance (%/y on total fixed capital)	2
Operating supplies & control lab (% of operating labor)	30	Depreciation (y)	10
Plant overhead (% of total labor cost)	80	General & Administrative, Sale (% of product value)	5
Rate of return (%/yr on total fixed capital)	15	45Q carbon credits ($/tonne CO_2)	60

Table 39. Pricing data in 2020 U.S. dollars.

	Value		Value
Hydrogen ($/kg)	1-4	Cooling water ($/MGal)	13
Ru/Al_2O_3 catalyst ($/kg)	275	Electricity (¢/kWh)	5.04
		Steam (¢/tonne)	860
		Wastewater treatment ($/m^3)	28
		EEMPA solvent ($/kg)	10
		Labor ($/h/operator)	46.8

Life-cycle Assessment. Environmental impact assessment was conducted in OpenLCA v1.11 using Environmental Protection Agency's (EPA) Tool for Reduction and Assessment of Chemicals and Other Environmental Impact (TRACI) 2.1 method for SNG production from CO_2 in NGCC flue gas via IC^{3}M. Impact categories including acidification potential, eutrophication potential, photochemical smog formation potential, ozone depletion potential, particulate matter formation potential and global warming potential (GWP) were evaluated with the cradle-to-gate system boundary presented in **Figure 51.** The results were also compared the conventional SC^{3}M route as the industrial baseline. Cradle-to-gate $CO_{2,eq}$ emission including downstream SNG transportation and combustion steps was also evaluated to quantify the life-cycle $CO_{2,eq}$ emission reduction against fossil baseline, assuming SNG is combusted as fuels at their end use stage. For simplification, one megajoule (MJ) of energy produced/combusted was selected as the functional unit for LCA. Lower heating value (LHV) was used to determine the energy density. GWP will be reported using the 100-year characterization factors with climate carbon feedback based on the default values from the Intergovernmental Panel on Climate Change (IPCC) Sixth Assessment Report (AR6) [28].

Table 40. List of unit processes used in LCA.

Unit Process	Database
Green Hydrogen Production (PME)	GREET 2022
Hydrogen Transportation	GREET 2022
Natural Gas Through Transmission – U.S. Mix	NETL CO2U LCI
NGCC Power Plant, no capture, cradle-to-gate – US-IL	NETL CO2U LCI
NGCC Power Plant, capture, cradle-to-gate – US-IL	NETL CO2U LCI
Renewable electricity mix - US	NETL CO2U LCI
Fuel Product Transportation	GREET 2022

The life cycle inventory (LCI) data of Mass and energy balance from either process models or literature described in the process modeling section informed the CO_{2eq} emission calculation. LCI of other key unit processes, listed in **Table 40**, were collected from CO2U and other LCI databases from NETL [29, 30], greenhouse gases, regulated emissions, and energy use in technologies (GREET) tool from Argonne National Laboratory (ANL) [31], both using U.S.-based background data. In both IC^{3}M and SC^{3}M cases, electricity was treated as co-products, of which the environmental impacts were allocated using the displacement approach, also called system expansion. The associated $CO_{2,eq}$ emission is credited with the load that would appear if produced from a conventional NGCC power plant without carbon capture.

1.1.2. Results and Discussion.

This section presents the key performance, economic and environmental measures of the IC^{3}M platform for methane production, and comprehensive comparisons with the conventional SC^{3}M route as well as fossil-based industrial practice. Detailed cost and emission breakdowns are provided to identify the key cost and emission drivers and potential research directions that can further improve IC^{3}M platform.

Carbon, Hydrogen, and Energy Efficiencies. The mass and energy balance of the CCUS unit for the IC^{3}M case generated from Aspen Plus process model and presented in **Table 41**. For methane production from IC^{3}M, only one case was evaluated, as relatively high conversion and product selectivity were achieved via experimental study [20]. Carbon, hydrogen, and energy efficiencies are shown in **Figure 52** for both IC^{3}M and SC^{3}M cases including both capture and conversion processes. The values were derived from mass and energy balance via Equations (7) to (9), where $\dot{F}$, P, LHV, η_{NGCC}, and $W_{eq,CCS}$ are mass flow rate, electric power, lower heating value, net plant efficiency of NGCC power plant (59.4% [23]), and equivalent work of capturing 90% CO_2 from NGCC power plant (50.2 kJ/mol CO_2 [23]), respectively. Note that the term $\dot{F}_{CO_2} \times W_{eq,CCS}/\eta_{NGCC}$ was only applied to the SC^{3}M cases. It is because in the SC^{3}M cases, carbon capture and conversion are two separated steps and, while the mass and energy balance data collected from literature only included the conversion step (**Table 37**). On the other hand, for the IC^{3}M cases, the mass

and energy balance shown in **Table 6** included both carbon capture and conversion, as they were fully integrated.

Table 41. Mass and energy balance of the CCUS unit for IC^{3}M cases derived from process models.

	SNG Production
Inputs	
H_2 (kg/h)	37,024
CO_2 in NGCC flue gas (kg/h)	224,986
Steam (GJ/h)	
Electricity (kW)	
Catalysts (kg/h)	18
Outputs	
Electricity (kW)	14,752
Methane (kg/h)	73,606
CO_2, emitted to air (kg/h)	21,748

$$C\% = \frac{\sum \dot{F}_{C\ in\ products}}{\dot{F}_{C\ in\ flue\ gas}} \quad (7)$$

$$H\% = \frac{\sum \dot{F}_{H\ in\ products}}{\dot{F}_{H_2}} \times 100\% \quad (8)$$

$$\eta_{LHV}\% = \frac{\sum \dot{F}_{product} \times LHV_{product} + P_{generated}/\eta_{NGCC}}{\dot{F}_{H_2} \times LHV_{H_2} + P_{consumed}/\eta_{NGCC} + \dot{F}_{CO_2} \times W_{eq,CCS}/\eta_{NGCC}} \times 100\% \quad (9)$$

Figure 52 suggested that IC^{3}M platform can produce SNG with carbon and hydrogen efficiency comparable to the conventional SC^{3}M platform, but with a higher energy efficiency (80.8% vs 75.6%). For both cases, the hydogen efficiency is about 49%, very close to the theoretical maximum 50%. According to Reaction (9), at the idea condition, only 50% of H_2 ends in SNG product, while the remaining goes to H_2O by-product. Similarly, for both cases, the carbon efficiency is around 88-89%, close to the designed

carbon capture rate of 90%, which means almost all captured CO_2 is converted to SNG. The energy efficiency of the IC^{3}M case is higher than that of the SC^{3}M case mainly because of (1) the absence of energy-intensive CO_2 compressor, and (2) the use of exothermic reaction to off-set energy required in stripper.

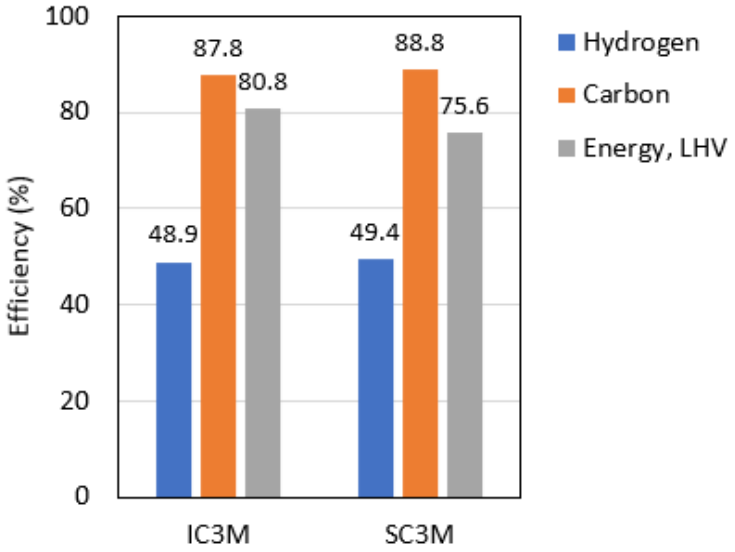


Figure 52. Carbon, hydrogen, and energy efficiencies for SNG production via CCUS processes.

Capital Costs. **Figure 53** presents the total plant cost of producing SNG via the IC^{3}M platform and comparisons with the conventional SC^{3}M routes. Here, the total plant cost of the IC^{3}M cases were estimated based on rigorous process model developed in this study and the approach detailed in the TEA section. The total plant cost of both SC^{3}M cases were obtained from existing literature. For a fair comparison, the original values were converted via Equation (6) to represent the design scale listed in Table 4 and 2020 pricing basis.

As shown in **Figure 53**, for SNG production, a capital cost reduction of 34% has been achieved by replacing the coventional SC^{3}M route with the IC^{3}M platform. Note that for SNG production, the IC^{3}M case was designed based on measured performance acheived at lab-scale experiment [20]. These findings further emphasize that upon achieving the R&D target, the IC^{3}M platform has the potential to significantly lower the capital cost of CCUS for a diverse range products.

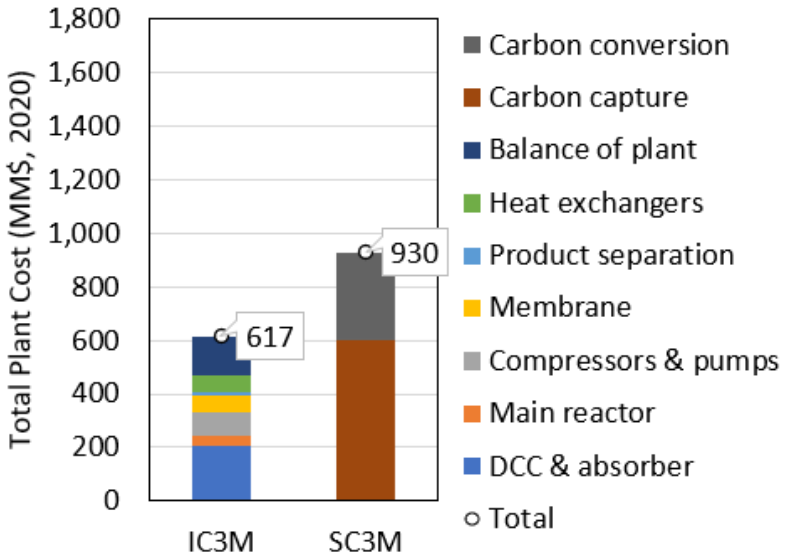


Figure 53. Comparison in total plant cost for SNG production between IC^{3}M and SC^{3}M cases.

Minimum Product Selling Price. The MPSP of SNG production were evaluated based on the approach detailed in the TEA section for both IC^{3}M and SC^{3}M routes and compared with the market prices of fossil-based natural gas. In addition, a sensitivity study was conducted to illustrate the impacts of H_2 price and carbon capture solvent loss/degradation rate on the economic feasibility of both CCUS applications, as H_2 is used as the key raw material and energy source for both CCUS applications. A H_2 price of \$4/kg represents the current SOT for green H_2 production via water electrolysis [32], while a H_2 price of \$1/kg represents the targeted cost of clean H_2 production by 2031 from U.S. Department of Energy's Hydrogen Shot program [33]. The solvent loss per day is defined based on the total solvent inventory of the IC^{3}M system including holdups in the absorber, reactors, piping and other operation units. In the baseline, the solvent loss per day was set to 0.03% of the total inventory, the same as what was observed in a typical solvent based carbon capture system [34]. However, the present of catalyst may accelerate solvent loss, and therefore a sensitivity study was conducted for a solvent loss per day up to 10%. Based on the experimental observation, a solvent loss rate greater than 10% per day is highly unlikely. Detailed cost breakdown and sensitivity study regarding H_2 price were illustrated in **Figure 54** for SNG production.

Figure 54 demonstrates that H_2 price has a significant impact on the MPSP of SNG produced from either IC^{3}M or SC^{3}M platform. However, the catalyst cost has minor impacts. This is mainly because a high single-pass CO_2 conversion has already been demonstrated experimental at a high WHSV, as discussed in the methane production via IC^{3}M section. As the catalyst performance of IC^{3}M platform for SNG production has already been optimized experimentally, only one case was explored in this work, which gives an estimated MPSP 5% lower than the SC^{3}M case when H_2 available at \$4/kg, and

13% lower when H_2 available at \$1/kg. The potential cost saving brought by IC^{3}M platform is not as significant as methanol application, mainly because of the higher H_2 consumption of the SNG application. Additionally, a sensitivity study was conducted to evaluate the impact of solvent loss rate and price on the economic performance of IC^{3}M technologies (**Figure 55**). Here, the solvent loss or degradation rate is defined as present of total solvent inventory in the system per day and ranges from 0 to 10% inventory/day. The solvent price ranges from \$3/kg (i.e., representing first generation aqueous amine) to \$10/kg (the target production cost of EEMPA at scale). The results suggest that when IC^{3}M platform is used, the MPSP of methanol production is more sensitive to solvent price and loss rate than that of SNG production. This is mainly because a lower WHSV is required for methanol production, resulting in a higher solvent inventory. For methanol production via IC^{3}M, the impact of solvent loss rate can be minimized if using a solvent less expensive than EEMPA.

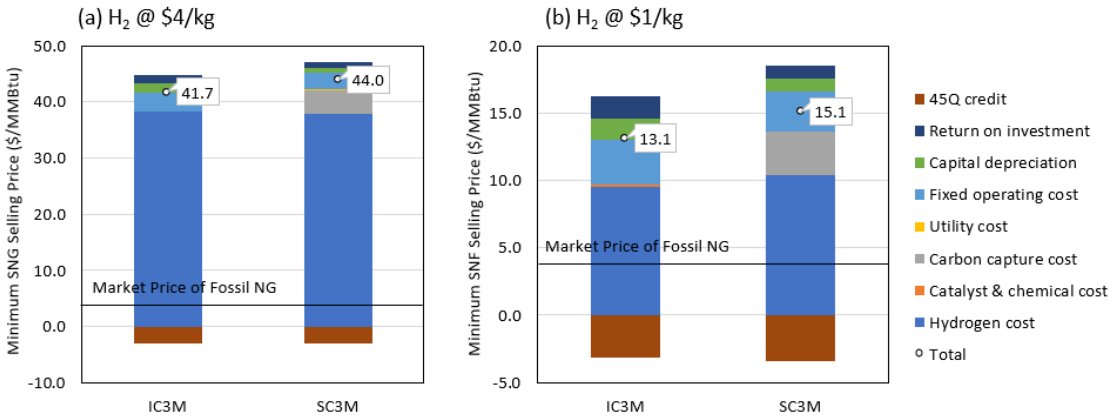


Figure 54. Estimated minimum SNG selling price at different H_2 prices.

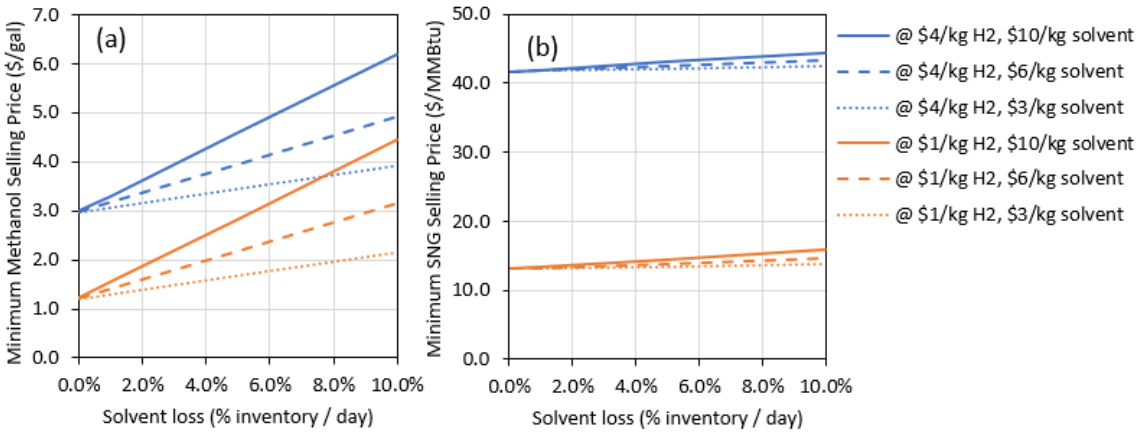


Figure 55. Impacts of solvent loss/degradation and price on estimated minimum selling price.

Cradle-to-gate Life-cycle Environmental Impacts and Cradle-to-grave CO_2,eq Emissions. The cradle-to-gate life-cycle environmental impacts of two CO_2-to-SNG cases are presented in **Table 42**. For methane production, the IC^{3}M case has less environmental

impacts than SC^{3}M case on global warming, acidification, eutrophication, smog formation and respiratory effects categories mainly due to the higher energy efficiency, but comparable impacts on ozone depletion due to the similar H_2 consumption per MJ SNG generated.

A cradle-to-grave system boundary was used to evaluate the life-cycle $CO_{2,eq}$ emission reduction compared to fossil fuels. **Figure 56** suggests a cradle-to-grave $CO_{2,eq}$ emission reduction of 80.8% and 63.5% of SNG produced from IC^{3}M and SC^{3}M approach, respectively, when compared with fossil-based natural gas. The $CO_{2,eq}$ emission of the IC^{3}M case is 47% lower than that of SC^{3}M case, mainly because of the lower energy consumption and higher energy efficiency.

Table 42. Cradle-to-gate LCA impacts (SNG generated).

	SNG	
	IC^{3}M	SC^{3}M
Ozone depletion (kg CFC-11$_{eq}$)	4.47E-12	4.42E-12
Global Warming (kg CO_{2eq})	-4.11E-02	-2.85E-02
Acidification (kg SO_{2eq})	8.71E-05	9.68E-05
Eutrophication (kg N_{eq})	4.04E-06	4.73E-06
Smog Formation (kg O_{3eq})	2.05E-03	2.28E-03
Respiratory effects (kg PM2.5$_{eq}$)	7.28E+06	7.34E-06

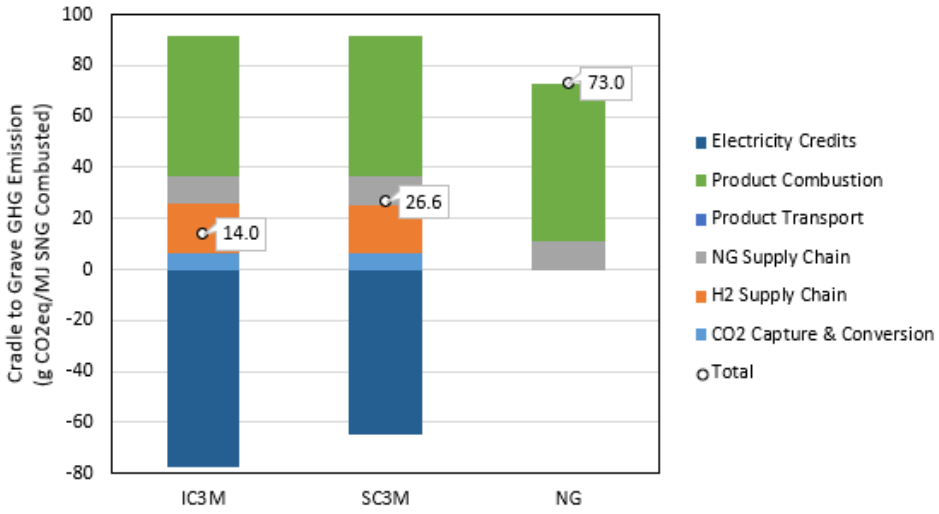


Figure 56. Cradle-to-grave $CO_{2,eq}$ emission of SNG/natural gas cases.

XX. Q2 FY25 Milestone: (B) [T4] Demonstrate if catalyst can achieve at least 10% CO2 conversion with >70% selectivity to ethanol in the gas phase.* [T4] Determine if catalyst can achieve at least 10% CO2 conversion with >20% selectivity to ethanol in the liquid

phase.* Decision point [T4]: if unable to achieve both criteria we will down select ethanol and redirect this scope to assist with methanol [T1]

During this budget period, activities are mainly focused on meeting the milestone for gas phase CO_2 conversion to ethanol using the double tandem system.

1.1 The double tandem approach

Building on the promising results of Rh-Fe/SiO_2 for CO_2 hydrogenation, and recognizing its superior ethanol selectivity for CO hydrogenation, a new tandem system approach is investigated to bridge two catalyst systems for highly selective CO_2-to-ethanol conversion. This two-step approach involves first converting CO_2 to CO using a reverse water-gas shift (RWGS) catalyst, followed by the hydrogenation of CO to ethanol over Rh-Fe/SiO_2 (**Figure 57**). The RWGS reaction is described as:

$$CO_2 + H_2 \rightarrow CO + H_2O$$

And the subsequent CO hydrogenation to ethanol:

$$2CO + 4H_2 \rightarrow C_2H_5OH + H_2O$$

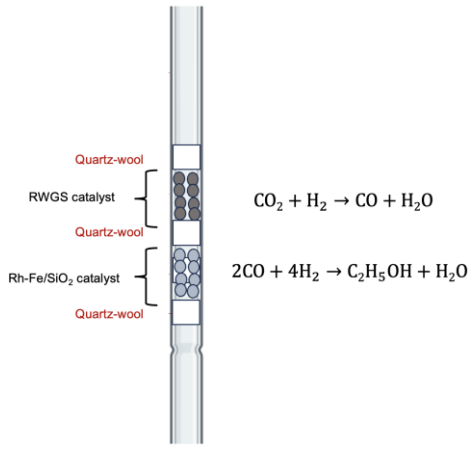


Figure 57. Schematic of double tandem approach system in the reactor tube.

1.2 Evaluation of Pt/CeO_2 as RWGS catalyst

Pt/CeO_2 is selected as the first catalyst for RWGS reaction according to a previous publication[35]. This catalyst is synthesized and evaluated firstly using reported conditions and the results are shown in **Figure 58**. As expected, high CO selectivity is achieved at 210 ^oC, with only methanol as a major byproduct. In the beginning, this catalyst provides 12% CO_2 conversion and >97% CO selectivity, but this excellent performance is not maintained for a long time. A fast deactivation is observed, and CO_2 conversion is stabilized at ~6% with 90% CO selectivity. Higher temperature leads to the formation of CH_4, which can no longer be converted to ethanol based on the current reaction conditions. Also, lower temperatures are required thermodynamically for alcohol production from CO_2 (much

higher selectivity to CO and CH_4 is predicted by thermodynamics and confirmed by our results and many other reports). Therefore, the following exploration adopts 210 °C as the reaction temperature.

For the double tandem system, two catalysts are typically working together in one reactor. Therefore, it is critical to explore the compatibility of the two catalysts in simple operation processes. With this consideration, the evaluation conditions of the first catalyst are adjusted to better accommodate the second catalyst in our system. Specifically, the calcination temperature of Pt/CeO_2 is enhanced to 400 °C to avoid possible incomplete calcination and cross-contamination of the two catalysts. Meanwhile, the activation temperature is also enhanced to 370 °C so that two catalysts can be activated simultaneously without the need to create different temperature zones in one reactor. The evaluation of Pt/CeO_2 for RWGS under modulated conditions is given in **Figure 59**. Compared to the original operation in **Figure 58**, no significant difference in CO_2 conversion is observed. Interestingly, although CO selectivity slightly decreases from 90% to 75%, ethanol is observed as a main byproduct. It can be beneficial for the overall performance of the double tandem system since the ethanol produced here also contributes to the final ethanol selectivity. With increased time on stream, the ethanol selectivity gradually decreases, while CO begins to reappear. In general, this additional test ensures that the first catalyst demonstrates good compatibility with the double tandem approach.

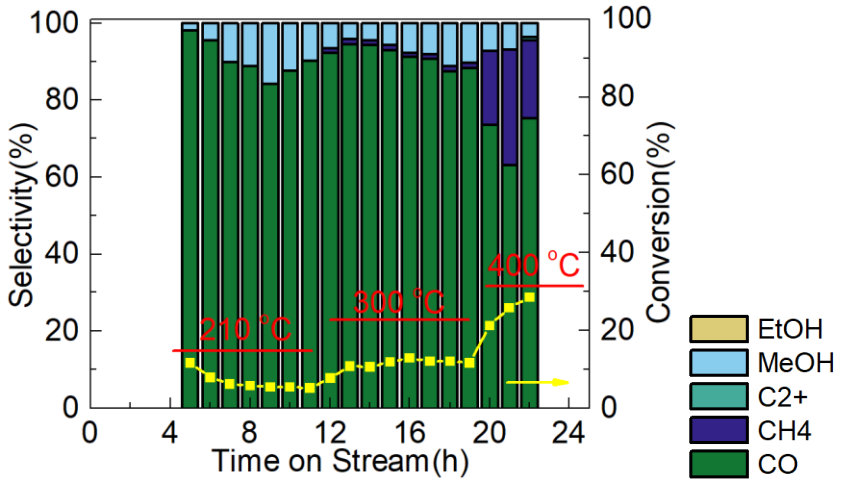


Figure 58. Performance of Pt/CeO_2 for RWGS reaction. Catalyst calcination: 290 °C, air, 2 h. Activation: 300 °C, 10 sccm H_2, 1 h. Reaction conditions: flow reactor, 0.2 g catalyst diluted by 1 g SiC, pressure 30 bar, H_2:CO_2=3:1, GHSV=6000 mL $gcat^{-1}$ h^{-1}.

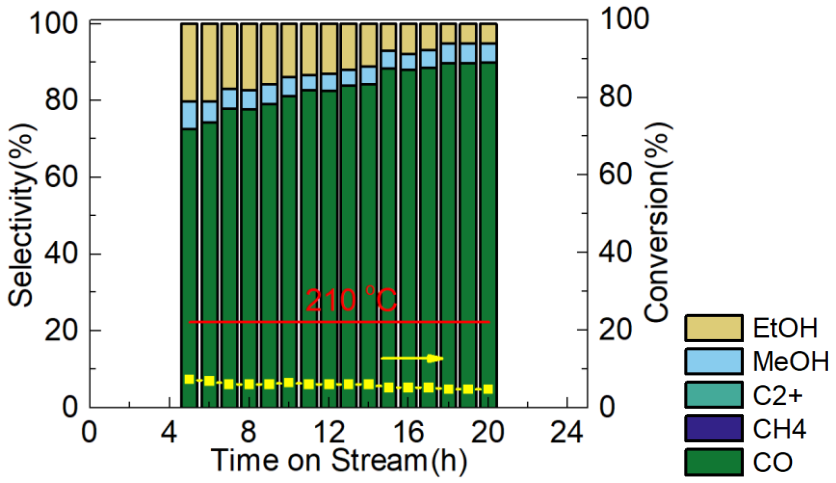


Figure 59. Performance of Pt/CeO_2 for RWGS reaction with adjusted processes. Catalyst calcination: 400 °C, air, 6 h. Activation: 370 °C, 10 sccm H_2, 1 h. Reaction conditions: flow reactor, 0.2 g catalyst diluted by 1 g SiC, pressure 30 bar, H_2:CO_2=3:1, GHSV=6000 mL $gcat^{-1}$ h^{-1}.

1.3 Optimization of $RhFe/SiO_2$ for CO to ethanol

To achieve higher ethanol selectivity and meet the milestone target, the CO hydrogenation reaction conditions of the second catalyst $RhFe/SiO_2$, which is the key catalyst for ethanol production, are modulated as follows.

Firstly, the H_2:CO ratio is tuned and results are shown in **Figure 60**. It is observed that a higher H_2:CO ratio (4:1) favors CH_3OH synthesis, while a lower H_2:CO ratio (1:1) facilitates C_{2+} production. For ethanol selectivity, the effect of the H_2:CO ratio is marginal. Hence, the stoichiometric ratio (2:1) still seems to be the optimal value and is maintained in the following explorations.

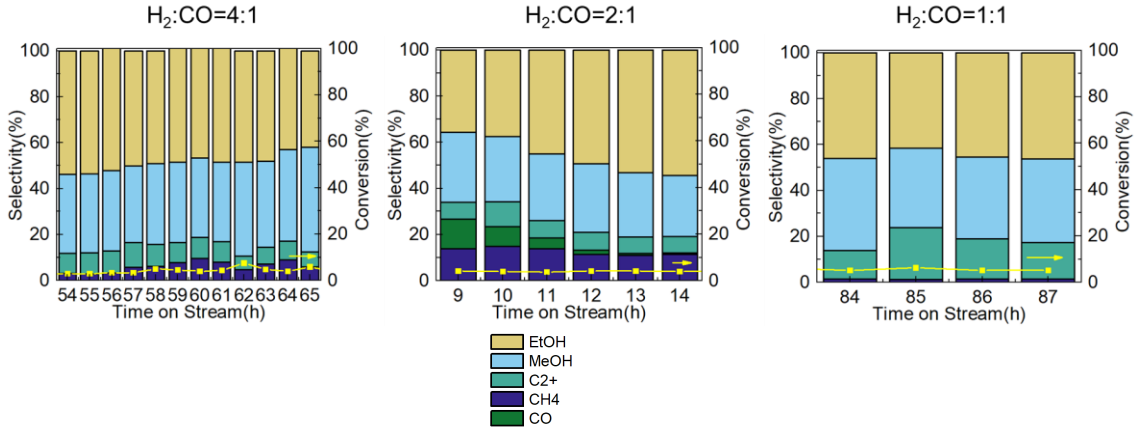


Figure 60. Performance of $RhFe/SiO_2$ for CO hydrogenation with different H_2:CO ratios. Reaction conditions: flow reactor, 0.2 g catalyst diluted by 1 g SiC, pressure 30 bar, GHSV 4500 mL $gcat^{-1}$ h^{-1}, activation under temperature 320 °C, H_2 10 sccm for 30 min.

The catalyst is also evaluated with different gas hourly space velocity (GHSV) as shown in **Figure 61**. Higher GHSV favors ethanol selectivity, at a cost of CO conversion. 65% ethanol selectivity and 27% methanol selectivity are achieved at 9000 mL $gcat^{-1}$ h^{-1} with ~2% CO conversion. With lower GHSV, the CO conversion increases to more than 10%, but the ethanol (also methanol) selectivity drops significantly with an obvious increase in methane production. Since the main target of the project is to demonstrate catalyst systems with highly selective ethanol production, a suitable GHSV must be carefully selected as a trade-off between conversion and selectivity.

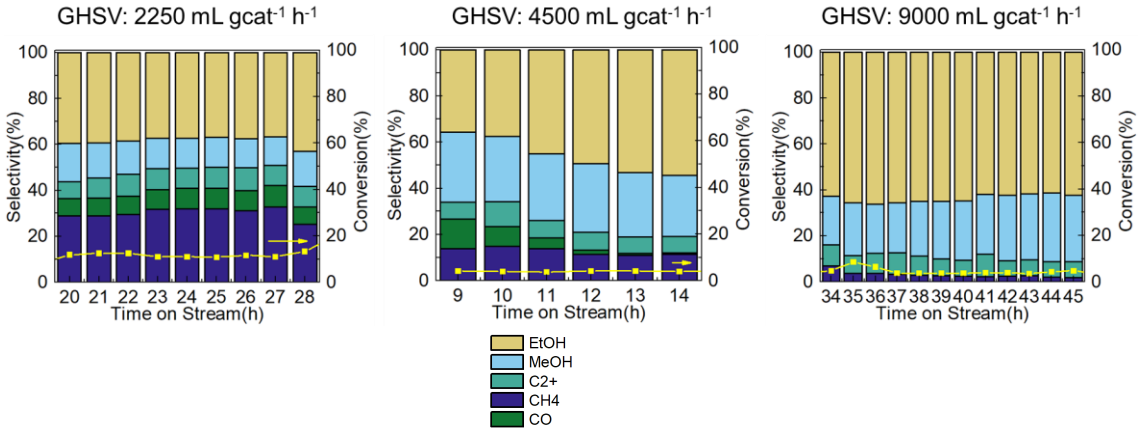


Figure 61. Performance of $RhFe/SiO_2$ for CO hydrogenation with different GHSV. Reaction conditions: flow reactor, 0.2 g catalyst diluted by 1 g SiC, pressure 30 bar, CO:H_2=3:1, activation under temperature 320 °C, H_2 10 sccm for 30 min.

Then, the effect of activation temperature is also investigated with results listed in **Figure 62**. Increasing activation temperature helps to enhance ethanol selectivity. As a result, 70% ethanol and ~30% methanol are produced, with only 1% selectivity to methane. Clearly, with all the optimizations, this catalyst system is tuned to be extremely highly selective for ethanol-rich alcohol production. It should be noted that the CO conversion is lowered to 2%, which still needs to be enhanced to meet the milestone target.

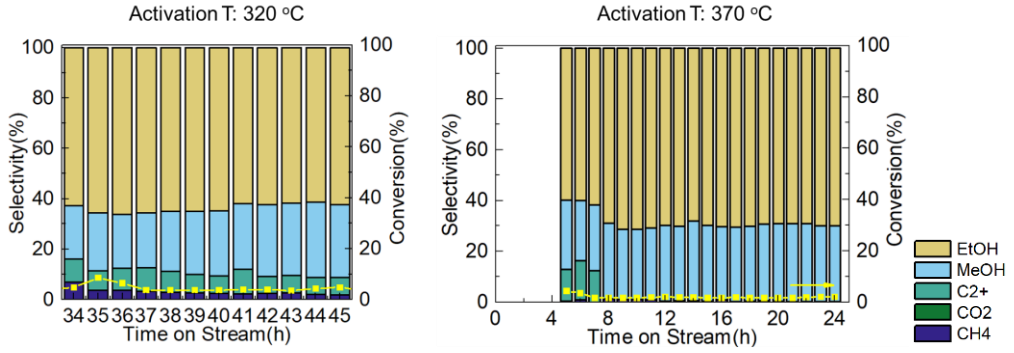


Figure 62. Performance of $RhFe/SiO_2$ for CO hydrogenation with different activation temperatures. Reaction conditions: flow reactor, 0.2 g catalyst diluted by 1 g SiC, pressure 30 bar, GHSV=9000 mL $gcat^{-1}$ h^{-1}, $CO:H_2$=3:1, activation under temperature 320 °C, H_2 10 sccm for 30 min.

1.4 Integration of two catalysts and optimization of double tandem system

Finally, two catalysts are integrated into one reactor with a simple activation and reaction process. Two configurations including the double tandem (two catalyst beds are separated and laid consecutively) and mixed catalysts (two catalysts are physically mixed in one single bed) are both evaluated. The results are given in **Figure 63**. Both configurations lead to promising results. The double tandem configuration provides 6% CO_2 conversion, 54% ethanol, and 32% methanol on average. In contrast, mixed catalyst configuration gives 5% CO_2 conversion, 40% ethanol, and 52% methanol on average. In comparison, the double tandem system appears to exhibit higher ethanol selectivity and ensures an ethanol-rich final product. Consequently, it is maintained as anticipated for further exploration.

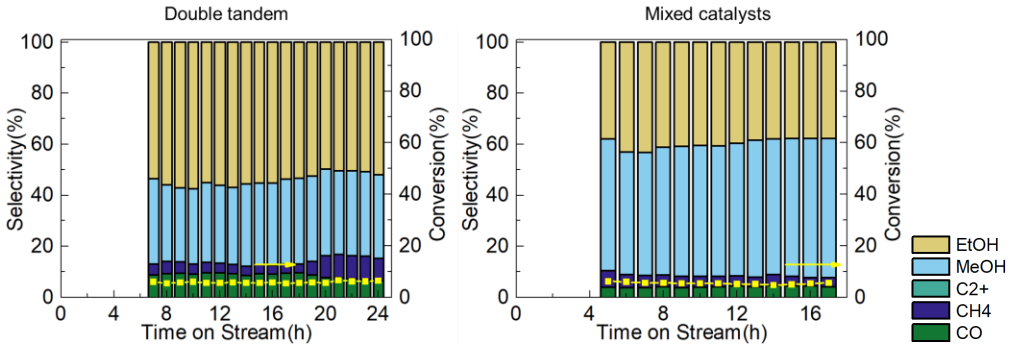


Figure 63. Performance of double tandem and mixed catalyst configurations for CO_2 hydrogenation. Reaction conditions: flow reactor, each 0.2 g catalyst diluted by 1 g SiC, temperature 210 °C, pressure 30 bar, $H_2:CO_2$=3:1, GHSV=6000 mL $gcat^{-1}$ h^{-1} (to each catalyst).

The reaction conditions are further fine-tuned to meet the milestone target. As shown in **Figure 64**, lower GHSV is used to facilitate CO_2 conversion (left vs middle). As a result, 10% CO_2 conversion is achieved without significant compromise of ethanol selectivity. On average, 11% CO_2 conversion with 45% ethanol and 37% methanol selectivity under favorable conditions. These results suit well with the milestone target of realizing 10% CO_2 conversion with >70% selectivity to ethanol-rich alcohol production. Additional exploration is performed with a slightly higher temperature of 230 °C (right one in **Figure 64**). Although CO_2 conversion is slightly enhanced, alcohol selectivity decreases significantly along with higher methane production, which is not favorable for the main target.

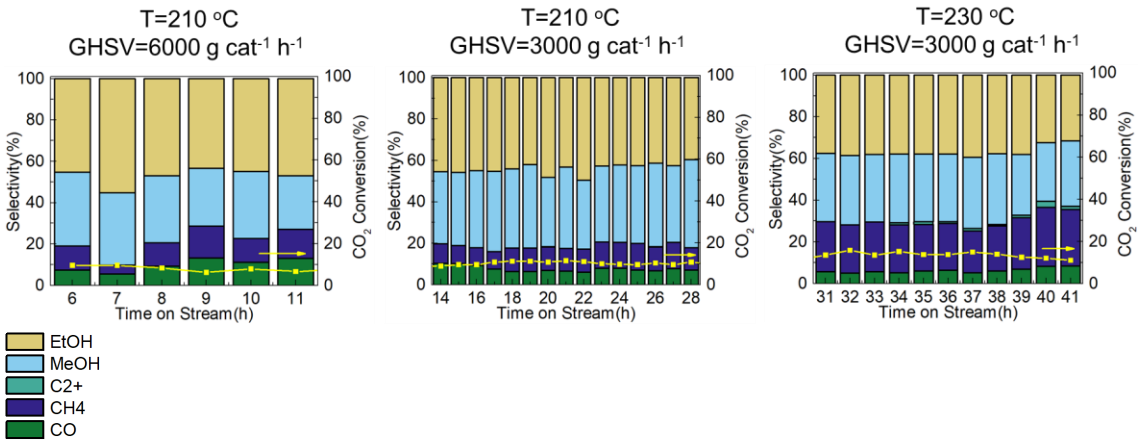


Figure 64. Performance of double tandem configurations for CO_2 hydrogenation with different reaction conditions. Similar reaction conditions for all runs: flow reactor, each 0.2 g catalyst diluted by 1 g SiC, pressure 30 bar, H_2:CO_2=3:1.

In summary, after careful catalyst design and process optimization, **the double tandem system successfully meets the milestone target, achieving an 11% CO_2 conversion with 82% ethanol-rich alcohols as the products.**

1.5. Condensed phase conversion of captured CO_2 to ethanol

Here, the conversion of captured CO_2 into ethanol was assessed using Pt/CeO_2 in condensed phase testing of catalysts. The primary goal was to enhance CO formation, which would then be integrated with RhFe/SiO_2 for CO hydrogenation to ethanol. However, the results with Pt/CeO_2 indicated challenges that affected the initial testing plans for further catalysis stages.

The Pt/CeO_2 catalyst achieved a conversion rate of 4.8% with high selectivity towards CO at 81.4%, at a space velocity of 0.15 gCO_2/gCat/h (**Table 43**). By further reducing the space velocity to 0.15 gCO_2/gCat/h, the conversion increased to 21.2%, but CO selectivity decreased to 34.9%. Additionally, methanol and methane were produced, with selectivities of 42.2% and 22.9%, respectively.

A significant observation was the noticeable degradation of the solvent EEMPA during the process with Pt/CeO_2. Although some ethanol was formed, it is believed that the degradation of EEMPA, rather than CO_2, may have been responsible for this ethanol formation. Consequently, due to this solvent degradation issue, further planned testing with RhFe/SiO_2 for dual-bed catalysis was not carried out this quarter.

Table 43. Hydrogenation of captured CO_2 in a continuous-flow reactor system.

Entry	Catalysts	Space Velocity (gCO_2/gCat/h)	CO_2 Conv. (%)	CH_3OH Sel. (%)	CH_4 Sel. (%)	CO Sel. (%)

1	Pt/CeO_2	**0.15**	4.8	0.0	18.6	81.4
2	Pt/CeO_2	**0.015**	21.2	42.2	22.9	34.9

Reaction conditions: 1g of catalyst, pressure: 860psi, 33.8 sccm H_2, 5 sccm N_2, 5%w CO_2 loaded 2-EEMPA solvent, space velocity change is achieved by adjusting the flow of CO_2-loaded 2-EEMPA solvent.

XXI. Single Step Simultaneous Production of Methanol and Glycol from Epoxide, CO_2 and H_2 Using Heterogeneous Cu-based Catalysts (Q2 FY25)

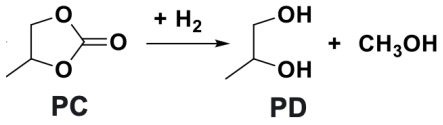
In our previous studies, we demonstrated that the sequential coproduction of methanol and glycol was facilitated when produced from epoxide, CO_2, and H_2 via cyclic carbonate.[36] For the synthesis of cyclic carbonate from epoxide, CO_2, and H_2, amine-based catalysts were identified as suitable. Various amines were tested to promote cyclic carbonate formation, with polyethyleneimine (PEI) achieving a cyclic carbonate yield of over 95% in THF solvent. For the subsequent step, i.e., the hydrogenation of cyclic carbonate to ethylene glycol, we used a homogeneous Ru-based catalyst. To improve the catalyst's productivity, selectivity, separation, reuse, and potentially stability, a heterogeneous catalytic system was evaluated for the coproduction of methanol and propylene glycol from propylene oxide (PO), CO_2, and H_2 in one pot. Recent literature has reported Cu-based catalysts for the hydrogenation of cyclic carbonate to methanol and glycol.[37] Prior to assessing the feasibility of producing methanol and glycol in a single step directly from PO, CO_2, and H_2, we initially examined the performance of similar Cu-based catalysts under our testing conditions for the hydrogenation of cyclic carbonate, as the single-step process is also expected to proceed via a cyclic carbonate intermediate. The results are shown in **Table 44**.

The commonly used methanol synthesis catalyst, $Cu/ZnO/Al_2O_3$ produced methanol at only 16.8% selectivity (**Table 44**, entry 1). This low selectivity was mainly due to the formation of other C_1 products, such as CO and CO_2, resulting from the decarbonylation and decarboxylation of propylene carbonate (PC). The selectivity for propanediol (PD) was also low, around 52%, with side products such as propane, propanol, and bis(2-hydroxypropyl) ether forming. However, the use of a silica support (prepared by ammonia evaporation hydrothermal (AEH) method) significantly improved selectivity towards the desired products, methanol and PD, which were formed at 78.3% and 93.4% selectivities, respectively (**Table 44**, entry 2).

When Cu/silica synthesized by the sol-gel (SG) method was used, methanol selectivity slightly reduced to 68%, with a modest improvement in PD selectivity. This is in agreement with prior work[38] where silica-based supports were identified as the preferred choice for Cu-based catalysts in the hydrogenation of cyclic carbonates due to their intermediate acidic and basic sites. Excessive acidic or basic sites were identified to promote the formation of side products through decarbonylation or decarboxylation of the carbonate.[38]

To assess the impact of reaction time on product selectivities, we reduced the reaction time from the standard 15 hours to 7 hours. (**Table 44**, entry 4) Although PC conversion remained high (>99%), methanol selectivity further decreased to 58%, with a corresponding increase in CO and CO_2 selectivities. This suggests that longer reaction times likely facilitate the conversion of CO and CO_2 (byproducts) to the desired product, methanol.

Table 44. Cyclic carbonate hydrogenation to coproduce methanol and glycol.



Entry	Catalysts	PC Conv. (%)	C_1 Selectivities (%)			PD Sel. (%) [a]
			CH_3OH Sel. (%)	CO Sel. (%)	CO_2 Sel. (%)	
1	$Cu/ZnO/Al_2O_3$	88	16.8	23.1	60.1	52
2	Cu/SiO_2-AEH	>99	78.3	6.1	15.7	93.4
3	Cu/SiO_2-SG	>99	68.5	11.7	19.8	98.5
4	Cu/SiO_2-SG[b]	>99	57.8	15.0	27.2	99.3

Propylene carbonate (PC) = 20 mmol, Catalyst=200 mg, H_2=45 bar, 170 °C, t=15h, THF=5mL, [a] The formation of side products, including propane, propanol, and bis(2-hydroxypropyl) ether, accounts for the reduced selectivity of PD (propanediol). [b]t=7h.

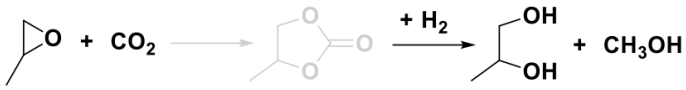
The best-performing catalyst (Cu/SiO_2-AEH) identified from **Table 44** for cyclic carbonate hydrogenation was tested for the single-step coproduction of glycol and methanol from PO, CO_2, and H_2. As expected, the selectivities for both methanol and PD (propanediol) were low, ~20%. The low methanol selectivity was due to CO formation, while the low PD selectivity was attributed to hydrogenation and dehydration products such as propanol, propane, and bis(2-hydroxypropyl) ether.

Subsequently, PEI was added as a co-catalyst to facilitate the formation of the cyclic carbonate intermediate. This addition improved PD selectivity to around 33% but suppressed CO_2 conversion (**Table 45**, entry 2). The $Cu/ZnO/Al_2O_3$ catalyst enhanced the selectivities of both methanol and PD to 43% and 28.5%, respectively (**Table 45**, entry 3). On the other hand, $Cu/ZnO/SiO_2$ was not active for methanol production, and no detectable amount of C_1 products was identified. The selectivity for PD was low due to the formation of side products.

Doubling the $Cu/ZnO/Al_2O_3$ catalyst loading significantly improved both methanol and PD selectivities to 78.4% and 42%, respectively (**Table 45**, entry 4). Next, the productivity for

CO_2 hydrogenation to methanol was studied under the same reaction conditions (170°C) in the absence of propylene oxide. The CO_2 conversion was 3.7%, and the methanol selectivity was 52.5% (**Table 45**, entry 6). Under the same reaction conditions, with the presence of propylene oxide, CO_2 conversion increased to 21.4%, and methanol selectivity improved to 78.4%. Thus, the coproduction approach significantly improved methanol productivity by more than five-fold (**Figure 65**)

Table 45. Single-step Coproduction of Methanol and Glycol from PO, CO_2 and H_2.



Entry	Catalysts	CO_2 Conv. (%)	PO: CO_2	C_1 Selectivities (%)		PD Sel.[a] (%)
				CH_3OH	CO	
1	Cu/SiO_2-AEH	19.8	1:3	22.5	77.5	17.6
2	Cu/SiO_2-AEH + PEI[c]	0.8	1:3	59.3	40.7	33.5
3	$Cu/ZnO/Al_2O_3$	25.6	1:3	43.0	57.0	28.5
4	$Cu/ZnO/SiO_2$	0	1:3	0	0	17.2
5	$Cu/ZnO/Al_2O_3$[b]	21.4	1:3	78.4	21.6	42.0
6	$Cu/ZnO/Al_2O_3$[b]	3.7	0:3	52.5	47.5	0
7	$Cu/ZnO/Al_2O_3$[b] + PEI[c]	12.9	1:3	31.8	68.2	86.7
8[d]	$Cu/ZnO/Al_2O_3$[b] + PEI[c]	25.7	1:2	55.5	44.5	84.6
9[d][e]	$Cu/ZnO/Al_2O_3$[b] + PEI[c]	16.8	1:2	54	46	79.5

PO = 20 mmol, Catalyst=200 mg, H_2=45 bar, 170 °C, t=15h, THF=5mL, PO conversion >99% in all the cases, [a]the formation of side products, including propane, propanol, and bis(2-hydroxypropyl) ether, accounts for the reduced selectivity of PD (propanediol), [b]400mg, [c]100mg, [d] H_2=60 bar, [e]7h.

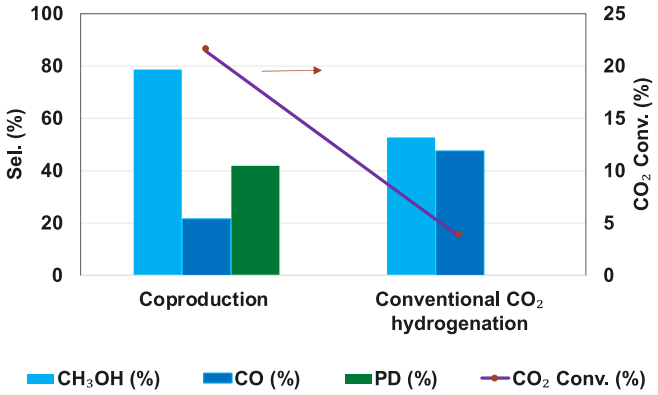


Figure 65. Comparison of conventional CO_2 hydrogenation (Entry 6, Table 9) and coproduction (Entry 5, Table 9) approaches.

Interestingly, with the addition of PEI (**Table 45**, entry 7), the PD selectivity soared from 42% (in the absence of PEI) to 86.7%. However, methanol selectivity dropped from 78.4% in the absence of PEI to 31.8% with the addition of PEI. Thus, the addition of PEI positively influenced PD formation, likely by facilitating the cyclic carbonate intermediate formation. However, methanol selectivity reduced, possibly because, as shown in **Table 44**, entry 1, $Cu/ZnO/Al_2O_3$ likely facilitated the decarbonylation and decarboxylation of the cyclic carbonate instead of methanol formation. With an increase in the PO:CO_2 ratio from 1:3 to 1:2 and increased hydrogen pressure, both methanol and PD selectivities improved to 55.5% and 84.6%, respectively (**Table 45**, entry 7 vs 8). Next, with the reduction in reaction time from 15 hours to 7 hours (**Table 45,** entry 8 vs 9), the selectivity for methanol decreased due to the increased concentration of CO. This suggests that the reaction is likely proceeding via a CO intermediate, with CO forming from both the reverse water-gas shift (RWS) reaction and cyclic carbonate decarbonylation.

Given that the addition of the co-catalyst (PEI) significantly influenced both methanol and PD selectivity, we next varied the PEI content, and the results are shown in **Figure 66**. The CO_2 conversion exhibited a volcano-like trend. The CO_2 conversion increased from 25.7% to 36.8% with a reduction in PEI content from 100 mg to 50 mg. Selectivity of over 75% for both PD and methanol was achieved using 50 mg of PEI, demonstrating the feasibility of the coproduction concept.

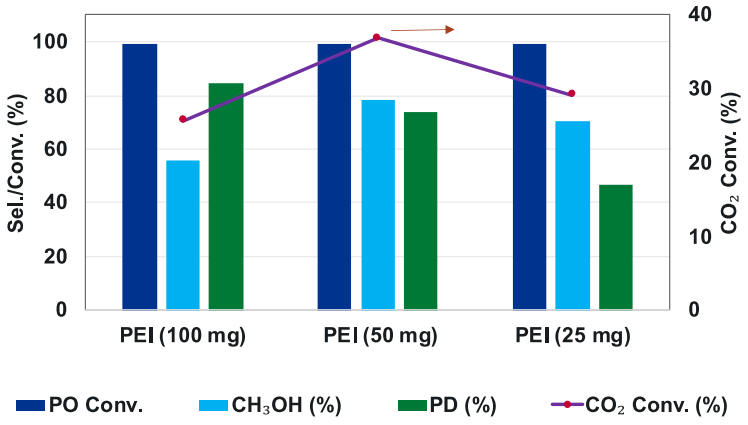


Figure 66. Effect of PEI content on CO_2 conversion and product selectivity. Propylene oxide (PO)=20 mmol, Catalyst=200 mg, H_2=60 bar, 170 °C, t=15h, THF=4.5mL, PO conversion >99% in all the cases.

XXII. Milestone (FY25 Q3): Using the knowledge obtained from previous milestones/tasks, select capture solvent/catalyst/conditions to achieve single pass conversion of at least >50% and selectivity >90% to methanol in a continuous flow system

To meet this quarter's milestone (FY25 Q3) of achieving over 50% single-pass conversion of captured CO_2, our efforts were focused on enhancing the hydrogenation rate and selectivity of CO_2 to methanol in the condensed phase. A systematic evaluation of catalyst performance was undertaken, assessing CO_2 conversion and methanol selectivity at varying space velocities (SV). As the CO_2 source, we utilized a model feed of CO_2 captured in EEMPA with a 5 wt% loading, mimicking typical carbon capture operating conditions. The subsequent hydrogenation experiments using various catalysts are summarized in **Table 2**.

Catalyst Performance in Previous Quarters

In previous experiments, Pt/ZrO_2 exhibited outstanding methanol selectivity, achieving close to 100%, but with a relatively low CO_2 conversion of 33% compared to Pt/TiO_2 and Pt/MoO_3 catalysts. The exceptional selectivity of Pt/ZrO_2 towards methanol is attributed to its high density of strong basic sites, which reduce methanol adsorption and effectively suppress the formation of undesired methane byproducts. Methanol temperature-programmed desorption (TPD) experiments (**Figure 67**) supported this explanation, revealing that Pt/ZrO_2 binds methanol more weakly than Pt/MoO_3 and Pt/TiO_2. This weak binding allows methanol to desorb selectively before further hydrogenation to methane occurs, thereby favoring its accumulation as the primary product.

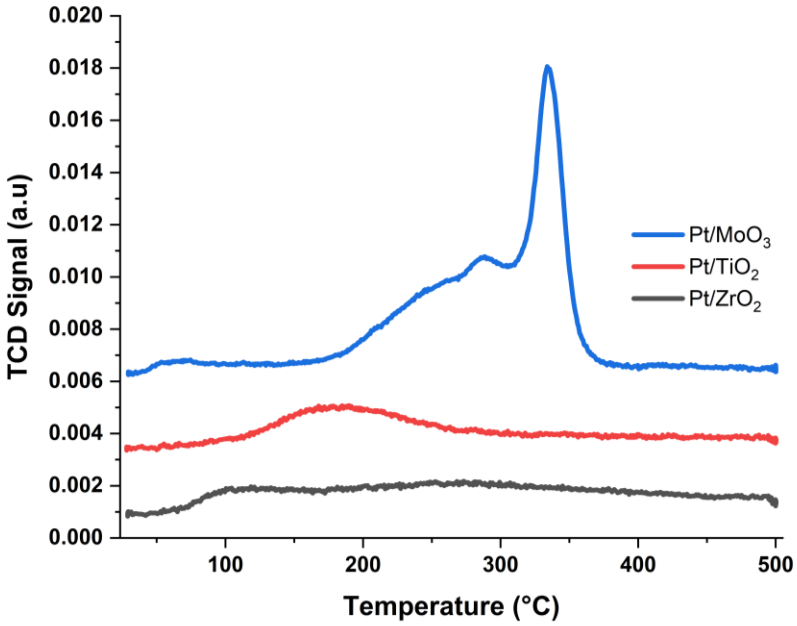


Figure 67. Methanol-TPD of the calcinated post synthesis catalysts**.**

Conversely, Pt/TiO_2 and Pt/MoO_3 achieved significantly higher CO_2 conversions, ~77%, but at the cost of reduced methanol selectivity. Both catalysts generated product mixtures consisting of ~60% methanol and ~40% methane, indicating less effective suppression of undesired side reactions. Notably, Pt/ZrO_2 and Pt/MoO_3 demonstrated excellent catalytic stability over 100 hours of continuous operation. Additionally, Pt/MoO_3 exhibited superior solvent durability due to its inert surface, which lacks acidic or strongly basic sites that might otherwise degrade the EEMPA solvent over time.

Catalyst Modification to Boost Methanol Selectivity

To enhance methanol selectivity while maintaining high CO_2 conversion efficiency, the Pt/MoO_3 catalyst was selected for further optimization, given its robust productivity and stability. Basic additives (MgO, ZrO_2, ZnO, CeO_2) were incorporated into the Pt/MoO_3 system to suppress methanol adsorption and mitigate methane formation. The influence of these additives on CO_2 conversion and product selectivity was studied under varying space velocities, with key findings detailed in **Table 46**.

The addition of 5 wt% MgO to Pt/MoO_3 (Entries 3 and 4) resulted in minimal CO_2 conversion, with values as low as 0.9% and 1.8% at space velocities of 0.15 $gCO_2/gCat/h$ and 0.015 $gCO_2/gCat/h$, respectively. This significant drop suggests that MgO disrupted the interaction between Pt and MoO_3, potentially poisoning the interface or altering synergetic active sites.

Similarly, the incorporation of 5 wt% ZrO_2 (Entries 5 and 6) showed mixed results. At higher space velocity (0.15 $gCO_2/gCat/h$), CO_2 conversion dropped to 20.8% with methanol selectivity of only 21.1%. At lower space velocity (0.015 $gCO_2/gCat/h$), CO_2 conversion increased to 73.9%, but methanol selectivity remained moderate at 46.1%. Additionally, methane formation (47.4%) and CO production (6.4%) were higher than the baseline Pt/MoO_3 catalyst, indicating inefficiencies in suppressing byproducts.

With the 5 wt% ZnO-modified Pt/MoO_3 composition (Entries 7 and 8), an intriguing trend emerged. Methanol selectivity reached 100% under very low space velocity (Entry 8, 0.015 $gCO_2/gCat/h$), but CO_2 conversion was negligible (0.7%). This indicates positive effects on methanol adsorption suppression but suggests a significant loss of active sites for CO_2 activation.

In contrast, the addition of 5 wt% CeO_2 to the Pt/MoO_3 catalyst produced exceptional results (Entries 9 and 10). Under optimized conditions (Entry 10, 0.015 $gCO_2/gCat/h$), **CO_2 conversion reached 78.8%, the highest observed, while methanol selectivity improved to 78%, surpassing the baseline Pt/MoO_3 performance.** Methane formation was effectively managed at 16.5%, and CO production was substantially suppressed (5.4%). However, at higher space velocity (Entry 9, 0.15 $gCO_2/gCat/h$), CO_2 conversion dropped to 19.4%, with CO selectivity rising to 70.8%.

The incorporation of CeO_2 into a high-surface-area (HSA) MoO_3 support resulted in further performance improvements. At lower space velocity (Entry 12, 0.015 $gCO_2/gCat/h$), CO_2 conversion reached 57.7%, slightly below the standard CeO_2-modified catalyst (78.8%, Entry 10). However, methanol selectivity reached a remarkable 83.2%, the highest achieved across all formulations. Furthermore, methane formation was controlled (16.8%), and CO formation was completely eliminated.

The results highlight the role of CeO_2 as a promoter in enhancing methanol selectivity in Pt/MoO_3-based systems. Among the formulations investigated, the 5 wt% Pt/(5 wt% CeO_2)MoO_3 catalyst achieved the best balance between CO_2 conversion (78.8%) and methanol selectivity (78%) under low space velocity conditions. In comparison, the use of an HSA MoO_3 support further improved methanol selectivity to 83.2%, albeit at the expense of CO_2 conversion. The superior performance of CeO_2-modified catalysts is likely due to the optimized distribution of basic sites, which effectively suppress methanol adsorption and mitigate methane formation.

Table 46. Hydrogenation of captured CO_2 in a continuous-flow reactor system across a range of operating temperatures and space velocities.

Entry	T (°C)	SV $gCO_2/gCat/h$	Conv. (%)	MeOH Sel. (%)	CH_4 Sel.(%)	CO Sel. (%)
5wt% Pt/MoO_3, 5wt%CO_2 EEMPA feed						
1	**190**	**0.15**	**32.1**	**59.4**	**24.3**	**16.3**

2	**190**	**0.015**	**77.6**	**59.1**	**40.9**	**0**
5wt% Pt/(5wt% MgO)MoO_3, 5wt%CO_2 EEMPA feed						
3	**190**	**0.15**	**0.9**	**0**	**91.9**	**8.1**
4	**190**	**0.015**	**1.8**	**0**	**72.9**	**27.1**
5wt% Pt/(5wt% ZrO_2)MoO_3, 5wt%CO_2 EEMPA feed						
5	**190**	**0.15**	**20.8**	**21.1**	**27.5**	**51.4**
6	**190**	**0.015**	**73.9**	**46.1**	**47.4**	**6.4**
5wt% Pt/(5wt% ZnO)MoO_3, 5wt%CO_2 EEMPA feed						
7	**190**	**0.15**	**0.4**	**0**	**0**	**100**
8	**190**	**0.015**	**0.7**	**100**	**0**	**0**
5wt% Pt/(5wt% CeO_2)MoO_3, 5wt%CO_2 EEMPA feed						
9	**190**	**0.15**	**19.4**	**22.3**	**6.9**	**70.8**
10	**190**	**0.015**	**78.8**	**78**	**16.5**	**5.4**
5wt% Pt/(5wt% CeO_2)HSA MoO_3, 5wt%CO_2 EEMPA feed						
11	**190**	**0.15**	**22.6**	**27.1**	**5.5**	**67.4**
12	**190**	**0.015**	**57.7**	**83.2**	**16.8**	**0**

Reaction conditions: 1g of catalyst, pressure: 860psi, 33.8 sccm H_2, 5 sccm N_2, 5%wt CO_2 loaded 2-EEMPA solvent, space velocity change is achieved by adjusting the flow of CO_2-loaded 2-EEMPA solvent.

Influence of CeO_2 Loading on Catalyst Performance

To optimize methanol production, the influence of CeO_2 loading on the catalytic performance of Pt/MoO_3-based systems was systematically investigated, as summarized in **Table 47**. A lower CeO_2 loading (1 wt%) significantly impaired performance under higher space velocity conditions, yielding a CO_2 conversion of 15.1% and methanol selectivity of only 6.6%, while CO formation dominated the product distribution at 86.6%. Notably, at lower space velocity, this catalyst demonstrated complete methanol selectivity (100%), albeit with a modest CO_2 conversion of 27.5%, indicating that insufficient CeO_2 loading compromised the catalyst's overall efficiency in CO_2 activation and methanol production.

In contrast, increasing the CeO_2 content to 10 wt% induced a pronounced shift in selectivity toward CO formation, with CO selectivity exceeding 98% across both high and low space velocity regimes. CO_2 conversion under these conditions was limited to ~20%, suggesting that excessive CeO_2 loading altered the catalytic behavior, likely due to an overabundance of basic sites and disruption of the active-site synergy between Pt and MoO_3. This shift appears to favor the reverse water-gas shift reaction over methanol synthesis.

A control experiment using a Pt/CeO_2 catalyst (without the MoO_3 support) further underscored the critical role of the MoO_3 support. The Pt/CeO_2 catalyst exhibited minimal activity at higher space velocity, with CO_2 conversion of just 4.8% and no measurable

methanol production. At lower space velocity, CO_2 conversion improved to 21.2%, accompanied by methanol selectivity of 42.2%; however, substantial byproduct formation was observed, with CO and methane contributing 34.9% and 22.9%, respectively, to the overall product distribution. These findings emphasize the importance of the Pt-MoO_3 interaction in facilitating selective methanol synthesis and suppressing undesired byproducts. Among the tested catalysts, the addition of 5 wt% CeO_2 emerged as the optimal formulation, achieving the most favorable balance between CO_2 conversion (78.8%) and methanol selectivity (78%) under low space velocity conditions.

Table 47. Hydrogenation of captured CO_2 in a continuous-flow reactor system across a range of operating temperatures and space velocities.

Run	T (C)	SV $gCO_2/gCat/h$	Conv. (%)	MeOH Sel. (%)	CH_4 Sel.(%)	CO Sel. (%)
5wt% Pt/MoO_3, 5wt%CO_2 EEMPA feed						
1	**190**	**0.15**	**32.1**	**59.4**	**24.3**	**16.3**
2	**190**	**0.015**	**77.6**	**59.1**	**40.9**	**0**
5wt% Pt/(1wt% CeO_2)MoO_3, 5wt%CO_2 EEMPA feed						
3	**190**	**0.15**	**15.1**	**6.6**	**6.8**	**86.6**
4	**190**	**0.015**	**27.5**	**100**	**0**	**0**
5wt% Pt/(5wt% CeO_2)MoO_3, 5wt%CO_2 EEMPA feed						
5	**190**	**0.15**	**19.4**	**22.3**	**6.9**	**70.8**
6	**190**	**0.015**	**78.8**	**78**	**16.5**	**5.4**
5wt% Pt/(10wt% CeO_2)MoO_3, 5wt%CO_2 EEMPA feed						
7	**190**	**0.15**	**9.1**	**0**	**0**	**100**
8	**190**	**0.015**	**21.4**	**2.4**	**0**	**97.6**
5wt% Pt/CeO_2, 5wt%CO_2 EEMPA feed						
9	**190**	**0.15**	**4.8**	**0**	**18.6**	**81.4**
10	**190**	**0.015**	**21.2**	**42.2**	**22.9**	**34.9**

Reaction conditions: 1g of catalyst, pressure: 860psi, 33.8 sccm H_2, 5 sccm N_2, 5%w CO_2 loaded 2-EEMPA solvent, space velocity change is achieved by adjusting the flow of CO_2-loaded 2-EEMPA solvent.

Performance of CeO_2-Modified Catalysts on Different Supports

The Pt/(5 wt% CeO_2)MoO_3 catalyst demonstrated strong performance under low space velocity conditions (0.015 $gCO_2/gCat/h$), achieving a CO_2 conversion of 78.8% and methanol selectivity of 78% (**Table 47**). However, this fell short of the 90% methanol selectivity required to meet this quarter's milestone. To explore further optimization, an intermediate space velocity (0.061 $gCO_2/gCat/h$) was assessed (**Table 48**), but while methane formation was reduced,

methanol selectivity dropped to 53%. This reduction was attributed to the inefficient conversion of in situ-formed CO intermediate.

Beyond MoO_3 support, the hydrogenation of CO_2 to methanol was further investigated using 5 wt% Pt/(5 wt% CeO_2)-based catalysts supported on ZrO_2 and TiO_2. **Table 48** provides a summary of the performance of these catalysts across various operating conditions and space velocities. The Pt/(5 wt% CeO_2)ZrO_2 catalyst showed promising performance under low space velocity conditions. At 0.015 gCO_2/gCat/h (Entry 5), CO_2 conversion was 53.1% with a methanol selectivity of 69.8%, demonstrating good activity. However, at higher space velocity (0.15 gCO_2/gCat/h, Entry 4), conversion and methanol selectivity dropped significantly to 17.4% and 4.4%, respectively, while CO selectivity rose dramatically to 94.4%. This indicates that at insufficient residence time, the RWGS pathway becomes dominant, favoring CO as the primary product. Remarkably, under ultra-low space velocity conditions (0.0061 gCO_2/gCat/h, Entry 6), the catalyst achieved a CO_2 conversion of 60.5% and an exceptional methanol selectivity of 92.6%. These results not only exceeded the Q3-FY25 milestone of >50% conversion and >90% methanol selectivity but also underscored the robustness of ZrO_2 as an effective support for selective catalytic CO_2 hydrogenation to methanol.

Conversely, the Pt/(5 wt% CeO_2)TiO_2 catalyst demonstrated inferior performance across all tested conditions, lagging behind both MoO_3 and ZrO_2 supports. Even at low space velocity (0.015 gCO_2/gCat/h, Entry 8), CO_2 conversion was limited to 25.4%, with a methanol selectivity of just 49.8%. The product distribution strongly favored undesired byproducts, with methane selectivity at 19.3% and CO selectivity at 30.9%. Under higher space velocity conditions (0.15 gCO_2/gCat/h, Entry 7), the catalyst's performance deteriorated further, with conversion reduced to 4.9% and methanol selectivity falling to 6.7%. These findings suggest that TiO_2, as a support, lacks the cooperative interaction between Pt and CeO_2 necessary to selectively drive methanol formation.

Overall, the Q3-FY25 milestone of **achieving >50% CO_2 conversion and >90% methanol selectivity was successfully met using the Pt/(5 wt% CeO_2)ZrO_2 catalyst at a space velocity of 0.0061 gCO_2/gCat/h**. Additionally, the **Pt/(5 wt% CeO_2)MoO_3 catalyst achieved a high CO_2 conversion of 78.8% alongside 78% methanol selectivity at a space velocity of 0.015 gCO_2/gCat/h**, further demonstrating its effectiveness as a promising alternative for methanol synthesis, particularly at slightly higher throughput conditions. To further elucidate the mechanistic origins of these trends, CO_2 and NH_3 TPD experiments are currently being conducted on these catalysts to characterize the distribution, strength, and functionality of acidic and basic sites.

Table 48. Hydrogenation of captured CO_2 in a continuous-flow reactor system across a range of operating temperatures and space velocities.

Run	T (C)	SV gCO_2/gCat/h	Conv. (%)	MeOH Sel. (%)	CH_4 Sel.(%)	CO Sel. (%)
5wt% Pt/(5wt% CeO_2)MoO_3, 5wt%CO_2 EEMPA feed						

1	190	0.15	19.4	22.3	6.9	70.8
2	190	0.061	39.4	53.1	5.7	41.2
3	190	0.015	78.8	78	16.5	5.4
5wt% Pt/(5wt% CeO_2)ZrO_2, 5wt%CO_2 EEMPA feed						
4	190	0.15	17.4	4.4	1.2	94.4
5	190	0.015	53.1	69.8	4.9	25.3
6	190	0.0061	60.5	92.6	7.4	0
5wt% Pt/(5wt% CeO_2)TiO_2, 5wt%CO_2 EEMPA feed						
7	190	0.15	4.9	6.7	14.6	78.7
8	190	0.015	25.4	49.8	19.3	30.9

XXIII. Single Step Simultaneous Production of Methanol and Glycol from Epoxide, CO_2 and H_2 Using Heterogeneous Cu-based Catalysts (FY25 Q3)

In our previous studies, we demonstrated that methanol and glycol can be sequentially coproduced from epoxide, CO_2, and H_2 via cyclic carbonate as an intermediate [36]. Specifically, the synthesis of cyclic carbonate from epoxide, CO_2, and H_2 was shown to be effectively facilitated by amine-based catalysts, with polyethyleneimine (PEI) achieving a remarkable cyclic carbonate yield of over 95% in THF solvent. For the subsequent hydrogenation step, which converts cyclic carbonate into ethylene glycol and methanol, a homogeneous Ru-based catalyst was successfully employed.

To overcome limitations in productivity, selectivity, separation, reuse, and potential stability associated with homogeneous catalysts, we shifted our focus to a heterogeneous catalytic system in the last quarter (**FY25 Q2**). This evaluation targeted the one-pot coproduction of methanol and propylene glycol (PG) from propylene oxide (PO), CO_2, and H_2. Among the tested systems, a heterogeneous Cu/ZnO/Al_2O_3 catalyst demonstrated promising results, particularly when combined with the PEI catalyst. This dual-catalyst system facilitated the formation of both PG and methanol with selectivity exceeding 75%.

Thermodynamic Modeling

As part of this quarter's activities, we conducted equilibrium modeling to investigate CO_2 conversion and product selectivity trends by minimizing Gibbs free energy (**Figure 68)**. In conventional gas-phase CO_2 hydrogenation, [39-41] the equilibrium CO_2 conversion reaches 41.4% at 200 °C, with a methanol selectivity of 97.4%. With the addition of ethylene oxide (EO) at an EO/CO_2 ratio of 0.5, CO_2 conversion increases significantly to 62%, while methanol selectivity remains high at 96.8%. Remarkably, at an EO/CO_2 ratio of 1, the CO_2 conversion approaches near-complete conversion of 99.7% at 200 °C, accompanied by a moderate decrease in methanol selectivity to 90.7%. Additionally,

reducing the temperature to 150 °C further enhances methanol selectivity to 96.5% without compromising CO_2 conversion.

In all cases, methanol selectivity decreases with increasing reaction temperature. CO_2 conversion also declines with temperature in the conventional and $EO/CO_2 = 0.5$ cases. However, in the $EO/CO_2 = 1$ case, CO_2 conversion remains high across the temperature range. The enhanced performance with EO addition is attributed to the consumption of water, which shifts the reaction equilibrium toward greater CO_2 conversion.

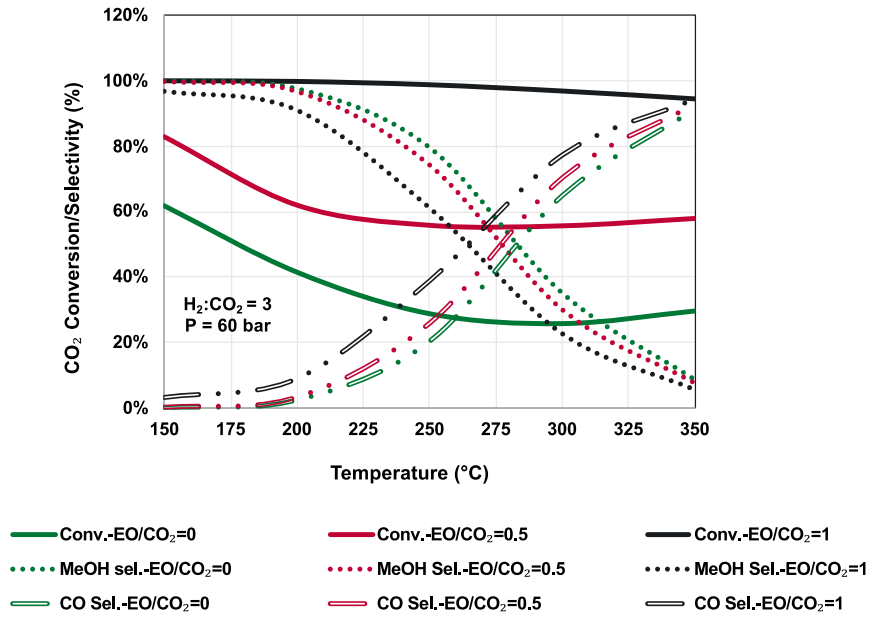


Figure 68. Equilibrium conversion of CO_2 and selectivity to methanol

Catalyst Screening and Structure-Activity Relationship

This quarter also involved screening various catalysts to elucidate the structure-activity relationship under optimized reaction conditions. As discussed earlier (in the previous quarter), the $Cu/ZnO/Al_2O_3$ (CZA) catalyst exhibited the highest CO_2 conversion (36.8%), along with excellent selectivities for both methanol and PG (>75%). In contrast, the 30 wt% Cu/Al_2O_3 catalyst (without ZnO) exhibited significantly lower CO_2 conversion (<1%) despite maintaining moderate PG selectivity (62.8%) (**Figure 69**). Methanol selectivity was notably poor (7.9%). These results are consistent with previous reports, [42-44] wherein ZnO was shown to enhance the dispersion and stabilization of active Cu species, thereby promoting CO_2 activation and hydrogenation.

An increase in Cu loading to 60 wt% on the Al_2O_3 support resulted in a slight improvement in PG selectivity (70.2%), however, CO_2 conversion remained negligible. This suggests that although higher Cu content may enhance selectivity toward PG, the absence of ZnO compromises overall activity, likely due to the lack of well-dispersed active sites. The use

of SiO_2 as an alternative support offered moderate improvements in activity. The 30 wt% Cu/SiO_2 catalyst achieved a CO_2 conversion of 13.2%, with methanol and PG selectivities of 39.1% and 14.4%, respectively. Increasing the Cu loading to 60 wt% led to a pronounced decline in CO_2 conversion (2.1%), while PG selectivity improved to 36.4%. This inverse relationship between Cu loading and CO_2 conversion may be attributed to particle aggregation and weakened metal–support interactions at higher Cu concentrations.[45-47] Among all the catalysts evaluated, the 60 wt% $Cu/ZnO/Al_2O_3$ catalyst demonstrated the best overall performance, balancing high CO_2 conversion with favorable product selectivity.

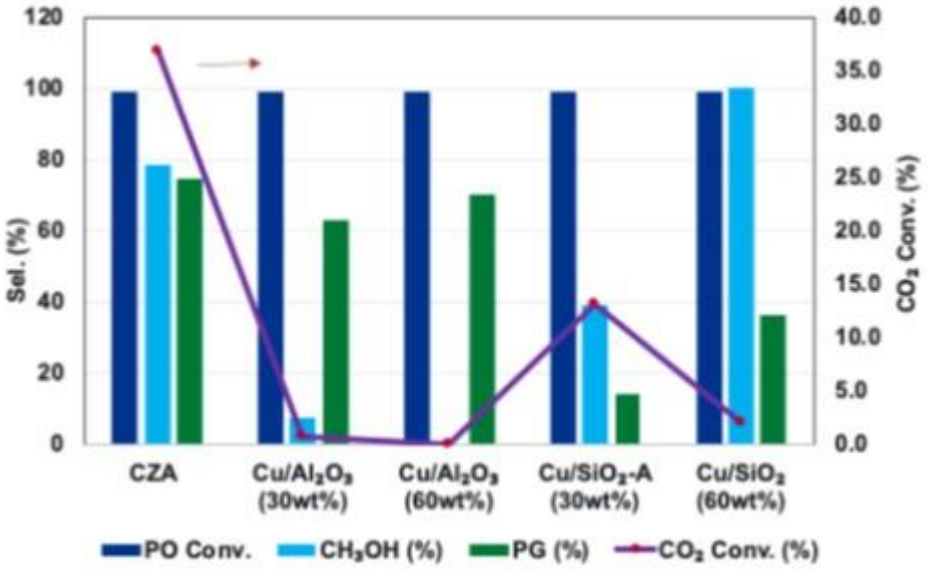


Figure 69. Evaluation of catalysts for coproduction of methanol and glycol. Propylene oxide (PO)=20 mmol, Catalyst=400 mg, H_2=60 bar, 170 °C, t=15h, THF=4.5mL, PEI = 50mg, PO conversion >99% in all the cases. PG = propylene glycol. Cu/Al_2O_3 (30wt%), Cu/Al_2O_3 (60wt%) and Cu/SiO_2 (60wt%) were synthesized using the wet impregnation method.

Catalyst Characterization and Proposed Reaction Mechanism

X-ray diffraction (XRD) analysis was performed to investigate the structural properties of the catalysts and to correlate these with their catalytic performance (**Figure 70**). Prior to analysis, all samples underwent in situ reduction at 190 °C under a flow of H_2. Following reduction, Cu was predominantly present in the metallic form in all catalysts, as indicated by diffraction peaks at 43.3°, 50.4°, 74.1°, 89.9°, and 95.2°.[48] However, in the 60 wt% Cu/Al_2O_3 sample, CuO was also detected, evidenced by additional peaks at 35.5°, 38.7°, and 48.7°,[49] alongside metallic Cu. Cu^0 crystallite size was calculated using the Scherer equation based on the 2θ peak at 43.5°.

A clear trend was observed between Cu loading and crystallite size. In general, increasing Cu content led to larger Cu crystallites.[50] Specifically, the 30 wt% Cu/SiO_2-A catalyst exhibited the smallest Cu crystallite size (~12.9 nm), indicative of good dispersion on the silica support. Conversely, the 60 wt% Cu/SiO_2 catalyst showed markedly larger crystallites (~41.4 nm), consistent with extensive particle aggregation at higher loading. A comparable pattern was noted for the Cu/Al_2O_3 series, where Cu crystallite sizes increased from ~37.7 nm at 30 wt% Cu to ~41.3 nm at 60 wt%. These observations support the hypothesis that higher metal loading promotes crystallite growth and reduces the fraction of accessible active sites.

Interestingly, the CZA catalyst exhibited an intermediate Cu crystallite size of approximately 36.5 nm, suggesting that ZnO may play a stabilizing role. This stabilization is likely due to stronger metal–support interactions and the formation of a Cu–Zn interfacial phase,[51-53] which could help suppress excessive particle growth. Notably, neither Zn/ZnO crystallites nor a CuZn alloy were detected by XRD, implying that ZnO is either highly dispersed or amorphous.[54, 55] Additionally, a minor diffraction peak at 36.9° corresponding to the Cu_2O (111) plane was observed,[56] suggesting that Cu_2O is also highly dispersed or exists in an XRD-amorphous state.

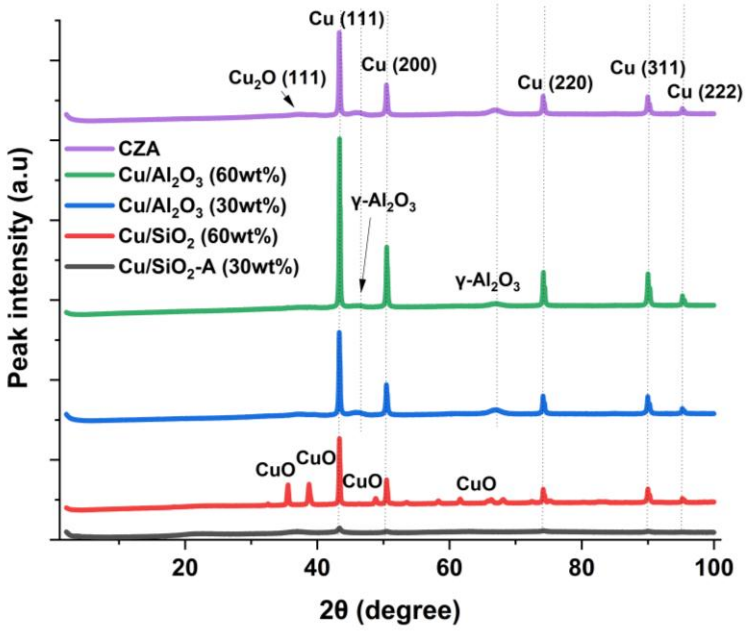


Figure 70. XRD of reduced Cu catalysts.

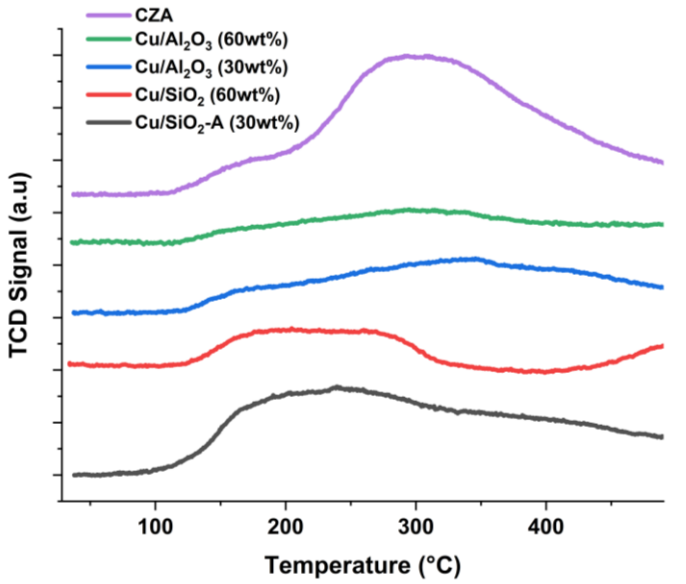


Figure 71. NH_3 TPD of the as synthesized/commercially obtained catalysts

Next, ammonia and CO_2 TPD were performed to evaluate the surface acidity and basicity of the catalysts (**Figure 71** and **72**). The NH_3-TPD profiles revealed distinct differences in acid site distribution among the samples. The CZA catalyst exhibited the most intense and broad desorption peak, centered around 250–350 °C, indicating a high concentration of medium to strong acid sites. Both Cu/Al_2O_3 and Cu/SiO_2 catalysts showed lower overall acidity, with desorption occurring primarily in the 120–370 °C range, corresponding to weaker and moderately strong acid sites.

CO_2-TPD results reflected similar trends in surface basicity. The CZA catalyst again showed the strongest CO_2 desorption, with a broad peak spanning 200–500 °C, indicating a high density of basic sites of varying strength. Notably, the Cu/Al_2O_3 (30 wt%) sample displayed a distinct desorption feature around 100°C, suggesting the presence of mild basic sites, likely associated with the alumina support. Cu/Al_2O_3 (60 wt%) sample showed a slightly broader basicity profile, while Cu/SiO_2 catalysts exhibited weak and diffuse desorption features, consistent with the low basicity typically associated with silica.

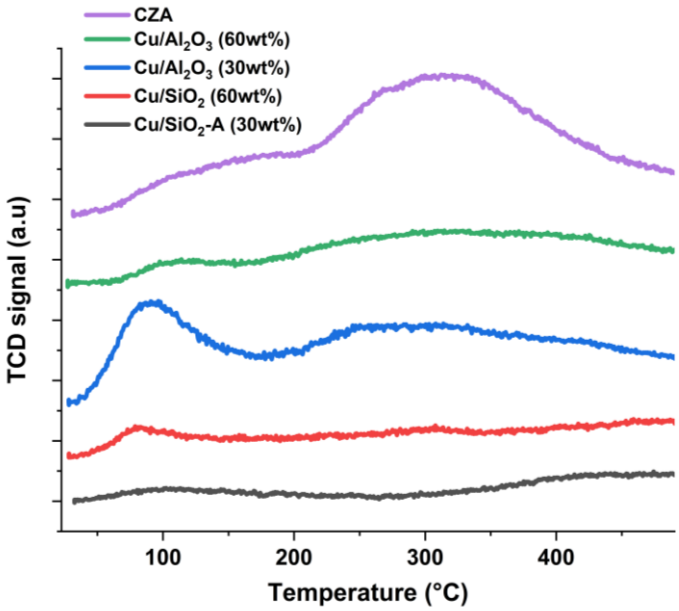


Figure 72. CO_2 TPD of the as synthesized/commercially obtained catalysts

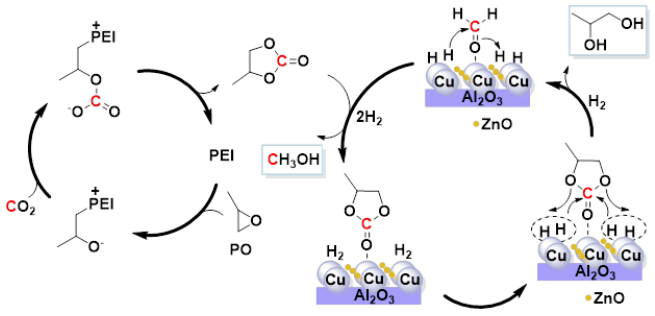


Figure 73. Proposed reaction mechanism involving a cyclic carbonate intermediate.

As PEI was identified as playing a key role in the coproduction of methanol and glycol in this study, and based on our previous reports[36], in which catalytic amounts of PEI facilitated epoxide ring-opening to form cyclic carbonates, a reaction mechanism involving a cyclic carbonate intermediate is proposed (**Figure 73**). Due to its high density of primary, secondary and tertiary amine groups, PEI may act as a nucleophile. In the initial step, nitrogen atoms from PEI attack the less substituted carbon of the electrophilic epoxide ring, resulting in ring opening.[57, 58] This is followed by the insertion of free CO_2 (or PEI captured CO_2) and an intramolecular cyclization to form a cyclic carbonate intermediate, with concurrent regeneration of free PEI. Additionally, CO_2 captured by PEI in the form of carbamate species (PEI^{+}–CO_2^{-}), together with the strong Lewis basic and acidic sites on the CZA catalyst (as identified by TPD), may cooperatively activate CO_2 and the epoxide. This cooperative effect is consistent with earlier work by Islam et al.,[59, 60] who reported similar reactivity using MgO and a quaternary ammonium salt (tetrabutylammonium bromide).

Subsequently, the in situ formed cyclic carbonate can undergo hydrogenation in the presence of the copper-based catalyst (CZA). Metallic Cu, identified by XRD, is known to dissociate molecular hydrogen, thereby supplying atomic hydrogen for the hydrogenation of the cyclic carbonate and other intermediates.[61] The strong Lewis acidic sites of the CZA catalyst, as suggested by NH_3-TPD analysis, may further polarize the carbonyl oxygen atoms, potentially enhancing electrophilicity at the carbon center and facilitating nucleophilic attack by hydrogen.[37] This sequence may initially yield glycol and formaldehyde, as illustrated in Figure 8. The formaldehyde could then undergo further hydrogenation to form methanol. Overall, the synergistic interaction between the Lewis acidic and basic sites of the CZA catalyst and the cocatalyst PEI effectively enabled the coproduction of methanol and glycol.

XXIV. Milestone: Assess at least 10 commercially available/inexpensive amine-based solvents, targeting methanol performance of at least 50% relative to the EEMPA baseline case (FY25 Q4)

To meet this quarter's milestone (FY25 Q4), efforts were focused on evaluating at least ten commercially available or low-cost amine-based solvents. The following secondary amines with varying functionalities (hydroxy, ether, and tertiary amine groups), steric profiles, and hydrocarbon frameworks were tested for both CO_2 capture and subsequent hydrogenation of the captured CO_2: 2-(ethylamino)ethanol (EAE), N-methylcyclohexylamine (MCHA), 1-(2-hydroxyethyl)piperazine (HEP), 1-[2-(2-hydroxyethoxy)ethyl]piperazine (HEEP), 2,2,6,6-tetramethylpiperidine (CRABMO), 1-methylpiperazine (MP), N,N,N'-trimethylethylenediamine (TMED), pentaethylenehexamine (PEH), N-(2-ethoxyethyl)-3-morpholinopropan-1-amine (EEMPA), 2,6-dimethylpiperidine (DMP), and di-sec-butylamine (DSBA). Structures of these amines are shown in **Figure 74**.

CO_2 Capture

Each solvent (5 g) was subjected to CO_2 absorption under batch CO_2 sparging conditions at ambient temperature and pressure. Carbon dioxide was sparged through the stirred amine until the cumulative CO_2 uptake reached 0.250 g, with periodic mass monitoring to track absorption progress. **Figure 74** presents the resulting gravimetric CO_2 loadings.

Five of the ten tested amines, EAE, HEP, HEEP, TMED, and DMP, successfully achieved the 0.250 g CO_2 loading target and remained liquid post-capture. Most of these amines contained secondary amine groups alongside hydroxy and/or tertiary functionalities, which likely stabilized solvated ionic species and prevented crystallization. The only exception was DMP, which, despite lacking hydrogen-bonding groups, remained liquid. This stability is attributed to favorable steric hindrance around the amine center, which limits intermolecular hydrogen bonding and prevents formation of an ordered carbamate lattice.

Interestingly, CRABMO and DSBA, both heavily substituted at the α-carbons, exhibited significantly reduced capture capacities, likely due to excessive steric shielding that limits CO_2 access to the nitrogen lone pair. Similarly, PEH captured less CO_2, consistent with its high viscosity, which hinders gas–liquid mass transfer and diffusion.

In contrast, MCHA and MP both solidified during CO_2 absorption. For MCHA, solidification is attributed to formation of a rigid carbamate network stabilized by strong N–H···O hydrogen bonding and the conformational rigidity of the cyclohexyl ring, which promotes crystallization. MP, on the other hand, contains two secondary nitrogen sites within a small cyclic framework, facilitating bifunctional carbamate crosslinking and dense ionic association. These effects collectively lead to rapid solid-phase formation once CO_2 uptake approached partial loading levels.

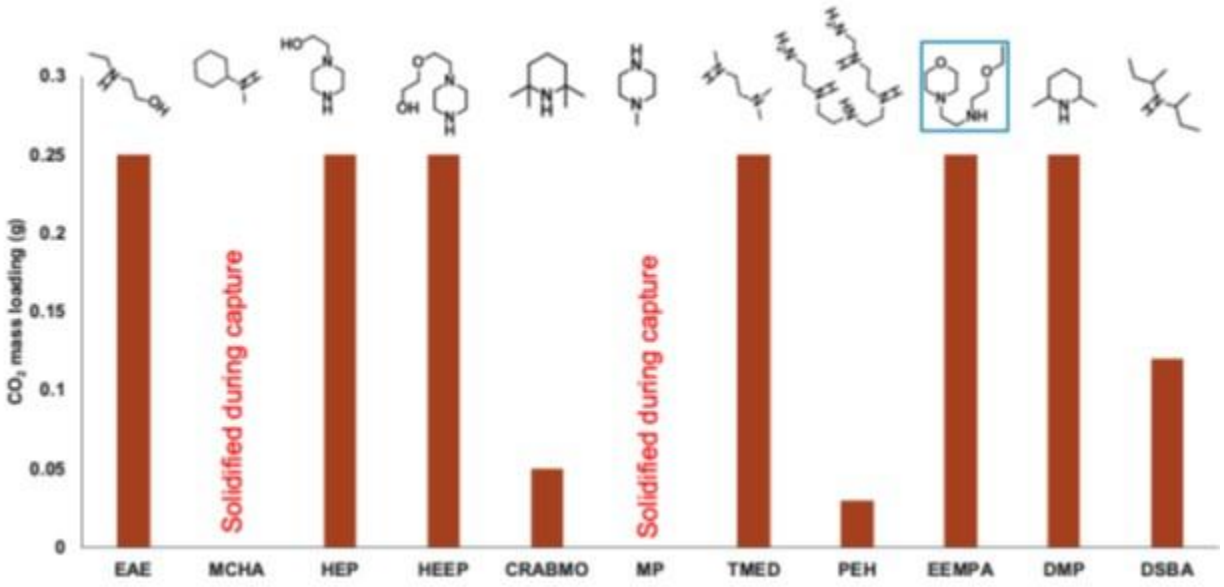


Figure 74: CO_2 gravimetric loadings on 5 g of selected amines.

CO_2 Hydrogenation Performance

Following CO_2 capture, the loaded amine solvents were transferred into a batch reactor and reacted with the Pt/MoO_3 catalyst under a 60 bar H_2 atmosphere at 190 °C for 15 hours. The catalytic results are summarized in **Figure 75**. In the baseline EEMPA case, CO_2 conversion reached 43%, with a methanol selectivity of 55.6%. Minor products included CO, methane, N-formamide, and N-methylated amines, each at selectivities between 8–15%. Among the amines exhibiting strong CO_2 absorption capacity (EAE, HEP, HEEP, and TMED), hydrogenation primarily yielded N-formamide intermediates (>40% selectivity), indicating that hydrogenation of the formamide intermediate to methanol is likely the rate-limiting step. MCHA and MP were not tested for hydrogenation, as both solidified during the CO_2 capture step.

Interestingly, amines bearing α-methyl substitutions, DMP, CRABMO, and DSBA, did not produce detectable quantities of N-methylated amines or formamides. This suggests that in these systems, methanol formation proceeds predominantly through a CO intermediate, since steric hindrance from α-methyl groups likely inhibits amine participation in the formamide pathway. As a result, methanol selectivity increased significantly, reaching 80% for CRABMO and 68% for DSBA.

The methanol space-time yields (STY_{MeOH}) for all evaluated systems are summarized in **Table 49**. Notably, DSBA exhibited a STY_{MeOH} of 0.45 mmol MeOH g/cat/h, on par with EEMPA (0.46 mmol MeOH g/cat/h), indicating comparable catalytic efficiency despite its lower CO_2 uptake capacity. Overall, **DSBA achieved methanol productivity exceeding 50% relative to the EEMPA baseline, thereby satisfying the performance criterion established for this milestone**.

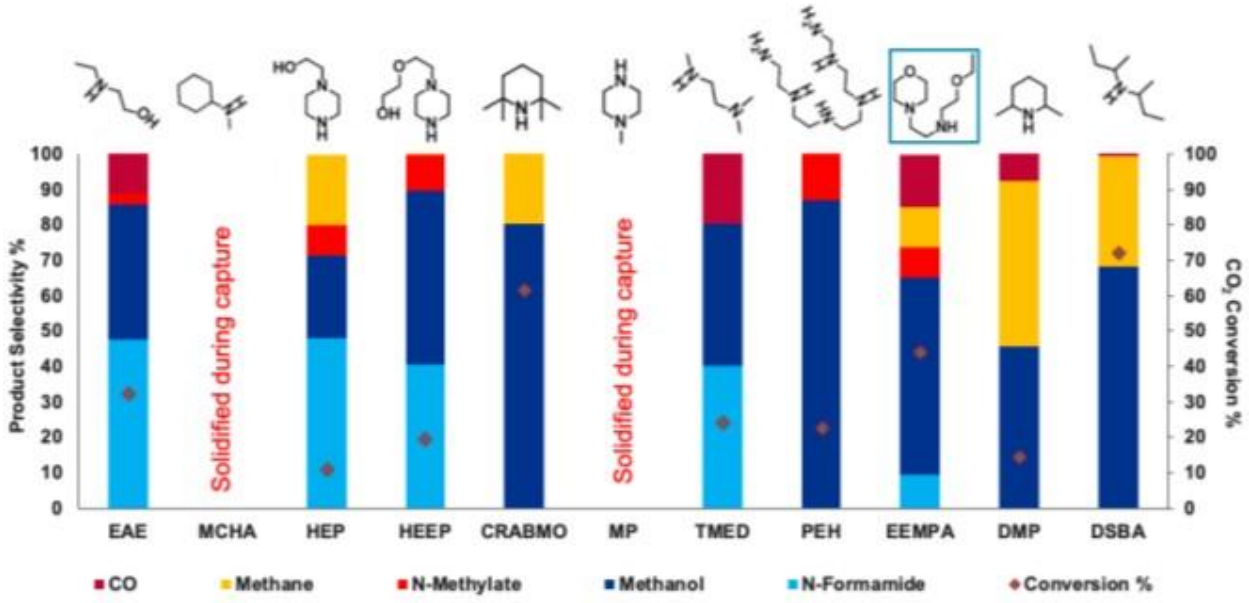


Figure 75: Results of amine screening for catalytic activity. Reaction conditions: 5 g amine, CO_2-loaded solvent from **Figure 74**, 0.2g Pt/MoO_3, 60 bar H_2, 190°C, 15 hrs.

Table 49. Reported methanol space time yields of screened amines (from **Figure 75**)

Amine	STY_{MeOH} ($mmol_{MeOH}/g_{catalyst}/h$)
EAE	0.23
HEP	0.05
HEEP	0.18
CRABMO	0.19
TMED	0.18
PEH	0.04

EEMPA	0.46
DMP	0.13
DSBA	0.45

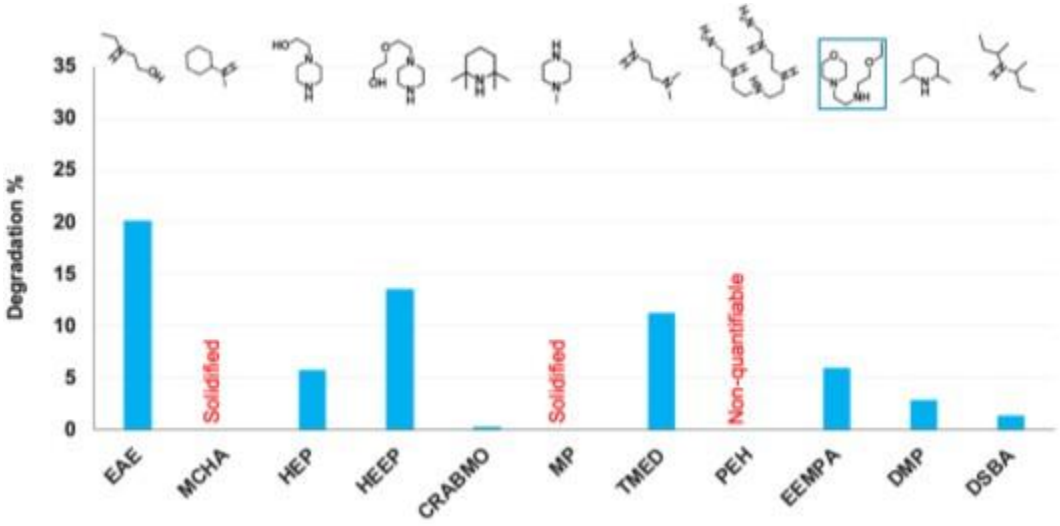


Figure 76: Degradation of the solvent under the hydrogenation reaction conditions (spent solvent from **Figure 75**).

Solvent Stability under Hydrogenation Conditions

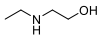
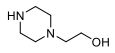
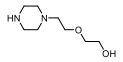
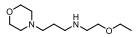
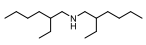
To assess solvent robustness under hydrogenation conditions, the spent amines from the catalytic tests were analyzed by GC-MS. The extent of solvent degradation is summarized in **Figure 76**. The results show that solvent stability varied markedly with molecular structure. EAE exhibited the highest degree of degradation (~20%), forming a mixture of low-molecular-weight fragments. This behavior is characteristic of ethanolamine derivatives, which are susceptible to dehydrogenation and condensation pathways under reducing conditions.

In contrast, HEP, HEEP, and TMED showed moderate degradation (5-15%), likely arising from partial N-dealkylation and C–N bond cleavage. The ether and tertiary linkages in these systems provide some stabilization but remain vulnerable to hydrogenolysis over Pt-based catalysts. PEH displayed limited stability, undergoing chain shortening and condensation reactions, consistent with its highly reactive polyamine framework. Conversely, CRABMO, DMP, and DSBA demonstrated excellent stability relative to the EEMPA baseline, with degradation levels below 5%. Their resistance to decomposition is attributed to steric protection around the amine center and the absence of labile hydroxy groups, both of which suppress undesired hydrogenolysis and condensation.

Based on the initial stability we investigated additional substituted amines under standardized conditions to make direct comparisons of stability to chemical structure. In this set, amines were loaded to a 10 $\%_{mol}$ CO_2 to represent CO_2-rich loadings achieved at

the National Carbon Capture Center pilot tests in 2025. Here, we can study the influence of IC3M conditions against thermal conditions experienced in the pilot test. The amines shown in **Table 50** were screened in the same manner as the amines shown in **Figure 75**.

Table 50: Amine utilized in second generation screening

IUPAC Name	Abbreviation	Chemical Structure
2- (Ethyl amino) ethanol	EAE	
1-(2-Hydroxyethyl) piperazine	HEP	
1-[2-(2-Hydroxyethoxy) ethyl] piperazine	HEEP	
N-(2-ethoxyethyl)-3-morpholinopropan-1-amine	EEMPA	
Bis(2-Ethylhexyl) amine	BEH	
Di-Sec-Butylamine	DSBA	
Di-Iso-Butylamine	DIBA	
2,6 Dimethyl Piperidine	26DMP	
3,5 Dimethyl Piperidine	35DMP	
2,2,6,6-Tetramethyl Piperidine	CRABMO	

Due to the elevated volatilities of some of the amines, the loading technique was slightly modified: the CO_2needle was moved above the amine solution, rather than being contained within and CO_2 flowrates were decreased to <1 ml min^{-1}. All amines were able to achieve 10 $\%_{mol}$ loading, with exception to DSBA and CRABMO, currently attributed to the large steric hinderance present slowing capture rates upon the approach to equilibrium. This series of reactions utilized the same reaction conditions as the previous generation (5g of amine loaded with 10$\%_{mol}$ CO_2, 0.2 g Pt/MoO_3, 15 hours, 60 bar H_2, 190ºC). Further, the water concentration and pH were measured for each amine before and after the reaction. **Figure 77** summarizes these results, with CRABMO and DSBA removed due to their sub 10 $\%_{mol}$ loadings.

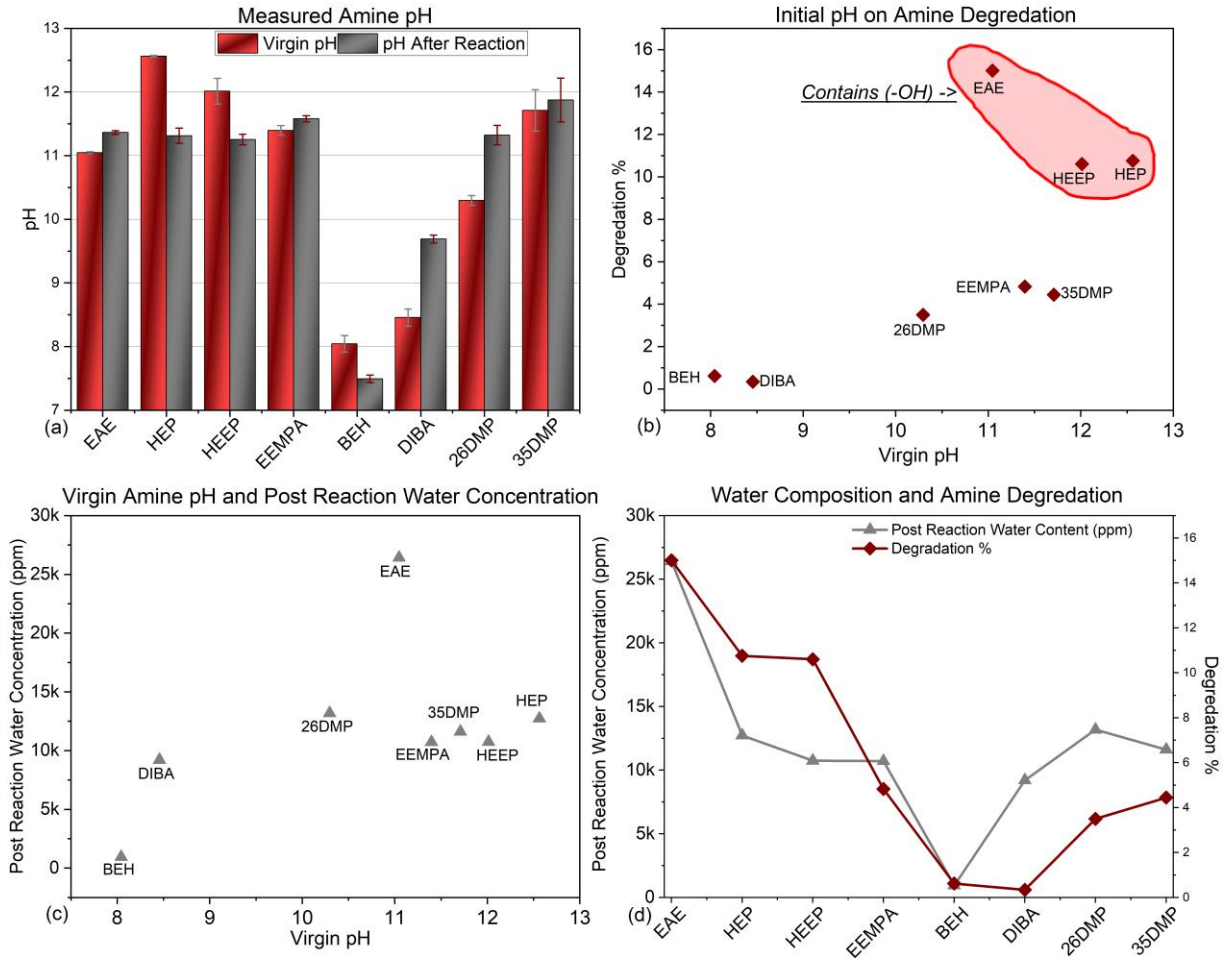


Figure 77:(a) Experimentally measured pH's of neat amines, prior to CO_2 loading, (b) amine degradation % against virgin amine pH, (c)post-reaction water content against virgin amine pH, and (d) post-reaction water content and degradation % by amine tested. Reaction Conditions: 5g of amine loaded with 10%$_{mol}$ CO_2, 0.2 g Pt/MoO_3, 15 hours, 60 bar H_2, 190ºC.

Again, we found that the substituted amines showed superior stability compared to other amines. With this round of screening, a correlation between virgin amine pH, water content and degradation was observed, indicating that solution phase chemistry was playing a role in solvent durability. There is seemingly a positive correlation between amine degradation and both pH and water concentration, with pH appearing to be the more dominant factor. These observations suggest that the greater stability provided from the substituted amines could be from higher pH , rather than a steric effect. While requiring further elucidation, it would seem that amine pH is a strong predictor of reaction stability. The pH values of EAE, HEP, HEEP, EEMPA, BEH, DSBA, DIBA, 26DMP, 35DMP, and CRABMO were measured at around 20°C, with results ranging from 8.0 to 12.6. These amines were tested as delivered, in different solvents and with varying initial water concentrations. The reported pH values indicate the basicity of the reaction environment rather than absolute measures of solvent pH. Substituted amines (BEH, DSBA, DIBA, 26DMP, CRABMO) generally exhibited lower pH than unsubstituted ones, with 35DMP similar to its unsubstituted counterparts. α and β carbon substitution appears to improve stability consistent with the know primary degradation mechanisms (α and β extraction) which is driven by deprotonation by a base. Thus, we see a clear correlation between degradation

and the availability of an adjacent proton to a heteroatom to be abstracted by these basic amines. After 15 hours, EAE, HEP, HEEP, and EEMPA showed higher degradation rates (15%, 11%, 11%, and 5%) compared to substituted amines (<1%, 3%, <1%, 3%, 4%, <1%). Increased degradation is likely due to heteroatom-centered attacks. Two main degradation mechanisms are proposed: amine-assisted E_2 elimination and catalytic hydrogenolysis. Both of which are promoted by strong bases and elevated temperatures. A key mitigation strategy for improving the durability of CI3M is to lower the temperature, lower the pH or the time exposure that solvents are exposed to these conditions. All of which can be engineered around in follow on work.

Similarly, the solution phase chemistry influences product selectivity, likely by changing the catalyst interface structure, the method by which hydrogen is split and the overall reaction mechanism. We suggest that amine pH mainly (1) influences C-N bond strength, (2) controls bulk phase decomposition rate, and (3) modifies catalyst selectivity by adjusting surface charge ratios. While not the sole factor, pH is significant; higher pH correlates with increased N-methylation, N-formamide formation, water content, and amine degradation, supporting E_2-related decomposition. Substitution at both α and β positions improves stability. The effect of pH on surface charges, determined by the support's point of zero charge (PZC), influences catalyst interactions with charged intermediates—higher pH makes metal oxide surfaces increasingly negative, possibly repelling N-formamide and attracting negative carbamate intermediates to positive surfaces, resulting in greater methanol selectivity at lower pHs. It is pertinent to note, that different pHs can change the dominant mechanism of H_2 cleavage between homolytic (on the Pt surface) and heterolytic (at metal oxide Lewis pairs). In this study, we kept the catalyst constant and varied solvent to tune surface charge, while in previous work we observed that supports with lower PZC led to more negative surfaces and reduced methanol selectivity (Figure 78).

Ultimately what we have discovered is that durability, selectivity and productivity are all linked to the pH of the solution under IC3M conditions. Future work should assess more detailed mechanism studies on how to control the pH and a given catalyst structure, because they are interconnected. A future catalyst will have to be designed around a new amines' pH at reaction conditions.

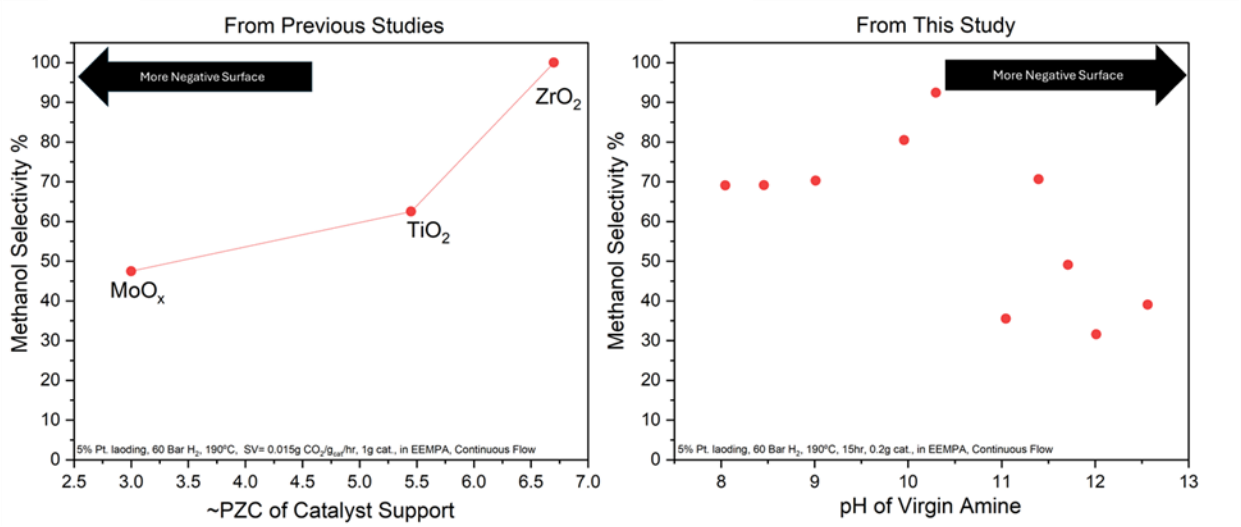


Figure 78 (L) Plot of methanol selectivity correlated to the PZC of the catalysts support from previous work, and (R) plot of pH of virgin amine and the methanol selectivity from the results of the current work.

Overall, these findings highlight the critical role of steric hindrance and reduced protic functionality in enhancing amine stability under hydrogenation conditions. Further, it seems that pH plays an important role in both amine stability and methanol selectivity, an idea novel to this field. Notably, DSBA, in addition to meeting the methanol productivity milestone, demonstrated superior thermal and catalytic durability. These results support the proposed direction for IC^{3}M 3.0, which aims to substitute hydrogen atoms at the α- and β-carbons adjacent to the amine nitrogen with carbon-based groups to further suppress C–heteroatom bond cleavage and improve solvent longevity**. However, more than likely, more simply controlling the pH and the time of amine exposure to high temperature and water concentration will lead to higher solvent longevity**. Future explorations should include the pursuit of understanding the role of pH and temperature in these complex environments.

Ethylene Glycol as co-solvent

Since MCHA and MP solidified during the CO_2 capture step, ethylene glycol (EG) was introduced as a co-solvent to facilitate CO_2 absorption and enable catalytic testing of these low-solubility amines (**Figure 79**). Using a 1:4 amine-to-glycol ratio, the targeted 0.25 g CO_2 loading was successfully achieved for both systems. Under hydrogenation conditions, both MCHA–EG and MP–EG mixtures produced >50% methanol selectivity, indicating that the active hydrogenation pathway remained accessible. However, the overall CO_2 conversion remained below 11%, suggesting that dilution by EG suppressed the effective amine-CO_2 interaction and reduced catalyst–substrate contact.

For comparison, EEMPA was also evaluated with EG as a co-solvent. The CO_2 conversion dropped markedly from 44% (neat EEMPA) to 24% in the EG-diluted system, confirming that solvent dilution adversely affects reaction kinetics. In addition, ethylene glycol degradation was significant across all cases. In both MCHA-EG and MP-EG systems, extensive decomposition of EG was observed by GC-MS. Even in the EEMPA–EG mixture, total degradation (due to EG) reached 32%, compared to only 6% in neat EEMPA. This instability is attributed to metal-catalyzed hydrogenolysis of EG under high-temperature, high-pressure H_2 conditions. This is congruent with our previous finding regarding the instability of the terminal hydroxide in IC^{3}M conditions. Overall, **while EG enabled testing of otherwise solidifying amines, its chemical instability and dilution effect on CO_2 conversion make it unsuitable as a long-term co-solvent for the IC^{3}M process**.

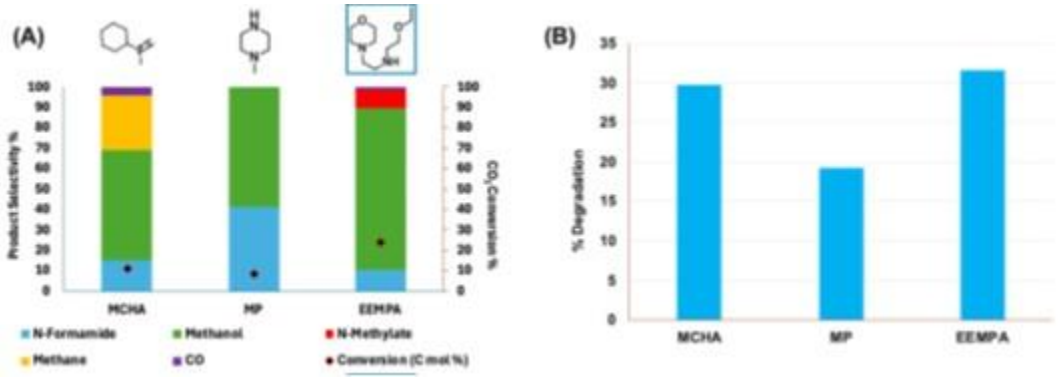


Figure 79: (A) Catalytic performance of amine-EG mixtures. Reaction conditions: 1 g amine + 4 g ethylene glycol + 0.25 g CO_2, 0.2 g Pt/MoO_3, 60 bar H_2, 190 °C, 15 h. (B) Degradation of the solvent under the hydrogenation reaction conditions (spent solvent from **Figure 77A**).

XXV. Conversion of Captured CO_2 to Formate Using Aqueous Solvents (FY25 Q4)

Compared to methanol synthesis, adapting our IC^{3}M platform to formic acid production is advantageous. Formic acid synthesis requires a lower H_2:CO_2 stoichiometric ratio (1:1 versus 3:1), operates at substantially lower temperatures (<100°C versus ~170–190°C), and offers favorable cost projections. Although the current market for formate is modest, formate serves as a versatile platform intermediate for upgrading to fuels and chemicals. Selective production of formic acid from captured CO_2 is influenced by both the capture solvent and the hydrogenation catalyst.

Our previous evaluation of CO_2 captured in EEMPA revealed low formic acid selectivity due to condensation between the solvent's -NH functionality and formic acid, yielding N-formamide. To suppress this pathway, we transitioned to water-lean non-nucleophilic or tertiary amine post-combustion capture solvents. When paired with a Pd/C catalyst, these systems achieved >80% CO_2 conversion to formate at temperatures below 100°C. Water-

lean tertiary amine formulations can deliver high conversions but are limited by viscosity and solubility; therefore, we pursued aqueous solvents to balance catalytic performance and operability.

In this project quarter, to elucidate structure-property relationships governing both CO_2 capture and downstream hydrogenation to formate in aqueous systems, we screened thirteen amines: tetramethylguanidine (TMG), 1,4-diazabicyclo[2.2.2]octane (DABCO), 1,8-diazabicyclo[5.4.0]undec-7-ene (DBU), N-methyldiethanolamine (MDEA), triethylamine (TEA), 1,2-dimethylimidazole, N-methylpyrrolidine (NMP), N-butylimidazole (1-BuIm), 4-dimethylaminopyridine (DMAP), N-methylimidazole (1-MeIm), 1,4-dimethylpiperazine (DMP), and pyridine (Py). These candidates spanned heterocycles (pyridine, imidazoles), cyclic amidines (DBU, DABCO), and alkanolamines (MDEA, DEEA), enabling correlation of molecular structure with CO_2 capture and formate yield performance. Across this series, CO_2 capture efficiency increased with amine basicity (pKa) for water-miscible bases (**Figure 80a**), consistent with an acid–base controlled mechanism where stronger bases promote rapid bicarbonate formation. The pKa trend is modulated by phase behavior: amines with limited water solubility, including TEA, DMP, and DMAP, deviate from the pKa–capture correlation and exhibit reduced capture, likely due to lower effective base concentration and mass-transfer limitations at liquid–liquid interfaces. Low-pKa species such as pyridine perform poorly, reflecting insufficient thermodynamic driving force to shift the hydration equilibrium.

Formate yield also increases with pKa (**Figure 80b**). Superbases such as TMG and DBU facilitate deprotonation and stabilize the formate anion, lowering the barrier for CO_2/bicarbonate reduction to formate. Notably, the influence of phase behavior differs from capture: certain hydrophobic bases (e.g., TEA and DMP) deliver comparatively high formate yields once CO_2 is available, suggesting conversion benefits from an organic-rich, base-dense microenvironment even when capture is limited. These trends are shown in **Figure 80a and b**, where both capture efficiency and formate yield generally rise with pKa, and deviations correspond to low water solubility. Candidate assessment highlights both performance and practicality. Although TMG and DBU exhibit high capture and conversion efficiencies, they may pose limitations for large-scale operation, including cost, handling, and potential side reactions. MDEA offers a pragmatic baseline for optimization, combining moderate capture and conversion (0.70 mmol CO_2 per mmol amine and 45% formate yield) with excellent solubility, stability, and an established industrial record.

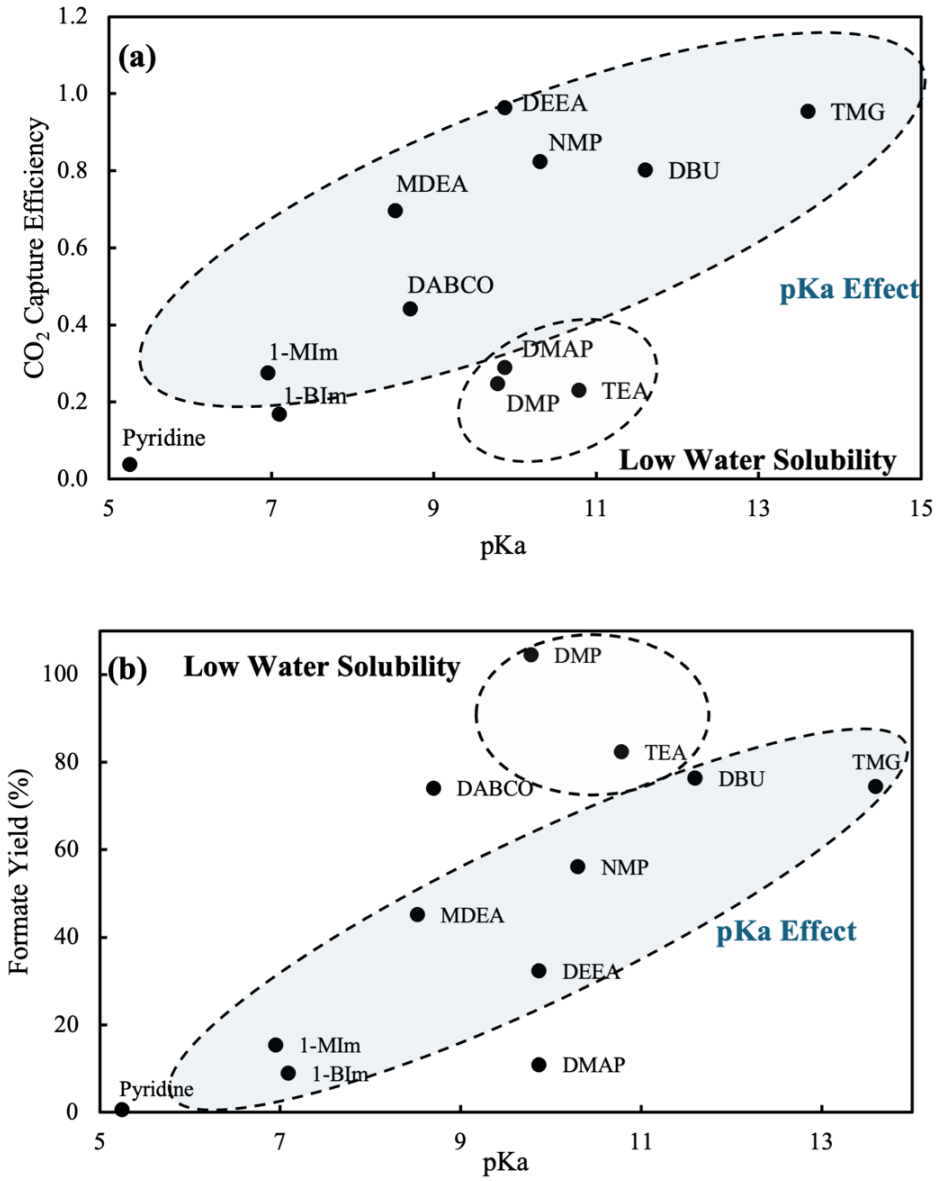


Figure 80. (a) CO_2 capture efficiency as a function of the amine's pKa value (b) Formate yield as a function of the amine's pKa value. All amines (10 mmol) were dissolved in 5 mL of H_2O. CO_2 capture was performed at room temperature by sparging CO_2 through the solution for 30 min. For the hydrogenation studies, 200 mg of 3 wt% Pd/C was used. The reaction was carried out at 60 bar H_2 and 50 °C for 10 h. The amount of formate produced was quantified by ^{1}H NMR, and yield was calculated with respect to the amount of CO_2 captured by the amine.

XXVI. CO_2 Hydrogenation to Ethanol (FY25 Q4)

During this period, activities are mainly focused on understanding the Rh-Fe interactions and elucidating the specific roles of Rh and Fe individually in gas-phase CO_2 conversion to ethanol by designing targeted experiments and employing advanced characterization techniques.

Active sites for CO_2 activation: role of Rh^{d+}

Comparison of mono- and bimetallic catalysts highlights the distinct roles of Rh and Fe in CO_2 activation and product formation in Figure 6. The Fe/SiO_2 catalyst shows no detectable CO_2 conversion, indicating that Fe alone is inactive under the reaction conditions. In contrast, Rh/SiO_2 achieves ~1% CO_2 conversion with 100% selectivity toward methane, confirming that Rh sites are responsible for CO_2 activation but favor over-hydrogenation pathways. This conclusion is supported by theoretical calculations of CO_2 adsorption and activation energies on Rh and Fe.[1] CO_2 adsorption is more favorable on Rh (-1.5 to -1.2 eV) than on Fe (-1.0 to -0.7 eV), indicating a more stable structure. The activation energy for forming the CO* intermediate is also lower on Rh (0.8-1.2 eV) than on Fe (1.0-1.7 eV). Regarding Rh valence, positively charged Rh^{d+} has a lower energy barrier for CO_2 activation (1.3-1.7 eV) compared to metallic Rh^0, which shows higher barriers (2.0-2.2 eV), indicating that CO_2 is more easily activated on Rh^{d+} sites.[2] In addition to theoretical calculations, another study also reported that the presence of partially oxidized Rh correlates with enhanced CO_2 conversion.[3]

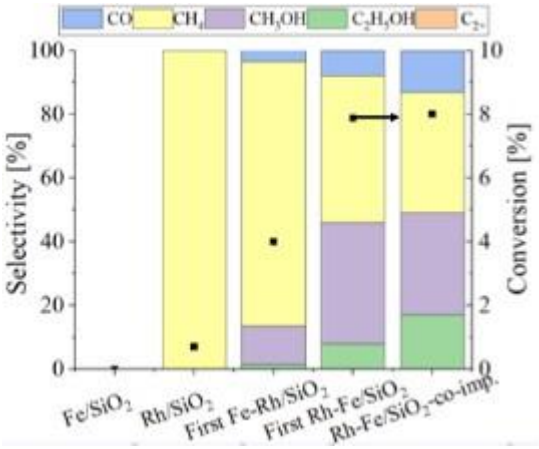


Figure 81: CO_2 hydrogenation over different catalyst structures. Reaction conditions: flow reactor, temperature 240 °C, pressure 30 bar, CO_2 5 sccm, H_2 15 sccm, catalyst loading: 100 mg diluted with 1000 mg SiC, WHSV= 12000 mL $gcat^{-1}$ h^{-1}. Activation conditions: temperature 350 °C, H_2 20 sccm for 30 min.

Tuning ethanol selectivity: metal-metal interactions between Rh and Fe

Another significant finding from **Figure 81** is that ethanol is produced only in the presence of both Rh and Fe active components, providing strong evidence for the essential role of Fe in promoting ethanol formation on Rh-based catalysts. Incorporation of Fe, whether by sequential impregnation or co-impregnation, leads to ethanol production, indicating a synergistic interaction between the two metals. However, the Rh and Fe catalyst prepared by co-impregnation exhibits the highest ethanol selectivity, which can be attributed to the

close spatial proximity and strong electronic interactions between Rh and Fe.

The nature of the interactions between closely contacted Rh and Fe is further investigated. Energy-dispersive X-ray (EDX) spectroscopy mapping in **Figure 82** shows the spatial distribution of Rh and Fe within the catalyst. Rh–Fe/SiO_2-co-imp. has the highest degree of Rh–Fe co-localization, indicating intimate contact. In contrast, the first Rh-Fe/SiO_2 shows separate Fe regions, and the first Fe-Rh/SiO_2 shows Fe agglomeration, reflecting poor dispersion. These results highlight that the metal loading sequence critically affects catalyst structure and potential synergistic interactions.

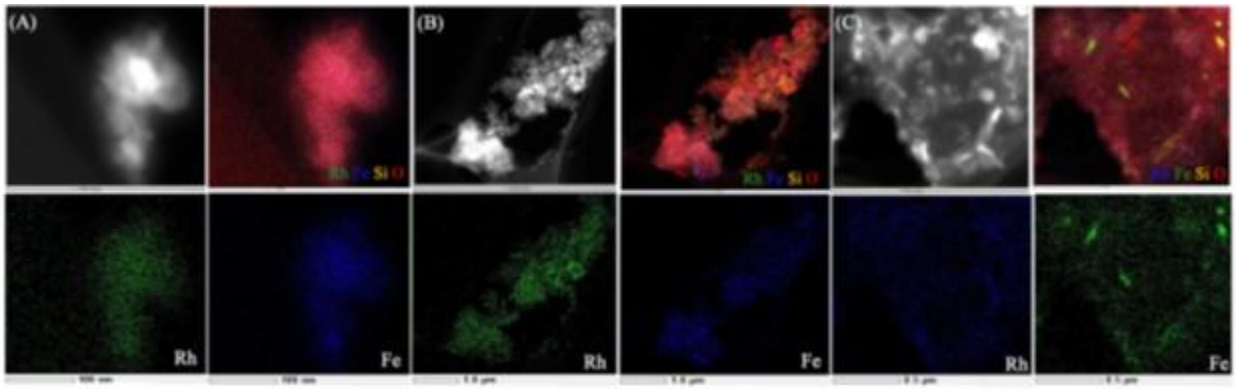


Figure 82: EDX elemental and combined mapping of Rh and Fe distribution in reduced catalyst (A) Rh-Fe/SiO_2-co-imp. (B) First Rh-Fe/SiO_2 (C) First Fe-Rh/SiO_2.

X-ray photoelectron spectroscopy (XPS) analysis further confirms the electron property differences among the catalysts. In **Figure 83**, the Rh–Fe/SiO_2-co-imp. catalyst has a higher fraction of metallic Rh (Rh^0) and more Fe^{2+} compared to catalysts prepared via stepwise-impregnation method. This indicates that co-impregnation enhances Rh–Fe interactions, promoting more efficient co-reduction of Rh^{3+} to Rh^0 and Fe^{3+} to Fe^{2+} and Fe^0, due to electron transfer between closely interacting metals.

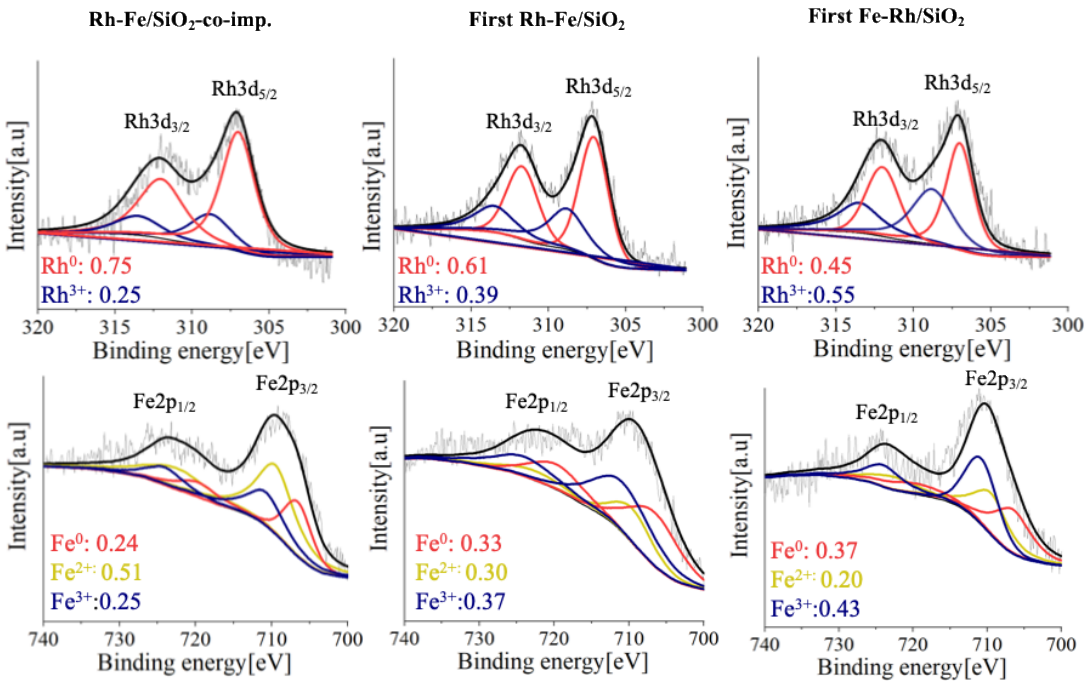


Figure 83: XPS spectra for reduced Rh-Fe/SiO_2-co-imp., First Rh-Fe/SiO_2 and First Fe-Rh/SiO_2 catalysts.

Active sites for the formation of CH_x intermediates: role of Rh^0 nanoparticles

CH_x* intermediates are essential for ethanol formation via C–C coupling with CO*, but excess CH_x* can react with H* to form methane. **Figure 84** shows XRD patterns with a broad SiO_2 peak at $2\theta \approx 21.8^{\circ}$ and a metallic Rh peak at 41°. The calculated Rh crystallite sizes listed in **Table 51** decrease in the order Rh/SiO_2, First Fe-Rh/SiO_2, First Rh-Fe/SiO_2, and Rh-Fe/SiO_2 co-imp., indicating that Fe promotes smaller, more dispersed Rh particles. The enhanced dispersion achieved through co-impregnation is linked to a decrease in methane formation, as shown in **Figure 85**.

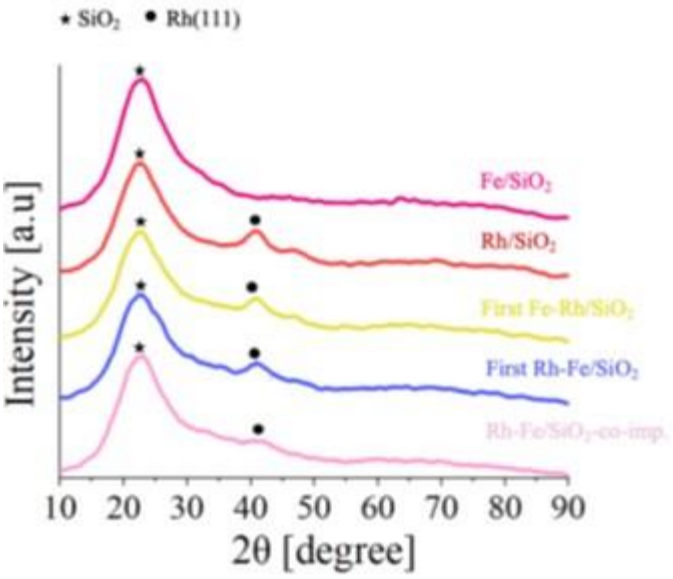


Figure 84: XRD patterns of reduced catalysts.

Table 51. Particle size calculation using the Scherrer equation.

Catalyst	Rh Particle size [nm]
Rh/SiO_2	3.4
First $Fe-Rh/SiO_2$	2.7
First $Rh-Fe/SiO_2$	2.3
$Rh-Fe/SiO_2$-co-imp.	2.1

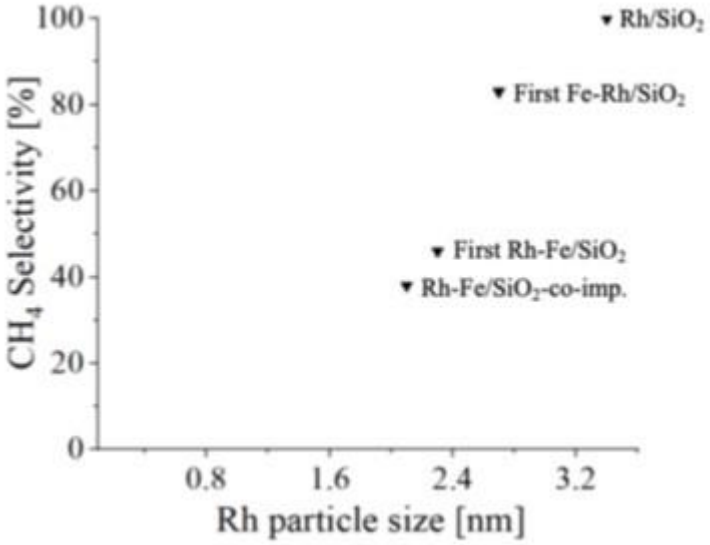


Figure 85: The relationship between particle size and methane selectivity.

Active sites for C-C coupling: role of iron carbides

Beyond CO* and CH_x* formation, efficient C–C coupling is essential for ethanol production from CO_2. To clarify the active sites, CO hydrogenation is used as a probe to assess the role of iron carbides. As shown in **Figure 86**, CO_2 hydrogenation yields 20% ethanol selectivity at 8% conversion, whereas CO hydrogenation achieves 60% ethanol selectivity at 25% conversion. The higher activity under CO conditions suggests that iron carbides, which form more readily with CO as a carburizing agent, are crucial active sites for C–C coupling and ethanol synthesis.

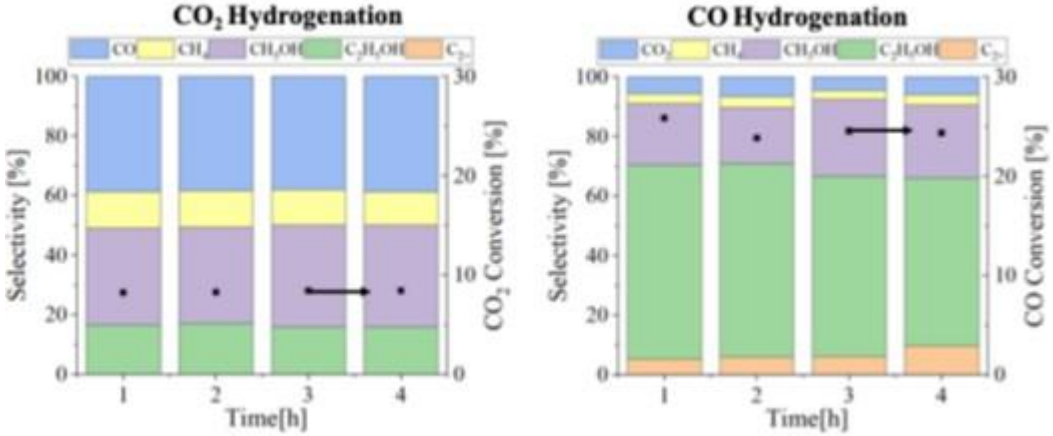


Figure 86: (a) CO_2 hydrogenation over Rh-Fe/SiO_2-co-imp. catalyst. Reaction conditions: flow reactor, 0.1 g catalyst diluted by 1g SiC, temperature 240°C, pressure 30 bar, CO_2 5 sccm, H_2 15 sccm. Activation under temperature 350 °C, H_2 20 sccm for 30 min. (b) CO hydrogenation over Rh-Fe/SiO_2-co-imp. Reaction conditions: flow reactor, 0.1 g catalyst diluted by 1 g SiC, temperature 240°C, pressure 30 bar, CO 5 sccm, H_2 10 sccm, (H_2:CO=2:1), activation under temperature 350 °C, H_2 20 sccm for 30 min.

To confirm the claim above, XRD analysis is performed to identify and compare the formation of iron carbide phases in catalysts after exposure to CO and CO_2 hydrogenation. XRD analysis is conducted to compare iron carbide formation after CO and CO_2 hydrogenation. The patterns in **Figure 87** reveal stronger Fe_3C peaks following CO hydrogenation, indicating a higher Fe_3C concentration that promotes C–C coupling and ethanol formation. Characteristic reflections at 43.0° and 60.3° correspond to the (211) and (221) planes of Fe_3C (JCPDS 35-0772).

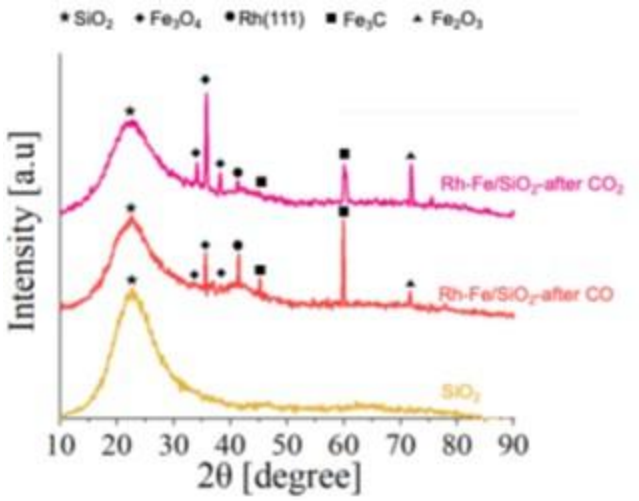
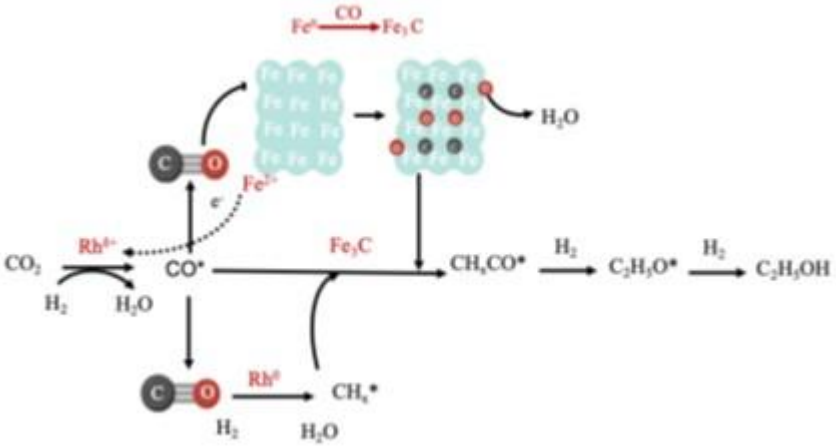


Figure 87: XRD pattern of spent catalysts after CO_2 and CO hydrogenation.

Summary: Multiple roles of Rh and Fe for CO_2 hydrogenation to ethanol

Our results show that CO_2 hydrogenation over Rh–Fe/SiO_2 is driven by strong Rh–Fe synergy, as illustrated in **Scheme 3**. Rh^{d+} sites adsorb and activate CO_2 to form CO*, which then dissociates and hydrogenates on metallic Rh to produce CH_x*. Fe tunes Rh size and electron properties, balancing CO* and CH_x* formation. CO carburization on Fe generates iron carbides, which serve as active sites for C–C coupling between CO* and CH_4* intermediates. Therefore, both Rh and Fe play crucial roles in selective ethanol production from CO_2 hydrogenation.



Scheme 3. Proposed reaction mechanism for ethanol formation via CO_2 hydrogenation over Rh–Fe/SiO_2 catalyst.

XXVII. Conversion of Captured CO_2 to Formate Using Aqueous Solvents (FY26 Q1)

Last quarter (FY25 Q4), twelve amines were screened to evaluate structural diversity and basicity in relation to CO_2 capture and aqueous hydrogenation to formate. As previously reported, CO_2 capture and formate yield generally increase with amine pK_a for water-miscible bases, while deviations arise for poorly soluble amines due to mass-transfer and phase effects, and low-pK_a bases show weak performance. Although superbases (TMG, DBU) deliver the highest efficiencies, practical considerations favor methyldiethanolamine (MDEA) as a balanced and scalable benchmark, combining moderate performance with high stability and industrial relevance. As proposed in the previous quarter update, efforts focused on optimizing MDEA solvent conditions to enhance CO_2 capture and conversion, as well as on separating the formate ion using ion-exchange resins.

From optimization studies using MDEA solvents, several parameters influencing formate yield were investigated, including MDEA concentration (20 wt% vs 40 wt%), base activator (piperazine and TMG), and catalyst dosage (200 mg and 400 mg Pd/C) (**Figure 88**). Notably, the baseline condition of 20 wt% MDEA achieved 0.70 mol CO_2 capture per mol base, resulting in a 45.1% formate yield after hydrogenation. Increasing the MDEA concentration negatively impacted both CO_2 capture and conversion, with only 0.32 mol CO_2 capture per mol base and a 15.9% formate yield. This reduction is attributed to changes in physicochemical properties (e.g., density, surface tension, and viscosity) at higher MDEA concentrations, which affect CO_2 absorption capacity and formate conversion. Therefore, 20 wt% MDEA in water, an industry standard in mature CO_2 capture processes, was selected as the optimal concentration.

The use of base activators to promote CO_2 capture and formate conversion was examined using piperazine (PZ) and TMG. The use of base activators to promote CO_2 capture and formate conversion was examined using piperazine and TMG. Piperazine (0.05 M) improved both CO_2 capture efficiency and formate conversion, as it promotes bicarbonate formation, which is beneficial for both the capture process and the subsequent hydrogenation step. In contrast, TMG (0.05 M) did not improve CO_2 capture or conversion, which may be attributed to catalyst poisoning caused by its high basicity. A higher piperazine concentration (0.1 M) significantly improved CO_2 capture but decreased formate yield. This behavior is attributed to the presence of secondary amine groups in piperazine, which are prone to form formamides rather than formate, in contrast to tertiary amines. Increasing the catalyst dosage in the presence of piperazine had a significant effect, resulting in a formate conversion of 90%. The additional active sites provided by Pd/C promoted hydrogenation, enabling greater conversion to formate.

Previous studies have supported the use of anion-exchange resins for separating formic acid from aqueous solutions. The present results demonstrated effective separation of the formate ion using basic Amberlyst resin at different solvent-to-resin ratios (**Figure 89**). At solvent-to-resin ratios of 1:0.5 and 1:1, 73.0% and 99.8% of the formate ion were removed from solution after 60 min, respectively. These results confirm that increasing the number of available binding sites on the resin enhances formate uptake. The presence of piperazine during ion exchange was evaluated using the optimized 1:1 solvent-to-resin ratio and showed negligible impact, with 99.8% of the formate ion removed after 60 min.

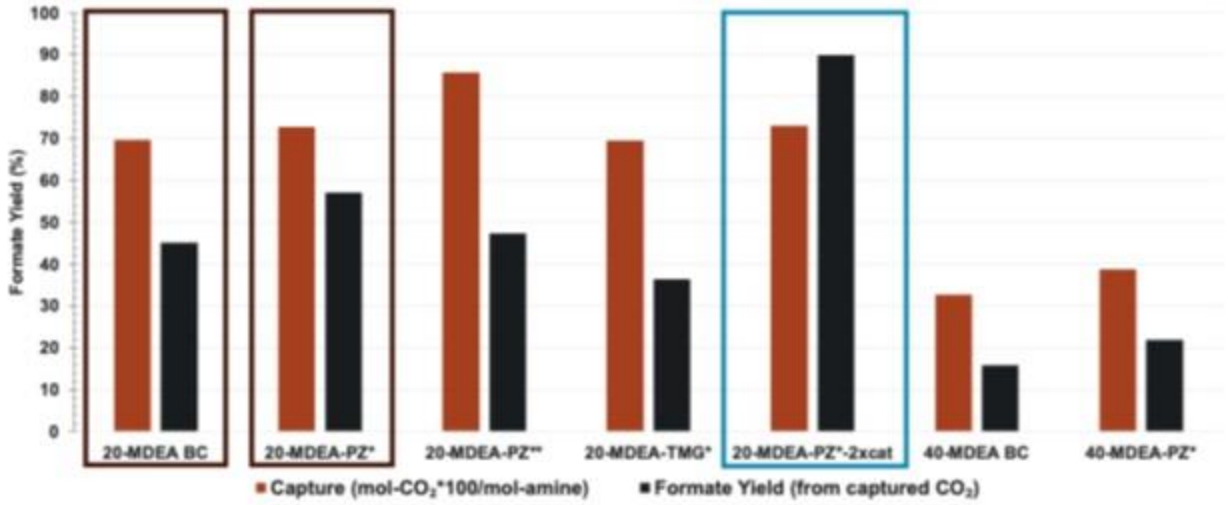


Figure 88 Optimization Studies for MDEA Hydrogenation to formate.

Optimization Hydrogenation Study: Baseline Conditions (BC): Cat = 200 mg of Pd/C (3wt. %), 60 bar H_2, Reaction temperature maintained at 50 °C for 10 h. *Added Base Initial Concentration = 0.05M, **Added Base Initial Concentration = 0.1M, *2-xcat 400 mg of Pd/C (3wt.%).

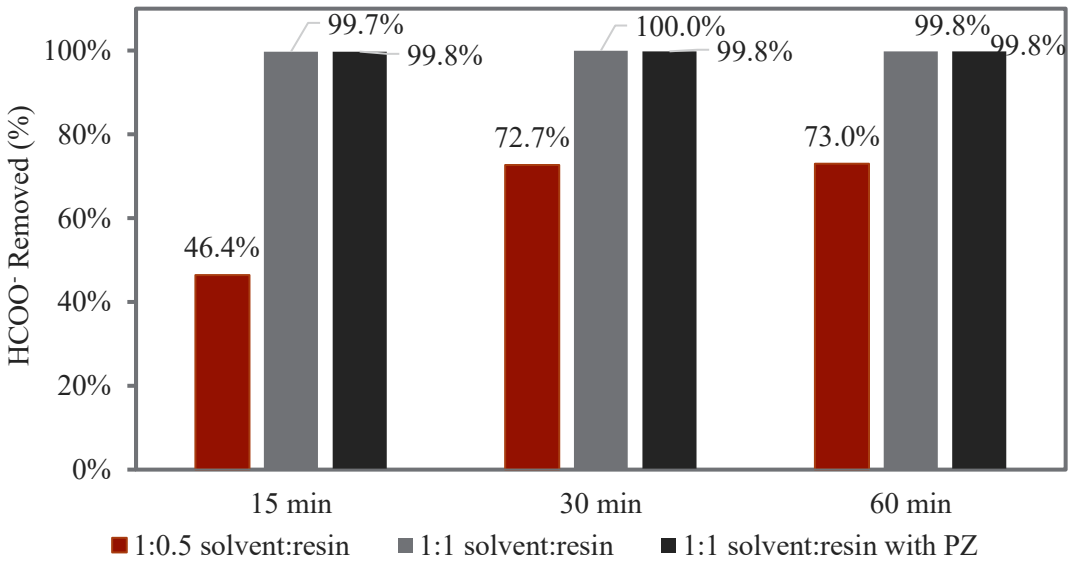


Figure 89 Results from formate ion exchange using Amberlyst A26 hydroxide form resin at varying solvent mixture to resin ratios.

XXVIII. FY26 Q1 Milesone: "[T5] Report state of technology performance and costing for each of the three major catalytic pathways being investigated. [T6] Report full environmental LCA for process and compare to two baseline cases."

In this quarter (Q1 FY26), techno-economic analysis and life-cycle assessment were conducted to evaluate the economic and environmental performance of formic acid production via IC^{3}M platform. The results were compared with those of commercial formic acid production technologies and with a published separated carbon capture and conversion (SC^{3}M) route.

Using the Aspen Plus built-in property package for the solvent-CO_2-H_2O system and lab-scale experimental data for conversion and product separation, a process model for formic acid production via IC^{3}M was developed in Aspen Plus (**Figure 90**).

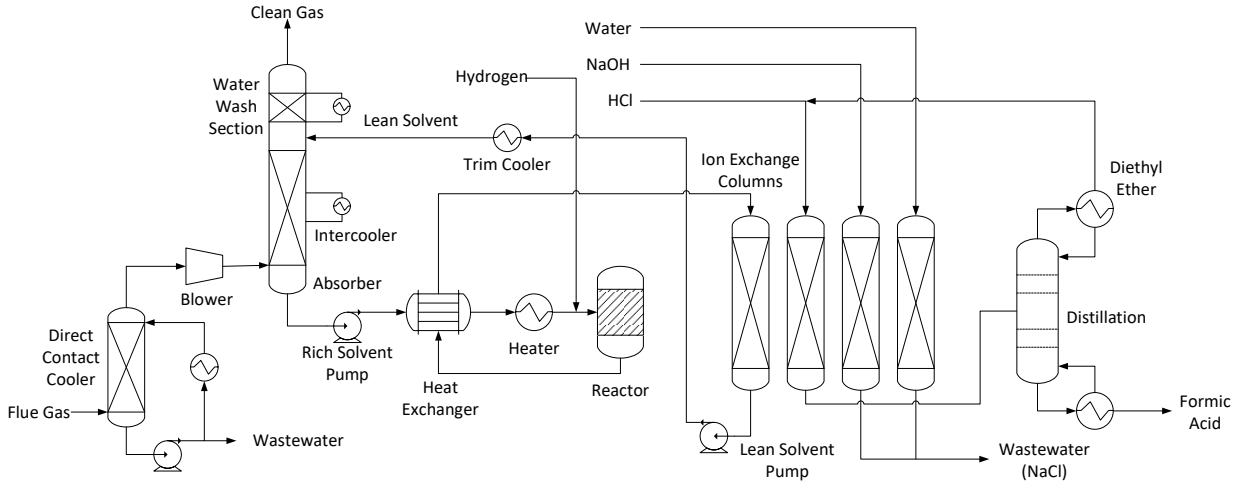


Figure 90. Process configuration for formic acid production via IC^{3}M.

Flue gas from a 650 MW natural gas combined-cycle (NGCC) power plant is first cooled in a direct-contact cooler and then sent to an absorber column. A 20 wt% MDEA solution with 0.05 M PZ is used for CO_2 capture in the absorber. The CO_2-rich solvent is subsequently fed, together with hydrogen, to a condensed-phase reactor packed with Pd (3 wt%)/C catalyst and operated at 50 °C and 60 bar. A weight hourly space velocity of 0.084 g formate g^{-1}cat h^{-1}, determined from experimental studies, was used to size the reactor. In the reactor, H_2 reacts with CO_2-loaded MDEA/PZ solvent according to Eq. (1, below), with the extent of conversion set to 90% based on experimental observations.

Formic acid is recovered from the intermediate $MDEAH^+/HCOO^-$ species via a three-step ion-exchange process using Amberlyst A26 (OH^- form) resin. Equations (2)–(4), below, illustrate the major reactions occurring during adsorption, formic acid recovery, and resin regeneration, respectively. To avoid formation of the formic acid–water azeotrope, HCl in diethyl ether rather than aqueous HCl was used in the recovery step. The formic acid/diethyl ether mixture from the second ion-exchange step is then separated in a distillation column. The consumption of HCl and NaOH in the ion-exchange columns was assumed to be approximately 1 mol per mol of formic acid produced.

$$MDEAH^+ + HCO_3^- + H_2 \leftrightarrow MDEAH^+ + HCOO^- + H_2O \qquad (1)$$

$$MDEAH^+ + HCOO^- + Resin^+OH^- \leftrightarrow Resin^+ + HCOO^- + MDEA + H_2O \quad (2)$$

$$Resin^+ + HCOO^- + HCl\ (in\ (C_2H_5)_2O) \leftrightarrow Resin^+Cl^- + HCOOH \quad (3)$$

$$Resin^+Cl^- + NaOH\ (aq) \leftrightarrow Resin^+OH^- + NaCl\ (aq) \quad (4)$$

The mass and energy balances generated from the Aspen Plus model, together with the pricing assumptions listed in **Table 52**, were used to estimate variable operating costs and to generate the life-cycle inventory (LCI) for greenhouse gas (GHG) emissions. Capital costs for major equipment were estimated using Aspen Process Economic Analyzer (v14). A simplified annualized cost method was applied to determine the minimum selling price (MSP) of formic acid.

OpenLCA, coupled with supply-chain LCI data from NETL and Ecoinvent v3.8, was used to estimate cradle-to-gate GHG emissions (**Figure 91**). The functional unit was defined as 1 kg of formic acid. Electricity from the NGCC plant was treated as a by-product, and its environmental burden was accounted for using the displacement method. A similar approach was applied to estimate MSP and GHG emissions for the SC3M route using mass and energy balances (**Table 53**) and capital cost data for a thermochemical SC^3M process reported by Cuevas-Castillo et al. (Cleaner Engineering and Technology 26, 100929, 2025).

Table 52. Mass and energy balance and pricing assumptions for the IC^3M process.

	price	Consumption (per kg formic acid)
Catalyst (3wt% Pd)	$49.1/kg	0.0014 kg
Resin	$200/kg	0.0006 kg
HCl	$1.02/kg	0.7906 kg
NaOH	$0.44/kg	0.8672 kg
Hydrogen	$1-4/kg	0.0437 kg

Table 53. Mass and energy balance and pricing assumptions for the SC^3M process.

	price	Consumption (per kg formic acid)
Catalyst (Ru)	$964/kg	2.7E-6 kg
Catalyst (Ph)	$653/kg	1.4E-6 kg
Methanol	$1/gallon	0.0615 kg
Hydrogen	$1-4/kg	0.0620 kg
Carbon dioxide (pure)	$80/metric ton	1.0136 kg

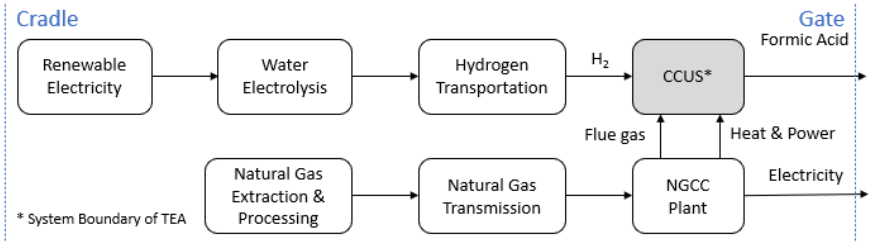


Figure 91. System boundary for TEA and LCA.

The TEA and LCA results are presented in **Figures 92** and **93**. At the current state of technology (SOT), the IC3M route exhibits an estimated MSP for formic acid approximately 2.5 times higher than the market price, while achieving a cradle-to-gate GHG emission reduction of approximately 60% relative to the market baseline. Hydrogen and utility costs have minor impacts on MSP due to their relatively low consumption, which is also significantly lower than in the SC3M route. However, in the IC^{3}M configuration, the consumption of HCl and NaOH during ion exchange accounts for more than 80% of the total production cost and cradle-to-gate GHG emissions, rendering IC3M less competitive than SC3M at present. If formic acid can be recovered without reliance on costly ion-exchange technology, IC3M could outperform SC3M and achieve an MSP comparable to current market values.

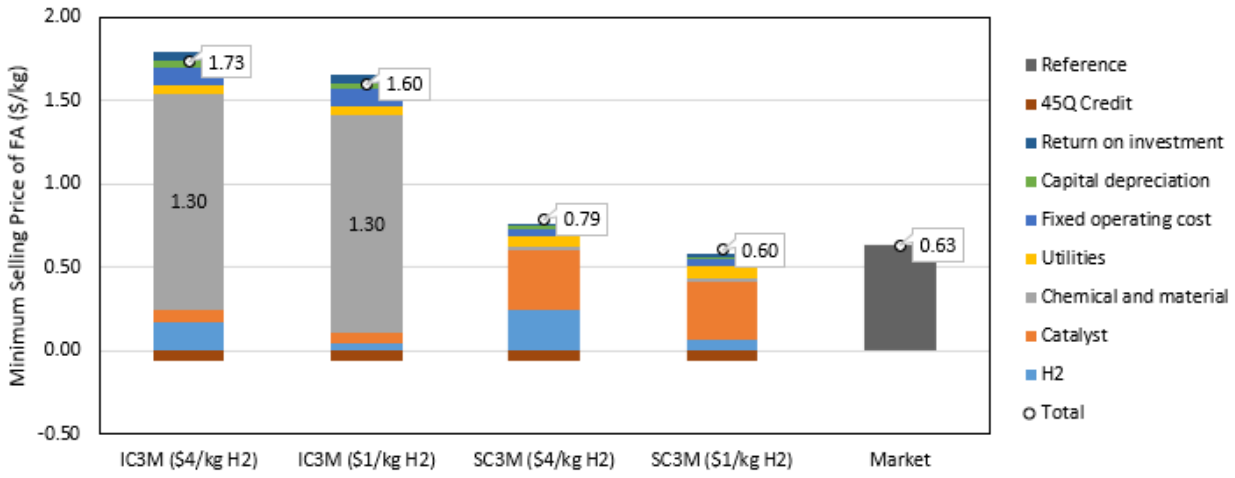


Figure 92. Estimated MSP of formic acid.

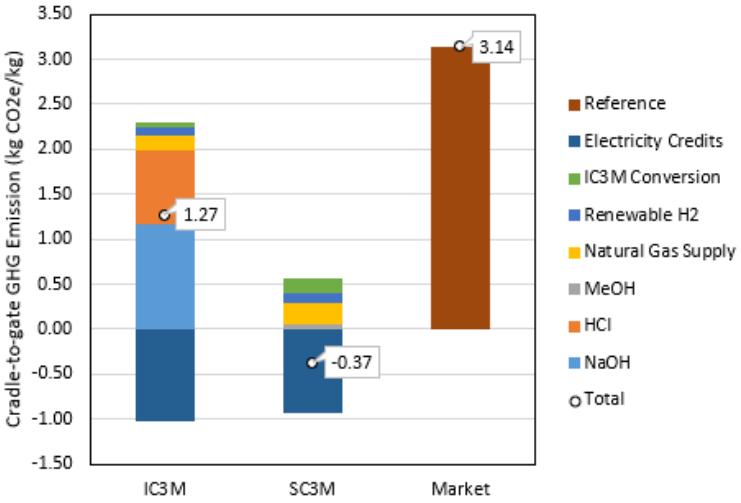


Figure 93. Estimated cradle-to-gate GHG emissions of formic acid.

Completion of the TEA and LCA for formic acid production via IC3M, along with comparison to the SC3M route and market baseline, fulfills the FY26 Q1 milestones:

"[T5] Report state-of-technology performance and costing for each of the three major catalytic pathways being investigated.
[T6] Report full environmental LCA for the process and compare to two baseline cases."

To recap, TEA and LCA for the other two catalytic pathways (methanol and methane) were completed last year. **Figures 94–96** summarize these results, which indicate that IC3M can potentially increase process efficiency by up to 10%, reduce capital investment by up to 55%, lower MSP by up to 28%, and decrease life-cycle GHG emissions by up to 47% relative to SC3M approaches for methanol and methane production. Further details are discussed earlier in this report.

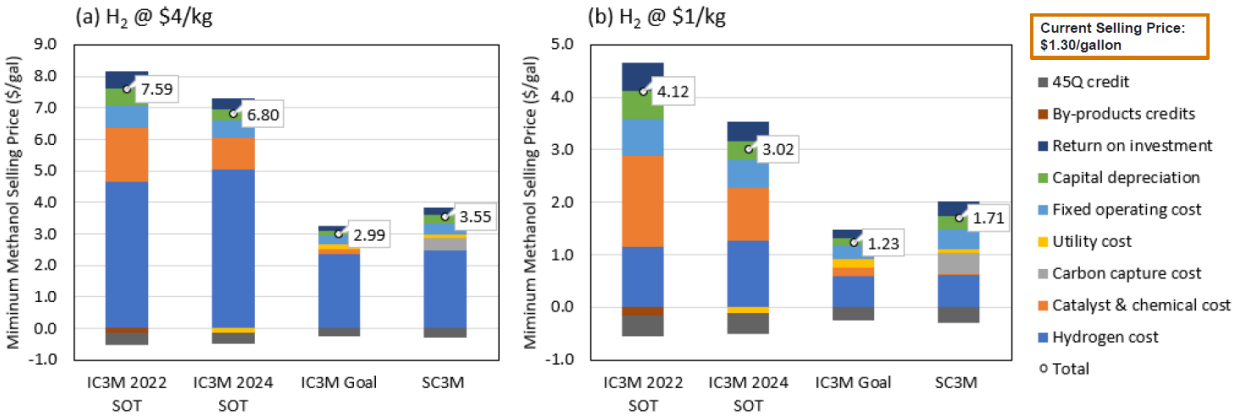


Figure 94. Estimated MSP of methanol.

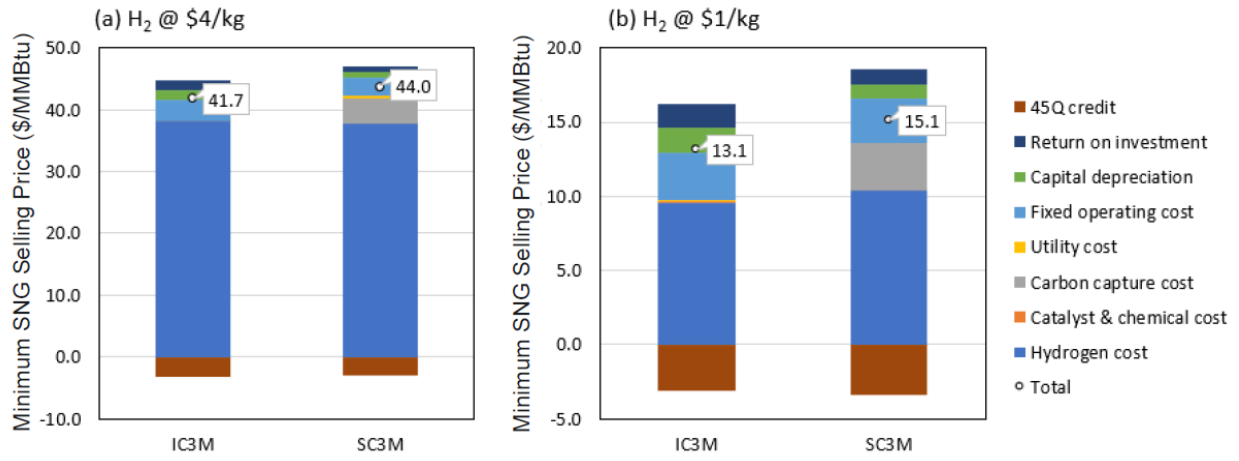


Figure 95. Estimated MSP of methane.

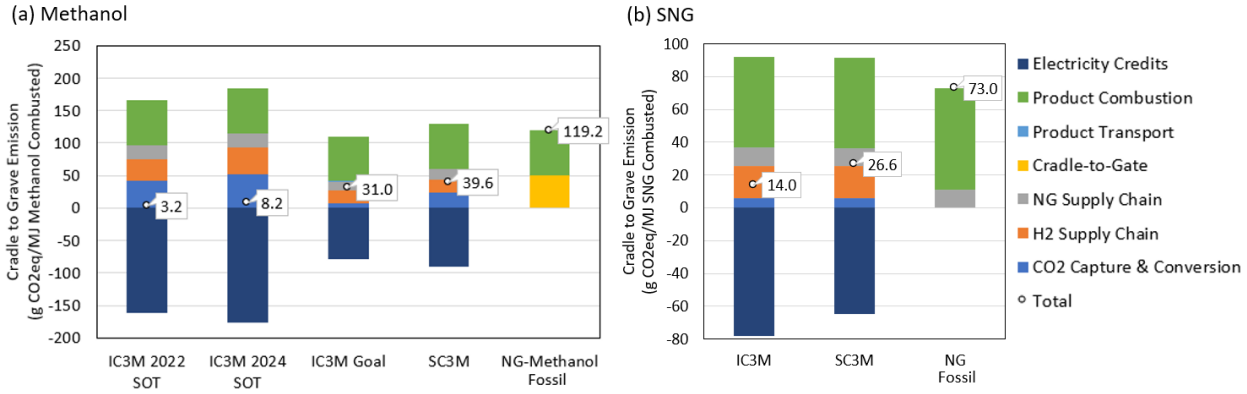


Figure 96. Cradle-to-grave GHG emissions for (a) methanol and (b) methane cases.

I.4 Cost Status

The project budget totals $3.30 M over three years, with 20% cash cost share provided by SoCalGas ($2.64 M DOE funding and $660,000 SoCalGas cost share). As shown in the table below, total project costs remained within budget. There is $51,357 in unspent DOE funds and $851 in remaining CRADA partner funding are still available for potential future work (e.g., IC3M "3.0" as proposed) or redirected scope.

Total Budget Variance Reporting ($)			
	Spend Plan	Costs	Variance
3-Year Project			
DOE-HGEO	$2,640,000	$2,588,643	1.9%
CRADA Partner (SoCalGas)	$660,00	$659,149	0.13%
Total	$3,300,000	$3,247,792	1.6%

Total Funding Received ($)	
3-Year Project	
DOE-HGEO	$2,640,000
CRADA Partner (SoCalGas)	$660,00
Total	$3,300,000

II Issues, Risks, and Mitigation

None

III Changes in Approach

None

IV Changes in Key Personnel

None.

V Project Output

Presentations:

- An integrated capture and utilization approach to produce CO_2-derived chemicals in a post-combustion capture solvent (Invited talk), Division of Energy and Fuels, Session: Closing the Carbon Cycle, Presented by Jothi Kothandaraman at ACS Spring 2023, Indianapolis, IN.
- Integrated CO_2 Capture and Conversion into Value-added Products using an Economically Viable Post-combustion CO_2 Capture Solvent (Invited talk), Division of Energy and Fuels, Session: Closing the Carbon Cycle, Presented by Jothi Kothandaraman at ACS Spring 2025, San Diego, CA.

Accepted Manuscripts:

In the DOE-TCF project (FY20-22), that led to this current project, two manuscripts were published in high impact journals:

- "Integrated Capture and Conversion of CO_2 to Methanol in a Post-Combustion Capture Solvent: Heterogeneous Catalysts for Selective C-N Bond Cleavage" in Adv. Energy Mater., 2022, 2202369 [1]
- "Integrated Capture and Conversion of CO_2 to Methane Using a Water-lean, Post-Combustion CO2 Capture Solvent" in ChemSusChem, 2021,14,4812– 4819 [2]

In the current DOE-HGEO funded effort, the following manuscripts have been **published**:

- Selective and Stable Pt Catalysts for the Catalytic Conversion of Captured CO_2 to Methanol in an Advanced Water-Lean Post Combustion Solvent, **ACS Catalysis**, 2026, DOI: 10.1021/acscatal.5c07059
- Single Step Simultaneous Production of Methanol and Glycol from Epoxide, CO_2 and H_2 Using Heterogeneous Cu-Based Catalysts, **Journal of Materials Chemistry A**, 2026, DOI: 10.1039/D5TA08763E
  The Relationship Between Catalyst and Solvent in Hydrogenation via Condensed Phase Heterogeneous Catalysis, **ChemSusChem**, 2026, DOI: 10.1002/cssc.70614
- Combined Capture and Conversion of CO_2 to Methanol in a Post Combustion Capture Solvent, **US Patent Application**, 2025, App. No. 18/354,571
- Single-Pass Demonstration of Integrated Capture and Catalytic Conversion of CO_2 from Simulated Flue Gas to Methanol in a Water-Lean Carbon Capture Solvent, **ACS Omega**, 2024, DOI: 10.1021/acsomega.4c06919
- Mechanistic Insights to Drive Catalytic Hydrogenation of Formamide Intermediates to Methanol via Deaminative Hydrogenation, **Frontiers in Energy Research**, 2023, DOI: 10.3389/fenrg.2023.1158499

The following additional manuscripts are **in progress or submitted**:

- Techno-economic and Life-cycle Analyses of Energy-Efficient Carbon Capture and Utilization Platform: Integrated Capture and Conversion of CO_2 into Materials (IC_3M) – <u>In peer review</u>
- Towards a Predictive Understanding of Solvent and Catalyst Design for Reactive Carbon Capture – <u>In peer review</u>
- Coupling Amine-Based CO_2 Capture with Pd/C Hydrogenation: Formate Production and Process-

Scale Feasibility – In peer review
- Indispensable roles of Rh and Fe in multi-functional bimetallic CO_2 hydrogenation catalysts for ethanol production (WSU lead) – Drafted
- Integrated CO_2 to Methanol: Manuscripts in progress focusing on catalyst development – Drafting

Awarded United States Patents:

The DOE-TCF project (FY20–22), which led to the current project, resulted in the award of two patents.
- U.S. patent 10,961,173
- U.S. patent 11,492,302

Media Coverage:
Rob Dagle, Dave Heldebrant, Yuan Jiang and Dushyant Barpaga were quoted/featured in a CNBC article titled "New technique from U.S. national lab promises to strip carbon dioxide emissions from power plants and factories at record-low cost". The article highlights recent PNNL publications related to carbon capture, utilization, and sequestration.

https://www.cnbc.com/2023/01/24/new-technique-from-us-national-lab-to-remove-co2-at-record-low-cost.html

VI Project Schedule

The milestones for the project are shown in **Table 18**. These completion dates for these milestones are with a January 1, 2023 start date.

Project start date: January 1, 2023
Project end date: December 31, 2025

Table 54. Project activity description for a 36 month period of performance (task number in brackets).

	FY23			FY24				FY25				FY26
Research Activity Description	Q2	Q3	Q4	Q1	Q2	Q3	Q4	Q1	Q2	Q3	Q4	Q1
[T1] Synthesize catalysts and test for conversion of captured CO_2 to EEMPA N-formamide (step A).												
[T1] Evaluate the catalyst/solvent system at temperature below 100 °C to produce formate.												
[T1] Identify catalyst formulations that leads to at least 95% selectivity for C-N cleavage to produce methanol (Step B).												
HGEO Annual Review												
Budget period project continuation report due September 30, 2023, with DOE meeting to follow the next month.												
[T6] Preliminary LCA for IC^{3}M process for GHG reduction **[T4] Establish baseline performance of single atom catalyst for gas phase CO_2 conversion to ethanol.**												
[T1] Combine steps A and B, and achieve >20% single pass conversion of captured CO_2 to methanol. Also, assess separability of methanol and at least one other target product to inform TEA												
[T1] Characterize at least 5 new catalyst formulations using NH_3 TPD, and H_2 chemisorption (or XRD) and correlate properties of acid												

and metal sites on methanol productivity												
HGEO Annual Review												
Budget period project continuation report due September 30, 2024, with DOE meeting to follow the next month.												
[T7] A proposed scope of work (SOW) for the next phase of IC3M development ("IC3M 3.0") will be drafted and proposed. This SOW will comprise of project objectives, goals, tasks, and schedule of milestones. This will first be developed (due by Nov 15, 2024) for discussions with DOE in PowerPoint form, and then included as text in the quarterly report after iteration (due by Jan 31, 2025).												
[T2] Coproduce methanol and glycol in the presence of a post combustion capture solvent. Sequential reactions will be performed to produce >90% yield for cycle carbonate from epoxide and CO_2, which then will be hydrogenated in the presence of a catalyst to produce methanol and glycol.												
[T3] Improve the rate of hydrogenation of condensed phase CO_2 to methane comparable to or better than gas phase reaction and achieve >90% single pass conversion												
Milestone #1 **[T4] Demonstrate if catalyst can**												

achieve at least 10% CO_2 single pass conversion with >70% selectivity to ethanol in the gas phase. ***Milestone #2*** **[T4] Determine if catalyst can achieve at least 10% CO_2 single pass conversion with >20% selectivity to ethanol in the liquid phase.** ***Decision point:*** **If unable to meet both criteria, we will down-select ethanol as a potential product to further develop in this project (thus down-selecting Task 4). In this scenario, we will re-scope the last Task 4 related milestone (currently due Sept 30, 2025) at this time and redirect this scope to support methanol synthesis (Task 1).**												
[T1] Using the knowledge obtained from previous milestones/tasks, select capture solvent/catalyst/conditions to achieve single pass conversion of at least >50% and selectivity >90% to methanol in a continuous flow system												
[T1] Assess at least 10 commercially available/inexpensive amine-based solvents, targeting methanol performance of at least 50% relative to the EEMPA baseline case												
HGEO Annual Review												
[T5] Report state of technology performance and costing for each of the three												

major catalytic pathways being investigated. **[T6] Report full environmental LCA for process and compare to two baseline cases.**												
Final Report due January 31, 2026 (30 days from project end date).												

VII References

[1] J. Kothandaraman, J.S. Lopez, Y. Jiang, E.D. Walter, S.D. Burton, R.A. Dagle, D.J. Heldebrant, Integrated Capture and Conversion of CO2 to Methanol in a Post-Combustion Capture Solvent: Heterogeneous Catalysts for Selective C N Bond Cleavage, Advanced Energy Materials, (2022) 2202369.

[2] J. Kothandaraman, J. Saavedra Lopez, Y. Jiang, E.D. Walter, S.D. Burton, R.A. Dagle, D.J. Heldebrant, Integrated Capture and Conversion of CO2 to Methane Using a Water-lean, Post-Combustion CO2 Capture Solvent, ChemSusChem, 14 (2021) 4812-4819.

[3] J. Kothandaraman, D.J. Heldebrant, Catalytic coproduction of methanol and glycol in one pot from epoxide, CO2, and H2, RSC Advances, 10 (2020) 42557-42563.

[4] X. Ye, C. Yang, X. Pan, J. Ma, Y. Zhang, Y. Ren, X. Liu, L. Li, Y. Huang, Highly Selective Hydrogenation of CO2 to Ethanol via Designed Bifunctional Ir1–In2O3 Single-Atom Catalyst, Journal of the American Chemical Society, 142 (2020) 19001-19005.

[5] R.A. Dagle, A.D. Winkelman, K.K. Ramasamy, V. Lebarbier Dagle, R.S. Weber, Ethanol as a renewable building block for fuels and chemicals, Industrial & Engineering Chemistry Research, 59 (2020) 4843-4853.

[6] X. Wang, P.J. Ramírez, W. Liao, J.A. Rodriguez, P. Liu, Cesium-Induced Active Sites for C–C Coupling and Ethanol Synthesis from CO2 Hydrogenation on Cu/ZnO(000$\bar{1}$) Surfaces, Journal of the American Chemical Society, 143 (2021) 13103-13112.

[7] S. Bai, Q. Shao, P. Wang, Q. Dai, X. Wang, X. Huang, Highly Active and Selective Hydrogenation of CO2 to Ethanol by Ordered Pd–Cu Nanoparticles, Journal of the American Chemical Society, 139 (2017) 6827-6830.

[8] Y. Lou, F. jiang, W. Zhu, L. Wang, T. Yao, S. Wang, B. Yang, B. Yang, Y. Zhu, X. Liu, CeO2 supported Pd dimers boosting CO2 hydrogenation to ethanol, Applied Catalysis B: Environmental, 291 (2021) 120122.

[9] K. Zheng, Y. Li, B. Liu, F. Jiang, Y. Xu, X. Liu, Ti-doped CeO2 Stabilized Single-Atom Rhodium Catalyst for Selective and Stable CO2 Hydrogenation to Ethanol, Angewandte Chemie International Edition, 61 (2022) e202210991.

[10] T.J. Skone, G. Schivley, M. Jamieson, J. Marriott, G. Cooney, J. Littlefidld, M. Mutchek, M. Krynock, Life Cycle Analysis: Natural Gas Combined Cycle (NGCC) Power Plant, National Energy Technology Laboratory, 2018.

[11] NETL, NETL Life Cycle Inventory Data – Unit Process: Methanol production from natural gas. Last Updated: August 2013 (version 01). www.netl.doe.gov/LCA, U.S. Department of Energy, National Energy Technology Laboratory, 2013.
[12] J. Kothandaraman, J.S. Lopez, Y. Jiang, E.D. Walter, S.D. Burton, R.A. Dagle, D.J. Heldebrant, Integrated Capture and Conversion of CO2 to Methanol in a Post-Combustion Capture Solvent: Heterogeneous Catalysts for Selective C□N Bond Cleavage, Advanced Energy Materials, 12 (2022) 2202369.
[13] G. Zang, P. Sun, A. Elgowainy, M. Wang, Technoeconomic and Life Cycle Analysis of Synthetic Methanol Production from Hydrogen and Industrial Byproduct CO2, Environmental Science & Technology, 55 (2021) 5248-5257.
[14] A. Elgowainy, E.D. Frank, P. Vyawahare, C. Ng, A. Bafana, A. Burnham, P. Sun, h. Cai, U. Lee, K. Reddi, M. Wang, Hydrogen Life-Cycle Analysis in Support of Clean Hydrogen Production, Argonne National Laboratory, 2022.
[15] Methanol-Institute, Carbon Footprint of Methanol, Methanol Institute, 2022.
[16] M.A.S.S. Ravagnani, M.H.M. Reis, R.M. Filho, M.R. Wolf-Maciel, Anhydrous ethanol production by extractive distillation: A solvent case study, Process Saf. Environ. Prot., 88 (2010) 67-73.
[17] C. Molinet-Chinaglia, S. Shafiq, P. Serp, Low Temperature Sabatier CO2 Methanation, ChemCatChem, 16 (2024).
[18] S. Chen, A.M. Abdel-Mageed, M. Dyballa, M. Parlinska-Wojtan, J. Bansmann, S. Pollastri, L. Olivi, G. Aquilanti, R.J. Behm, Raising the CO(x) Methanation Activity of a Ru/gamma-Al(2) O(3) Catalyst by Activated Modification of Metal-Support Interactions, Angew. Chem. Int. Ed., 59 (2020) 22763-22770.
[19] Y. Jiang, P.M. Mathias, C.J. Freeman, J. Swisher, R.F. Zheng, G.A. Whyatt, D.J. Heldebrant, Techno-economic comparison of various process configurations for post-combustion carbon capture using a single-component water-lean solvent, International Journal of Greenhouse Gas Control, 106 (2021) 103279.
[20] J. Kothandaraman, J.S. Lopez, Y. Jiang, E.D. Walter, S.D. Burton, R. Dagle, D.J. Heldebrant, Integrated Capture and Conversion of CO2 to Methane Using a Water-lean, Post-Combustion CO2 Capture Solvent, ChemSusChem, 14 (2021) 4812-4819.
[21] P. Marchetti, M.F. Jimenez Solomon, G. Szekely, A.G. Livingston, Molecular Separation with Organic Solvent Nanofiltration: A Critical Review, Chemical Reviews, 114 (2014) 10735-10806.
[22] L.M. Vane, Review: Membrane Materials for the Removal of Water from Industrial Solvents by Pervaporation and Vapor Permeation, Journal of Chemical Technology and Biotechnology, 94 (2019) 343-365.
[23] R.E. James, D. Keairns, M. Turner, M. Woods, N. Kuehn, A. Zeolle, Cost and Performance Baseline for Fossil Energy Plants Volume 1: Bituminous Coal and Natural Gas to Electricity, National Energy Technology Laboratory, United States, 2019.
[24] Sulzer, Membrane Technology, Sulzer Chemtech, 2025.
[25] W.L. Becker, M. Penev, R.J. Braun, Production of Synthetic Natural Gas From Carbon Dioxide and Renewably Generated Hydrogen: A Techno-Economic Analysis of a Power-to-Gas Strategy, Journal of Energy Resources Technology, 141 (2019) 021901.
[26] S&PGlobal, Process Economics Program, 2020.
[27] K.M. Van Allsburg, F.G. Baddour, L. Snowden-Swan, CatCost Documentation and User Guide V 1.1.0, National Renewable Energy Laboratory, 2021.
[28] IPCC, Climate Change 2022: Mitigation of Climate Change. Contribution of Working Group III to the Sixth Assessment Report of the Intergovernmental Panel on Climate Change, 2022.

[29] NETL, NETL Life Cycle Inventory Data – Unit Process: Methanol production from natural gas. Last Updated: August 2013 (version 01), U.S. Department of Energy, National Energy Technology Laboratory, 2013.
[30] M. Jamieson, T.J. Skone, M. Krynock, NETL CO2U LCA Guidance Toolkit - Version 2.1, National Energy Technology Laboratory (NETL), Pittsburgh, PA, Morgantown, WV, and Albany, OR (United States), 2022.
[31] M. Wang, A. Elgowainy, U. Lee, K. Beak, A. Bafana, P.T. Benavides, A. Burnham, etc., Greenhouse gases, Regulated Emissions, and Energy use in Technologies Model ® (2022 Excel), USDOE Office of Energy Efficiency and Renewable Energy (EERE), 2022.
[32] M. Penev, G. Saur, C. Hunter, J. Zuboy, H2A Hydrogen Production Model: Version 3.2018 User Guide (DRAFT), National Renewable Energy Laboratory, 2018.
[33] E. Penrod, DOE doubles down on $1/kg clean hydrogen, sets sights on additional hydrogen cost targets, Utility Dive, 2024.
[34] Y. Jiang, P. Mathias, F. Zheng, C.J. Freeman, D. Barpaga, D. Malhotra, P. Koech, A. Zwoster, D.J. Heldebrant, Energy-effective and low-cost carbon capture from point-sources enabled by water-lean solvents, Journal of Cleaner Production, 388 (2023) 135696.
[35] A. Goguet, F. Meunier, J. Breen, R. Burch, M. Petch, A. Faurghenciu, Study of the origin of the deactivation of a Pt/CeO catalyst during reverse water gas shift (RWGS) reaction, Journal of Catalysis, 226 (2004) 382-392.
[36] J. Kothandaraman, D.J. Heldebrant, Catalytic coproduction of methanol and glycol in one pot from epoxide, CO_2, and H_2, RSC Adv., 10 (2020) 42557-42563.
[37] B.A. Fayisa, Y. Yang, Z. Zhen, M.-Y. Wang, J. Lv, Y. Wang, X. Ma, Engineered Chemical Utilization of CO2 to Methanol via Direct and Indirect Hydrogenation Pathways: A Review, Ind. Eng. Chem. Res., 61 (2022) 10319-10335.
[38] F. Li, L. Wang, X. Han, Y. Cao, P. He, H. Li, Selective hydrogenation of ethylene carbonate to methanol and ethylene glycol over Cu/SiO2 catalysts prepared by ammonia evaporation method, Int. J. Hydrogen Energy, 42 (2017) 2144-2156.
[39] A. Alvarez, A. Bansode, A. Urakawa, A.V. Bavykina, T.A. Wezendonk, M. Makkee, J. Gascon, F. Kapteijn, Challenges in the Greener Production of Formates/Formic Acid, Methanol, and DME by Heterogeneously Catalyzed CO_2 Hydrogenation Processes, Chem. Rev., 117 (2017) 9804-9838.
[40] K. Stangeland, H.L. Li, Z.X. Yu, Thermodynamic Analysis of Chemical and Phase Equilibria in CO Hydrogenation to Methanol, Dimethyl Ether, and Higher Alcohols, Ind. Eng. Chem. Res., 57 (2018) 4081-4094.
[41] O.A. Ojelade, S.F. Zaman, A Review on Pd Based Catalysts for CO Hydrogenation to Methanol: In-Depth Activity and DRIFTS Mechanistic Study, Catal. Surv. Asia., 24 (2020) 11-37.
[42] G. Pacchioni, From CO2 to Methanol on Cu/ZnO/Al2O3 Industrial Catalyst. What Do We Know about the Active Phase and the Reaction Mechanism?, ACS Catal., 14 (2024) 2730-2745.
[43] H. Zhang, J. Chen, X. Han, Y. Pan, Z. Hao, S. Tang, X. Zi, Z. Zhang, P. Gao, M. Li, J. Lv, X. Ma, High-Performance Cu/ZnO/Al2O3 Catalysts for CO2 Hydrogenation to Methanol, Ind. Eng. Chem. Res., 63 (2024) 6210-6221.
[44] K. Stangeland, H. Li, Z. Yu, CO2 hydrogenation to methanol: the structure–activity relationships of different catalyst systems, Energ. Ecol. Environ., 5 (2020) 272-285.

[45] P.H. Finger, T.A. Osmari, Natalia M. Cabral, J.M.C. Bueno, J.M.R. Gallo, Direct synthesis of Cu supported on mesoporous silica: Tailoring the Cu loading and the activity for ethanol dehydrogenation, Catal. Today, 381 (2021) 26-33.
[46] L.H. Vieira, M.A. Rossi, L.F. Rasteiro, J.M. Assaf, E.M. Assaf, CO(2) Hydrogenation to Methanol over Mesoporous SiO(2)-Coated Cu-Based Catalysts, ACS Nanosci. Au., 4 (2024) 235-242.
[47] W. Wang, X. Zhang, S. Weng, C. Peng, Tuning Catalytic Activity of CO(2) Hydrogenation to C1 Product via Metal Support Interaction Over Metal/Metal Oxide Supported Catalysts, ChemSusChem, 17 (2024) e202400104.
[48] M. Salavati-Niasari, F. Davar, Synthesis of copper and copper(I) oxide nanoparticles by thermal decomposition of a new precursor, Mater. Lett., 63 (2009) 441-443.
[49] Z. Bian, W. Zhong, Y. Yu, B. Jiang, S. Kawi, Cu/SiO2 derived from copper phyllosilicate for low-temperature water-gas shift reaction: Role of Cu+ sites, Int. J. Hydrog. Energy., 45 (2020) 27078-27088.
[50] R. van den Berg, G. Prieto, G. Korpershoek, L.I. van der Wal, A.J. van Bunningen, S. Laegsgaard-Jorgensen, P.E. de Jongh, K.P. de Jong, Structure sensitivity of Cu and CuZn catalysts relevant to industrial methanol synthesis, Nat. Commun., 7 (2016) 13057.
[51] S. Kattel, P.J. Ramirez, J.G. Chen, J.A. Rodriguez, P. Liu, Active sites for CO2 hydrogenation to methanol on Cu/ZnO catalysts, Science, 355 (2017) 1296-1299.
[52] Y. Wang, S. Kattel, W. Gao, K. Li, P. Liu, J.G. Chen, H. Wang, Exploring the ternary interactions in Cu-ZnO-ZrO(2) catalysts for efficient CO(2) hydrogenation to methanol, Nat. Commun., 10 (2019) 1166.
[53] R. Wang, H. Wang, X. Weng, J. Dai, Z. Gong, C. Zhao, J. Lu, Y. Cui, X. Bao, Exploring the phase transformation in ZnO/Cu(111) model catalysts in CO2 hydrogenation, J Energy Chem, 60 (2021) 150-155.
[54] H. Chen, S. Xie, Z. Jiang, J. Xu, M. Zhu, Cu/ZnO/Al2O3 Catalyst Promoted with Amorphous MgO for Enhanced CO2 Hydrogenation to Methanol, ChemCatChem, 17 (2025).
[55] L. Wang, U.J. Etim, C. Zhang, L. Amirav, Z. Zhong, CO(2) Activation and Hydrogenation on Cu-ZnO/Al(2)O(3) Nanorod Catalysts: An In Situ FTIR Study, Nanomater., 12 (2022).
[56] J. Ding, T. Popa, J. Tang, K.A.M. Gasem, M. Fan, Q. Zhong, Highly selective and stable Cu/SiO2 catalysts prepared with a green method for hydrogenation of diethyl oxalate into ethylene glycol, Appl. Catal. B: Environ, 209 (2017) 530-542.
[57] R.A. Shiels, C.W. Jones, Homogeneous and heterogeneous 4-(N,N-dialkylamino)pyridines as effective single component catalysts in the synthesis of propylene carbonate, J. Mol. Catal. A: Chem., 261 (2007) 160-166.
[58] J. Sun, W.G. Cheng, Z.F. Yang, J.Q. Wang, T.T. Xu, J.Y. Xin, S.J. Zhang, Superbase/cellulose: an environmentally benign catalyst for chemical fixation of carbon dioxide into cyclic carbonates, Green Chem., 16 (2014) 3071-3078.
[59] A.H. Chowdhury, P. Bhanja, N. Salam, A. Bhaumik, S.M. Islam, Magnesium oxide as an efficient catalyst for CO 2 fixation and N-formylation reactions under ambient conditions, Mol Catal, 450 (2018) 46-54.
[60] A.A. Marciniak, K.J. Lamb, L.P. Ozorio, C.J.A. Mota, M. North, Heterogeneous catalysts for cyclic carbonate synthesis from carbon dioxide and epoxides, Curr. Opin. Green Sustain. Chem., 26 (2020).
[61] A. Beck, M.A. Newton, L.G.A. van de Water, J.A. van Bokhoven, The Enigma of Methanol Synthesis by Cu/ZnO/Al(2)O(3)-Based Catalysts, Chem. Rev., 124 (2024) 4543-4678.



Pacific Northwest
NATIONAL LABORATORY

Proudly Operated by **Battelle** *Since 1965*

U.S. DEPARTMENT OF
ENERGY

902 Battelle Boulevard
P.O. Box 999
Richland, WA 99352
1-888-375-PNNL (7665)

www.pnnl.gov